REPORT DOCUMENTATION PAGE

AFRL-SR-BL-TR-98-

0605

Public reporting burden for this collection of information is estimated to average 1 hour per response, including the
gathering and maintaining the data needed, and completing and reviewing the collection of information. Send comi
collection of information, including suggestions for reducing this burden, to Washington Headquarters Services, Dir
Davis Highway, Suite 1204, Arlington, VA 22202-4302 and to the Office of Management and Budget, Paperwork Rec

1. AGENCY USE ONLY *(Leave blank)*

2. REPORT DATE

3. REPORT TYPE AND DATES COVERED
Final 15 Apr 93 To 14 Apr 98

4. TITLE AND SUBTITLE
BASIC SOLUTIONS TO CARBON/CARBON OXIDATION: SCIENCE AND TECHNOLOGY

5. FUNDING NUMBERS
F49620-93-1-0311
3484/HS
61103D

6. AUTHOR(S)
Dr. Ian R. Harrison, Dr T-C. Chung, Dr Carlo Pantano
Dr Ljubisa Radovic and Dr Peter Thrower

7. PERFORMING ORGANIZATION NAME(S) AND ADDRESS(ES)
Pennsylvania State University
325 Steidle Building
Unviersity Park, PA 16802

8. PERFORMING ORGANIZATION REPORT NUMBER

9. SPONSORING/MONITORING AGENCY NAME(S) AND ADDRESS(ES)
AFOSR/NL
110 Duncan Ave Room B115
Bolling AFB DC 20332-8050

Maj Hugh C. De Long

10. SPONSORING/MONITORING AGENCY REPORT NUMBER

11. SUPPLEMENTARY NOTES

12a. DISTRIBUTION/AVAILABILITY STATEMENT
DISTRIBU[illegible]MENT A
App[illegible]
Distr[illegible]

12b. DISTRIBUTION CODE

13. ABSTRACT *(Maximum 200 words)*

The goal of this study was to gain a fundamental understanding of the role of boron in carbon oxidation. Boron-doped carbons were synthesized via CVD, ion implantation and high temperature doping ans subsequently characterized. It was found that high temperature doped HOPG carbons were ideal for oxidation studies because their surface could be reproduced, their surface structures were determined and they were able to be characterized by XPS, AFM and SEM. The direct analysis of the chemical structures and atomic arrangements in boron-doped carbon or carbor surfaces by these techniques was critical in determining the effect of boron on carbon oxidation. XPS was utilized in this work to determine the local bonding environment of boron in carbon before and after oxidation. It was necessary to obtain an accurate calibration of the B1s binding energy scale which was accomplished by obtaining photoemission spectra of boron-doped carbons with known structures (local boron bonding environments), such as boron oxide, boron carbide, triphenylboroxine, tourmaline, boric acid, danburite and high temperature boron-doped graphite. All of the aforementioned standards contain boron in a unique bonding envoronment and thus their spectra formulated a complete conversion of B1s binding energies to boron chemical environments which has not been

14. SUBJECT TERMS

DTIC QUALITY INSPECTED 1

15. NUMBER OF PAGES

16. PRICE CODE

17. SECURITY CLASSIFICATION OF REPORT
(U)

18. SECURITY CLASSIFICATION OF THIS PAGE
(U)

19. SECURITY CLASSIFICATION OF ABSTRACT
(U)

20. LIMITATION OF ABSTRACT
(UL)

reported in the past. It was clearly established that a chemical shift for substitutional boron in graphite exists at 186.5 eV with a FWHM of 1.2. The chemical structures of the boron in the standards were related to the binding energy using a Pauling charge distribution model and a modification of the Sanderson electronegativity method. This approach was used to determien whether the B1s binding energy would change depending upon the specific location of boron in the graphite or graphite surface. This model was used, along with XPS, TEM and Raman results, to show that edge sites are preferred lattice sites in graphite for boron substitution.

AF #F49620-93-1-0311

BASIC SOLUTIONS TO CARBON/CARBON OXIDATION: SCIENCE AND TECHNOLOGY

1998 FINAL TECHNICAL REPORT

April 15, 1993 - April 14, 1998

19980908 055

Dr. Ian R. Harrison
Dr. T-C. Chung
Dr. Carlo Pantano
Dr. Ljubisa Radovic
Dr. Peter Thrower

The Pennsylvania State University
325 Steidle Building
University Park, PA 16802

TABLE OF CONTENTS

TASK 1. **SYNTHESIS OF BORON CONTAINING POLYMERS AS B/C CARBON PRECURSORS**

Synthesis of B/C Materials via Boron Containing Precursors 1

ATTACHMENT I Papers:

(a) Poly(acrynitrile-co-vinylcatecholborane): A New Precursor for Carbon Containing B/C, B/N and B/O Species," R. Hu and T. C. Chung,Carbon, 34, 595 (1996).

(b) "Synthesis and Structure Characterization of B/C Materials Prepared by 9 Chlorobora-fluorene Precursor," Raymond Hu and T. C.Chung, Carbon, 34, 1181 (1996).

(c) "Synthesis of B/C Materials from Boron Containing PhenylAcetylides Precursors," M. Chasmawala and T. C. Chung, Carbon, 35, 641 (1997).

(d) "Co-carbonization of 9-Chloroborafluorene and Pitch; Synthesis of B/C Materials," R. Hu and T. C. Chung, Carbon, 35, 1101 (1997).

TASK 2. **PROCESSING OF B/C POLYMERS AND CARBONS**

High-Temperature Doping of Carbon with Boron and Its Effect Upon Oxidation 10

ATTACHMENT II Paper

(e) "Semi-Empirical Studies on Electronic Structures of a Boron-Doped Graphene Layer - Implications on the Oxidation Mechanism," X. Ma, Q. Wang, L.-Q. Chen, W. Cermignani, H. H. Schobert and C. G. Pantano, Carbon, 35**(10-11)**, 1517-1525 (1997).

THEORETICAL CALCULATIONS 17

TASK 2.2 **FIBER FORMATION OF B/C POLYMERS AND TRANSFORMATION TO CARBONS**

Post-spining Modification of Polyacrylonitrile (PAN Precursor Fiber 20

ATTACHMENT III Papers

(f) "New Aspects in the Oxidative Stabilization of Pan-Based Carbon Fibers," A. Gupta and I. R. Harrison, Carbon, 34 **(11)** 1427-1445 (1996)

(g) "New Aspects in the Oxidative Stabilization of Pan-Based Carbon Fibers: II," A. Gupta and I. R. Harrison, Carbon, 35 **(6)** 809-818 (1997)

TASK 3 OXIDATION RESISTANCE OF INHIBITED C/C COMPOSITES

ATTACHMENT IV PAPER (submitted) 53

(h) "Effects of the Substrate on Deposit Structure and Reactivity in the Chemical Vapor Deposition of Carbon

ATTACHMENT V PHOTOGRAPHS

ATTACHMENT VI PAPER (submitted) 93

(i) "On the Role of Substitutional Boron in Carbon Oxidation," L. R. Radovic, M. Karra, K. Skokova and P. A. Thrower (submitted to *Carbon*)

SUMMARY OF TASKS 2.1 AND 3 148

TASK 1.

Synthesis of Boron Containing Polymers as B/C Carbon Precursors

Dr. T.-C. Chung

Title: Synthesis of B/C materials via Boron Containing Precursors

Principal Investigator: T. C. Mike Chung

Senior Research Personnel: R. Hu and M. Chasmawala

Publications:

1. "Poly(acrynitrile-co-vinylcatecholborane): A New Precursor for Carbon Containing B/C, B/N and B/O Species," R. Hu and T. C. Chung, Carbon, 34, 595 (1996).
2. "Synthesis and Structure Characterization of B/C Materials Prepared by 9-Chloroborafluorene Precursor," Raymond Hu and T. C. Chung, Carbon, 34, 1181 (1996).
3. "Synthesis of B/C Materials from Boron Containing PhenylAcetylides Precursors," M. Chasmawala and T. C. Chung, Carbon, 35, 641 (1997).
4. "Co-carbonization of 9-Chloroborafluorene and Pitch; Synthesis of B/C Materials," R. Hu and T. C. Chung, Carbon, 35, 1101 (1997).

Abstract of Objectives and Accomplishments:

The research objective is to develop a new synthetic route to prepare B/C material containing various concentration of substitutional boron and uniform composition distribution. In the past few years, we have discovered two new borane-containing carbon precursors, i.e. (i) boron containing phenyl acetylides and (ii) 9-chloroborafluorene, which can be transformed to B/C materials with upto 10 % substitutional boron in the graphitic structure. Both transformation reactions showed high yields and resulted in B/C materials with highly crystalline layered structure (i.e. large crystallite size and small d-spacing) at relatively low temperature (2200 ^{o}C). In addition, both precursors exihibit catalystic activity in the co-carbonization reaction of FCC-decant oil pitch. By adding small amounts of boron containg precursor, the yield of low temperature anisotropic carbon was dramatically improved, and the graphitization temperature was lowered by several hundred degrees to produce B/C material with large crystal size and low d-spacing, similar to Sp-1 graphite.

Detail Accomplishments

In the modification of carbon (C) materials, boron by far is the most favorable element that can be substituted into the carbon (graphitic) structure to product B/C material. Due to the similarity of atomic size and the ability to form strong tricovalent bonds with adjacent carbons, the substitutional boron minimizes the distortion of lattice and preserve the multi-layer crystalline structure. Although the properties of B/C materials have been extensively interested for very long time, the process of synthesizing these materials has not been improved upon. In the past, the method has been based on doping carbon with boron (boron or boron oxide powders) via solid state diffusion. The diffusional process usually requires very high temperatures (> 2800 ^{o}C) as well as long residence times. As a result of the additional heat treatment during doping, only well ordered crystalline structure was obtained. Several researchers also reported that inhomogeneous distribution arises during the doping process because boron preferentially enters into the most disordered regions of the carbon. Lowell determined that the solid solubility of boron in carbon approached a maximum value of 2.35 % at 2350 ^{o}C and thereafter decreased dramatically with increasing temperature.

Our research in the preparation of B/C materials has been focusing on the precursor approach using the **pre-designed boron containing carbon precursors** which are soluble and melt-processible. By taking into account the chemistry of boron and the mechanism of carbonization, we have tailored several precursors which can be effectively transformed to B/C materials with high yields of carbon and boron and various physical shapes. Equation 1 shows the chemical transformation of 9-chloroborafluorene (CBF) to B/C material.

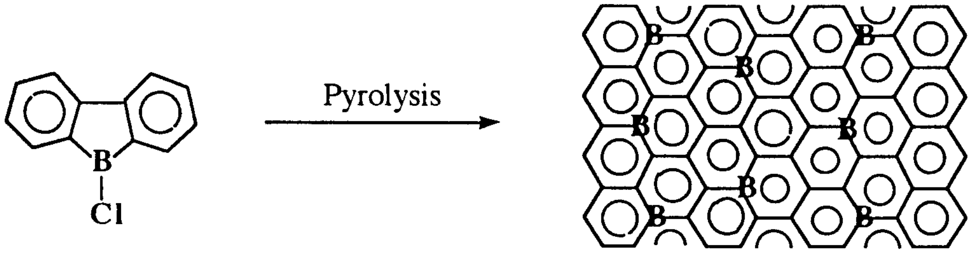

CBF

B/C Material

Equation 1

The principles of using this (CBF) organoborane as precursor were (i) directly provide the basic conjugated aromatic frame work for the B/C material, thus during the aromatic condensation reactions only minimum molecular structure rearrangement is needed, (ii) a planar geometry that has been shown to be a primary requirement for graphitizable carbons, and (iii) the reactive functional group (B-Cl) can be utilized for polymerization (stabilization) at relatively low temperature.

During the thermal transformation process, boron in situ catalyzes graphitization reaction. Only a low pyrolysis temperature (< 1000 °C) is needed to transform the 9-CBF precursor to an uniform B/C material with the substitutional boron in the graphitic structure. With increasing the pyrolysis temperature and time, B/C material increases its crystal size and decreases its d-spacing between interlayers as shown in X-ray diffractions (Figure 1) and summarized in Table 1. At as low as 2300 °C, the B/C material shows an unusually large crystalline size (La > 680 A) with a small d-spacing (3.347 A), smaller than XP-1 (best quality graphite). Almost no change in boron concentration (~ 7 %), similar to that of precursor, was observed even heating B/C material up to 2000 °C. The microtexture of B/C material is strongly dependent on the thermal procedures at low temperature (< 350 °C) prior to carbonization. With the procedures to enhance mesophase concentration, such as via vacuum distillation to remove non-mesogens, the viscous mesophase precursor was completely fusible (processible). Many anisotropic structures were also achieved by various methods, such as mechanical stirring or bubbling with inert gas, during thermal treatment.

The other class of new B/C precursors studied in our laboratory were phenyl acetylides, including three molecules with B/C ratios, 1/8, 1/16 and 1/24, as shown below.

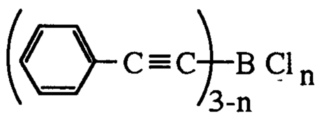

n = 0, 1 and 2

The experimental results show that the initial rate (< 1500 °C) at which the graphitic structure develop is strongly related to the molecular structure of the phenyl acetylides. The formation of non-coplanar molecular structure in the stabilization reaction slows down the graphitization reaction, which can be easily observed in the microstructure (porosity, crystal size, d-spacing, etc.). However, all three precursors show effective transformation reactions to produce the boron-substitutional graphitic (B/C) materials at 2200 °C, despite the significant differences in boron concentration and chemical nature of the precursors. Clearly, boron is not only substitutionally incorporated in the graphitic structure but also enhances the graphitization reaction. Almost no boron was lost during each transformation reactions, which result in three B/C materials with 12, 6 and 4 % of boron contents, respectively.

It is very interesting to note the co-carbonization reaction of B/C precursor with conventional carbon precursors, such as FCC decant oil pitch. The process represents an effective method to tailor B/C materials with desirable morphology and boron content. In a binary system containing both 9-CBF and FCC decant oil pitch, a broad range of B/C materials have been prepared with a pre-determined boron contents (proportional to the ratio between 9-CBF and FCC decant oil pitch) and controllable morphological structures (dependent on the pyrolysis temperature and the ratio between two precursors). At pyrolysis temperature (< 2000 °C), a two-phases morphological structure containing both "order" and "disorder" phases was observed, due to very different carbonization reactivities between two precursors. However, the system gradually becomes one phase at higher temperature. Figure 2 shows the (002) peak of the x-ray diffraction of the final B/C materials at 2000 °C. As the weight % of 9-CBF increases, the (002) peak shifts toward higher angle, i.e. lower d spacing. Interestingly, the calculated d spacing (shown in Table 2) for the sample containing 50 wt % boron precursor (3.369 A) is lower than the value obtained for the pure B/C material (3.374 A) under the same heat treatment. This result provides evidence that the decant oil is acting as a solvent to prevent excess crosslinking of the highly reactive boron precursor and thus improving the crystalline orientation of the material. The (002) peak for the sample containing 10 wt% boron precursor is especially broad with an shoulder resembling the diffraction pattern of the 2000 °C heat treated decant oil pitch, which illustrated that the carbonized residue is composed mainly of an isotropic matrix derived from decant oil. In fact, two peaks were observed for all the mixtures containing less than 30 wt% boron precursor. However, it is important to note that as the amount of boron is increased, d spacing of the isotropic portion shifts towards lower value. The presence of boron in the mixture is catalyzing graphitization even though the two precursor formed carbons with different optical texture. It is possible that high temperature diffusion of boron from the boron rich anisotropic droplets into the boron poor isotropic matrix is enhancing graphitization. Apparently, up to 70 wt% of decant oil pitch can be incorporated in the carbon and still maintain the same high degree of overall crystalline orientation. Interestingly, if we convert weight percent 9-CBF to weight percent boron, the amount at which the material starts to behave homogeneously is about 2.1 wt% B , e.g., the reported equilibrium solid solution concentration of boron in graphite.

To determine the effect of boron on graphitization at high temperatures, the B/C material was further heat treated at 2300 °C. As expected the d spacing decreased with higher heat treatment temperature for all samples as shown in Figure 3 and summarized in Table 3. This decrease in crystallite spacing is accompanied by a dramatic increase in crystal size Lc. For the sample containing 30 wt% boron precursor, the Lc was above the detection limit of the difffractometer at over 1000 A. Amazingly, the number of (002) peaks observed, became one for all cases. Apparently, not only did boron enhance the graphitic structure but it made the mixture of two distinctly different carbons homogeneous. Elemental analysis of the samples showed a decrease in boron content at 2300 °C. For the 30 wt% sample the concentration dropped to 1.44 wt% boron while for the 50 wt% sample it dropped to 2.75 wt% boron. Obviously, the loss of boron does play a role in the enhancement of graphitization as suggested previously.

Table 1. X-ray crystallite parameters and boron content of 9-CBF as function of graphitization tempearture and time.

	Pyrolysis Conditions		X-ray Results			Boron Content
Sample	Temp (°C)	Time (hr)	002 (A)	Lc (A)	La (A)	(Wt %)
BC-1	1000	1	3.461	----	----	7.65
BC-2	1500	1	3.411	----	----	11.39
BC-3	1800	1	3.383	88	----	7.42
BC-4.1	2000	1	3.379	177	336	6.96
BC-4.2	2000	5	3.363	168	297	5.62
BC-4.3	2000	8	3.356	270	321	8.21
BC-5	2300	1	3.347	456	689	3.46

Table 2. X-Ray Diffraction Results of 2000 °C Heat Treated Mixtures

Wt% 9-CBF	d(002) (A)	Lc (A)	# of (002) Peaks Observed
0	3.425	180	1
5	3.423	186	2
10	3.407	119	2
20	3.374	153	2
30	3.369	197	2
50	3.369	209	1
100	3.374	196	1

Table 3. X-Ray Diffraction Results of 2300 °C Heat Treated Mixtures

Wt % 9-CBF	d(002) (A)	Lc (A)	# of (002) Peaks Observed
0	3.403	297	1
5	3.362	415	1
10	3.369	314	1
20	3.363	283	1
30	3.358	>1000	1
50	3.358	578	1
100	3.347	456	1

Figure Caption:

Figure 1. X-ray diffractions of B/C materials prepared by 9-CBF precursor at (a) 1000, (b) 1500, (c) 1800, (d) 2100 and (e) 2300 °C.

Figure 2. X-ray diffraction (002) peak of 9-CBF and FCC decant oil mixture at 2000 °C, (a) 0 wt%, (b) 5 wt%, (c) 10 wt%, (d) 20 wt%, (e) 30 wt%, (f) 50 wt% boron precursor.

Figure 3. X-ray diffraction (002) peak of 9-CBF and FCC decant oil mixture at 2300 °C, (a) 0 wt%, (b) 5 wt%, (c) 10 wt%, (d) 20 wt%, (e) 30 wt%, (f) 50 wt% boron precursor.

Fig 1.

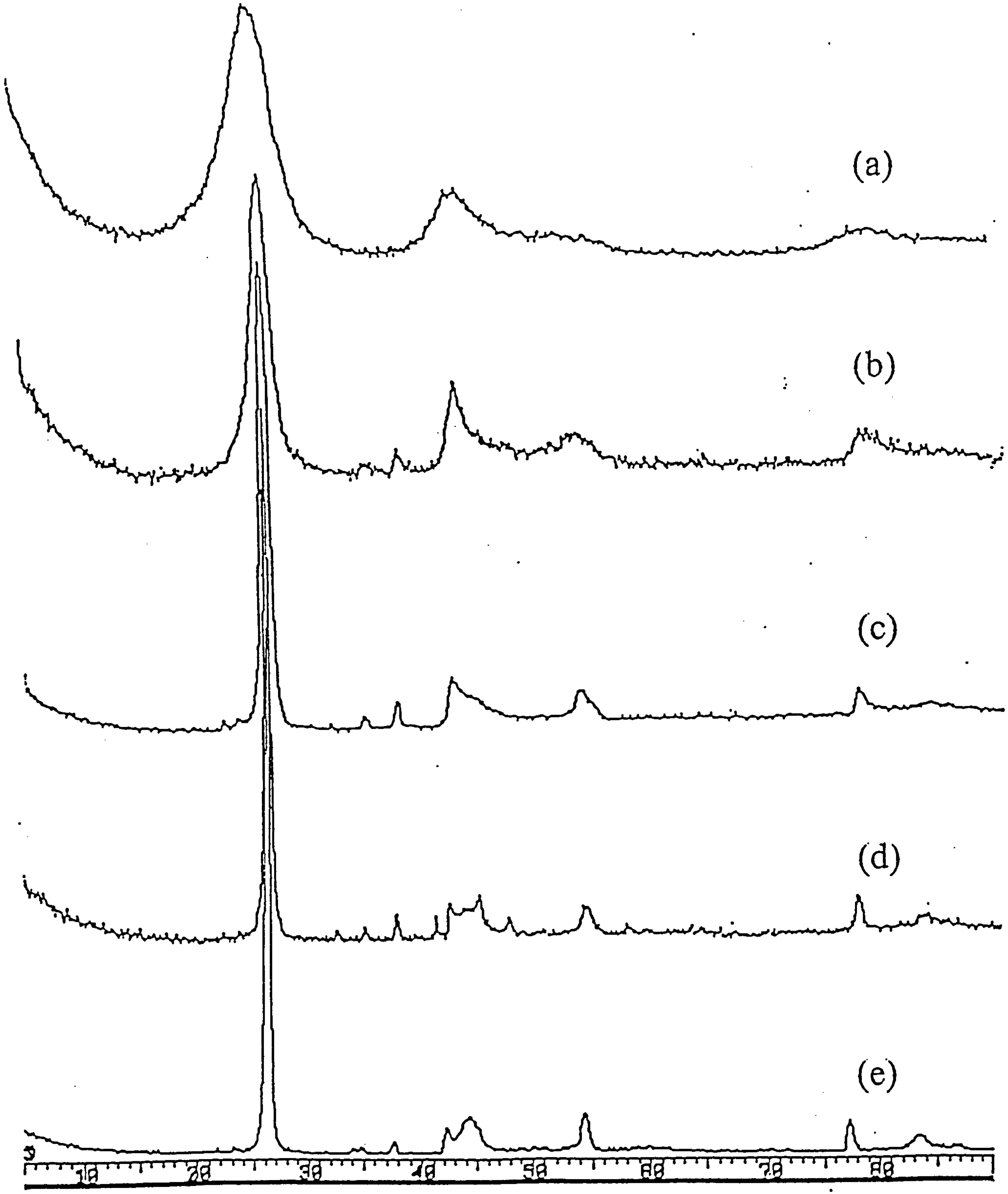

Fig. 2

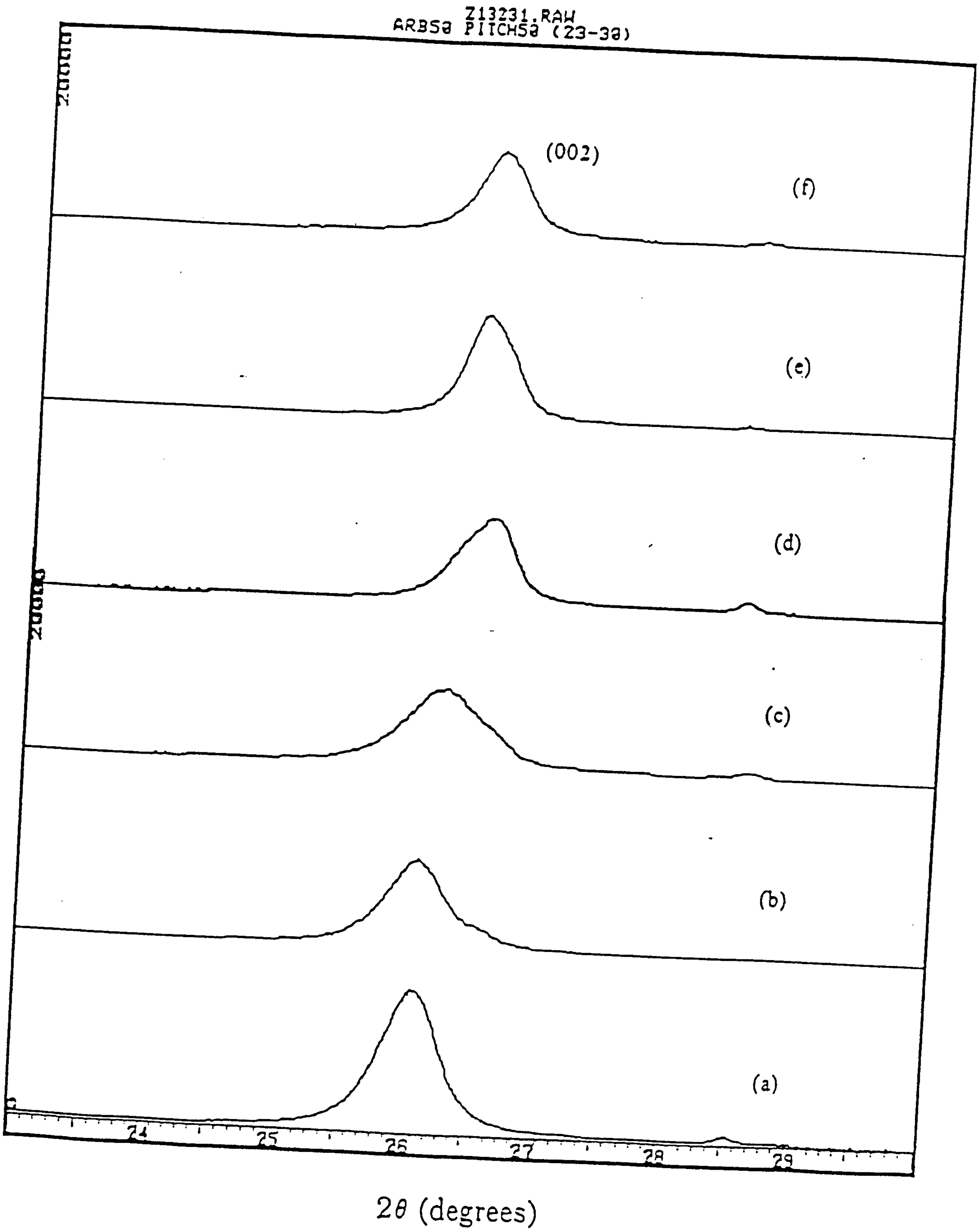
Z13231.RAW
ARB50 PITCH50 (23-30)
20000
20000
(002)
(f)
(e)
(d)
(c)
(b)
(a)
24
25
26
27
28
29
2θ (degrees)

Fig. 3

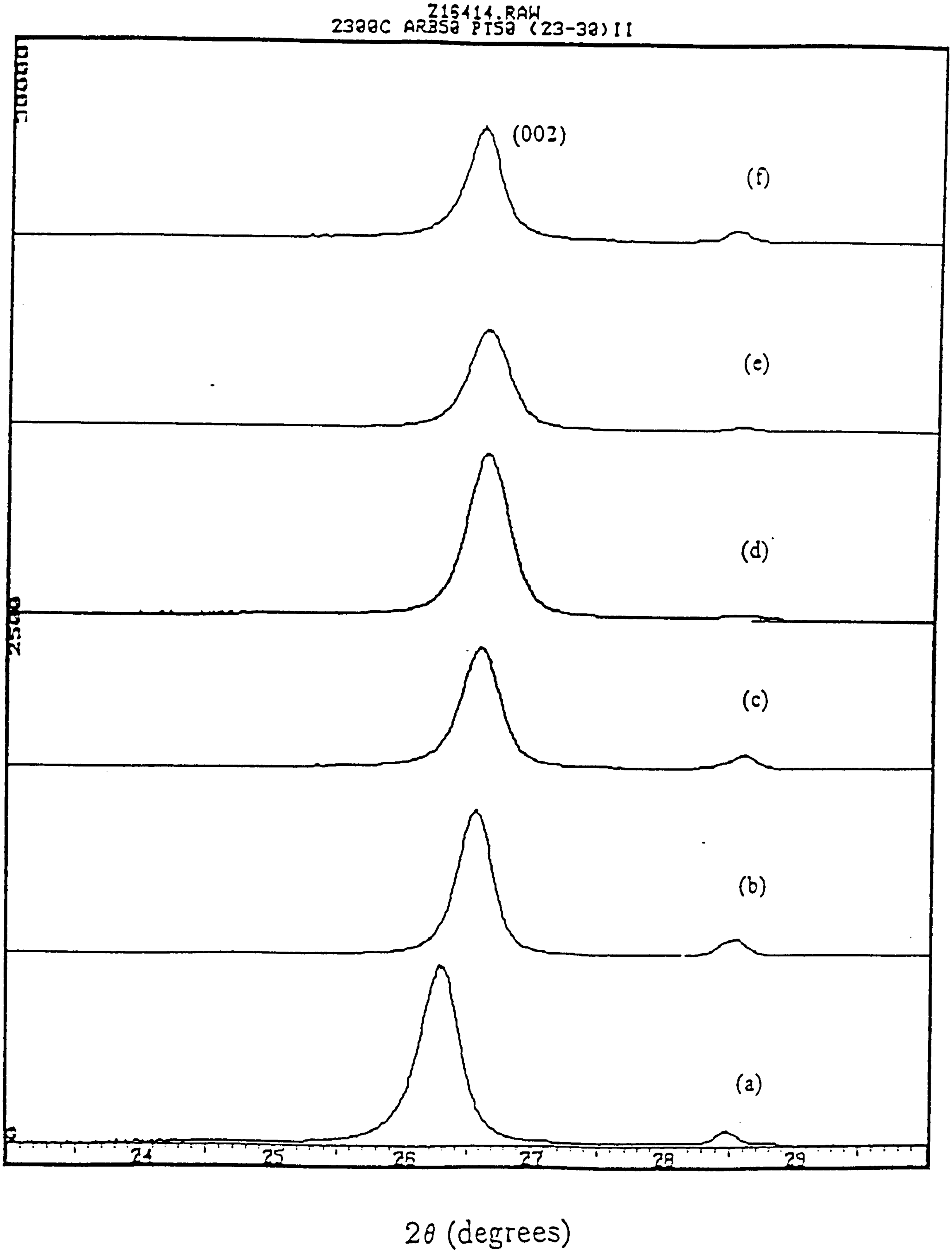
Z16414.RAW
2300C AR350 PT50 (23-30)II
10000
(002)
(f)
(e)
(d)
2500
(c)
(b)
(a)
0
24
25
26
27
28
29
2θ (degrees)

ATTACHMENT I

Papers (a-d)

Pergamon

Carbon Vol. 34, No. 5, pp. 595–600, 1996
Copyright © 1996 Elsevier Science Ltd
Printed in Great Britain. All rights reserved
0008-6223/96 $15.00 + 0.00

0008-6223(95)00212-X

POLY(ACRYLONITRILE-CO-VINYLCATECHOLBORANE): A NEW PRECURSOR FOR CARBON CONTAINING B/C, B/N AND B/O SPECIES

R. Hu and T. C. Chung*
Department of Materials Science and Engineering, Pennsylvania State University, University Park, PA 16802, U.S.A.

(*Received* 29 *June* 1995; *accepted in revised form* 7 *November* 1995)

Abstract—This paper describes a new PAN copolymer, poly(acrylonitrile-co-vinylcatecholborane), which is a precursor for carbon material containing B/C, B/N and B/O species in its molecular structures. Vinylcatecholborane, containing an appropriate protecting group in the borane moiety, can be copolymerized with acrylonitrile to high molecular weight copolymers under free radical polymerization conditions. The copolymers are processible by solution and melt methods. From ^{11}B NMR studies, a clear B–N complex was formed in poly(acrylonitrile-co-vinylcatecholborane) copolymer. The carbonation and oxidative studies of poly(acrylnitrile-co-vinylcatecholborane) indicate effective interconversions of copolymers to various graphite-like structures containing B/C, B/N and B/O species, which show significantly higher oxidative stability than pure carbon material obtained from PAN under the same conditions. Copyright © 1996 Elsevier Science Ltd

Key Words—Vinylcatecholborane, PAN copolymer, B/C material, oxidation stability.

1. INTRODUCTION

Polyacrylnitrile (PAN) is a traditional precursor [1–4] in the preparation of carbon fiber and carbon/carbon composites, both of which are lightweight structural materials for many applications, especially in the aerospace industry. However, the susceptibility to oxidation [5,6] of carbon materials, due to the *p*-electron-rich graphite-like structures, has limited applications in high temperature uses. Carbon/carbon composite materials begin to decompose above 500°C in air, and this process becomes more severe as the temperature rises. At about 800°C, the rate of oxidation is limited only by the diffusion rate of oxygen [5]. Attempts to use an oxidatively resistant protecting layer were only moderately successful, mainly due to the differences in thermal expension [7–11]. It is both a scientific challenge and a technologically important goal to develop a new method to increase the intrinsic oxidative stability of carbon.

Our approach has been focussed on the preparation of new precursors which can be converted to carbon materials containing some highly oxidative stable B/C, B/N and B/O species. In other words, the highly oxidative stable species are homogeneously distributed in the carbon materials, possibly incorporated in the graphite-like structures. The new molecular structures may alter the electronic state of carbon and provide homogeneously oxidative protection throughout the entire carbon matrix. To obtain the target material, it is logical to design a carbon precursor containing B, N and O elements which can maintain their presences throughout the carbonization process. In this paper, we will discuss a new precursor, poly(acrylonitrile-co-vinylcatecholborane) copolymer, which is processable by conventional solution and melting methods and can be converted to carbon with stable B/C, B/N and B/O species. The oxidative stability of resulting product will also be discussed.

2. EXPERIMENTAL

2.1 *Instrumentation and materials*

All ^{1}H NMR and ^{11}B NMR spectra were recorded on a Bruker AM-300 spectrometer with the DISNMR software. Quartz NMR tubes were used for the ^{11}B NMR measurements. Typical sample size was 15 mg of polymer dissolved in 0.5 ml of deuterated solvent. The internal standard for the ^{11}B NMR was boron trifluoride dietheyl etherate which has a chemical shift of 0 ppm. Thermogravimetric analysis (TGA) were accomplished using the Perkin Elmer TCS-2 analyzer. All O_2 and moisture sensitive manipulations were performed inside an argon filled Vacuum Atmosphere drybox equipped with a dry train. Benzene and THF were deoxygenated by argon sparging before being refluxed for 48 hours and then distilled from their respective sodium anthracide solutions. Hexane was refluxed with calcium hydride and potassium for 48 hours and then distilled. All solvents were stored within the drybox. Acrylonitrile obtained from Aldrich was dried over CaH_2 and then distilled prior to use.

2.2 *Synthesis of vinylcatecholborane monomer*

Vinylcatecholborane (VCB) was synthesized using two different methods: (a) Grignard reaction of vinyl magnesium bromide with chlorocatechol borane; and

---

*To whom all correspondence should be addressed.

(b) hydroboration of acteylene with catechol borane. In a typical Grignard synthesis of VCB, 19.62 g of 1 M vinyl magnesium bromide in THF and 3.08 g of chlorocatechol borane dissolved in excess THF were added simultaneously to a three necked flask containing dried THF at −70°C over a 2 hour period. The reaction was conducted under nitrogen atmosphere. After completion of the addition the reaction was allowed to continue for anther two hours at temperatures between −30 and −40°C. VCB was then distilled from the solution under reduced pressure. Usually a small amount of BHT was added to the solution prior to distillation since the monomer tends to polymerized at high temperatures.

The second method involves the hydroboration of acetylene with catechol borane in a high pressure reactor. The reactor was loaded with 22.5 g of catechol borane and 125 ml of THF in the drybox. Once the reactor was sealed, it was filled with 100–150 psi of acetylene. The hydroboration was carried out at 70°C for 24 hours after which the excess pressure was vented and the reactor was taken into the dry box. The clear VCB was again isolated by distillation under reduced pressure. The VCB was refrigerated in the dry box and remained stable.

2.3 *Copolymerization of acrylonitrile and vinylcatecholborane*

VCB (1.5 g) was mixed with the appropriate amounts of dried AN along with 20 mg of AIBN as initiator. The neat polymerization was carried out overnight at 60°C under nitrogen pressure. Over several hours the solution turns yellow and viscous. The product was dissolved in either benzene or THF depending on its solubility and then precipitated by hexane. By adding the dissolved polymer to excess hexane, yellow powder was obtained. The copolymer was then dried in vacuum for an extended period of time.

2.4 *Carbonization and oxidation studies*

Similar to the manufacturing process of high performance carbon fibers from PAN precursors, the heat treatment involves two steps, stabilization at low temperatures and carbonization to higher temperatures. The samples were contained in a porcelain boat and heated in a Lindberg split-tube furnace. Typically the stabilization of the copolymer precursors was performed under argon with the following steps: 30–225°C at 15°C/min, then 225–270°C at 1°C/min and hold at 270°C for 1 hour. After stabilization, the samples were cooled back to room temperature and then carbonized by heating to 900°C at 5°C/min. The oxidative stability was studied using the Perkin Elmer TCS-2 analyzer, with sample weight ranging from 10 to 20 mg. Weight loss vs temperature was measured by the TGA under argon with the same stabilization heat treatment as above. After stabilization, the samples were heated from 50 to 900°C under argon and then oxidized in pure oxygen at 700°C for several hours.

3. RESULTS AND DISCUSSION

3.1 *Precursor preparation and characterization*

The chemistry to prepare poly(acrylonitrile-co-vinylborabicyclonorane) involves free radical copolymerization of acrylonitrile (AN) and vinylcatecholborane (VCB), as illustrated in eqn (1).

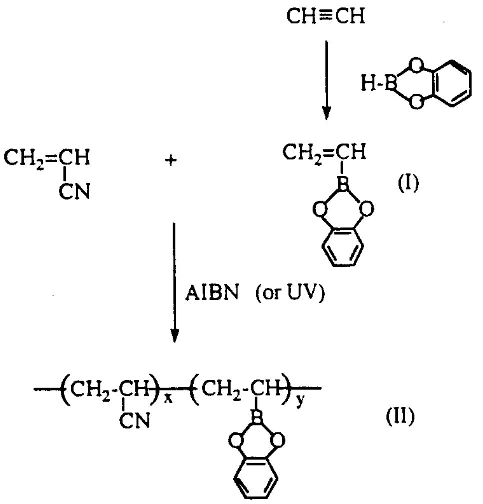

Several routes were tried to prepare vinylcatecholborane. The Grignard reaction between vinylmagnisium chloride and chlorodialkylborane shows an unsatisfactory yield due to complex formation. However, the reaction involving acetylene and catecholborane offers high yield (>70%) and convenient process. In fact, this route can be easily scaled-up to large-scale production. Usually, the hydroboration was carried out at 70°C for 24 hours, after which the excess pressure was vented. The clear VCB was isolated by distillation under reduced pressure. Under these conditions, the addition reaction selectively stops at the monohydroboration step. Fig. 1 shows the ^{1}H NMR spectrum of the distilled product.

In the ^{1}H NMR spectrum, the intensity ratio (3:5) between the chemical shifts of vinyl group (5.8–6.5 ppm) and aromatic group (6.7–7.1 ppm) clearly indicate the molecular structure of vinylcatecholborane. As will be seen in Fig. 4(a), the ^{11}B NMR spectrum shows a single chemical shift at 31 ppm in d^{6}-benzene corresponding to the boron with dialkoxy and vinyl ligands [12]. Both spectra provide direct evidence of the presence of vinylcatecholborane.

It is known that most of alkylborane moieties readily react with free radicals [13,14]. However, the vinylcatecholborane monomer, with two oxygen atoms in the catechol ligand that neutralize the electron deficiency of boron to produce a stable borane moiety, can be copolymerized with acrylonitrile by free radical process to high molecular weight copolymers with good yield: about 60% yield in 24 hours. It was found that higher ratio of acrylonitrile increases the overall copolymerization reactivity. Table 1 summarizes the experimental results.

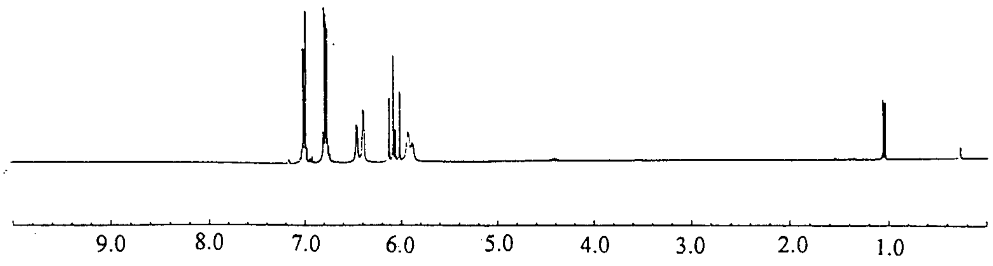

Fig. 1. ^{1}H NMR spectrum of vinylcatecholborane.

Table 1. Summary of copolymerization[a] between acrylonitrile and vinylcatecholborane

Sample	Monomer feed ratio (AN/VCB)	Reaction time (hours)	Yield (wt%)	Copolymer mole ratio (AN/VCB)	Color
I-A	1/1	24	60	1/1	Yellow
I-B	1/3	1	2.3	1/1.79	Yellow
I-C	1/1.65	1	3.7	1/0.73	Yellow
I-D	1/0.75	1	7.2	1/0.21	Yellow

[a] At 65°C using AIBN initiator.

Apparently, the catechol ligand is an effective protecting group to avoid any side reactions between boron compound and free radicals. Fig. 2 shows ^{1}H NMR spectra of poly(acrylonitrile-co-vinylcatecholborane) copolymers in d-THF.

The copolymer composition was determined by the proton intensities between chemical shifts (6.4–7.2 ppm), corresponding to aromatic protons in VCB units, and chemical shift at 3.05 ppm, corresponding to the methine proton in AN units.

To determine the comonomer reactivity ratios, the copolymerization reactions between I-B and I-E were terminated at low monomer conversions. The reactivity ratios between acrylonitrile ($r_1 = k_{11}/k_{12}$) and vinylcatecholborane ($r_2 = k_{22}/k_{21}$) were estimated by the Kelen–Tudos method [15]. The calculation is based on the following equation:

$$\eta = r_1\xi - r_2/\alpha(1-\xi)$$

$$\eta = G/\alpha + F \text{ and } \xi = F/\alpha + F$$

where $x = [\alpha\text{-olefin}]/[\text{HB}]$ in feed and $y = \text{d}[\alpha\text{-olefin}]/\text{d}[\text{HB}]$ mole ratio in copolymer, $G = x(y-1)/y$, $F = x^2/y$, $a = (F_m \times F_M)^{1/2}$, and F_m and F_M are the lowest and highest values of F. Figure 3 shows the plot η versus ξ and the least squares best fit line.

The extrapolation to $\xi = 0$ gives $-r_2/a$ and r_1. We obtain $r_1 = 7.23$ and $r_2 = 1.73$ for acrylonitrile and vinylcatecholborane, respectively. Despite only few data points, the results do provide a qualitative rather

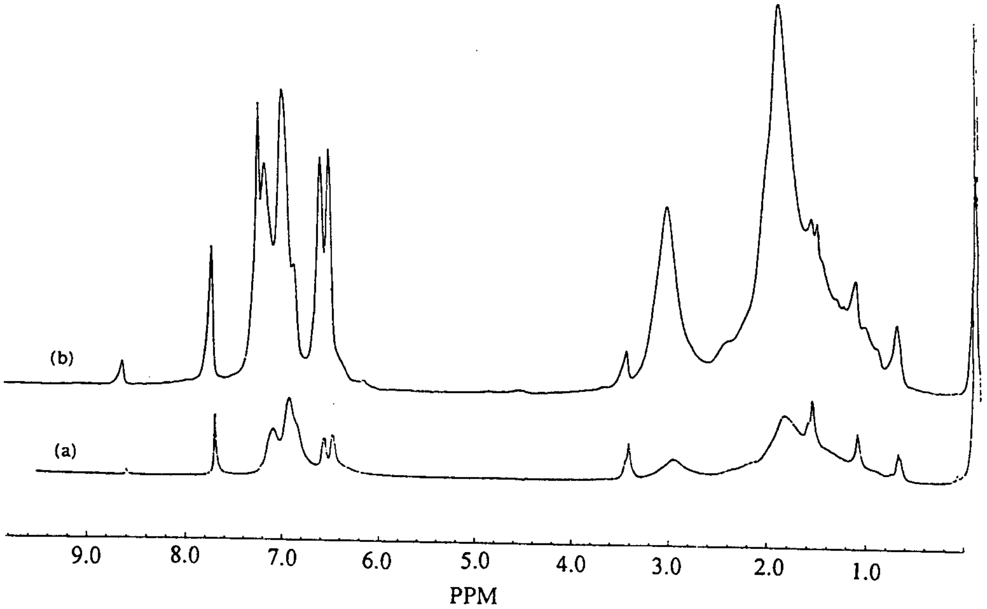

Fig. 2. ^{1}H NMR spectra of poly(acrylonitrile-co-vinylcatecholborane): (a) I-A and (b) I-B.

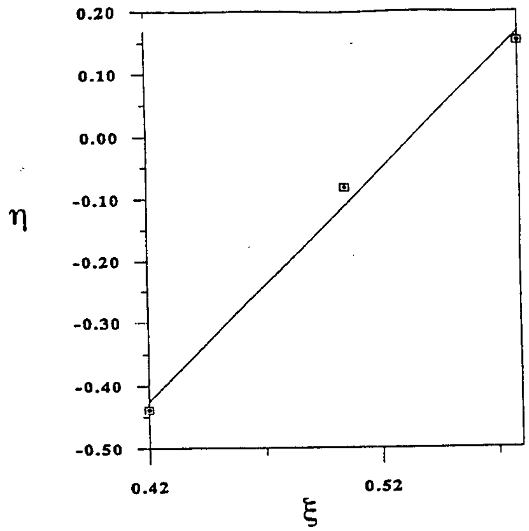

Fig. 3. Kelen–Tudos plots for copolymerization of VCB (r_1) and AN (r_2).

than quantitative expression of the monomer reactivities. It is clear that the copolymerization reaction is not ideal ($r_1 \times r_2 = 1$) copolymerization. Instead, it favors the incorporation of acrylonitrile. The fact that the copolymerization rate increased with higher concentration of AN also further supports the conclusion that incorporation of AN is favored.

The copolymers of poly(acrylonitrile-co-vinylcatecholborane) are yellow which indicates some complexes formed between acrylonitrile (base) and catecholborane (acid). It is interesting to note that the color of the two homopolymers, poly(acrylonitrile) and poly(vinylcatecholborane) (PVCB) [16], is white. Figure 4 compares ^{11}B NMR spectra of vinylcatecholborane, poly(vinylcatecholborane) and poly (acrylonitrile-co-vinylcatecholborane).

After polymerization from vinylcatecholborane to poly(vinylcatecholborane), the boron chemical shift moves downfield from 31 to 41 ppm corresponding to alkyldialkoxy borane. The difference (10 ppm) in chemical shifts clearly indicates a contribution of electron density from the vinyl group to the boron prior to polymerization. It is interesting to note that the catecholborane group in the polymer is more acidic than that in the monomer. The broadness of the ^{11}B peak, with long relaxation time, is due to the polymer nature of the product. On the other hand, the poly(acrylonitrile-co-vinylcatecholborane) copolymer shows about 5 ppm up-field shift from poly(vinylcatecholborane) homopolymer. It clearly indicates the complex formed between acrylonitrile (base) and catecholborane (acid) groups in the copolymers. GPC measurement was not performed to determine the molecular weight and molecular weight distribution of the copolymers due to the reactivity of boron species, which may potentially damage GPC columns. However, the solution viscosity of copolymer, similar to that of poly(acrylonitrile) homopolymer under the same solution concentration, seems to indicate high molecular weight copolymer.

3.2 *Stabilization and carbonization studies*

The pyrolysis of poly(acrylonitrile-co-vinylcatecholborane) precursors involves two steps, stabilization at low temperature (270°C) and carbonization to higher temperature (900°C), similar to the thermal procedures used in PAN precursor. Due to the sensitivity of B–C bonds to oxygen, both stabilization and carbonization of the copolymer precursors were performed under argon conditions. Table 2 shows the comparison of stabilization and carbonization results between PAN and the boron containing polymers.

It is clear from these results that the yield of carbon decreases as the concentration of VCB monomer units in the copolymer increases. Unlike PAN, where the polymer can easily cyclize to form a more stable conjugated system, poly(vinylcatecholborane) homopolymer [16] gave no significant carbon residue after undergoing the same heat treatment. The VCB unit simply degrades as the temperature increases. The cleavage of an alkyl–borane bond can occur through dehydroboronation to generate a C=C double bond in the polymer backbone. For the catechol group to be removed, two B–O bonds will have to be broken as compared with one weaker B–C bond in the case of dehydroboronation. Catechol is an unlikely leaving group since the boron–oxygen bond is so strong. However, some boron moieties can remain in the carbon if they react with the nitrile groups in the copolymer. During high temperature heat treatment, it is probable that the complexed moieties will form chemical bonds. In fact, in the simple mixture of the homopolymers PAN and PVCB, the carboniation yield (20.1%) is more than the combined yield (16.3%) of PAN and PVCB, assuming all of the PVCB decomposes and the yield of carbon only comes from the PAN fraction. Some interaction must occur between the two homopolymers. It is unclear what sort of effect the presence of boron has on the carbonization of PAN. Similar to the catalysis of graphitization by boron, it may be possible that boron catalyzes the carbonization of PAN. [17,18]

Sample I-A was also carbonized in a tube furnace to 1000°C under inert atmosphere, after the usual stabilization step. The 1000°C carbon residue was analyzed via elemental analysis. Table 3 summarizes the results that were obtained. The data indicate a very different composition from that of PAN, which transforms to >90% carbon after heat treatment to 1000°C. In the copolymer case, boron and nitrogen clearly stay within the system. The weight percent of oxygen in the pyrolyzed product, 12.03%, can be calculated by assuming that the only elements present are C, H, B, N and O. Apparently during carbonization, hydrogen was almost completely removed, which implies that significant cyclization reactions occurred. The large percentages of B, N and O present after heat treatment to 1000°C indicate that some highly thermal stable species, e.g. B/C, B/N and

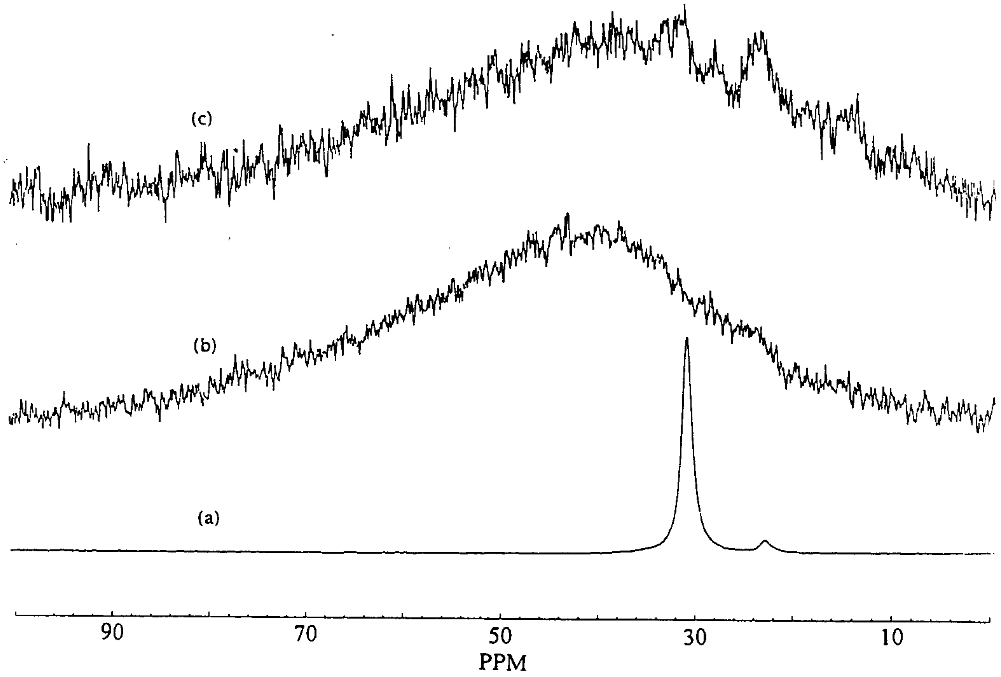

Fig. 4. ^{11}B NMR spectra of (a) vinylcatecholborane, (b) poly(vinylcatecholborane) and (c) poly(acrylonitrile-co-vinylcatecholborane).

Table 2. Comparison of carbonization and oxidation results of poly(acrylonitrile-co-vinylcatecholborane)copolymers and the corresponding homopolymers

Sample	AN/VCB mole ratio	Stabilization (wt%)	Carbonization (wt%)	Overall yield (wt%)	Oxidation yield[a] (wt%)
PAN	1/0	82.5	39.4	32.5	0
I-A	1/1	75.0	26.7	20.0	28
I-B	1/1.8	77.8	14.7	11.5	89
PVCB[b]	0/1		0	0	
PAN/PVCB mixture	3/1	79.1	25.4	20.1	0

[a] At 700°C in oxygen atmosphere.[b] PVCB = poly(vinylcatecholborane) homopolymer.

Table 3. Elemental analysis results of sample I-A before and after carbonization at 1000°C

Element	Carbon	Hydrogen	Boron	Nitrogen	Oxygen
Before carbonization on (wt%)	66.33	5.03	5.53	7.04	16.08
After carbonization on (wt%)	69.93	0.70	5.87	11.74	12.03[a]

[a] Experimentally undetermined, but calculated by assuming that the only elements present in the residue are C, H, B, N and O.

B/O, might exist in the pyrolyzed product. The detail reaction mechanism and product structures are currently under investigation.

3.3 *Oxidation studies*

The oxidative stability was studied by static thermal gravimetric analysis (TGA) at 700°C in oxygen atmosphere with the flow rate of 50 cm^3/min. About 10–15 mg sample powder was used in each measurement. Figure 5 compares the weight loss vs time between the pyrolyzed products obtained from the copolymers (I-A and I-B) and PAN precursors. All samples were prepared under the same thermal condition by heating the sample at 5°C/min to 900°C under argon atmosphere.

As expected, the char obtained from PAN was highly susceptible to oxidation, and almost loses all its weight in a few minutes. The presence of boron, nitrogen and oxygen in the carbon residue clearly increases the oxidation stability. Sample I-B with the highest heteroatom content had the lowest oxidative reactivity. The reactivity of this material is essentially zero after 10% burn off at 700°C. This inhibition of oxidation was also observed for I-A, but at a higher final burn off level (72%). It is interesting to note that the decrease in oxidative reactivity cannot be

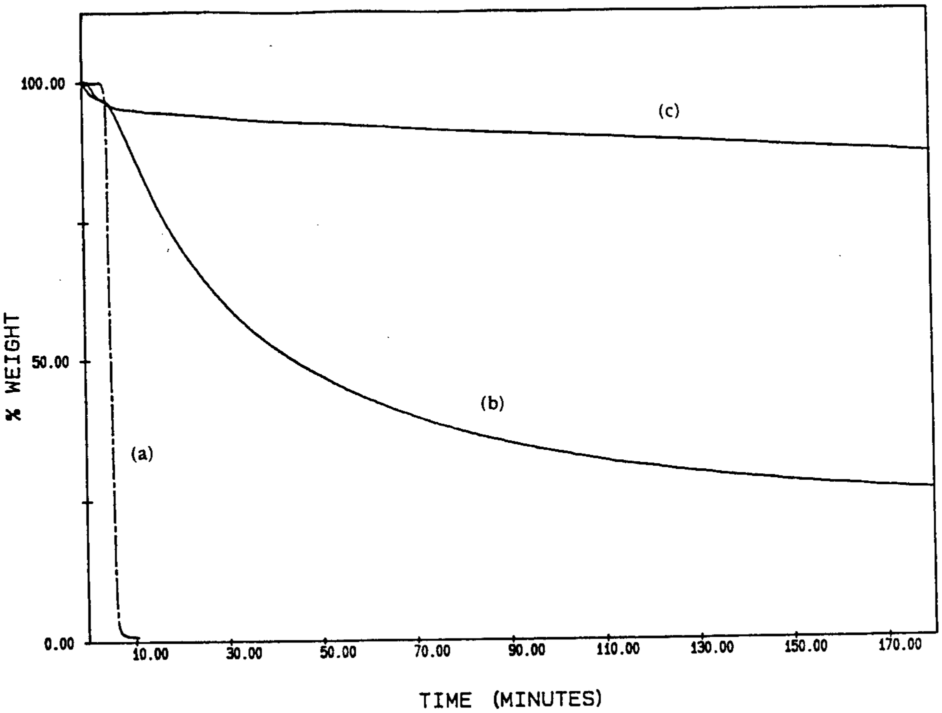

Fig. 5. TGA curves of the pyrolyzed products obtained from precursors: (a) PAN, (b) copolymer (I-A) and (I-B).

achieved by simply mixing boron containing polymer with PAN. As shown in Table 2, the sample was completely burned off in the case of PAN/PVCB mixture. The oxidation resistance must arise from the chemical interactions between heteroatoms and the carbon atoms within the carbon matrix.

4. CONCLUSION

In this paper, a new boron containing PAN precursor was prepared and evaluated. The chemistry involves the synthesis and polymerization of a novel boron containing monomer, vinylcatecholborane. Vinylcatecholborane is easily copolymerizable with acrylonitrile to produce boron containing PAN copolymers with various compositions. The chemical shift in the ^{11}B NMR spectrum of the copolymer indicates a donor–acceptor B/N complex within the copolymer structure. The copolymer of poly(acrylonitrile-co-vinylcatecholborane) can be carbonized to yield carbon containing B, N and O elements. The oxidative stability of this novel boron containing carbon, much greater than carbon produced from PAN, implies that some B/C, B/N and B/O species might exist in the carbon structures. Although the mechanism of this decrease in oxidative reactivity is not easy to determine, due to the many different elements that are present in the system, the success of this part of the project has given us more understanding of this type of compound and allows us to better design other polymeric B/C precursors.

Acknowledgements—The authors would like to acknowledge the financial support from the U.S. Air Force, Office of Scientific Research.

REFERENCES

1. H. Marsh, *Introduction to Carbon Science*. Butterworths, London (1989).
2. J. B. Donnett and R. P. Bansal, *Carbon Fibers*. Marcel Dekker, New York (1984).
3. W. Watt and W. Johnson, *Nature* **257**, 210 (1975).
4. E. J. Walker, In *Essentials of Carbon–Carbon Composites*, (Edited by C. R. Thomas). Royal Society of Science, Cambridge (1993).
5. D. W. McKee, *Chem. Phys. Carbon* **16**, 1 (1981).
6. D. W. McKee, *Carbon* **24**, 737 (1986).
7. G. R. Marin, U.S. Patent No. 3,936,574 (1976).
8. G. H. Schiroky, *Adv. Ceram. Mater.* **2**, 137 (1987).
9. L. E. Jones and P. Thrower, *J. Chimie Phys.* **84**, 1431 (1987).
10. L. F. Lynch, *Engineering Properties of Selected Ceramic Materials*. American Ceramic Society, Columbus (1966).
11. J. E. Sheehan, *Carbon* **27**, 709 (1989).
12. H. Noth and B. Wrackmeyer, *Nuclear Magnetic Resonance Spectroscopy of Boron Compounds*. Springer-Verlag (1978).
13. T. C. Chung, D. Rhubright and G. J. Jiang, *Macromolecules* **26**, 3467 (1993).
14. T. C. Chung, W. Janvikul, R. Bernard and G. J. Jiang, *Macromolecules* **27**, 26 (1994).
15. T. Kelen and F. Tudos, *React. Kinet. Catal. Lett.* **1**, 487 (1974).
16. T. C. Chung and R. Hu, unpublished results.
17. R. Hu, MS thesis, The Pennsylvania State University (1995).
18. L. E. Jones and P. Thrower, *Carbon* **29**, 251 (1991).

Pergamon

Carbon Vol. 34, No. 10, pp. 1181–1190, 1996
Copyright © 1996 Elsevier Science Ltd
Printed in Great Britain. All rights reserved
0008-6223/96 $15.00 + 0.00

S0008-6223(96)00064-4

SYNTHESIS AND CHARACTERIZATION OF NOVEL B/C MATERIALS PREPARED BY 9-CHLOROBORAFLUORENE PRECURSOR

RAYMOND HU and T. C. CHUNG*
Department of Materials Science and Engineering, The Pennsylvania State University,
University Park, PA 16802, U.S.A.

(*Received* 28 *February* 1996; *accepted in revised form* 22 *April* 1996)

Abstract—This paper describes a novel boron containing carbon (B/C) material which contains up to 7 mole% of boron atoms substitutionally incorporated in the graphitic structure. The chemistry involves the use of 9-chloroborafluorene precursor and the thermo-transformation reaction. 9-Chloroborafluorene was firstly oligomerized to mesophase boron containing pitch (B-pitch) which is processable by solution and melt. The mesophase B-pitch was then pyrolyzed at various temperatures (up to 2300°C) to produce B/C material with high yield (~80%). During pyrolysis, boron is not only substitutionally incorporated in the graphitic structure but also enhances the graphitization reaction. An unusually large crystallite size and small *d*-spacing between interlayers of the B/C product was observed by X-ray diffraction. Copyright © 1996 Elsevier Science Ltd

Key Words—B/C material, 9-chloroborafluorene, boron containing precursor.

1. INTRODUCTION

Boron is one of the few elements that can be substituted into the carbon structure. Boron occupies an unique position in the periodic table as it is a group III element with properties of both metals and nonmetals. An important non-metal characteristic of boron is its ability to form strong covalent bonds with carbon. Tricoordinated organoboranes are electron deficient since they only have 6 electrons in the valence band, i.e. 3 electrons from boron and 1 additional from each of the 3 carbons. The presence of the electron deficient boron alters the electronic structure of the substrate and leads to many interesting effects on the thermal, electrical as well as chemical properties of the carbon [1–4]. In addition, it has been shown that substitutional boron inhibits the oxidation of various carbons [5,6].

Although the properties of boron doped carbons have been extensively studied, the process of synthesizing these materials has not been improved upon. The method of doping carbon with substitutional boron via solid state diffusion has many drawbacks. The diffusional process requires very high temperatures as well as long residence times. As a result of the additional heat treatment during doping, it is often very difficult to separate the effect of boron from the effect of the increase in graphitization. This uncertainty hinders the characterization and understanding of B/C materials. Furthermore, the concentration of the dopant is limited by the temperature of the reaction and the dispersion of the dopant is often inhomogeneous. Lowell [7] determined that the solid solubility of boron in carbon approached a maximum value of 2.35 atomic% at 2350°C. In this case, substitution was accomplished by heating graphite with boron carbide, and the boron concentration was determined via titration. Similarly, Tunbull [8] has shown that the concentration of boron reached a maximum of 2% at 2000°C and thereafter decreased dramatically with increasing temperature. Interstitial boron, i.e. boron intercalated between graphitic planes, was found to diffuse out of the system around 1400°C. More recently, materials containing 25% B, BC_3, have been produced via chemical vapor deposition by several researchers [9,10]. Although the concentration of B is very high, the applicability of CVD is limited by the low rate of deposition and the lack of control of the final structure of the carbon.

The solid state formation of the substitutional solution in graphite requires the presence of vacancies since the process involves diffusion. Thus, typically, the doping of well ordered crystalline graphite is rather difficult. Several researchers reported that inhomogeneous distribution arises during the doping process because boron preferentially enters into the most disordered regions of the carbon [5,11]. It is clear that there is a scientifically challenging and technologically important need to develop a new method to prepare carbon of high boron concentration and uniform distribution.

Our research approach has been concentrating on a new synthetic route to prepare B/C materials by using specifically designed boron containing carbon precursors. By taking into account the chemistry of boron and the mechanism of carbonization, we can tailor the molecular composition of our precursor to produce B/C materials with high yields of carbon and boron. Many boron containing compounds were evaluated as possible precursors to B/C materials, including several boron containing polymers [12]. The focus of this paper is on heterocyclic aromatic boron containing hydrocarbons, specifically 9-chloroborafluorene.

---

*Author to whom correspondence should be addressed.

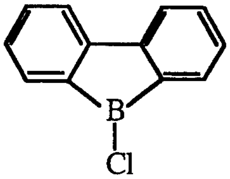

The principle of using this organoborane as precursor was to directly provide the basic conjugated aromatic frame work for the B/C material. Thus during the aromatic condensation reactions only minimum molecular structure rearrangement is needed. 9-Chloroborafluorene has a planar geometry that has been shown to be a primary requirement for graphitizable carbons [13]. Furthermore, the reactive functional group (B–Cl) can be utilized for polymerization (stabilization) at relatively low temperature.

2. EXPERIMENTAL

2.1 *Instrumentation*

All ^{1}H NMR and ^{11}B NMR were recorded on a Bruker AM-300 spectrometer with DISNMR software. Quartz NMR tubes were used for the ^{11}B NMR measurements. Typical sample size was 15 mg of polymer dissolved in 0.5 ml of deuterated solvent. The internal standard for the ^{11}B NMR was boron trifluoride dietheyl etherate which has a chemical shift of 0 ppm. The optical microscopy was performed in a Nikon Microphot-FXA. The specimen was mounted in a plastic resin and polished according to conventional methods and was examined under a reflected light microscope with cross polarizer/analyzer. X-ray diffraction measurements were made on the carbonized and graphitized B/C material using a Rigaku Geigerflex X-ray diffractometer with CuK radiation operating at 20 mA and 40 kV. Samples (45 mg) were grounded in an agar mortar and pestle and then mixed with methanol. Thereafter, a film was cast on the quartz slide and allowed to dry for 30 minutes. Pure silicon (NBS SRM 640) was the internal standard for the accurate determination of *d* spacing. Two measurements were made for each sample, one from the range of 5 to 90° at the scan speed of 4.2° per minutes the other from 23 to 30° at the scan speed of 1.2° per minute. The interlayer spacing (*d*) was determined from the (002) peak using the spectra obtained from 1°/minute scan speed. Sp-1 graphite was used as the standard for determining instrument broadening in the calculation of crystallite size, *Lc*.

All elemental analysis was conducted by Galbraith Laboratories, Inc., Knoxville, TN. Determination of C and H concentration was performed via combustion at 1050°C in a constant O_2 stream, using a Leco CHN 1000 determinator. The method used for boron analysis was inductively coupled plasma emission spectroscopy (ICP). The sample was digested by fusing with sodium carbonate and then dissolving the resulting melt in ASTM type I water with a small amount of hydrochloric acid. The sample was then introduced into a Perkin–Elmer P2000 instrument operating at 1400 w with flow rate of 15 l/minute. The relative standard deviation was 5.57% and the relative error was only 2.66%. Boron concentration determination was made at a primary wavelength of 249.77 nm and the detection limit for this technique is reported to be at 0.010 mg/l. The results are reported as wt% and are considered quantitative.

2.2 *Stabilization and processing of boron containing precursor*

9-Chloroborafluorene was synthesized by a published method [14]. The stabilization was carried out by the heat treatment of 9-chloroborafluorene at relatively low temperature under pressure. To study the effect of temperature and heat treatment time, small quantities of the organoborane were sealed within a glass tube under vacuum and then heat treated. The samples were transferred into the glass tubes in solution with hexane as solvent, and dried in vacuo. Typically the sample ranged from 265 to 365 mg and the volume of the sealed tube was approximately 3 ml. The prescribed heat treatments were set at 325, 375, 425 and 500°C for a duration of 3 to 10 hours. The sealed samples were heated in a Lindberg split tube furnace at a rate of 5°C per minute and after the isothermal hold, cooled to 250°C at 3°C per minute. Some of the specimens were then further treated via the vacuum distillation procedure, as will be discussed later. Those that were not distilled, including samples in Table 1, were carbonized directly.

For larger scale sample preparations, a high pressure stainless steel tube bomb (20 ml) equipped with a pressure gauge was used for the heat treatment of larger quantities of the organoborane. The loading of the samples, up to 2 g, were conducted in a dry box under argon. The bomb was purged several times and then pressurized to 150 psi of nitrogen. The heat

Table 1. Effect of pressurized heat treatment conditions on the final yield of B/C materials at 550°C

	Pressurized heat treament		
Sample	Temp. (°C)	Time (hours)	Final yield of B/C material (wt%)
1	325	5	34.7
2	375	3	39.4
3	375	5	47.0
4	375	10	54.7
5	425	5	61.0

treatment took place in a fluidized sand bath at 375°C. After soaking for 5 hours the sample was cooled slowly to room temperature. All of the specimens from the reactor were then treated via the vacuum distillation process described in the next section.

The pressure treated precursor was weighed in a pear shaped glass flask and distilled under vacuum at 225°C. Prior to increasing the temperature, the apparatus containing the sample was evacuated to 50 mTorr in order to degass the pitch and prevent the sample from bumping as the temperature increased. The heating was performed stepwise without agitation of the molten pitch in a sand bath. After distillation for 1 hour at 225°C and 50 mTorr the sample was slowly cooled down to room temperature. The solid distillation residue (B-pitch) was collected in an inert atmosphere dry box.

2.3 *Carbonization and graphitization*

The solid B-pitch obtained after distillation was pulverized and placed within a porcelain coated Coors crucible and carbonized at 550°C under an argon atmosphere. Again the loading of the sample was conducted in a dry box. In all cases, the heating rate was 10°C/minute and the soak time was 1 hour. The cooling rate was 3°C/minute to 350°C and then cooled in air to room temperature.

After carbonization, the fused product was pulverized again and ground to a fine powder. The powdered sample was then placed within a graphite crucible and subjected to high temperature graphitization. The loading of the sample was conducted in air since the samples had already been carbonized. Typical sample sizes in one crucible ranged from 100 to 200 mg. The furnace used was a graphite resistance type furnace manufactured by Centorr Vacuum Technology. The furnace was evacuated to 100 mTorr and pressurized to 2 psi with ultra high purity Ar (99.99%). This process was repeated at least three times to ensure the removal of oxygen from the furnace prior to heating. The furnace was controlled manually. The temperature of the furnace was monitored by a thermocouple up to 1450°C and then above that by an optical pyrometer. The quartz window from which the readings were made was cleaned regularly and the alignment of the pyrometer was checked frequently to ensure accurate measurement. The soak temperature and time are listed in Table 3.

3. RESULTS AND DISCUSSION

This paper shows a new precursor, 9-chloroborafluorene, which can be effectively transformed to B/C materials with substitutional borons homogeneously distributed in the graphilic structure as shown in eqn. (1).

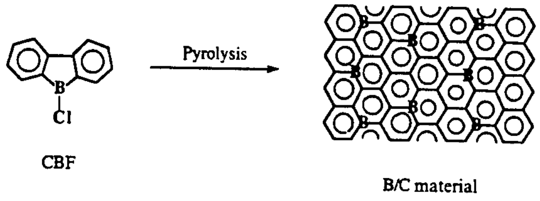

(1)

In addition to the planar geometry with conjugating aromatic framework in 9-chloroborafluorene, the precursor provides a reactive B–Cl functional group for intermolecular reactions at relatively low temperature. During the increase of molecular weight, it is speculated that the existence of boron in the multi-aromatic structure may increase the thermodynamic stability of the graphitic structure and enhance the graphitization process. Overall, 9-chloroborafluorene could be a good precursor which could produce highly crystalline B/C material with high yields of carbon and boron and at relatively low temperature.

3.1 *Synthesis of 9-chloroborafluorene*

The general procedure for the synthesis of 9-chloroborafluorene is illustrated in eqn. (2).

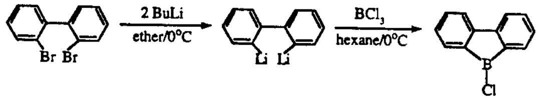

(2)

Both metallation and cyclization reactions are very effective. After isolation, yellow crystals of 9-chloroborafluorene were obtained with an overall product yield of approximately 85%. The chemical composition of the compound was verified via a ^{11}B NMR spectrum which shows a single chemical shift at 68 ppm, corresponding to 9-chloroborafluorene.

3.2 *Processing of boron containing precursor*

The general process for the heat treatment of the boron containing precursor can be summarized by the following diagram:

$$\text{9-Chloroborafluorene} \xrightarrow[\substack{\text{5–10 hours}\\ \text{100 psi N}_2}]{375^\circ\text{C}} \text{B-Pitch} \xrightarrow[\substack{\text{1 hour}\\ \text{vacuum}}]{225^\circ\text{C}}$$

$$\longrightarrow \substack{\text{Mesophase}\\ \text{B-Pitch}} \xrightarrow[550^\circ\text{C}]{\text{Carbonization}} \xrightarrow[<2300^\circ\text{C}]{\text{Graphitization}} \substack{\text{B/C}\\ \text{material}}$$

3.2.1 *Pressurized heat treatment.* In finding the optimum conditions for the pressurized heat treatment, the primary concern is the molecular weight. While low molecular weight boron containing pitch (B-pitch) tends to volatilize, high molecular weight pitch should also be avoided due to processing difficulties. Typically, a pressurized process was necessary in order to prevent the volatilization of low boiling precursors. The influence of the pressurized heat treatment conditions on the final 550°C carbonization yield is shown in Table 1.

The sealed tubes containing 9-chloroborafluorene were treated at the temperature and time indicated. The pitch residue yield after the initial pressurized treatment was greater than 98% in all cases. The final B/C yield was calculated from the weight of solid residue after the precursor was carbonized at 550°C. As is obvious, the yield increased as the temperature and time of the pressurized treatment increased. Although increasing the temperature improves the amount of B/C residue, we must take into account the nature, especially processibility, of B-pitch in determining the optimal thermal conditions. Sample 1, heated at 325°C, is a low viscosity oil that dissolved readily in organic solvents such as benzene, indicating that the molecular weight of the B-pitch was low. The oil was highly volatile during carbonization and resulted in a low yield of B/C product, 34.7 wt%. Furthermore, the highly porous and glassy nature of the resulting carbon can be observed by simple visual inspection. At 425°C and above, the rapid aromatic condensation of the starting compound caused the samples to be carbonized and thus infusible. Our investigation showed that the range of temperatures from which B-pitch of desired quality is obtained is between 325 to 425°C, with 375°C being optimum.

As the time of reaction at 375°C increased from 3 to 10 hours the yield of 550°C B/C material from the B-pitch increased by 15 wt%. It seems that 10 hours time was required to convert most of the 9-chloroborafluorene to B-pitch. It is interesting to note that when the 9-chloroborafluorene was heat treated in the tube bomb, B-pitch can be produced in half the time owing to a better heat transfer from the stainless steel reactor. Generally, the precursor B-pitch made in the reactor was also more uniform.

3.2.2 *Mesophase concentration via vacuum distillation.* Procedures for the preparation of mesophase pitch from various carbon precursors, such as petroleum and coal tar pitches, are well known [15–18]. The principle is to increase the molecular weight of the precursor by concentrating the mesogen. Park [19] has previously shown that 100% anisotropic mesophase pitch can be prepared from vacuum residue of FCC-decant oil (FCC–DOVR) by a two stage process involving first, pressurized heat treatment (1–5 MPa, 430–480°C) and second, vacuum distillation. Since the B-pitch was synthesized from the pressurized treatment of low molecular weight 9-chloroborafluorene, its characteristics more closely resemble that of the lighter petroleum pitches. Following the same principles, the B-pitch was distilled under vacuum in order to remove low molecular weight non-mesogens and thus concentrating the mesogens to produce a mesophase pitch.

Table 2 summarizes the yield of mesophase B-pitch and the weight% of B/C residue that remained after carbonization of such a precursor at 550°C.

The temperature and time of the pressurized treatment are also shown. The mesophase yield was calculated from the amount of distillate that remained after heat treatment at 225°C for 1 hour at 50 mTorr. After slow cooling to room temperature, black mesophase powder was obtained. The yield of meosphase B-pitch, greater than 65 wt%, was very high as compared to that from other carbon precursors. For example, Lewis [20] has shown that approximately 20% mesophase can be produced by pressurized heat treatment of model compounds such as anthracene and naphthalene. It is also interesting to note that heat treatment of fluorene, which in all aspects is similar to our precursor except it contains a methyl bridge instead of boron, does not yield any graphitizable carbon at all [21]. The presence of boron clearly increased the yield by *in situ* catalysis of mesophase formation.

Halo-boranes have been known to catalyze polymerization of many different vinyl and aromatic monomers. Mochida *et al.* [22,23] have successfully prepared mesophase pitch with 100% anisotropy by treating anthracene and naphthalene with BF_3/HF. The electron deficient BF_3 is believed to form a charge transfer complex with HF. This initiator then causes the rapid cationic polymerization of aromatic precursors. Although the B–Cl species is less reactive than BF_3, we also observed the formation of HCl during the polymerization reaction, which indicates a similar cationic catalysis with internal hydrogen transfer reaction. In the formation of the mesophase B/C precursor, the electron deficient 9-chloroborafluorene may serve as both catalyst and monomer, and boron is incorporated into the molecular structure of B/C precursor (B-pitch).

The mesophase B-pitch was completely fusible. During the heat treatment, the mesophase B-pitch passes through the viscous liquid phase, it should be possible to process the material. The prerequisite for low porosity, e.g. high yield of boron containing carbon residue can be obtained at over 85% conversion. Furthermore, it was found that this mesophase B-pitch is insoluble in non-polar organic solvents such as benzene, but soluble in tetrahydrofuran (THF) at room temperature. Likely, the interaction between the electron poor boron and the electron rich oxygen in THF gave rise to the increase in solubility of the boron containing mesophase. As is obvious, the processability of this B/C precursor is dramatically enhanced by its room temperature solubility. Due to the air/moisture sensitivity, the optical texture of the B/C mesophase was not characterized. Optical microscopy, discussed in the following section, was performed on a carbonized sample of the B/C pitch.

3.3 *Carbonization and graphitization of B/C mesophase*

3.3.1 *Optical microscopy.* Figure 1 shows the polarized micrograph of a B/C pitch that had been carbonized at 500°C.

Table 2. A summary of B/C materials prepared by two steps, isolation of mesophase precursor and carbonization at 550°C

Sample	Pressurized heat treament		Yield of mesophase (wt%)	Yield in carbonization (wt%)	Overall yield of B/C material (wt%)
	Temp. (°C)	Time (hours)			
6	350	10	66.4	85.0	56.44
7	375	10	70.6	85.0	60.01
8	375	5	67.3	87.0	58.55

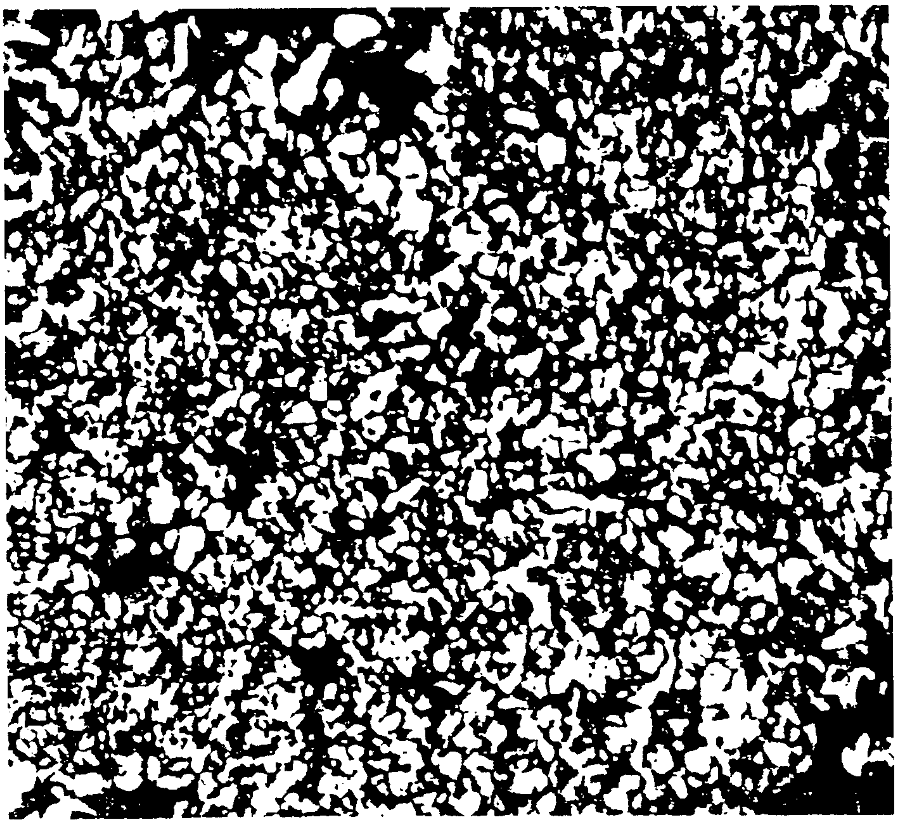

Fig. 1. Polarized micrograph of B/C pitch prepared at 500°C.

Note the sample was not distilled under vacuum prior to carbonization. The micrograph illustrates that the boron containing coke is 100% homogeneous and has complete optical activity. It has the appearance of a coke produced from Brooks and Taylor (BT) mesophase, in which there is complete local anisotropy while the material as a whole is statistically isotropic. BT mesophase differs from anisotropic mesophase, in that it does not undergo reversible thermotropic transition when heated. This type of behavior is often found in the direct pyrolysis of pitch [17,24]. Spinnable anisotropic pitch can be produced from BT mesophase pitch by various different methods such as mechanical stirring or bubbling with inert gas during heat treatment [24]. Indeed, even though the data are limited, the B-pitch mesophase produced from vacuum distillation behaves very similarly to the conventional mesophase pitches obtained with these procedures. The detailed characteristics of the B-pitch mesophase are currently under investigation. The results presented in the next section clearly indicate that the B-pitch mesophase is highly graphitizable.

3.3.2 *Graphitization of mesophase B-pitch.* The solid B-pitch was pulverized and placed in a graphite crucible and subjected to high temperature graphitization under ultra high purity Ar (99.99%). Overall, the transformation of B-pitch to B/C graphitic products is a smooth process with high yield (>85%). The resulting B/C materials (thin films) were examined by X-ray diffraction. Pure silicon (NBS SRM 640) was the internal standard for the accurate determination of *d* spacing. Sp-1 graphite was used as the standard for determining instrument broadening in the calculation of crystallite size. Figure 2 depicts the X-ray diffraction patterns of the B/C materials at different heat treatment temperatures.

Clearly, there is significant development of the (100) and (101) peaks as the temperature increased from 1800 to 2300°C. Table 3 summarizes the X-ray

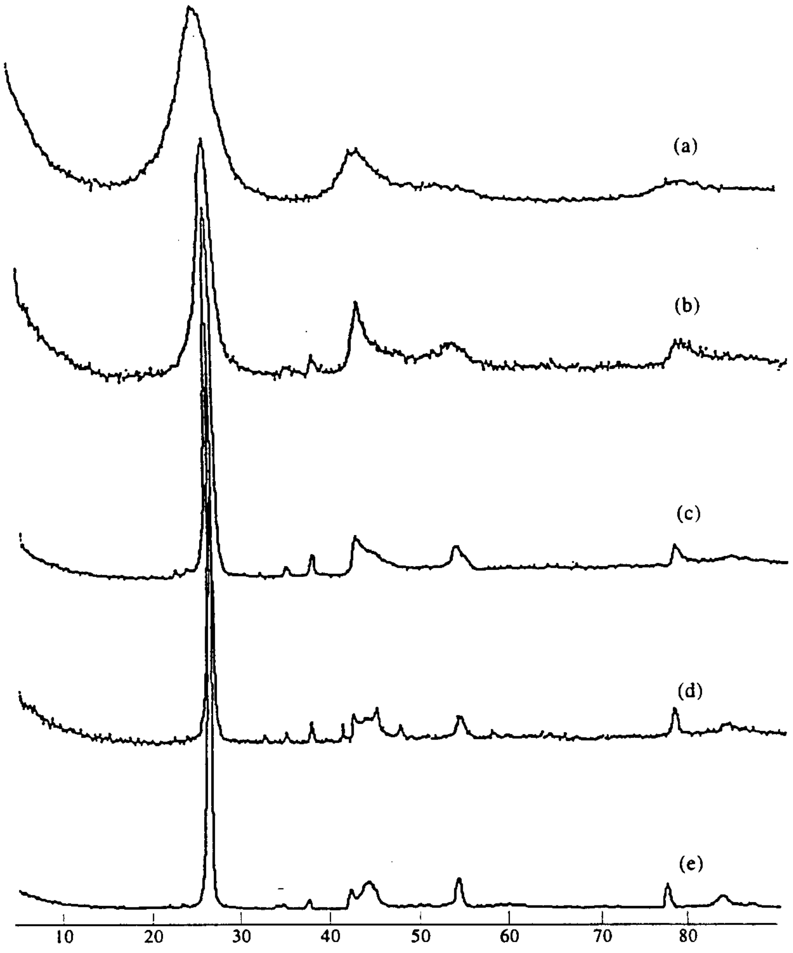

Fig. 2. X-ray diffractions of B/C materials prepared at (a) 1000°C, (b) 1500°C, (c) 1800°C, (d) 2100°C and (e) 2300°C.

Table 3. X-ray crystallite parameters and boron content as function of graphitization temperature and time

Sample	Pyrolysis conditions		X-ray results			Boron content(wt%)
	Temp. (°C)	Time (hours)	*d*002 (A)	*Lc* (A)	*La* (A)	
BC-1	1000	1	3.461	–	–	7.65
BC-2	1500	1	3.411	–	–	11.39
BC-3	1800	1	3.383	88	–	7.42
BC-4.1	2000	1	3.379	177	336	6.96
BC-4.2	2000	5	3.363	168	297	5.62
BC-4.3	2000	8	3.356	270	321	8.21
BC-5	2300	1	3.347	456	689	3.46

crystallite parameters of interlayer spacing *d*, crystallite size *Lc* and crystallite width *La*.

The *d* spacing decreases with heat treatment temperature and time, both *Lc* and *La* increase with temperature. Apparently, only 2300°C was necessary to obtain X-ray crystallite parameters that typically require much higher temperature (>3000°C) to achieve in traditional carbons. Clearly, the *in situ* boron is catalyzing graphitization of the B/C material.

It is very interesting to compare these graphitization results with the results obtained from other boron catalyzed graphitization systems. Murty [25] showed the apparent catalysis of graphitization by boron in three different industrial carbons. Figures 3 and 4 compare *d* spacing changes with heat treatment temperature and time, respectively.

Carbon A was a premium rotary calcined petroleum coke, carbon B was a well aligned vertically calcined petroleum coke, while carbon C was a rotary calcined isotropic coke prepared from the mineral gilsonite. The boronated samples were prepared by blending boron powder with recalcined coke flour. Heat treatment temperature and time, as well as the effect of boron concentration on graphitization were studied. For comparison, Murty's data on the effect of temperature on interlayer spacing of the samples

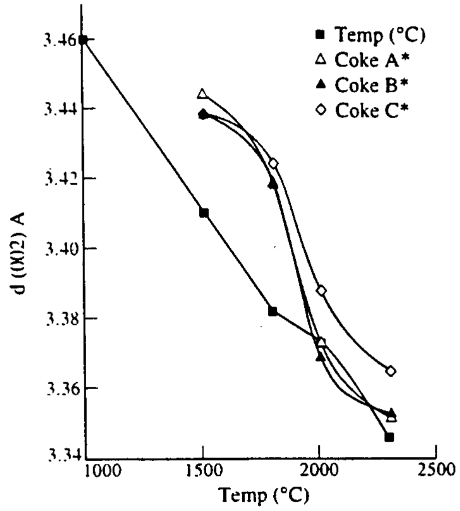

Fig. 3. A comparison of *d* spacing changes with graphitization temperature among the B/C pitch and three cokes catalyzed by boron powder (5 wt%). Carbon A is a premium rotary calcined petroleum coke, carbon B is a well aligned vertically calcined petroleum coke, while carbon C is a rotary calcined isotropic coke prepared from the mineral gilsonite.

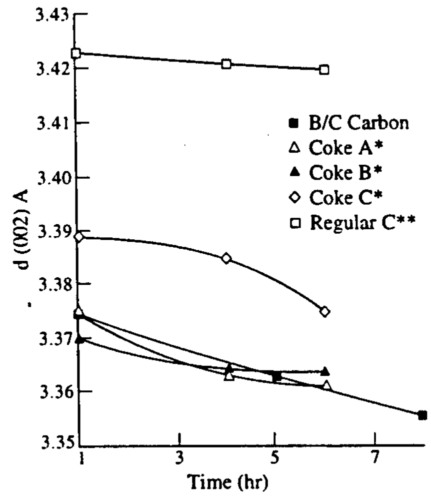

Fig. 4. A comparison of *d* spacing changes with graphitization time at 2000°C among the B/C pitch, regular carbon and three cokes catalyzed by boron powder (5 wt%). Carbon A is a premium rotary calcined petroleum coke, carbon B is a well aligned vertically calcined petroleum coke, while carbon C is a rotary calcined isotropic coke prepared from the mineral gilsonite.

containing the highest amount of boron, 5.0 wt%, is plotted in Fig. 3, along with results from this research. All the data were obtained for similar graphitization conditions, one hour at designated temperature. Clearly, all the data show that as heat treatment temperature increased the *d* spacing decreased. However, significantly lower interlayer *d* spacing can be achieved at the same temperature in our B/C material. Apparently the process of graphitization is greatly enhanced by having boron *in situ* during heat treatment. Furthermore, as shown in Fig. 4, whereas Murty has shown that the influence of boron is limited above 4 hours of heat treatment at 2000°C, our results show that *in situ* catalysis continues to lower *d* spacing up to the longest heat treatment time of 8 hours. It is well established that crystallite interlayer spacing approaches a limiting value within a few hours at each different temperature. Apparently at 2000°C, the minimum interlayer spacing of the B/C carbon has been shifted to that of graphite, thus no limiting *d* spacing was observed.

As for the mechanism of boron catalysis, enhanced diffusivity is widely believed to be the basic process involved in the high temperature graphitization of boronated carbons. Hennig [26] found that the diffusion constant of boron in graphite is more than three magnitudes higher than that of self diffusion, parallel to the layer planes. Two possible mechanisms have been postulated by Fischbach [11] in his comprehensive review of the kinetics and mechanism of graphitization. First, it is proposed that boron plays a similar role as vacancies in the carbon matrix. Graphitization is thereby accelerated by the increase in diffusivity of boron over carbon atoms. Since the diffusivity of boron is much higher in the *a* direction than the *c* direction, the catalytic effect of boron on graphitization should favor the growth of *La* over *Lc*. Alternatively, it was suggested that during annealing of boronated carbons, vacancy concentration increases as excess boron diffuses out of the lattice. In time, the removal of these vacancies during heat treatment enhances the graphitization reaction.

In the review, Fischbach [11] stated that development of (*hkl*) diffraction peaks, e.g. crystallite growth, should be used as the measure of graphitization since the presence of boron tends to lower *d* spacing, making it an unreliable crystallite parameter. However, although the decrease of crystallite interlayer spacing is well established, crystallite growth as the result of boron is yet unclear. Wagner [1] reported no catalytic effect on *La* or *Lc* when graphite was doped with boron at 2840°C. Jones *et al.* [5] found that doping of heat treated (216773K) pitch and PAN fibers had resulted in a small increase in *Lc*. They also found that boron had no significant effect on *La*. In fact, for PAN T300 fibers with 2000 ppm of B and *d* spacing of 0.3350 nm, the (100) and (101) reflections were lost upon boron addition. It was postulated that because the presence of substitutional boron has forced the *d* spacing to be below that of graphite, some break up and shortening of the *a* dimension occurred as more tilt boundaries were formed between crystallites.

In the current investigation, the significant increase of both *Lc* and *La* clearly demonstrates that *in situ* boron is catalyzing the graphitization process. Closer examination of the secondary peaks (Fig. 5) in X-ray diffraction patterns shows that there is significant development of the (100) and (101) peaks as the temperature increased from 1800 to 2300°C.

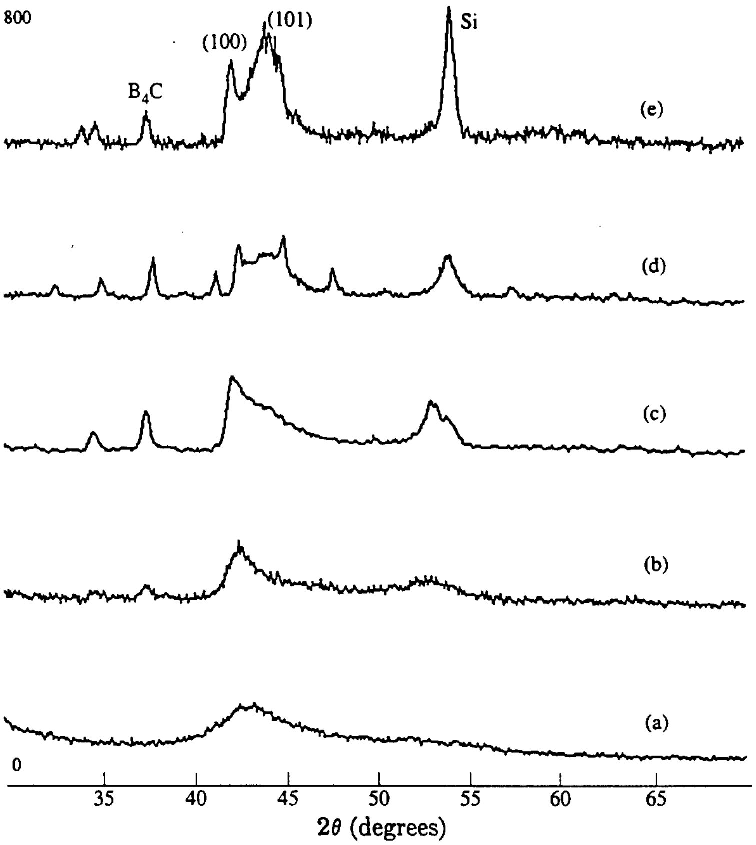

Fig. 5. The secondary peaks in X-ray diffraction patterns of B/C materials prepared at (a) 1000°C, (b) 1500°C, (c) 1800°C, (d) 2100°C and (e) 2300°C.

The (101) peak is traditionally broader than the (100) peak since it is as much a measure of *Lc* as a gauge of *La*. Although the increase in graphitization temperature has an augmenting effect on the crystallite size and width, the enlargement of *La* and *Lc* at such low temperatures can positively be attributed to catalysis by boron. Higher values of *La* and *Lc* were observed in the 2300°C B/C material even though the lattice spacing (3.347 Å) was well below that of graphite. As shown in Table 3, the dimensions for *Lc* and *La* for the 2300°C B/C material are 456 and 689 Å, respectively. Interestingly, the improvement of crystallite size was more pronounced in the *a* direction than in the *c* direction. If the mechanism of catalysis is based on enhanced diffusivity as is widely believed, then one would expect a faster growth of crystallite width (*La*), since the diffusion constant of boron parallel to the layer planes (6320 cm^2/s) is much greater than that in the perpendicular direction (7.1 cm^2/s) [26]. The activation energies for these two processes are almost equal, 157 kcal/mol for parallel and 153 kcal/mol for perpendicular. The result of this study provides the first evidence that supports the anisotropy in the catalysis of graphitization.

Lowell [7] studied the effect of boron doping on the X-ray crystallite parameter of graphite. It was found that *d* spacing decreased while the in plane lattice parameter increased with increase in boron concentration. Although the effect of heat treatment time on *d* spacing was measured, meaningful comparison with the time data from this investigation is difficult because Lowell's specimens were graphitized prior to the introduction of boron. Lowell stated that the limiting lattice constant as a function of boron concentration at a given temperature can be described by the following equation:

$$C_o = 6.71163 - 0.00594 K_B$$

where C_o is the lattice constant of a boronated carbon in angstroms and K_B is the atomic fraction of dissolved boron. Applying this empirical formula to the data from our 2300°C B/C carbon, the solid boron solution level of the sample is calculated to be 2.97 at%, which is over 25% greater than the literature accepted limit of 2.35 at%. In fact, as shown in the next section, a much higher boron concentration was determined using elemental analysis. Previously, a higher boron concentration was only achievable in less crystalline carbons [5,11]. In this study the lattice spacing of 3.347 Å at 2300°C was lower than the limit of 3.349 Å at 2350°C shown by Lowell.

It is interesting to note that small amounts of boron carbide were formed during heat treatment of the B/C material. The formation of B_4C could have increased the amount of vacancies in the specimen and thereby promoted graphitization. The presence of B_4C as well as the overall concentration of boron in the samples are discussed in more detail in the following section.

3.4 *Boron concentration in B/C materials*

The bulk boron contents as determined by elemental analysis are shown in Table 3. The initial boron concentration of the precursor is 7.69 wt% assuming that all the chlorine and hydrogen were lost upon high temperature carbonization. Since the B–Cl moiety is highly reactive, we expected reaction to occur below 1000°C. Indeed the boron content of the sample BC-1 (1000°C, 1 hour), e.g. 7.65 wt% matches very well with that of the initial value, taking into account that some hydrogen is still present at this low temperature. As is immediately apparent in Fig. 6, the boron content remains relatively constant up to 2000°C, which is indicative of the stability of boron in the carbon structure.

The 1500°C concentration was unusually high probably due to sample digestion problems that arose during analysis. Note that all of the specimens were analyzed twice except for the 1500°C sample. Clearly, by carefully designing the B/C precursor, we are able to assert very good control of the carbonization chemistry in order to obtain B/C carbon of desired composition and structure. Furthermore, by virtue of the fact that boron is introduced in the precursor stage, already chemically bonded to aromatic carbons, the boron content should be homogeneous and substitutional. However, the state of the boron within the B/C matrix merits more analysis. While it may be simpler to consider all the boron as bonded to carbon, there clearly exists an equilibrium between the boron containing carbon phase and boron carbide. Currently, spectroscopy techniques such as XPS are being used to determine the electronic state of the boron within our samples.

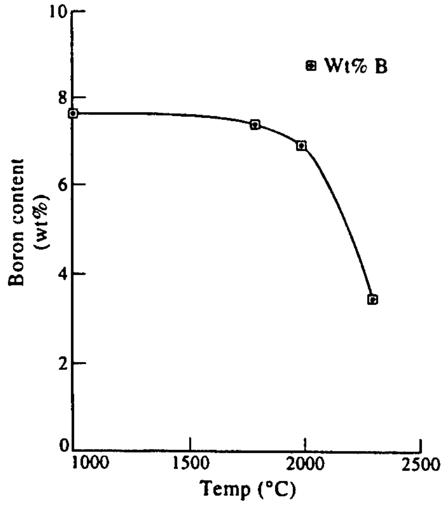

Fig. 6. Boron contents in B/C materials at various temperatures.

The wt% of boron within the B/C carbon decreases dramatically at 2300°C. This decrease of concentration has also been reported by Turnbull [8] and Lowell [7] at approximately 2250°C, although the boron content of sample BC-5 is still higher than that reported by the two authors. Apparently, at this temperature a reaction takes place in which excess boron is ejected from the matrix. Nevertheless, as shown above, high crystallinity and boron content can be achieved below this critical temperature by our synthetic method.

4. CONCLUSION

This paper has shown a new synthetic route to prepare boron containing carbon (B/C) material with high boron content and well ordered crystalline structure. By virtue of the fact that boron is chemically bonded to the aromatic carbons of the 9-chloroborafluorene precursor, an *in situ* boron catalyzing carbonization and graphitization reaction can effectively take place at relatively low temperature to form a uniform B/C material with the substitutional boron in the graphitic structure. A knowledge of boron and carbonization chemistry allows us to develop an intermediate of mesophase B-pitch, which by its nature should be processable. In addition, the new B-pitch allows us for the first time to evaluate the catalytic effect of boron on the graphitization process, without the effects of high temperatures (>2500°C). Interestingly, X-ray diffraction analysis demonstrated anisotropy in the catalysis of graphitization reactions by boron where *La* grows preferentially over *Lc*.

Acknowledgements—The authors would like to thank the financial support from the U.S. Air Force, Office of Scientific Research. The authors also thank Professor P. A. Thrower for useful discussions.

REFERENCES

1. P. Wagner and M. Dickinson, *Carbon* **8,** 313 (1970).
2. B. T. Kelly, A. Whittaker, D. Tobin and P. Wagner, *Carbon* **9,** 447 (1971).
3. A. Marchand, *Chemistry and Physics of Carbon* **7,** 155 (1971).
4. I. Spain, *Chemistry and Physics of Carbon* **16,** 119 (1981).
5. L. E. Jones and P. A. Thrower, *Carbon* **29,** 251 (1991).
6. D. J. Allardice and P. L. Walker, Jr., *Carbon* **8,** 375 (1970).
7. C. E. Lowell, *J. Amer. Cer. Soc.* **50,** 142 (1967).
8. J. A. Turnbull, M. S. Stagg and W. T. Eeles, *Carbon* **3,** 387 (1966).
9. D. L. Fecko, L. E. Jones and P. A. Thrower, *Carbon* **31,** 637 (1993).
10. R. B. Kaner, J. Kouvetakis, C. E. Warble, M. L. Sattler and N. Bartlett, *Mat. Res. Bull.* **22,** 339 (1987).
11. D. B. Fischbach, *Chemistry and Physics of Carbon* **7,** 86 (1971).
12. R. Hu and T. C. Chung, *Carbon* (accepted).
13. A. Weintraub and P. L. Walker, Jr., *Proc. Intern. Conf. Industrial Carbon and Graphite* **3,** 75 (1971).

14. G. E. Coates and J. G. Livingstone, *J. Chem. Soc.* 4909 (1961).
15. H. Marsh and P. L. Walker, Jr., *Chemistry and Physics of Carbon* **15**, 230 (1979).
16. I. C. Lewis, *Carbon* **20**, 519 (1982).
17. K. Lafdi, S. Bonnamy and A. Oberlin, *Carbon* **29**, 831 (1991).
18. H. Honda, *Carbon* **26**, 139 (1988).
19. Y. D. Park and I. Mochida, *Carbon* **6**, 925 (1989).
20. I. C. Lewis, *Carbon* **18**, 191 (1979).
21. E. Fitzer, K. Mueller and W. Schaefer, *Chemistry and Physics of Carbon* **7**, 237 (1971).
22. I. Mochida and Y. Sakai, U.S. Patent No. 4891126, (1990).
23. I. Mochida, K. Shimizu, Y. Korai and Y. Sakai, *Carbon* **30**, 55 (1991).
24. K. Lafdi, S. Bonnamy and A. Oberlin, *Carbon* **29**, 849 (1991).
25. H. N. Murty, D. L. Biederman and E. A. Heintz, *Fuel* **56**, 305 (1977).
26. G. Hennig, *J. Chem. Phy.* **42**, 1167 (1965).

Pergamon

Carbon Vol. 35, No. 5, pp. 641–650, 1997
Copyright © 1997 Elsevier Science Ltd
Printed in Great Britain. All rights reserved
0008-6223/97 $17.00 + 0.00

PII: S0008-6223(97)00019-5

SYNTHESIS OF B/C MATERIALS FROM BORON-CONTAINING PHENYL ACETYLIDES

M. CHASMAWALA and T. C. CHUNG*
Department of Materials Science and Engineering, The Pennsylvania State University, University Park, PA 16802, U.S.A.

(*Received* 15 *October* 1996; *accepted in revised form* 2 *January* 1997)

Abstract—This paper discusses the synthesis and graphitization of three boron-containing phenyl acetylides, with B/C ratios between 1/18 and 1/8. The experimental results show that the initial rate at which the graphitic structure develops is strongly related to the molecular structure of the phenyl acetylides. The formation of non-coplanar molecular structure in the stabilization reaction slows down the graphitization reaction. However, all three precursors show effective transformation reactions to produce the boron-substitutional graphitic (B/C) materials at relatively low temperature (2200°C), despite the significant differences in boron concentration and chemical nature of the precursors. Relatively large crystallite size and small *d*-spacing between interlayers of B/C products were observed by X-ray diffraction. Clearly, boron is not only substitutionally incorporated in the graphitic structure but also enhances the graphitization reaction. © 1997 Elsevier Science Ltd

Key Words—A. Doped carbons, B. graphitization, C. X-ray diffraction, D. crystallite size.

1. INTRODUCTION

Carbon fibers are very interesting materials [1–4] in that they offer excellent mechanical properties and high strength to weight ratios. However, their susceptibility to oxidation [5,6] at elevated temperatures is cause for concern and limits the range of applications that this class of materials can be employed in. A number of different approaches have been used to reduce this susceptibility of carbon under oxidizing environments. One of the most widely employed strategies for the inhibition of oxidation of carbon has been the doping of carbon fibers, at temperatures above 2700°C, with various boron-containing compounds [7,8]. Boron is believed to inhibit the oxidation of carbon fibers via any combination of a number of effects that substitutional boron might have on the oxidation reaction. One of the notable postulations on the inhibition mechanism is the formation of a glassy boron oxide layer on the surface of the carbon fiber which provides an impermeable layer precluding the passage of dry oxygen, thereby inhibiting the oxidation of carbon. Another theory is based on the improvement of the crystal structure of graphite due to the catalysis of the graphitization by boron, and the consequent reduction in the imperfections in the graphitic structure that are vulnerable to oxidation reactions. While the mechanism of oxidation-inhibition induced by the presence of boron is still subject to debate, it is incontrovertible that boron definitely has a beneficial effect.

One of the major disadvantages of employing doping as a route to the introduction of boron into graphitic carbon is the necessity of employing elevated temperatures for the doping reaction. Due to the elevated temperatures that must be employed for the introduction of boron, it becomes difficult to separate the effect of graphitization catalysis by boron from the effect of the high temperature exposure. The other important disadvantage is that the concentration of boron in the carbon fiber is in the form of a gradient that decreases as the distance from the surface of the fiber increases. Thus, the beneficial effect of boron extends to only a short distance below the surface of the fiber. Clearly, a better method for the introduction of boron into graphitic carbon is desirable, one which would introduce boron uniformly into the graphitic structure, and would not require the employment of high temperatures.

In our previous paper, we have reported a novel approach [9,10] by using specifically designed boron-containing precursors, such as 9-chloroborafluorene. This precursor can be thermally transformed to boron containing graphitic (B/C) materials with high crystallinity and large crystal size at relatively low temperature (2000°C). Up to 7% of boron (similar B concentration in the precursor) was homogeneously substituted in the graphitic structure. The overall results seem to indicate that by carefully taking into account the chemistry of boron and the mechanism of carbonization we can tailor the precursor to produce B/C materials with desirable compositions. It is very interesting to understand the scope and limitations of this new precursor approach, especially the development of new precursors which can be easily synthesized, and the effect of different amounts of boron in the precursor on the graphitization reaction. With this purpose in mind, we have systematically synthesized three boron-containing phenyl

---

*Corresponding author.

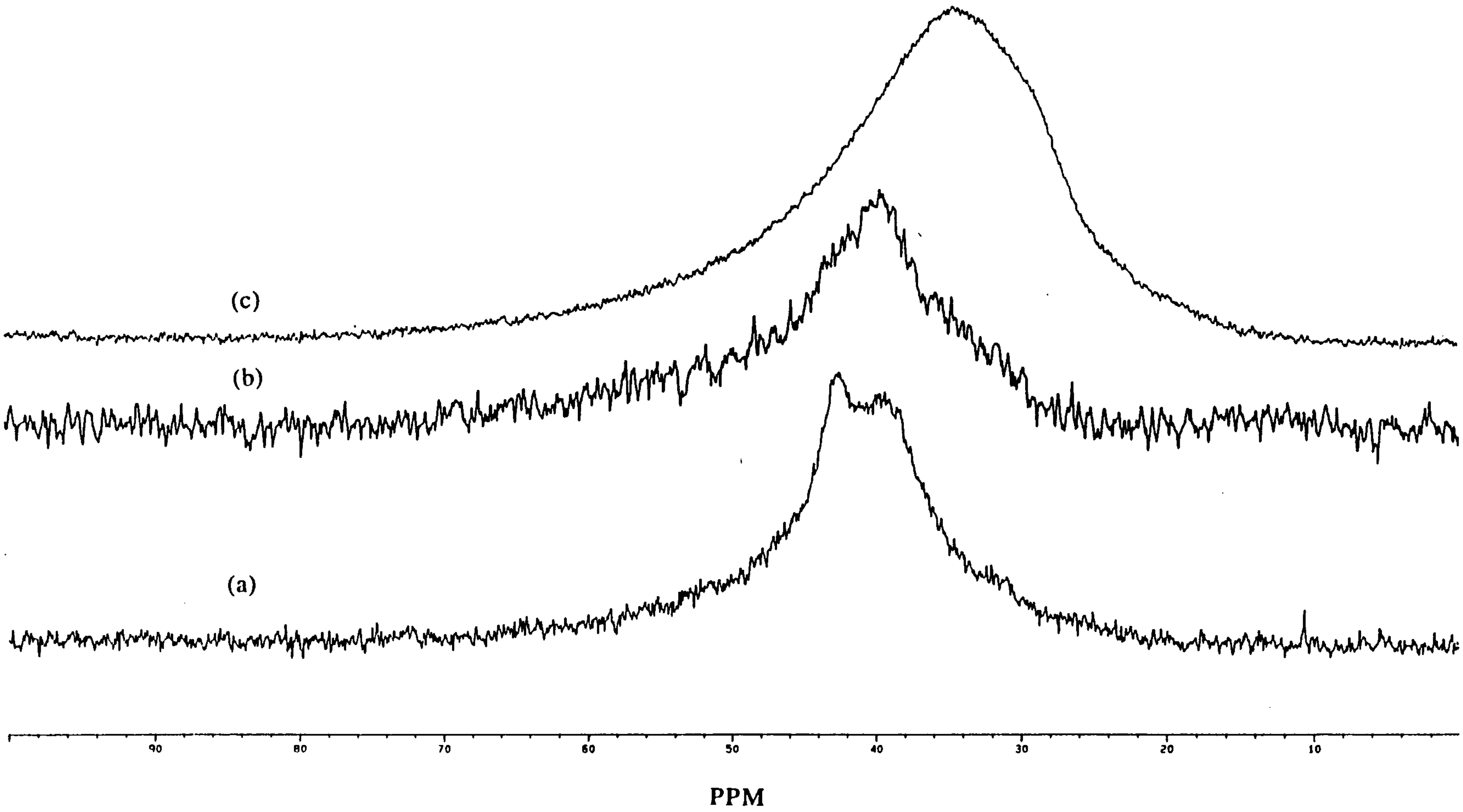

Fig. 1. The comparison of ^{11}B NMR spectra of three precursors: (a) tris(phenyl acetylide)borane (TPB), (b) bis(phenylacetylide)chloroborane (BCB) and (c) dichloro(phenyl acetylide)borane (DPB).

acetylide precursors which have similar molecular structures and different boron contents. The effects of boron concentration and chemical nature at various temperatures along the graphitization pathway were studied.

2. EXPERIMENTAL

2.1 *Materials and instrumentation*

Phenyl acetylene, butyl lithium (2.5 M solution in hexanes) and boron trichloride (1 M solution in heptane) were purchased from the Aldrich Chemical Company and used without further purification. Reagent grade benzene was purchased from the Aldrich Chemical Company, dried over calcium hydride, distilled into a Schlenk flask containing Na-anthracenide, distilled out of this flask and stored in a glove box. Reagent grade ether was purchased from Aldrich Chemical Company, stirred in a Schlenk flask containing Na-anthracenide, distilled out of this flask and stored in a glove box.

All ^1H NMR and ^{11}B NMR were recorded on a Bruker AM-300 spectrometer with DISNMR software. Quartz NMR tubes were used for the ^{11}B NMR measurements. Typical sample size was 15 mg of polymer dissolved in 0.5 ml of deuterated solvent. The internal standard for the ^{11}B NMR was boron trifluoride dietheyl etherate which has a chemical shift of 0 ppm. The thermal property of samples was performed in a Perkin–Elmer TGS-2 Thermogravimetric Analyzer. The data acquired from this instrument was analyzed on the Thermal Analysis Data Station System.

2.2 *Synthesis of precursors*

All synthetic reactions were performed under an atmosphere of nitrogen or argon. The synthesis of phenylethynyllithium was performed as described in the literature [11]. The compounds of interest were synthesized by the dropwise addition of the appropriate stoichiometric volume of boron trichloride (1 M solution in heptane) to a cold (ice–water bath) stirred 10% suspension of phenylethynyllithium in benzene. In a typical reaction, 1 g of phenylethynyllithium was suspended in 10 g of benzene in a 250 ml round-bottomed flask (with a side-arm) equipped with a magnetic stirrer, and sealed off with a vacuum valve. The vacuum valve was used to connect the flask to a vacuum line through which a steady purge of nitrogen was maintained. The flask was cooled by placing it in an ice–water bath, and 9.3 ml of boron trichloride (1 M solution in heptane) was added dropwise from a gastight syringe via the side-arm. The off-white suspension rapidly turned brown in color on the addition of boron trichloride. The reaction was kept cold during the course of the addition, and then allowed to slowly warm to room temperature. After stirring for an additional 4 hours, the benzene and residual boron trichloride were evaporated off on a vacuum line, and the reaction flask was taken into a glove box where the product from the reaction was stirred in 60 ml of benzene for a minimum of 6 hours. The soluble fraction was isolated by filtration, and the compound obtained in 65% (1.100 g) yield by the evaporation of benzene on a vacuum line. Samples were stored in a glove box, under an atmosphere of argon, prior to carbonization.

2.3 *Pyrolysis*

Stabilization and carbonizations were performed in one step by placing the sample in a ceramic holder and sealing off the sample from exposure to atmosphere by closing valves at both end of the quartz tube. After placing in the tube furnace, and ensuring that there existed a positive pressure of argon in the quartz tube, the sample was heated in the tube furnace under a flowing stream of argon. After having established by TGA analysis that carbonization was effectively completed by 550°C, the graphitization reactions were performed in a graphite resistance type furnace manufactured by Centorr Vacuum Technology. The furnace was evacuated to a vacuum of 150 mTorr and then pressurized to 2 psi with ultra high purity argon. This process was repeated twice thereafter to ensure the elimination of air from the furnace before any heating was undertaken. The heating of the furnace was controlled manually, and the temperature monitored by a thermocouple up to 1450°C, and thereafter, for higher temperatures by an optical pyrometer. To ensure that the errors in measurements by the optical pyrometer were minimal, the quartz window through which measurements were taken was cleaned regularly, and the alignment of the optical pyrometer was also checked periodically.

2.4 *X-ray diffraction*

X-ray diffraction measurements were made on the graphitized B/C materials on a Rigaku Geigerflex X-ray diffractometer which employed Cu K radiation operating at 20 mA and 40 kV. A slurry of the samples was made by grinding them in an agar mortar and pestle in methanol. A thin film of this slurry was then cast on a zero background quartz slide and air dried for a minimum of 10 minutes. The accurate determination of *d*-spacing was performed

Table 1. A summary of ^{11}B NMR chemical shifts of borane compounds

Compound	^{11}B NMR shift (ppm)^b
BCl_3^a	47
$PhAcBCl_2$	43
$(PhAc)_2BCl$	40
$(PhAc)_3B$	35
$(RO)_3B^a$	18

PhAc: Phenyl acetylide group.
^{a}Literature values.
^{b}ppm values relative to (BF_3). Et_2O.

by adding pure silicon (NBS SRM 640) to the slurry and employing the peak from silicon (28.443° 2θ) to ensure elimination of errors caused by film thickness. SP-1 graphite was employed to determine instrument broadening at the 2θ value of interest, to ensure accuracy of calculation of L_c. Measurements were made from 20°–30° 2θ at 1° $\min^{-1}$ (for determination of d-spacing and calculation of L_c), and from 10°–90° 2θ at 5° $\min^{-1}$ (to observe the general features of the diffraction patterns). The d-spacing and L_c were calculated from the corrected 2θ values of the (002) reflection.

3. RESULTS AND DISCUSSION

3.1 *Boron containing phenyl acetylides*

The basic reaction scheme for the synthesis of boron containing phenylacetylides is the condensation reaction [12] of phenylacetyl lithium and BCl_3. The metallation of phenyl acetylene is basically quantitative. The extent of subsequent substitution is governed by the stoichiometric ratio of phenylacetyl lithium and BCl_3 as illustrated in eqn (1). Three B/C precursors, including dichloro(phenyl acetylide)borane (DPB), bis(phenylacetylide)chloroborane (BCB) and tris(phenyl acetylide)borane (TPB), have been prepared for this study.

Both ^1H and ^{13}C NMR spectra show the phenyl group in these three products, but they are indistinguishable from each other. The extent of the substitution reaction was revealed by ^{11}B NMR measurements. Figure 1 shows the ^{11}B NMR spectra of three products produced by the stoichiometric ratio of 1/1, 2/3 and 1/3 between phenylacetyl lithium and BCl_3, respectively. The relatively broad peaks are partly due to the quadrapolar nature of the boron nucleus. In the case of 1/1 phenylacetyl lithium and BCl_3 reaction, Fig. 1(a) shows two chemical shifts, with a peak at 43 ppm and a shoulder around 40 ppm. Some minor di-substitution product (BCB) clearly coexists with the expected DPB material [13]. Despite the manipulation of reaction conditions, the di-substitution product was difficult to prevent. However, both di- and tri-substitution reactions are quite clean to produce BCB and TPB, with the ^{11}B chemical shifts at 40 and 35 ppm (shown in Figs 1(b) and (c)), respectively. It is clear that the increasing substitution of the chlorine atom in BCl_3 by the phenyl acetylide group leads to a chemical shift to higher field.

Table 1 compares the chemical shifts of three precursors with two reference compounds, BCl_3 and $(RO)_3B$. BCl_3 is a strong Lewis acid (electron-deficient) and $(RO)_3B$ is a stable compound (electron-neutral). Even though it is well documented [14] that boron in compounds with alkene groups attached to the boron enjoy significant shielding owing to the π–p interaction between the π electrons of the vinyl group and the empty p orbital on boron, the situation for the alkynyl–boron bond was speculated to have much less π–p interaction owing to the significantly lower p contribution in an sp hybridized alkynyl carbon atom. Thus, the upfield shift in ^{11}B NMR of the alkynyl boron-containing compounds was attributed to the diamagnetic anisotropy of the acetylene group [15]. A precedent for the non-interaction of the alkynyl group was said to be the propeller-like structure of triphenylboron [16], in the solid state, in which boron is attached to the three carbon atoms in a trigonal planar structure but with the individual phenyl groups at an angle of 30° to the plane defined by boron and the three carbon atoms to which it is attached, as shown below.

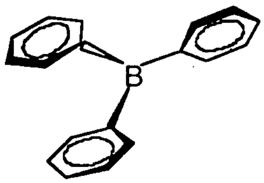

It was also found that a very low energy of activation exists for rotation about the boron–carbon bond in this compound [17] which was determined primarily by steric effects and, hence, conjugative effects were presumed to have very little contribution. The same factors were presumed to hold in studies on dihalogenophenyl boranes [18]. Subsequent work on a boron-containing alkynyl compound [19], such as dimesitylphenylethynylborane, has shown fairly con-

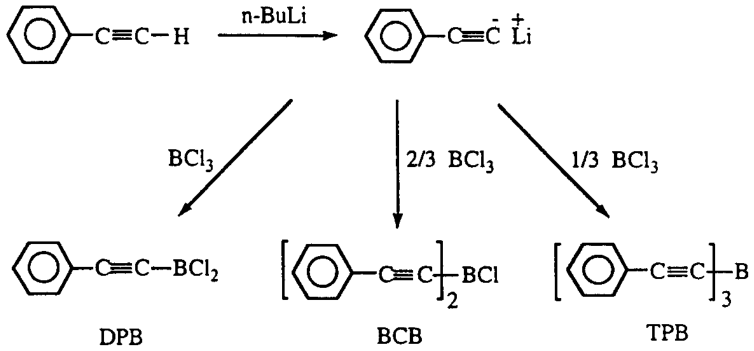

Equation 1

clusively that it is indeed π–p interaction that is the source of the upfield shift in ^{11}B NMR in alkynyl boranes, and that conjugative effects are indeed very strong in alkynyl–boron bonds, although the exact magnitude of the contribution of the π–p interaction cannot be determined due to an indeterminable contribution from the diamagnetic anisotropy of the alkynyl group. In fact, the shifts observed for the different molecule that we synthesized are monotonically decreasing as the extent of this substitution increases, bearing out the increasing contribution of π–p interaction towards shielding the boron nucleus.

The nature of the chemical shifts for the three compounds suggests that there might exist yet another mechanism for the inhibition of oxidation in boron-containing carbon fibers. This would be the reduction of electron density on the adjacent C-atoms and the consequent delocalization of electrons over the long range in the *x–y* plane of graphite, reducing the susceptibility of the graphite to oxidation. Obviously, there would be a requisite minimum homogeneous boron concentration for this effect to pervade the entire graphitic sample, so as to efficaciously retard oxidation and promote graphitization.

3.2 *TGA studies*

In this study, we attempted to understand the effect of boron (chemical nature and concentration) on the stabilization, carbonization and graphitization reactions. The initial concentration of boron (in terms of the C/B ratio) and the number of reactive B–Cl groups in the precursor compounds vary from 8/1 to 18/1 and 2 to 0, respectively. Attempts were made to relate these variations to the effect of boron on the pyrolysis reactions. Thermogravimetric analysis (TGA) of each of the three precursors was undertaken. The thermal history employed for thermogravimetric analysis is depicted below:

$$30^\circ C \xrightarrow{5^\circ C\ min^{-1}} 350^\circ C \xrightarrow[60\ minutes]{Isothermal} 350^\circ C \xrightarrow{5^\circ C\ min^{-1}}$$
$$550^\circ C \xrightarrow[240\ minutes]{Isothermal} 550^\circ C \xrightarrow{Cool} 30^\circ C$$

The results for each of the three compounds are compared in Fig. 2. In general, the weight loss for all three compounds started at about 230°C (40 minutes) with the extent of weight loss dependent on the precursors. It is very desirable to have the stabilization reactions completed below 230°C, because this increases the molecular weight and prevents precursor volatalization during the carbonization procedure (>230°C). For DPB, the weight loss during the carbonization procedure (up to 550°C) is theoretically (assuming loss of all hydrogen and halogen atoms) 41.5%, which is only 2% less than

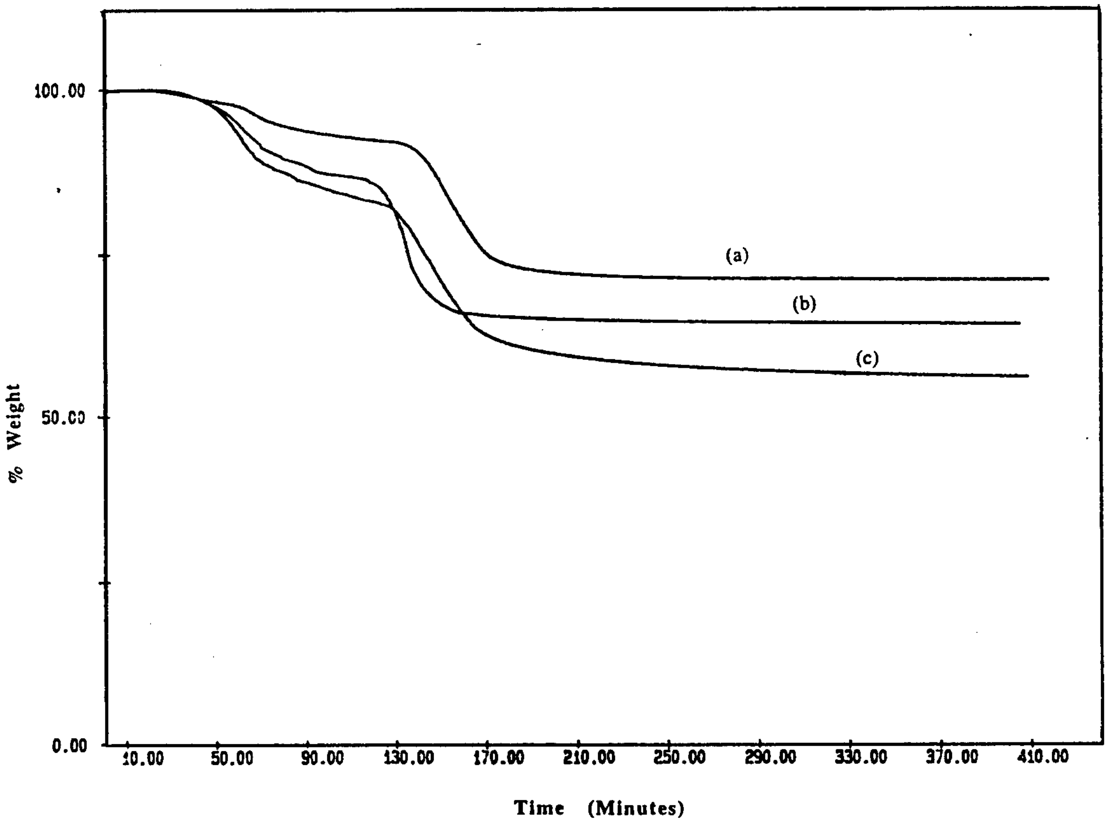

Fig. 2. DSC curves of (a) tris(phenyl acetylide)borane (TPB), (b) bis(phenylacetylide)chloroborane (BCB) and (c) dichloro (phenyl acetylide)borane (DPB).

the experimentally observed value of 43.66%. While the agreement of theoretical values with experimentally observed numbers may be fairly good for DPB, the weight losses for BCB and TPB are as high as 35.50 and 29.29%, respectively (the theoretical weight losses being 18.31 and 4.77%, respectively). Obviously, the higher than expected weight loss is directly linked to the more difficult stabilization reactions and the materials thus volatalized during the carbonization procedure, especially in the TPB case.

It is believed that the primary initial reactions that are responsible for the stabilization reactions in these three compounds are haloboration of the alkynyl group by the boron–halogen bond (shown in eqn (2)), and the formation of cyclic structures via ($2\pi+4\pi$), and ($2\pi+2\pi$) reactions (shown in eqn (3)). The haloboration reactions of alkynyl groups usually occur fairly easily even at subambient temperatures [20]. On the other hand, the normal ($2\pi+4\pi$) reactions require slightly elevated temperatures of 50–100°C, while the ($2\pi+2\pi$) reactions are only facilitated at temperatures in excess of 200°C [21].

The haloboration reactions shown in eqn (2) are only possible in DPB and BCB compounds, containing B–Cl groups and alkynyl groups. On the other hand, the ($2\pi+4\pi$) and ($2\pi+2\pi$) reactions are possible in all three precursor systems, each of which contains aromatic species along with alkynyl species. Since DPB has the highest concentration of facile B–Cl bonds, consequently, it would be expected that the haloboration reaction of alkynyl species by the boron–chlorine bond would be expected to occur with higher probability. As the larger steric bulks of BCB and TPB come into play with a fewer number of B–Cl bonds, it may be expected that the reactions do not occur quite as efficaciously as one might hope. In the case of TPB, which contains only boron–alkynyl bonds, haloboration is not possible. In other words, some molecules might be evaporated before any inter-molecular reaction, which could be the reason for the significant deviation of weight losses from theoretical expectations for BCB and TPB.

During the carbonization reaction (>230°C), along with the additional cyclization reactions, some other condensation reactions must also take place to reduce the residual weight (as shown in Fig. 2). In fact, most of H and Cl were removed below 550°C, since when the samples were heated in a tube furnace up to 1200°C (and maintained at that temperature for 6 hours) minimal additional weight loss was seen. This indicates that carbonization was mostly completed by the processing up to 550°C. Halo-boranes have been known to catalyze polymerization of many different vinyl and aromatic monomers. Mochida *et al.* [22,23] have successfully prepared mesophase

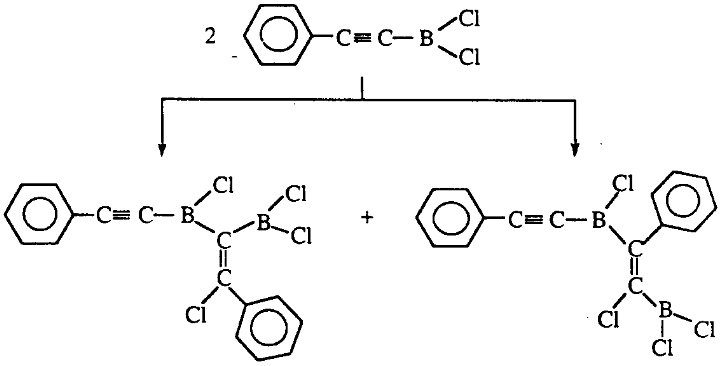

Equation 2

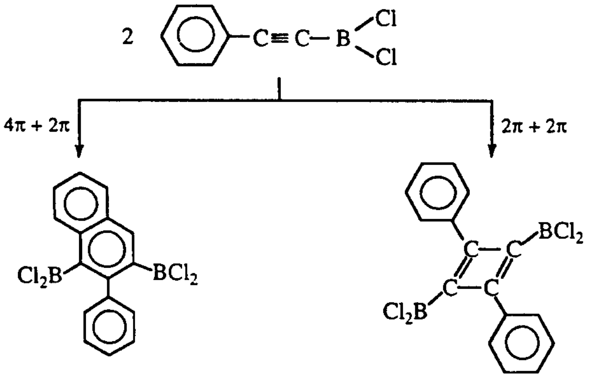

Equation 3

pitch with 100% anisotropy by treating anthracene and naphthalene with BF_3/HF. The electron deficient BF_3 is believed to form a charge transfer complex with HF. This initiator then causes the rapid cationic polymerization of aromatic precursors. Although the B–Cl species is less reactive than BF_3, the formation of HCl during the polymerization reaction indicates that a similar cationic catalysis with internal hydrogen transfer reaction is certainly possible.

3.3 *B/C materials*

After having established by TGA that carbonization was effectively completed by 550°C, the samples were carbonized by heating at $5°C\,min^{-1}$ to 550°C and held at this temperature for 6 hours. In the preparation of crystalline B/C materials, the product obtained from the carbonization reaction was further heated up to the desired graphitization temperature and maintained at that temperature for the desired period of time (generally 30 minutes). Relatively small weight loss (<15%) was observed in each case of the graphitization reactions. The carbonized compounds from DPB, BCB and TPB will henceforth be abbreviated to PDPB, PBCB and PTPB, respectively.

Figures 3–5 depict the X-ray diffraction patterns of the B/C materials from various precursors at different heat treatment tempeartures. Clearly, there is significant development of the secondary (100) and

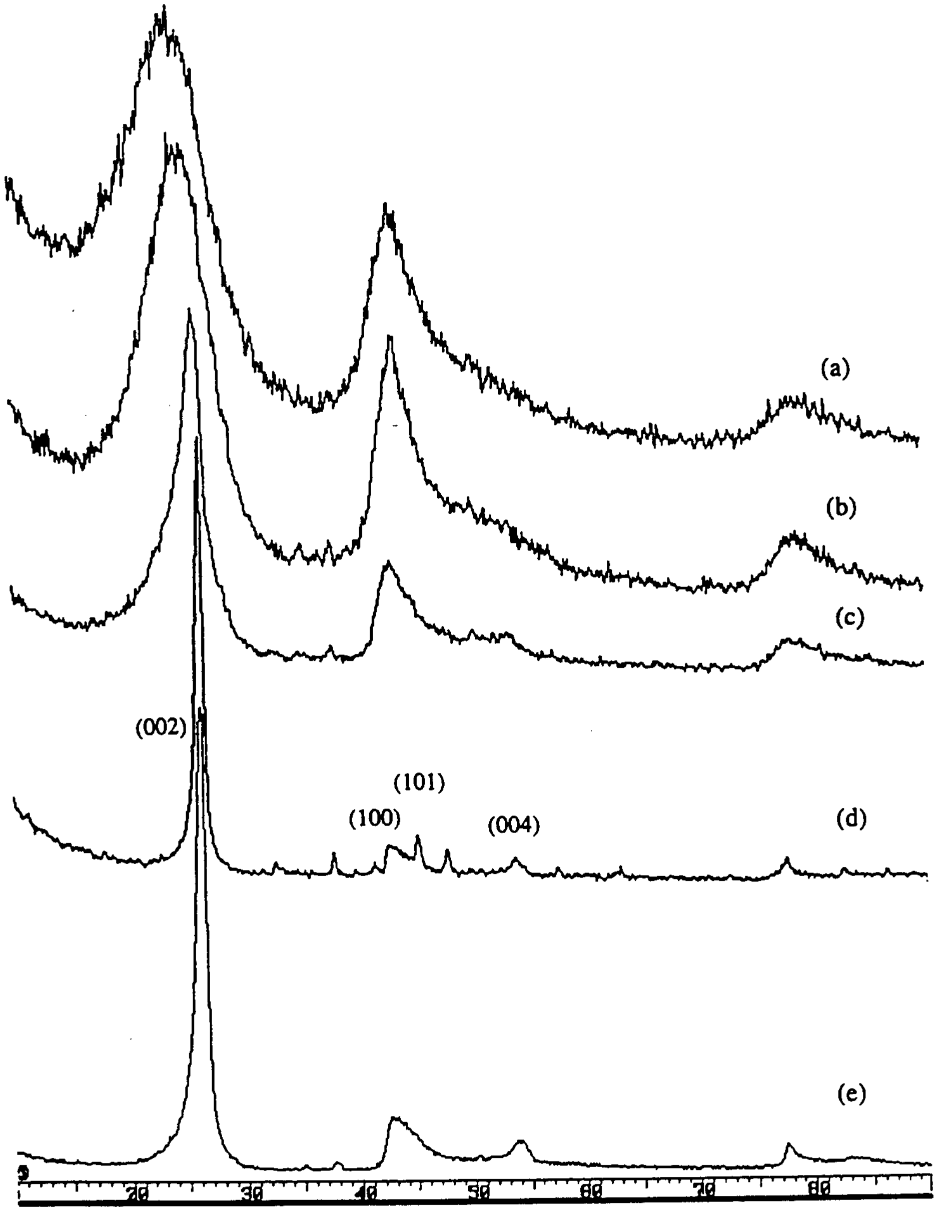

Fig. 3. X-ray diffractions of B/C materials prepared by tris(phenyl acetylide)borane at (a) 1200, (b) 1400, (c) 1600, (d) 2000 and (e) and 2200°C.

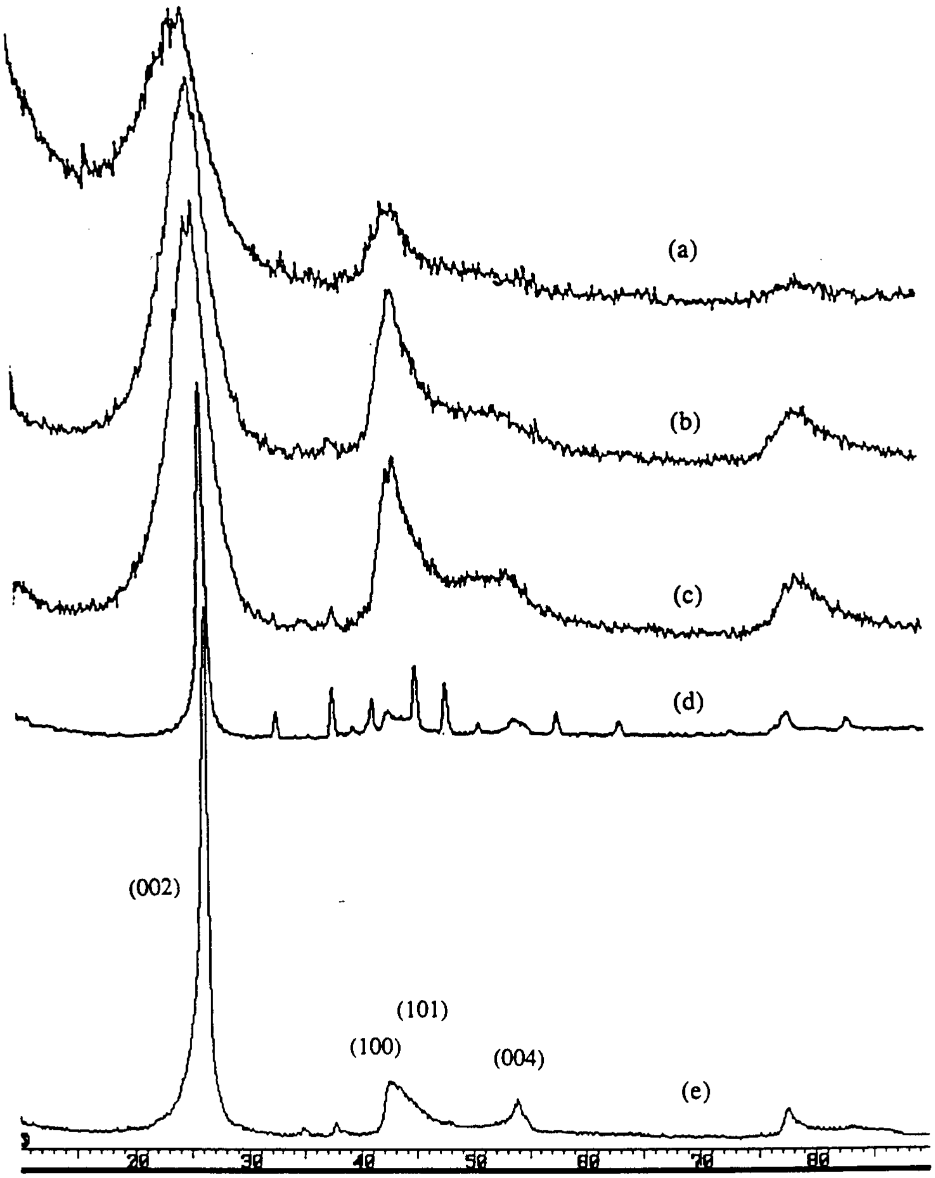

Fig. 4. X-ray diffractions of B/C materials prepared by bis(phenylacetylide)chloroborane at (a) 1200, (b) 1400, (c) 1600, (d) 2000 and (e) 2200°C.

(101) peaks (at $2\theta \sim 43°$) as the temperature increased from 1800 to 2200°C. Table 2 summarizes the X-ray crystallite parameters of interlayer *d*-spacing (i.e. the 002 reflection) and L_c (crystal size) of the different compounds at various processing temperatures. Apparently, only 2200°C was necessary to obtain X-ray crystallite parameters that typically require much higher temperature (>3000°C) to achieve in traditional carbons. Clearly, the *in situ* boron is catalyzing graphitization to form B/C material in all three cases, and the concentration of boron (B/C ratios between 1/8 and 1/18) in the precursor are adequate for enhancing the graphitization reaction.

It is also immediately apparent that the rate at which the graphitic structure develops in PTPB is fairly different from those in the PDPB and PBCB cases. The initial high layer plane *d*-spacing and low L_c values for PTPB may arise from the non-coplanar molecular structure during the stabilization and carbonization reactions. As discussed, PTPB was prepared from the precursor only containing boron–alkynyl bonds which can form non-coplanar molecular structure via out-of-plane ($2\pi + 2\pi$) reactions. Thus, these bonds would need to be cleaved and reformed to accommodate the development of graphitic structure. After passing the initial stage of graphitization reaction, with the temperature beyond 1600°C, PTPB seems to speed up the graphitization process. At 2200°C, the *d*-spacing of PTPB approaches that of natural graphite (3.35 Å). It is very interesting to note that despite having the lowest concentration of boron in the three cases, PTPB

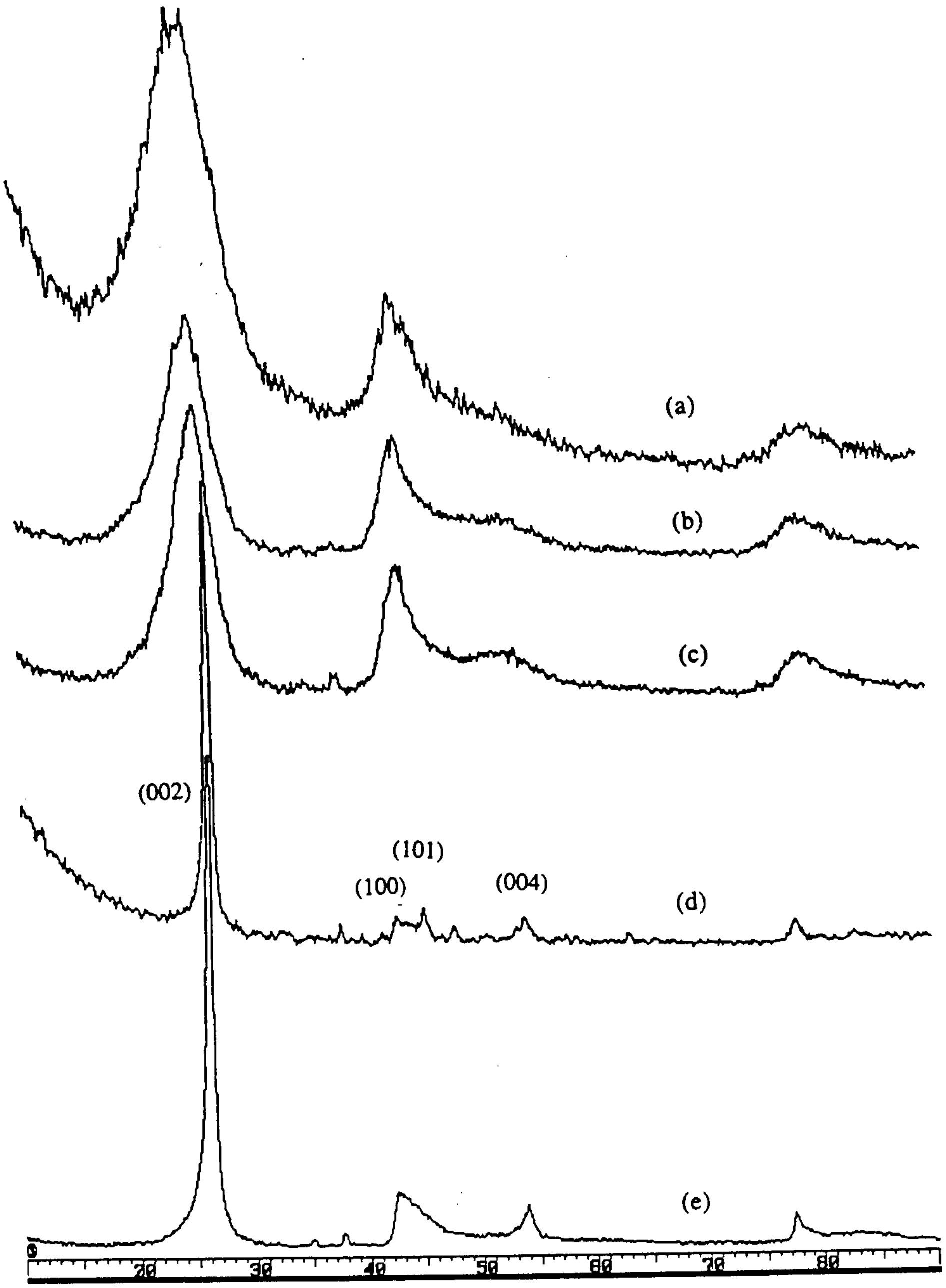

Fig. 5. X-ray diffractions of B/C materials prepared by dichloro(phenyl acetylide)borane at (a) 1200, (b) 1400, (c) 1600, (d) 2000 and (e) 2200°C.

Table 2. A summary of *d*-spacing and L_c in B/C material prepared under various temperatures

Temperature (°C)	*d*-spacing (Å) PDPB	PBCB	PTPB	L_c (Å) PDPB	PBCB	PTPB
1200	3.5495	3.5463	3.6935	20.2	18.9	19.4
1400	3.5401	3.5267	3.6976	22.1	21.4	18.4
1600	3.4938	3.4962	3.4312	24.7	23.8	40.3
1800	3.4919	3.4701	3.4277	35.8	29.2	29.9
2000	3.4387	3.4067	3.4035	35.8	40.4	39.1
2200	3.3898	3.3874	3.3797	177.4	136.6	405.9

forms a better graphitic structure, with smaller *d*-spacing and larger L_c crystal size. On the other hand, PDPB and PBC prepared from the precursors containing both boron–halogen and boron–alkynyl bonds show very similar graphitization processes. The differences in both *d*-spacing and L_c crystal size are not viewed as significant.

4. CONCLUSION

This research is part of our continuous efforts to develop a new precursor route to prepare boron-containing carbon (B/C) materials with desirable graphitic structure. Three boron containing phenyl acetylide precursors were synthesized and studied for the stabilization, carbonization and graphitization reactions. Despite the significant differences in boron concentration and chemical nature between precursors, all graphitization reactions were very effective and took place at relatively low temperatures. Clearly, the *in situ* boron is catalyzing graphitization to form B/C material in all three cases. By virtue of the precursors, containing both boron and carbon in their molecular structure, the graphitization reactions produce B/C materials with a uniform distribution of substitutional boron in the graphitic structure.

Acknowledgements—Authors would like to thank financial support from the U.S. Air Force, Office of Scientific Research and the Carbon Research Center at Pennsylvania State University.

REFERENCES

1. Marsh, H., *Introduction to Carbon Science*. Butterworths, London, 1989.
2. Donnett, J. B. and Bansal, R. P., *Carbon Fibers*. Marcel Dekker, New York, 1984.
3. Wagner, P. and Dickinson, M., *Carbon*, 1970, **8**, 313.
4. Walker, E. J. in *Essentials of Carbon–Carbon Composites*, ed. C. R. Thomas. Royal Society of Science, Cambridge, 1993.
5. McKee, D. W., *Chemistry and Physics of Carbon*, 1981, **16**, 1.
6. McKee, D. W., *Carbon*, 1986, **24**, 737.
7. Jones, L. E. and Thrower, P. A., *Carbon*, 1991, **29**, 251.
8. Allardice, D. J., Walker, P. L., Jr, *Carbon*, 1970, **8**, 375.
9. Hu, R. and Chung, T. C., *Carbon*, 1996, **34**, 595.
10. Hu, R. and Chung, T. C., *Carbon*, 1996, **34**, 1181.
11. Midland, M. M., *J. Org. Chem.*, 1975, **40**, 2250.
12. Steinberg, H., *Organoboron Chemistry*, Vol. 1. Interscience publishers, New York, 1964.
13. Noth, H. and Wrackmeyer, B., *Nuclear Magnetic Resonance Spectroscopy of Boron Compounds*, Springer–Verlag, Berlin, 1978.
14. Yamamoto, Y. and Moritani, I., *J. Org. Chem.*, 1975, **40**, 3434.
15. Wrackmeyer, B. and Noth, H., *Chem. Ber.*, 1977, **110**, 1086.
16. Zettler, F. and Hausen, M. D., *J. Organomet. Chem.*, 1974, **72**, 157.
17. Blount, J. F., Finocchiaro, P., Gust, D. and Mislow, M., *J. Am. Chem. Soc.*, 1973, **97**, 7019.
18. Caminat, W. and Lister, D. G., *J. Chem. Soc.*, *Faraday II*, 1978, **74**, 896.
19. Brown, N. M. D., Davidson, F. and Wilson, J. W., *J. Organomet. Chem.*, 1981, **209**, 1.
20. Hara, S., Dojo, H., Takinami, S. and Suzuki, A., *Tetrahedron Lett.*, 1983, **24**, 731.
21. Viehe, H. G., *Chemistry of Acetylenes*. Marcel Dekker, New York, 1969.
22. Mochida, I. and Sakai, Y., US Patent No. 4891126, 1990.
23. Mochida, I., Shimizu, K., Korai, Y. and Sakai, Y., *Carbon*, 1991, **30**, 55.

Pergamon

Carbon Vol. 35, No. 8, pp. 1101–1109, 1997
© 1997 Elsevier Science Ltd
Printed in Great Britain. All rights reserved
0008-6223/97 $17.00 + 0.00

PII: S0008-6223(97)00068-7

CO-CARBONIZATION OF 9-CHLOROBORAFLUORENE AND PITCH; SYNTHESIS OF B/C MATERIALS

RAYMOND HU and T. C. CHUNG*
Department of Materials Science and Engineering, The Pennsylvania State University, University Park, PA 16802, USA

(*Received* 5 *November* 1996; *accepted in revised form* 11 *March* 1997)

Abstract—This paper is a continuation of our research efforts in the development of boron containing carbon (B/C) materials. The chemistry is based on the co-carbonization reaction between 9-chloroborafluorene precursor and FCC decant oil pitch. By adding small amounts of 9-chloroborafluorene, the yield of low temperature anisotropic carbon from the commercial pitch was dramatically improved. This simple and effective method results in a broad range of B/C materials. In addition, the co-carbonization reaction provides direct evidence of boron-enhanced graphitization and the effect of boron content on crystal growth. In general, the graphitization temperature of pitch can be lowered by several hundred degrees by incorporating small amounts of boron precursor, and a large crystal size with low *d*-spacing, similar to Sp-1 graphite, is obtained at 2300°C. © 1997 Elsevier Science Ltd

Key Words—A. Doped carbons, B. graphitization, C. X-ray diffraction, D. crystal structure.

1. INTRODUCTION

Previously we reported on the preparation of highly crystalline carbon substitutionally doped with a large concentration of boron using a specifically designed B/C precursor [1]. The compound was shown to be processable and highly graphitizable. This paper describes a co-carbonization study of the B/C precursor with pitch. Since it is well established that boron catalyzes graphitization reactions [1–6], the incorporation of a small amount of B/C precursor should dramatically enhance the crystal structure of the resulting carbon. Furthermore, through co-carbonization, the boron content of the material can be modified effectively.

Co-carbonization is recognized as an effective means to tailor the properties of carbon by combining a variety of precursors. Many of the investigations on the carbonization of mixtures of pitches such as ethylene tar combined with coal tar pitch and petroleum vacuum residue with decant oil were conducted by Mochida et al. [7–9]. It was shown that the mixtures often produce cokes of higher quality than those from each feed alone. The carbonization of binary mixtures of graphitizable and non-graphitizable hydrocarbons was investigated by Weintraub and Walker [10]. Their study indicates that, in order for the two components to form a uniform carbon, the reactivity of the hydrocarbons must be very similar. Thus anthracene cannot be co-carbonized with biphenyl because its reactivity is 1200 times greater than that of biphenyl. Due to the presence of the highly reactive B–Cl species, the reactivity of the B/C precursor 9-chloroborafluorene is expected to be much higher than that of regular hydrocarbons. This limits the type of carbon precursors that can be co-carbonized with the boron-containing compound. In the present study, the effect of 9-chloroborafluorene at various concentrations on the carbonization and subsequent graphitization of FCC-decant oil pitch was evaluated. The co-carbonization of the boron precursor with pitch is much more complex because of the molecular weight difference between the two components. The catalytic effect of boron on the formation of the mesophase and carbonization was also investigated. It was found that both co-carbonization as well as catalytic carbonization occur between our precursor and pitch.

2. EXPERIMENTAL

2.1 *Instrumentation*

X-ray diffraction measurements were made on the carbonized and graphitized material using a Rigaku Geigerflex X-ray diffractometer with Cu K radiation operating at 20 mA and 40 kV. Samples were ground and mixed with methanol to produce a slurry. Thereafter a film was cast on a quartz slide and allowed to dry for 30 minutes. Pure silicon (NBS SRM 640) was the internal standard for accurate determination of the *d* spacing. Two measurements were made for each sample, one in the range from 5 to 90° at a scan speed of 4° 2θ per minute and the other from 23 to 30° at a speed of 1° 2θ per minute. The interlayer spacing was determined from the (002) peak. Sp-1 graphite was used as the standard for the determination of instrument broadening.

All elemental analyses were conducted by Galbraith Laboratories, Inc., Knoxville, TN. Boron concentration determination was performed at the primary wavelength of 249.77 nm and the detection limit for this technique is reported to be 0.010 mg l^{-1}. The relative standard deviation for the ICP technique used was 5.57% and the relative error was only 2.66%. The results are reported as wt% and are considered quantitative.

---

*Corresponding author.

Optical microscopy was performed using a Nikon Microphot-FXA. The specimen was mounted in a plastic resin, polished according to conventional methods and examined under a reflected light microscope with crossed polarizer/analyzer.

2.2 *Precursor synthesis and pressurized heat treatment*

The synthesis and processing of the B/C precursor 9-chloroborafluorene was discussed in detail in a previous paper [1]. The FCC decant oil was obtained from Conoco Inc., Ponca City, OK, USA. To study the effect of the B/C precursor on co-carbonization, various weight percents of 9-chloroborafluorene were mixed with powdered pitch. A high-pressure stainless steel tube bomb (20 ml) equipped with a pressure gauge was used for the heat treatment of the mixture. The loading of the samples, 1 g, was conducted in an inert atmosphere dry box. The bomb was purged several times and then pressurized to 150 psi nitrogen pressure. Heat treatment took place in a fluidized sand bath with slow vertical shaking of the tube reactor to improve homogeneity. After soaking for 5 hours the sample was cooled slowly to room temperature. The collected pitch was distilled under vacuum at 225°C, as reported in the previous paper, to produce a black mesophase powder.

2.3 *Carbonization and graphitization*

The solid B/C residue obtained after distillation was pulverized and placed in a porcelain-coated Coors crucible and carbonized at 550°C under argon atmosphere. In all cases the heating rate was 10°C min^{-1} and the soaking time 1 hour. The cooling rate was 3°C min^{-1} to 350°C and then air cooled to room temperature.

After carbonization, the product was then graphitized at 2000 and 2300°C for 1 hour in a graphite resistance type furnace manufactured by Centorr Vacuum Technology. The heating of the furnace was controlled manually.

3. RESULTS AND DISCUSSION

The general procedure for the heat treatment of the boron-containing precursor and pitch mixture can be summarized by the following diagram:

$$\begin{array}{c}\text{9-Chloroborafluorene}\\ +\\ \text{Pitch}\end{array} \xrightarrow[\substack{\text{5-10 hours}\\ \text{100 psi } N_2}]{375\,^{\circ}\text{C}} \text{B/C Pitch} \xrightarrow[\substack{\text{1 hour}\\ \text{vacuum}}]{225\,^{\circ}\text{C}}$$

$$\text{B/C Mesophase} \xrightarrow[\substack{10\,^{\circ}\text{C/min.}\\ \text{hold 1 hour}}]{550\,^{\circ}\text{C}} \text{B/C Material}$$

Initial heat treatment at 375°C was selected for the B/C precursor and decant oil mixture because it was previously determined to be the optimal processing temperature of 9-chloroborafluorene. A pressurized process was necessary to prevent volatilization of the low boiling 9-chloroborafluorene.

3.1 *Low temperature carbonization*

Table 1 summarizes the yield of residue for each processing step. Note that the residue yield after the initial pressurized heat treatment was >98% in all cases. The addition of the boron-containing precursor to the pitch did not affect the yield for the vacuum distillation step. Both pure decant oil and boron precursor gave approximately 70 wt% vacuum residue and thus accordingly the mixture of these two components gave a similar yield. However, it is important to note the differences between the two residues obtained from distillation of 100% decant oil pitch and 100% boron pitch. Whereas the distillation of B/C pitch gave 100% anisotropic mesophase, the distillation of the decant oil residue after 375°C pressurized heat treatment yielded material with very fine domains. A detailed discussion of the optical texture of the carbons is presented in later sections.

In Table 1, the final 550°C carbon yield was calculated by multiplying the vacuum yield by the carbonization yield. It is clear that the overall yield increased with increasing wt% of 9-chloroborafluorene added. Since the boron-containing precursor produced a larger amount of residue carbon at 550°C, it is expected that an increased wt% of 9-chloroborafluorene will increase the carbon yield. However, the results clearly show that the actual yield was much higher than the theoretical yield in all cases. The electron-deficient boron may cause a rapid electrophilic substitution reaction and induce aromatic condensation, leading to the formation of larger, more stable polyaromatic species. On the other hand, the decant oil can prevent excess cross-linking of the aromatic hydrocarbons by solvation of the B/C pitch. It is clear that dilution of the boron precursor in the molten pitch reduces its reactivity. Therefore, the advantageous effect of mixing is two-fold: (1) the presence of boron catalyses the carbonization of the decant oil, (2) the decant oil acts as a solvent and improves the polymerization of the B/C mesophase.

Although there are many possible reactions that can take place during low-temperature heat treatment, the initial process most likely involves two steps. First is the formation of a charge transfer complex between the reactive B–Cl moiety and an aromatic precursor whether it be with 9-chloroborafluorene or FCC pitch. The second sequence involves the elimination of hydrogen chloride from the complex to form a boron–carbon bond. As indicated in our previous paper [1], we observed the formation of HCl during high-pressure, low-temperature heat treatment. Muetterties has shown

Table 1. Yield of carbon residue from vacuum distillation and 550°C carbonization as a function of wt% of 9-chloroborafluorene

Wt%	Yield wt% after vacuum distillation (*A*)	Yield wt% after carbonization (*B*)	Overall wt% ($A \times B$)	Theoretical
0	69.6	39.8	27.7	27.7
5	75.1	49.7	37.3	29.5
10	73.7	44.6	32.9	31.3
20	62.7	73.8	46.2	34.8
30	74.8	59.0	44.1	38.4
50	68.7	91.3	62.7	45.5
100	70.2	90.1	63.3	63.3

that aromatic hydrocarbons such as benzene, biphenyl and naphthalene react readily with BCl_3 to form aryldichloroboranes through this mechanism [11,12]. In his experiment, $AlCl_3$ was used as a catalyst to allow the reaction to take place at 35°C. During co-carbonization, the heat treatment temperature is more than high enough for chloroboronation to occur without $AlCl_3$. In addition to this process, halo-boranes have been known to catalyze the polymerization of many different vinyl and aromatic monomers. BF_3/HF has been used to catalyze the formation of mesophase pitch from carbon precursors such as anthracene and naphthalene [13,14]. The electron-deficient BF_3 is believed to form a charge transfer complex with HF. This initiator then causes the rapid cationic polymerization of the aromatic precursors. Even though it is less reactive than BF_3, the B–Cl functional group of 9-chloroborafluorene can complex with HCl to act as the cationic catalyst for aromatic condensation. Thus in the formation of the mesophase B/C precursor, 9-chloroborafluorene may serve as both catalyst and monomer, and boron is incorporated into the molecular structure.

Optical micrographs of samples containing 0, 10 and 50 wt% boron precursor are shown in Fig. 1. The 550°C carbon from decant oil exhibits a fine elongated mosaic texture (Fig. 1(a)) with narrow isochromatic regions. The 10% sample exhibits a similar texture except there are small spherical anisotropic domains (Fig. 1(b)) dispersed within the more isotropic matrix. When the content is increased to 50 wt%, the anisotropic droplets become much larger, as evident in the Fig. 1(c). Clearly, it is the boron-containing precursor that is coalescing during heat treatment to form these highly oriented domains. The 9-chloroborafluorene component will tend to aggregate because of its relatively higher reactivity as compared to that of decant oil. The formation of anisotropic droplets can also be caused by inadequate mixing. Obviously, more uniformity can be achieved by directly agitating the mixture during low-temperature heat treatment.

3.2 *Graphitization of boron-containing carbon at 2000°C*

The 550°C carbonized samples were graphitized at 2000°C for 1 hour. Overall, the transformation of the 550°C carbonized product to B/C graphitic carbon is a smooth process with high yield (>85 wt%). The X-ray diffraction patterns of the final carbons are depicted in Figs 2 and 3. Table 2 clearly shows that as the wt% of 9-chloroborafluorene is increased, overall the (002) peak shifts toward a higher angle, i.e. lower *d* spacing. Interestingly, the calculated *d* spacing for the sample containing 50 wt% boron precursor (3.369 Å) is lower than the value obtained for the pure B/C material (3.374 Å) at the same heat treatment temperature and time. This result provides further evidence that the decant oil is acting as a solvent to prevent excess cross-linking of the highly reactive boron precursor and thus improving the crystalline orientation of the material.

Figure 2 shows that the (002) peak for the sample containing 10 wt% boron precursor is especially broad with an obvious predominant shoulder resembling the diffraction pattern of the 2000°C heat-treated decant oil pitch. This corresponds to the results obtained from optical microscopy, which illustrated that the carbonized residue is composed mainly of an isotropic matrix derived from decant oil. In fact, two peaks were observed for all the mixtures containing <30 wt% boron precursor. However, it is important to note that as the amount of boron is increased, the *d* spacing of the isotropic portion shifts towards a lower value. Obviously, the presence of boron in the mixture catalyzes graphitization even though the two precursors form carbons with different optical texture. It is possible that high-temperature diffusion of boron from the boron-rich anisotropic droplets into the boron-poor isotropic matrix enhances graphitization. The effects of boron on graphitization of carbon precursors have been reported by many other investigators [2–5]. Above 30 wt%, the diffraction results clearly show that the graphitized sample is much more uniform. Apparently, up to 70 wt% of decant oil pitch can be incorporated in the carbon and still maintain the same high degree of overall crystalline orientation. Interestingly, if we convert weight percent 9-chloroborafluorene to weight percent boron, we see that the amount at which the material starts to behave homogeneously is about 2.1 wt% B, i.e. the reported equilibrium solid solution concentration of boron in graphite [4]. The calculated *d* spacing and

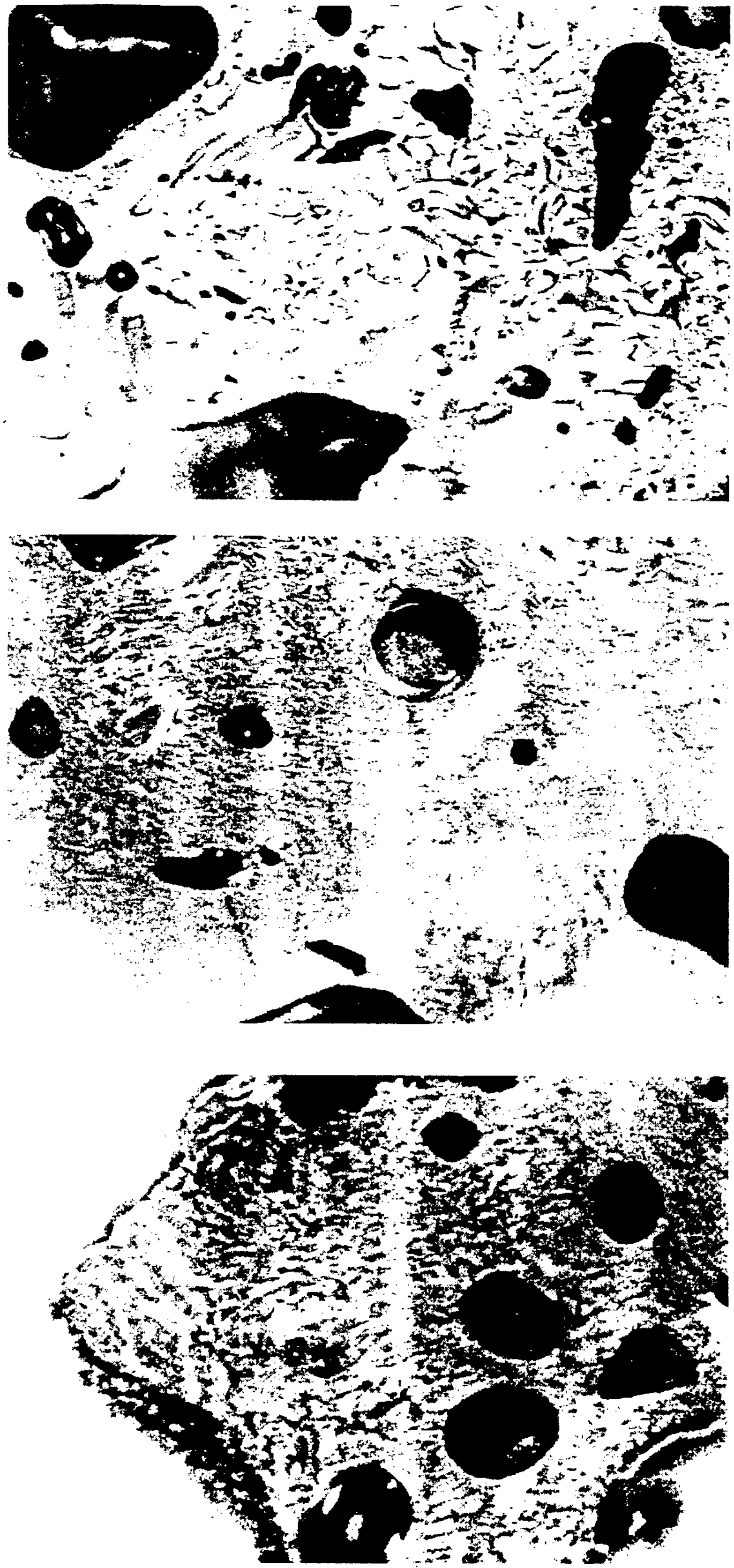

Fig. 1. Optical texture of coke prepared by the carbonization of FCC decant oil pitch and boron precursor at 550°C: (a) 100% pitch, (b) 10 wt% boron precursor, (c) 50 wt% boron precursor.

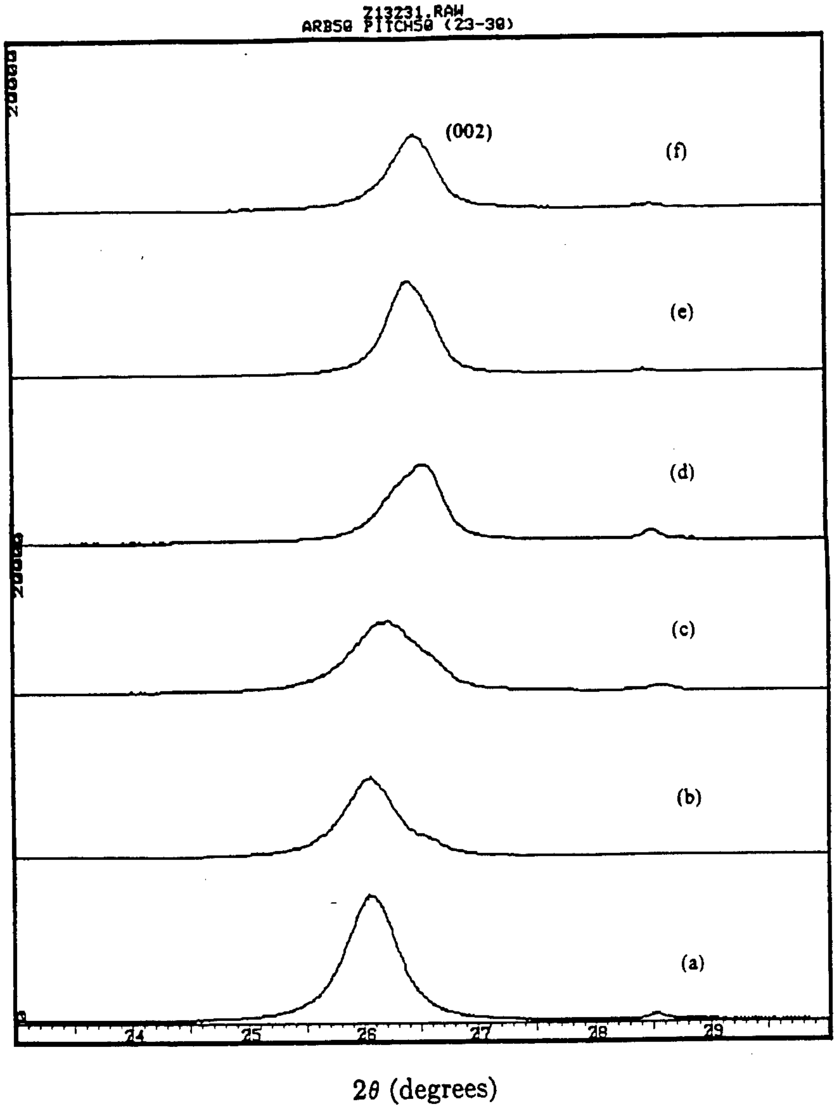

Fig. 2. X-ray diffraction patterns of a mixture of pitch with (a) 0 wt%, (b) 5 wt%, (c) 10 wt%, (d) 20 wt%, (e) 30 wt% and (f) 50 wt% boron precursor at 2000°C.

Lc, as well as the number of (002) peaks observed, are summarized in Table 2. The decrease of the *d* spacing with increasing boron precursor content is illustrated graphically in Fig. 4. Apparently, the saturation of the catalytic effect is reached at about 30 wt% boron precursor corresponding to about 2 wt% boron. Both Murty [2] and Lowell [4] reported a similar phenomenon at approximately this level of boron content. Lastly, the improvement of the crystalline orientation in the *a* direction with increased wt% boron precursor is demonstrated by the increasing sharpness of the (100) and (101) peaks shown in Fig. 3.

The boron contents of the 30 and 50 wt% samples were analyzed by elemental analysis and were determined to be 2.05 and 4.17 wt%, respectively. The results indicate that boron is stable within the carbon matrix at 2000°C even though the material is produced from a mixture of two distinctly different carbons. Clearly, co-carbonization is an effective means to control the boron content of B/C materials.

3.3 *Graphitization at 2300°C*

Boron-enhanced graphitization is believed to be caused by the enhanced diffusivity of boron as compared to carbon [3,5]. Two possible diffusion mechanisms have been postulated. First, it is proposed that boron plays a similar role as vacancies in the carbon matrix and, second, it was suggested that, during annealing, the removal of boron leads to an increase in the vacancy concentration which helps graphitization. In the case of our B/C carbon, both these mechanisms are applicable only at higher temperatures such as 2300°C. Taking the activation energy and diffusion coefficient determined by Hennig [15], we find that the length scale of boron diffusion only

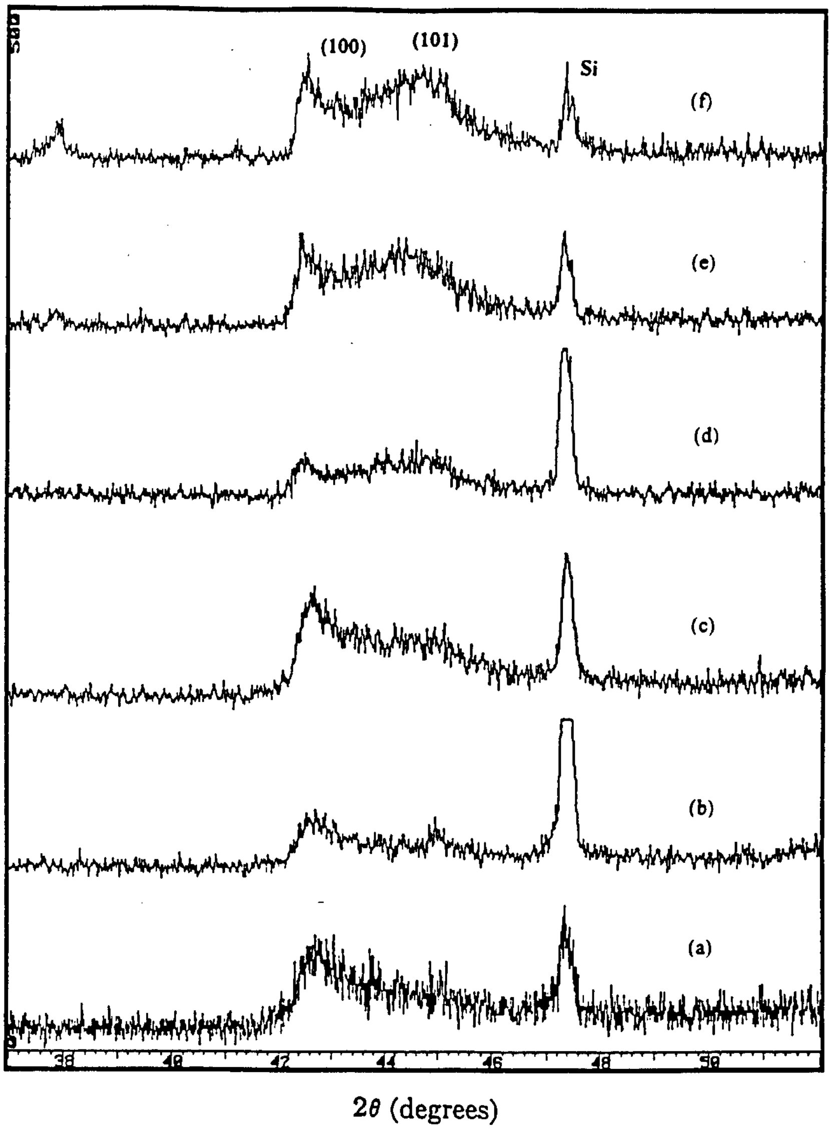

Fig. 3. The secondary peaks in X-ray diffraction patterns of a mixture of pitch with (a) 0 wt%, (b) 5 wt%, (c) 10 wt%, (d) 20 wt%, (e) 30 wt% and (f) 50 wt% boron precursor at 2000°C.

Table 2. X-ray diffraction results of 2000°C heat treated samples

Wt%	*d*(002) (Å)	*Lc* (Å)	No. of (002) peaks observed
0	3.425	180	1
5	3.423	186	2
10	3.407	119	2
20	3.374	153	2
30	3.369	197	2
50	3.369	209	1
100	3.374	196	1

becomes significant above 2000°C. The calculated diffusion constants are 5.0×10^{-12} and $2.9 \times 10^{-10}\ cm^2\ s^{-1}$ for 2000 and 2300°C, respectively. Furthermore, our previous study of B/C carbon based on the 9-chloroborafluorene precursor demonstrated that boron content decreases dramatically at 2300°C [1]. The loss of boron should play a significant role in enhancing the graphitization process.

To determine the effect of boron on graphitization at high temperature, the B/C material was further heat treated at 2300°C. The X-ray diffraction patterns are shown in Figs 5 and 6 and the results are summarized in Table 3. As expected the *d* spacing decreases with higher heat treatment temperature for all samples. This decrease in crystallite spacing is accompanied by a dramatic increase in crystal size *Lc*. For the sample containing 30 wt% boron precursor, the *Lc* was above the detection limit of the diffractometer at >1000 Å. Amazingly, the number of (002) peaks observed was one for all cases. Apparently, not only did boron enhance the graphitic structure, but it made the mixture of two distinctly different carbons

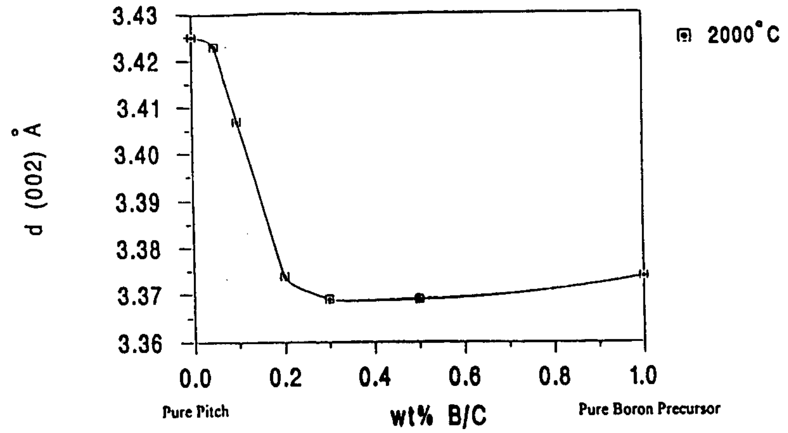

Fig. 4. Decrease of *d* spacing with increase of boron precursor content after heat treatment at 2000°C.

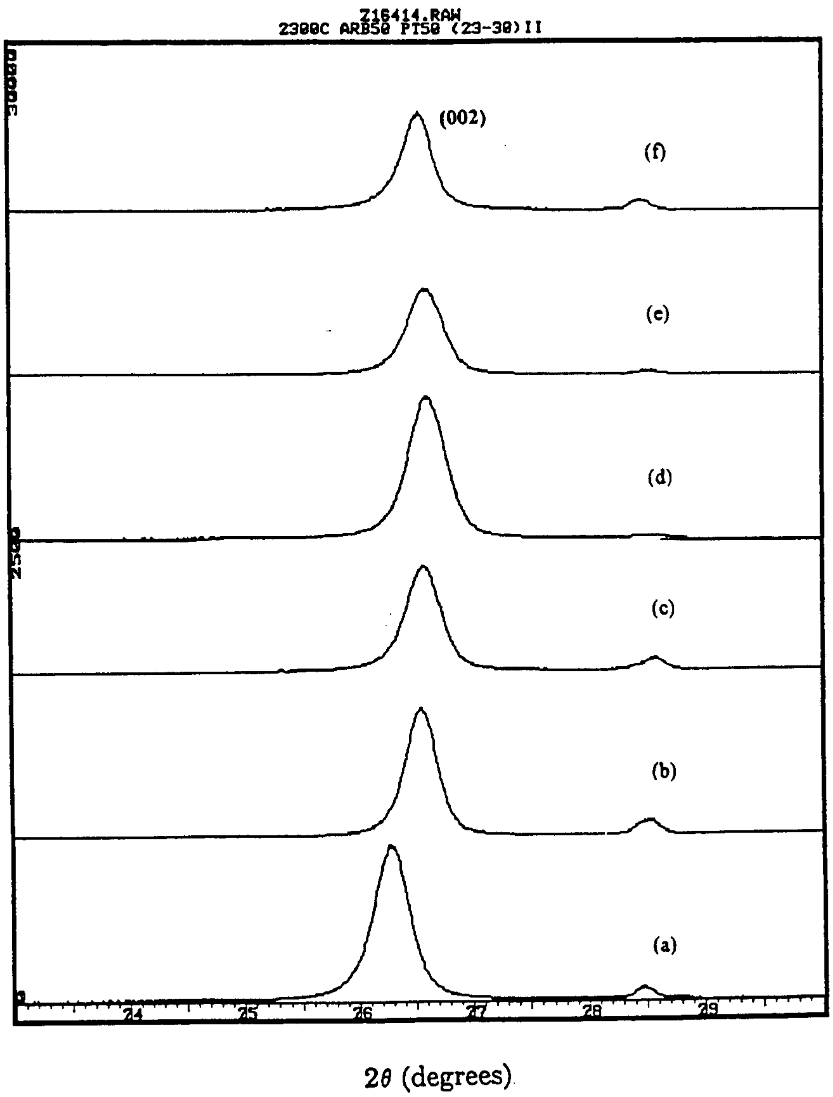

Fig. 5. X-ray diffraction patterns of a mixture of pitch with (a) 0 wt%, (b) 5 wt%, (c) 10 wt%, (d) 20 wt%, (e) 30 wt% and (f) 50 wt% boron precursor at 2300°C.

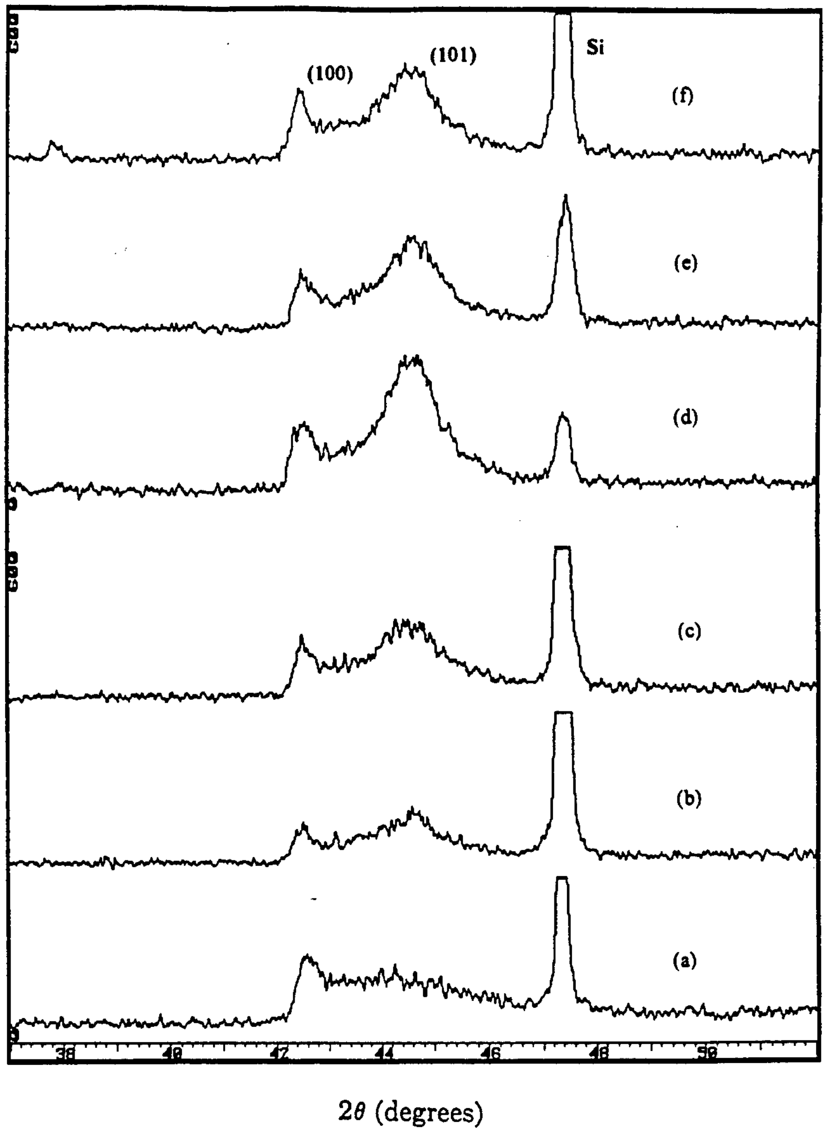

Fig. 6. The secondary peaks in X-ray diffraction patterns of a mixture of pitch with (a) 0 wt%, (b) 5 wt%, (c) 10 wt%, (d) 20 wt%, (e) 30 wt% and (f) 50 wt% boron precursor at 2300°C.

Table 3. X-ray diffraction results of 2300°C heat treated sample

Wt%	*d*(002) (Å)	*Lc* (Å)	No. of (002) peaks observed
0	3.403	297	1
5	3.362	415	1
10	3.369	314	1
20	3.363	283	1
30	3.358	> 1000	1
50	3.358	578	1
100	3.347	456	1

homogeneous. Elemental analysis of the samples showed a decrease in boron content at 2300°C. For the 30 wt% sample the concentration dropped to 1.44 wt% boron, while for the 50 wt% sample it dropped to 2.75 wt% boron. Obviously, the loss of boron does play a role in the enhancement of graphitization as suggested previously.

4. CONCLUSION

Co-carbonization with a boron precursor is a simple and effective way to modify the properties of carbon produced from commercial pitch. By adding small amounts of B/C precursor, the yield of low-temperature anisotropic carbon was dramatically improved. The advantages are two-fold: (i) the boron catalyzes aromatic condensation and (ii) the pitch acts as a solvent to moderate the carbonization reactions. High-temperature heat treatment of the mixture demonstrated the effect of the B/C precursor on graphitization, and elemental analysis demonstrated that the boron content can be controlled. The graphitization temperature of pitch can be lowered by several hundred degrees by incorporating small amounts of boron precursor. Lastly, dramatic improvements in crystal spacing and crystallite size were obtained at 2300°C, further illustrating the mechanism of enhanced graphitization.

REFERENCES

1. R. Hu and T. C. Chung, *Carbon* (accepted).
2. Murty, H. N., Biederman, D. L. and Heintz, E. A., *Fuel*, 1977, **56**, 305.
3. Fischbach, D. B., *Chem. Phys. Carbon*, 1971, **7**, 86.
4. Lowell, C. E., *J. Am. Ceram. Soc.*, 1967, **50**, 142.
5. Jones, L. E. and Thrower, P. A., *Carbon*, 1991, **29**, 251.
6. Turnbull, J. A., Stagg, M. S. and Eeles, W. T., *Carbon*, 1966, **3**, 387.
7. Mochida, I., Fei, Y. Q., Korai, Y. and Oishi, T., *Fuel*, 1990, **69**, 672.
8. Mochida, I., Korai, Y. and Oyama, T., *Carbon*, 1989, **27**, 359.
9. Toshima, H., Mochida, I., Korai, Y. and Hino, T., *Carbon*, 1992, **30**, 773.
10. A. Weintraub and P.L. Walker Jr., *Proc. Int. Conf. Industrial Carbon and Graphite* **3**, 75 (1971).
11. Muetterties, E. L., *J. Am. Chem. Soc.*, 1960, **83**, 4163.
12. Muetterties, E. L., *J. Inorg. Chem.*, 1963, **7**, 2663.
13. I. Mochida and Y. Sakai, U.S. Patent No. 4891126 (1990).
14. Mochida, I., Shimizu, K., Jorai, Y. and Sakai, Y., *Carbon*, 1991, **30**, 55.
15. Hennig, G. J., *Chem. Phys.*, 1965, **42**, 1167.

TASK 2.

Processing of B/C Polymers and Carbons

Dr. Carlo Pantano
Dr. L.-Q.Chen

HIGH-TEMPERATURE DOPING OF CARBON WITH BORON AND ITS EFFECTS UPON OXIDATION

W. Cermignani and C. G. Pantano
Department of Materials Science and Engineering
The Pennsylvania State University, University Park, PA 16802

ABSTRACT

A high-temperature reaction has been used to boron-dope vitreous carbon, and both highly and lowly oriented pyrolytic graphite (HOPG and LOPG). X-ray photoelectron spectroscopy (XPS) shows that a large fraction of the boron enters substitutional sites - especially in regions of disorder. The boron doping significantly inhibits the oxidation of the carbon, primarily because it limits the nucleation and/or growth of etch pits. The preferential doping of bulk defect sites inhibits pit nucleation. The stabilization of zig-zag edge-site surfaces due to the substitution of boron, as well as passivation due to a boron oxide surface reaction product, both play a role in the inhibition of pit growth.

INTRODUCTION

A number of studies have been conducted to understand the oxidation inhibiting effect of boron in carbon and in carbon/carbon composites.[1-12] McKee[3] *et al.* studied the oxidation behavior of graphite impregnated with aqueous solutions of boric oxide and organoborates, and proposed that oxidation was prevented by the blocking of active sites with boron-oxide.

Jones and Thrower[7] studied the inhibiting effect of substitutional boron on carbon fibers and proposed three different possible mechanisms of oxidation inhibition. One was similar to that of McKee[3] *et al.'s* where it is suggested that boron-oxide builds up on the surface and "caps off" active sites. The second proposed mechanism is that boron-oxide restricts CO desorption through the redistribution of π-electrons. The third proposed mechanism suggests that boron catalyzes further graphitization of the carbon and, thereby, lowers the oxidation rate.

On the other hand, a study by Thomas and Roscoe[1] showed that boron-oxide deposited on graphite acted as a catalyst to the gasification process of carbon materials in moist oxygen around 800°C. This was attributed to the reactive nature of boron-oxide to water. Karra[11] *et al.* also found substitutional boron, at low levels, to have a catalytic effect on carbon oxidation. This catalytic effect could not be masked by the inhibiting effect of boron-oxide due to the high surface area of the carbons. The catalytic effect was attributed to a weakening of the carbon-carbon bonds and strengthening of the carbon-oxygen bonds discussed by Allardice and Walker[2]. Similar effects were noted in a low pressure study by Rodriquez and Baker[13]. More recently, theoretical methods have been used to show the influence of boron substitution upon the distribution of electrons on carbon surfaces[14,15].

It is clear that a fundamental understanding of the role of boron in carbon oxidation still does not exist. Some of the reasons for this apparent confusion are: (i) a multitude of methods have been used to introduce the boron; (ii) a wide range of carbons have been used; and, (iii) a lack of quantitative characterization of where and how the boron is located in the carbon (micro)structure before and after oxidation.

In this study, attention was focused on first characterizing various boron-doped carbons, and then on the oxidation behavior of these well-characterized materials. In particular, a high temperature reaction was chosen to introduce boron into ordered and disordered forms of carbon using three different boron sources. Subsequently, the concentration, distribution and chemical structure of the boron was evaluated using x-ray photoelectron spectroscopy (XPS), Raman spectroscopy and electron microprobe analysis. Finally, the oxidation behavior was evaluated with thermal gravimetric analysis (TGA) and the oxidized basal-plane surface of the boron-doped HOPG was studied with atomic-force microscopy (AFM). This surface was chosen because of its ordered structure and it's suitability for AFM studies.

EXPERIMENTAL

Small monolithic plates of HOPG, LOPG and vitreous carbon were placed in graphite crucibles and surrounded with a mixture of ultrapure flake graphite (SP-1) and either boron-oxide, elemental boron, or boron carbide. The boron compounds were thoroughly mixed with the graphite flake using an equal concentration in each crucible; an effective concentration of 5% boron was used in all cases. The crucibles were subsequently heated to 2450°C for 40 minutes in argon using a carbon furnace.

Thermal Gravimetric Analysis (TGA) was conducted with a Netzsch STA 429 thermal-analyzer. The sample chamber was evacuated to a pressure of ~80 Pa, it was back-filled with UHP argon, and then heated under 20 sccm of argon until the desired temperature was reached. After the desired temperature was reached, the flow of argon was changed to 20 sccm of UHP oxygen. The use of the TGA not only provided isothermal weight loss data, but yielded samples (for the surface analyses) whose degree of burn-off was known. Other oxidation experiments were performed in a tube furnace under flowing oxygen.

All of the XPS spectra (Bls, Cls and Ols) were recorded on a Kratos 800 using MgKα radiation (1253.6 eV). The binding energy scale was calibrated by assigning the Cls peak at 284.6eV. The peak positions and FWHM's for boron-oxide, substitutional boron and the two forms of boron oxycarbide were determined in an earlier study[12].

RESULTS

Figure 1 presents electron microprobe analyses for the vitreous carbon after doping with the various boron sources. The zero depth corresponds to the surface that was exposed to the doping environment. It is clear that the boron is not uniformly distributed throughout the depth of the carbon substrate, but rather, is concentrated near the surface. All of the substrates showed a higher concentration of boron for the boron-oxide dopant. However, only the vitreous carbon substrate showed penetration of boron beyond 20 μm. This is presumably due to the more open structure of vitreous carbon. Surface concentrations varied between .5 and 1.2 weight percent boron, in general; these are less than the reported solubility limit for boron in graphite[16].

Chemsage is a computer program which can be used to predict the partial vapor pressures of materials at elevated temperatures. This program was used to determine the major boron gaseous species, and their partial vapor pressures, above boron-oxide, elemental boron and boron carbide at 2450°C. It was found that boron gas is the major gaseous species above elemental boron and boron carbide at 2450°C. The vapor pressure of boron gas above elemental boron is predicted to be 4.8 x 10^{-4} atm, while the predicted partial vapor pressure of boron gas above boron carbide is 4.3 x 10^{-4} atm. The predicted major gaseous species above boron-oxide at 2450°C are B_2O_3 and BO_2 gas with partial vapor pressures of 2.88 x 10^{-2} and 1.05 x 10^{-2}, respectively. Apparently, there is a higher concentration of boron species above the boron-oxide than the boron carbide and the elemental boron. This is qualitatively consistent with the microprobe analysis of the boron distribution in these carbon substrates.

Figure 2 shows the Raman spectra of a boron-free and boron-doped HOPG. The undoped HOPG, which was heat treated in argon to 2450°C for 40 minutes, shows an intense band at 1582 cm^{-1} and a very weak band at 1365 cm^{-1}. The former band has been assigned by Tuinstra and Koenig[17] to a doubly degenerate stretching vibrational mode, whereas the latter band is Raman inactive for perfect graphite crystals. Boron doping at 2450°C results in an enhancement of the 1365 cm^{-1} band, which is Raman inactive for perfect graphite, and has been assigned to defect-induced vibrational mode. This was accompanied by an enhancement of a band at 1615 cm^{-1}; this band is also observed for oxidized glassy carbon, and ground or irradiated graphite. The change in width and relative intensity of the 1365 cm^{-1} and 1615 cm^{-1} bands suggests that boron doping influences the defect structure/order of the graphite lattice.

All of the boron doped substrates showed a Bls peak at a binding energy of 186.5 eV. This is a unique chemical shift for boron that corresponds to its substitution within the graphite lattice; e.g., elemental boron yields a peak at 188 eV, boron carbide at 187.5 eV and boron-oxide at 193.2 eV. However, the doped carbon surfaces showed other chemical forms of boron, especially boron-oxycarbide; this species is believed to be a substitutional boron in the surface monolayer or at an internal surface or defect. Table 1 summarizes the distribution of boron, carbon and oxygen chemical states observed on the various surfaces. Clearly, the more disordered carbons and carbon surfaces exhibit the highest total concentration of boron. This suggests a preferential doping of surface and defect sites by boron.

Table 1. Boron Surface Concentrations by XPS (in atomic percent)

	HOPG basal plane	LOPG basal plane	HOPG edge	LOPG edge	Vitreous Carbon
			before oxidation		
B-substitutional	.48	.43	.55	.36	.34
B-oxycarbide	.33	.69	.66	.87	.64
B-oxide	.16	.38	.17	.28	.28
			after oxidation		
B-substitutional	1.3				
B-oxycarbide	1.8				
B-oxide	13.0				

The TGA data for the HOPG and vitreous carbon are presented in Figure 3; the LOPG data was virtually identical to the vitreous carbon data. It is obvious that the boron-doping has an inhibiting effect upon weight loss due to oxidation. The effects of doping are not so dramatic in the case of HOPG due to the anisotropy of the material, but the data presented later shows that oxidation of the HOPG basal plane surface has been significantly passivated. The steady-state rates of weight loss were reduced by a factor of five in the case of the doped HOPG and LOPG, and by a factor of more than 10 in the case of vitreous carbon. The primary effect of doping upon the kinetics of oxidation was to eliminate Region II, where the rate of weight loss increases due to increases in surface area. Thus, it is not surprising that there were distinct effects on the microscopic nature and behavior of the oxidation-induced etch-pitting of the surfaces (see below).

The XPS analyses reveal that boron-oxide and boron-oxycarbide surface species form during the oxidation (see Table 1 for HOPG data; the other surfaces were not quantitatively analyzed, but qualitatively, they also showed formation of oxide and especially oxycarbide, due to oxidation). But it is more significant to point-out that oxidation of the HOPG did not deplete the basal plane surface of the substitutional boron. In fact, exposure of the oxidized sample to water eliminates the boron-oxide species with no effect upon the peak 186.5 eV. In many cases, the concentration of substitutional boron (and/or boron-oxycarbide) increased substantially after oxidation. For example, one sample of HOPG showed a more than 2x increase in the concentration of substitutional boron on the basal plane surface after ~50% burn-off at 800°C (oxidation performed in a TGA).

A field emission scanning electron microscope (FESEM) was used to examine the oxidized surfaces of undoped and boron-doped HOPG. There was a significant difference in the density, size, shape and orientation of the etch pits in the doped and undoped HOPG surfaces; another difference was the presence of small, sub-micron particles of a reaction-product on the doped HOPG surface after oxidation. These could be associated with the boron-oxide phase detected with XPS. The etch pits were randomly distributed over the surface of the undoped HOPG and the sizes ranged between 1 and 100 microns in diameter. Moreover, the majority of the hexagonal pits on the surface were oriented parallel to the observed twin bands in the HOPG. This suggests that the oxidation pits in the undoped HOPG have primarily armchair sites on the edges of pit walls. Conversely, the oxidation pits on the doped HOPG were less distinct; they were shallow and much smaller (10nm to 1μm). And in those cases where well-developed pits could be found, they were oriented perpendicular to the observed twin bands. If true, this suggests that the surface of these pit walls are made up primarily of zig-zag edge sites.

AFM revealed some unique features associated with the oxidized surfaces of the boron-doped HOPG. Figure 4 shows both the topographical (left) and phase contrast image (right) obtained on the basal surface of boron-doped HOPG after 2 hours oxidation at 700°C. The brightness in the phase-contrast image corresponds to the relative hardness of the material under the AFM-tip. Thus, it seems likely that the particulate phase in the base of some etch pits corresponds to the boron-oxide detected by XPS. The droplet shape of the particles indicates that they are most likely glassy. This conclusion was further verified by washing the oxidized boron-doped HOPG surfaces in water, and then re-analyzing their surfaces with XPS and AFM. The particulate phase was eliminated in the AFM image due to the washing, while the boron-oxide concentration determined with XPS was reduced by 75%. It is important to emphasize, though, that the substitutional boron concentration was not reduced by the washing.

The AFM images in Figure 4 show some other noteworthy features. Many of the pits do not contain any observable boron-oxide phase; in fact, some regions of the surface were not visibly oxidized in any way. It can also be seen that the size of the boron-oxide droplets increases towards the center/bottom of each pit. The droplets are considerably smaller on the sidewalls of the pit. Finally, the AFM analysis of the washed (oxidized) surfaces revealed that the pits which contained boron-oxide (before washing) had distinctly flat-bottomed pits, while many of the other pits were rounded on the bottom.

DISCUSSION

In general, the oxidative etching of the basal plane of HOPG was less severe in the boron doped samples than in the undoped samples as measured by pit sizes. The pit diameters were 2 orders of magnitude larger in the undoped sample as compared to the doped samples. The more interesting aspect of the oxidized surfaces of the doped HOPG was the preferred orientation of the pits, and the presence of a boron-oxide reaction product (in the form of glass droplets) in some, but not all, of the etch pits. However, the size of the pits did not depend upon the presence of the boron-oxide reaction product; i.e., all of the etch pits on the boron-doped HOPG surface were small and shallow. Finally, the pit walls of the doped HOPG were much smoother than the pit walls of the undoped HOPG; i.e., the steps that comprise the pit walls were more gradual in the doped samples.

XPS showed that a boron-oxide phase builds-up during gasification of the carbon surface, while there was little or no change in the substitutional boron components. This indicates that the boron-oxide does not build up at the expense of the substitutional boron, but rather, the surface sites containing substitutional boron are regenerated or stabilized during formation of the oxide phase. This was correlated with the detection of glassy boron-oxide particles on the oxidized surfaces. There are very few glassy particles located on the bottom surface of the pits in the samples oxidized for short times, but the samples that were oxidized for longer times contained large irregularly shaped boron-oxide droplets on the bottom of some of the etch-pits; smaller more uniform clusters appeared at the upper ridge of the pore walls. Since the bottom of the pit is exposed to oxygen for shorter times than the upper ridges of the pore walls, it can be concluded that the boron-oxide builds up along the edge sites on the pit walls, and after it agglomerates into a droplet of critical mass, it falls into the bottom of the pit. This is consistent with the AFM data which showed that the pits which contained the boron-oxide phase were much flatter and shallower than the pits without the oxide phase. It suggests that a boron-oxide liquid-phase gathers on the bottom surface of the pit during oxidation and physically blocks any active sites or defects where further pit growth may proceed. In this sense, boron inhibition of carbon oxidation occurs because a boron-oxide reaction product forms a physical barrier to the oxygen atoms, and in turn, prevents the increase in surface area that accelerates the oxidation process.

However, the absence of boron-oxide in most of the etch-pits indicates that there may be other mechanisms of inhibition. The fact that the etch-pit diameters are comparable, even though some contain the boron-oxide reaction product while others do not, may be the most important observation. Consequently, oxidation along the graphite planes must be prevented by some means other that the build-up of a liquid oxide phase along the pit walls. In this regard, the preferred orientation of the etch-pits in the doped-HOPG may be significant. It suggests that a prevalence of ziz-zag sites on the etch-pit walls can stabilize the pit against further oxidation (or at least slow it down). In a companion study[14,15], theoretical methods were used to calculate the local electron density of zig-zag vs armchair edge sites, and the corresponding influence of boron substitution. These calculations showed that boron substitution on armchair sites raises their reactivity (relative to pure carbon), while boron substitution on zig-zag sites lowers the relative reactivity. Consequently, the activation energy for reaction with oxygen is increased on zig-zag sites where boron has substituted for carbon, in general.

SUMMARY

The high-temperature reaction of various carbons with boron-compounds is an effective way to introduce substitutional boron dopant. The doping is most effective in regions of disorder within the carbon structure or surface. The oxidation behavior of the doped carbons is significantly inhibited because the boron slows the creation of surface area due to oxidative etch-pitting. The high-temperature doping procedure was shown to change the defect structure of HOPG; so in this sense, the boron may eliminate surface and internal defects (and thereby limits etch-pit nucleation). However, it was also found that boron substitution on the edge-site surfaces of graphite lowers the reactivity of those sites (and thereby limits further gasification and pit growth). A passivation effect of the boron-oxide reaction product phase was also found at the bottom of the pits.

ACKNOWLEDGMENT

The authors gratefully acknowledge the AFOSR URI program (F49620-93-1-0311).

REFERENCES

1. J. M. Thomas and C. Roscoe, "The Influence of Boron on the Reactivity of Graphite Crystals", *Proc. of the* 2nd Conf. on Carbon and Graphite, London, 249 (1965).
2. D. J. Allardice and P. L. Walker, Jr., "The Effect of Substitutional Boron on the Kinetics of the Carbon-Oxygen Reaction", Carbon **8** [3], 375 (1970).
3. D. W. McKee, C. L. Spiro, and E. J. Lamby, "The Effects of Boron Additives on the Oxidation Behavior of Carbon", Carbon **22** [6], 507 (1984).
4. A. Agrawal, H. Yinnon, D. R. Uhlmann, R. Pepper, C. R. Desper, "Boron Modification of Carbon Fibers", J. Mat. Sci., **21** [10], 3455 91986).
5. P. Ehrburger, P. Baranne and J. Lahaye, "Inhibition of the Oxidation of Carbon-Carbon Composite by Boron Oxide", Carbon, **24**[4], 495 (1986).
6. D. W. McKee, "Oxidation Behavior of Matrix-Inhibited Carbon/Carbon Composites", Carbon **26**[5], 659 91988).
7. L. E. Jones and P. A. Thrower, "Influence of Boron on Carbon Fiber Microstructure, Physical Properties, and Oxidation Behavior", Carbon **29** [2], 251 (1991).
8. M. Chesneau, F. Beguin, J. Conrad, R. Erre, J. Thebault, "The Antioxidation Effect of Boron Oxide on a Pyrocarbon", Carbon, **30** [4], 714 (1992).
9. W. Kowbel, Y. Huang and H. Tsou, "Effect of Boron Ion Implantion on the Oxidation Behavior of 3-Dimensional C/C Composites", Carbon **31** [2], 355 (1993).
10. J. W. Fergus, and W. L. Worrell, "Silicon-Carbide/Boron Containing Coatings for the Oxidation Protection of Graphite", Carbon **33** [4], 537 (1995).
11. M. Karra, R. J. Zaldivar, G. S. Rellick, P. A. Thrower, and L. R. Radovic, "Substitutional Boron in Carbon Oxidation: Inhibitor or Catalyst?", Proceedings of Carbon '95, 646 (1995).
12. W. Cermignani and C. G. Pantano, "X-Ray Photoelectron Spectroscopy of Boron-Doped Carbons", Proceedings of Carbon '95, 136 (1995).
13. N. M. Rodriquez and R. T. K. Baker, "Fundamental Studies of the Influence of Boron on the Graphite-Oxygen Reaction Using In-Situ Electron Microscopy Techniques", J. Mater. Res., **8**[8], 1886 (1993).

14. Q. Wang, X. L. Ma, L. Q. Chen, W. Cermignani, and C. G. Pantano, "Effect of Boron on Graphite Oxidation-A Theoretical Study", Carbon, **35**[2], 307 (1997).
15. Q. Wang, et al, "Semi-Empirical Studies on Electronic Structures of a Boron-Doped Graphene Layer-Implications on the Oxidation Mechanism", Carbon, (to appear).
16. C. E. Lowell, "Boron in Graphite", J. Am. Ceram. Soc., **50**[3], 142 (1967).
17. F. Tuinstra and J. L. Koenig, "Raman Spectrum of Graphite", J. Chem. Phys. **53** [3], 1126 (1970).

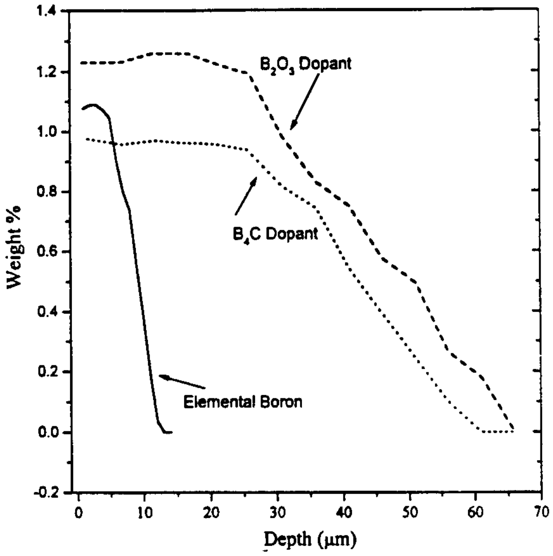

Figure 1. Concentration profiles (by electron microprobe) for boron in vitreous carbon.

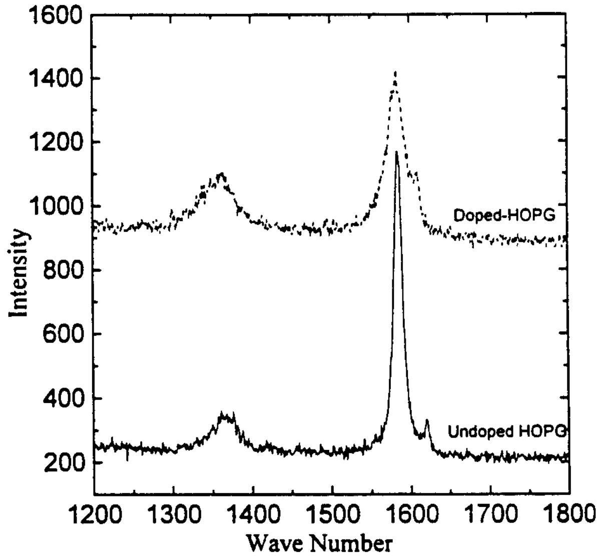

Figure 2. Raman spectra for undoped and boron-doped HOPG.

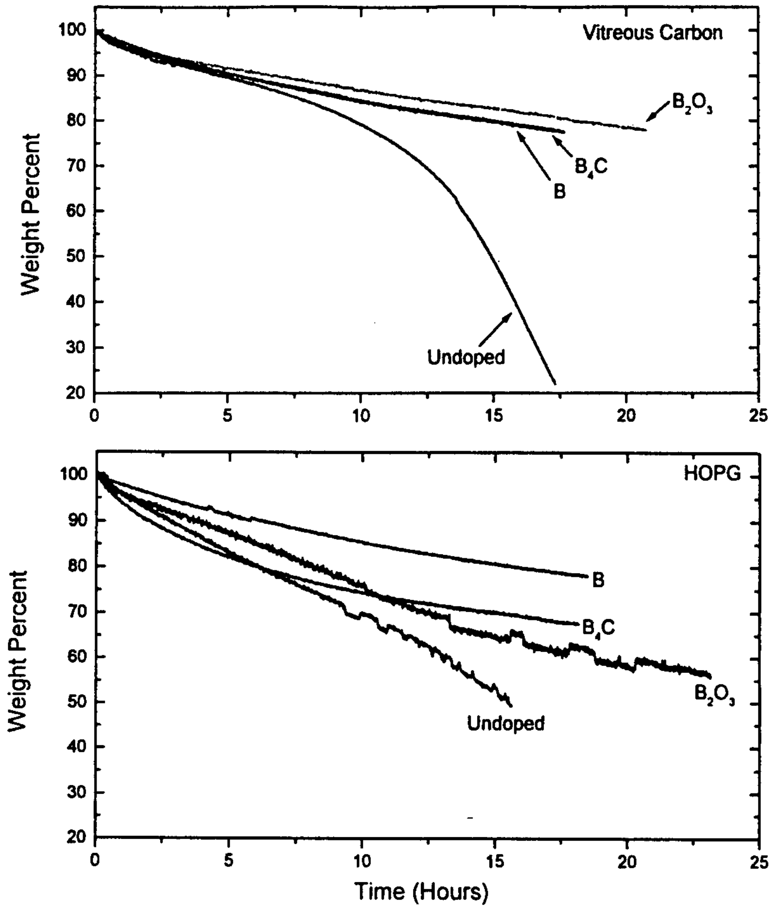

Figure 3. TGA data (in O_2 at 800°C) for vitreous carbon (upper) and HOPG (lower).

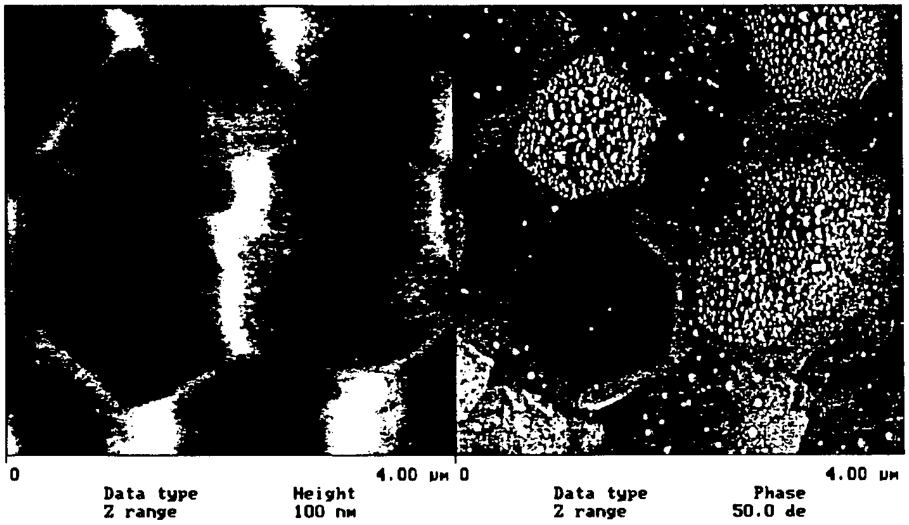
0
4.00 µm
Data type
Z range
Height
100 nm
0
4.00 µm
Data type
Z range
Phase
50.0 de

Figure 4. AFM images for the basal-plane surface of boron-doped HOPG (2 hrs @ 700°C)

ATTACHMENT II

Paper (e)

Pergamon

Carbon Vol. 35, No. 10–11, pp. 1517–1525, 1997
© 1997 Elsevier Science Ltd
Printed in Great Britain. All rights reserved
0008-6223/97 $17.00 + 0.00

PII: S0008-6223(97)00102-4

SEMI-EMPIRICAL STUDIES ON ELECTRONIC STRUCTURES OF A BORON-DOPED GRAPHENE LAYER – IMPLICATIONS ON THE OXIDATION MECHANISM

X. Ma, Q. Wang,* L.-Q. Chen, W. Cermignani, H. H. Schobert and C. G. Pantano
Department of Materials Science and Engineering, The Pennsylvania State University, University Park, PA 16802, U.S.A.

(*Received* 7 *January* 1997; *accepted in revised form* 24 *April* 1997)

Abstract—The electronic structures of pure and boron-doped graphene layers have been investigated using the semi-empirical Molecular Orbital Package (MOPAC) and large clusters of carbon atoms. It is shown that boron-doping on the edge and internal lattice sites of the graphene layer produces very different effects on the electronic structure around the edges. It is found that the substitutional boron atoms on the edges dramatically alter the density distribution of high energy electrons along the edges and the substitutional boron atoms in the deep internal lattice sites do not produce any significant effect on the density distribution along the edges. Based on the results obtained, a model is proposed for describing the oxidation process in boron-doped graphite. The mechanism of oxidation inhibition due to boron-doping of a graphene layer is chemical inhibition via the reduction of electron density with high energy at surface sites, and consequently, a reduction in the total number of active sites for gasification of the carbon. © 1997 Elsevier Science Ltd

Key Words—A. Natural graphite, B. oxidation, C. molecular simulation, D. electronic structure, D. surface properties.

1. INTRODUCTION

Since boron has been found to be a unique and efficient dopant for improving the oxidation resistance of graphite [1–4], there have been many studies on the synthesis [5,6], oxidation behavior [7,8], atomic and electronic structures [9–14], and possible ordered ground states [15] of boron-doped graphite. Based on their experimental observations, Jones and Thrower [3] proposed three possible mechanisms to explain the role of boron in oxidation inhibition of graphite: (1) physical blockage of the surface active sites by a B_2O_3 barrier layer formed on the surface during oxidation; (2) chemical inhibition via electron transfer between carbon and substitutional boron atoms on the internal graphite lattice sites, which increases the activation energy for the C–O_2 reaction; and (3) boron doping resulting in the improvement of graphite crystallinity, and thus a decrease in the total number of accessible active surface sites for oxygen. One of the main objectives of this paper is to investigate the electronic density redistribution of a graphene layer as a result of boron substitution using the semi-empirical Molecular Orbital Package (MOPAC), which will shed some light on the mechanism, or mechanisms, mainly responsible for the oxidation inhibition of boron-doped graphite.

Substitutional boron can occupy either a surface or an internal lattice site of graphene layers. Experimentally, the oxidation rates of boron-doped graphite are usually measured as a function of the overall boron content, which includes both surface and internal bulk boron atoms [3]. It is unclear whether internal and surface boron atoms contribute equally to the oxidation inhibition. Therefore, in this paper, the differences in the effectiveness of oxidation inhibition between surface and internal bulk boron substitution will be studied within an individual graphene layer.

The paper is arranged as follows: Section 2 describes the model and simulation procedures, the results are presented and discussed in Section 3, and the conclusions are given in Section 4.

2. THE MODEL

In our previous work [14], a cluster with 54 atoms arranged in a honeycomb structure was used to model the surface structure of a graphene layer. There are six edges in the cluster and only one active site on each edge. However, the cluster is still small compared to the typical size of the graphite crystallite used in experiments. In order to make the cluster a more realistic mimic of the surface structure of the graphene layers that comprise graphite, a new cluster with 56 carbon atoms having four active sites on the edge studied was designed as shown in Fig. 1. There are two long edges, labeled as top and bottom, and two short edges, labeled as left and right. On the top edge, there are four surface active sites, 4, 6, 8 and 10. The carbon atoms on the active sites of the bottom and two short edges are saturated by

---

*Corresponding author.

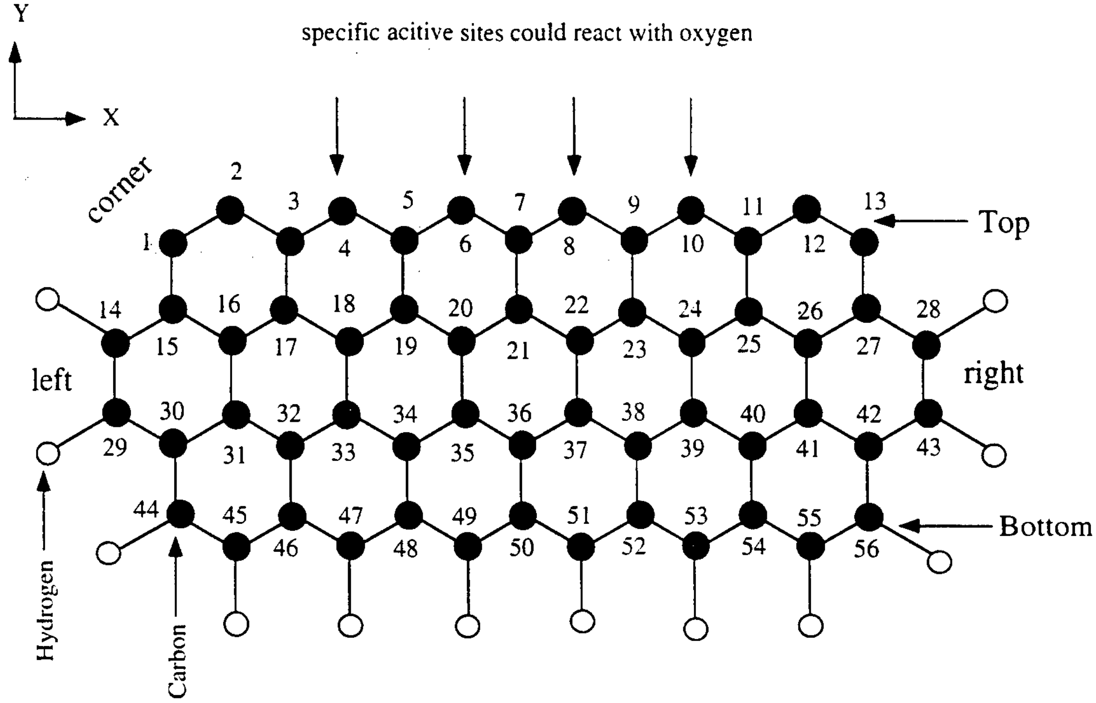
Y
X
specific acitive sites could react with oxygen
corner
2
3
5
7
9
11
13
Top
1
4
6
8
10
12
14
16
18
20
22
24
26
28
15
17
19
21
23
25
27
left
right
30
32
34
36
38
40
42
29
31
33
35
37
39
41
43
44
45
47
49
51
53
55
Bottom
46
48
50
52
54
56
Hydrogen
Carbon

Fig. 1. The atomic arrangement in the designed carbon cluster.

hydrogen atoms. The hydrogen saturation on the bottom, left and right edges of the cluster is made to simulate the behavior of internal bulk, or unreactive, carbon sites in a graphene layer. On the other hand, the hydrogen atoms have been left off the top edge of the cluster in order to simulate the most reactive carbon sites present in the layer. In order for the oxidation reaction between carbon and oxygen to take place, hydrogen would have to be extracted from the carbon surface. Hence, the cluster model shown in Fig. 1 accurately describes all the important features at the surface of the graphene layer during oxidation. There are a number of other steps involved in the oxidation process including removal of hydrogen (or other) surface species, splitting of molecular oxygen, and diffusion of reacting species to and from the surface of the graphene layer. Even though these steps will affect the overall reaction rates or activation energies of oxidation, they are ignored in this paper in order to fully understand site reactivity in boron-doped graphene layers. Therefore, the carbon atoms on the top edge (sites

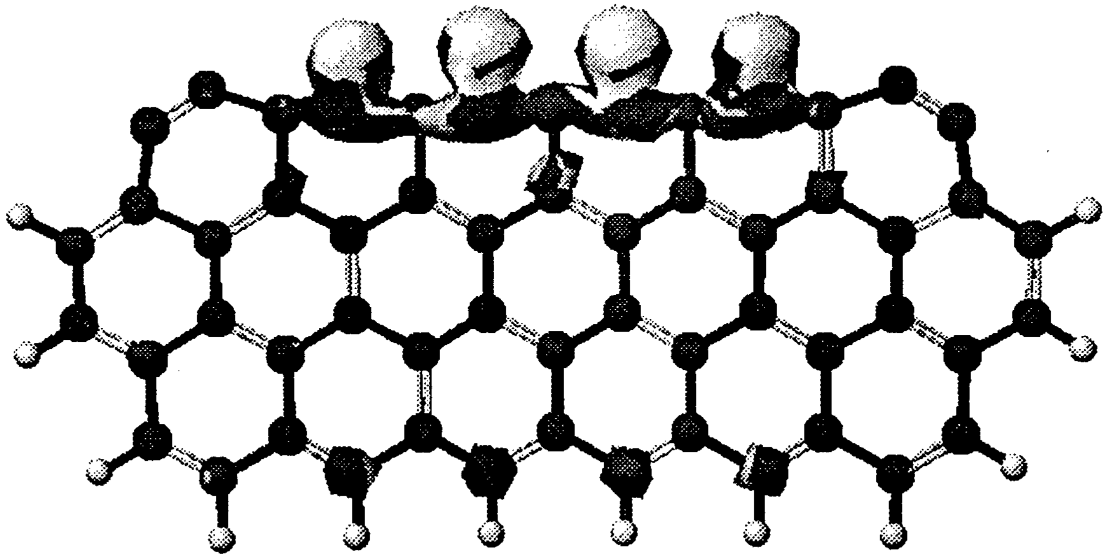

Fig. 2. The electron density distributions of the pure carbon cluster.

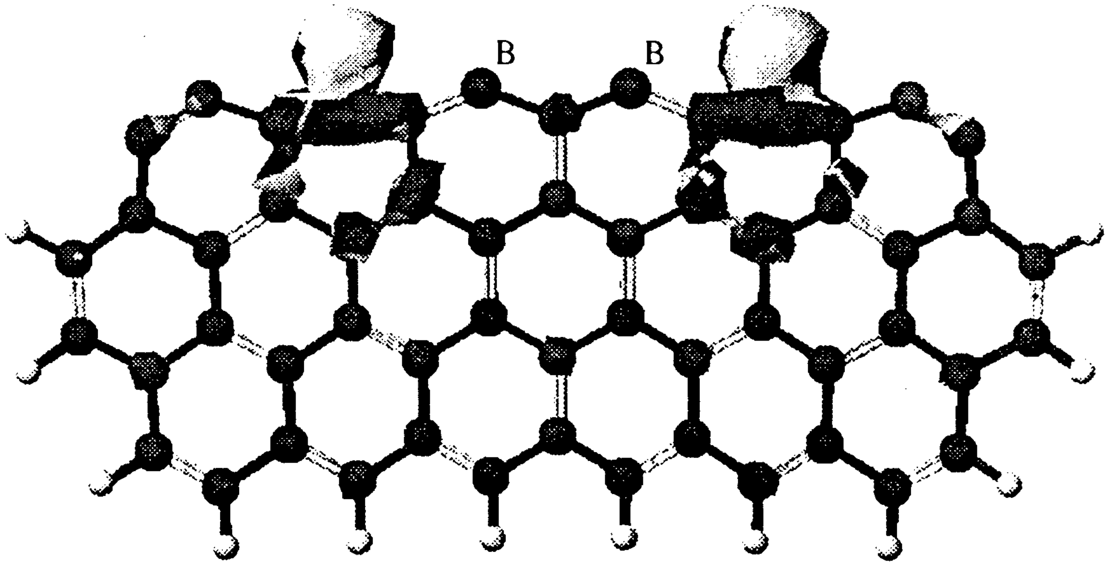

Fig. 3. The electron density distribution of the carbon cluster with two substitutional boron atoms on the surface sites 6 and 8.

4, 6, 8 and 10) and two up corners (sites 1, 2, 12 and 13) are open for simulating the bare surface of a graphene layer.

The geometric structure of the cluster is optimized by minimizing its energy, i.e. heat of formation. Minimum-energy geometries are stationary geometries for which the energy increases when the atoms are displaced in any direction. The bond length between, and the number of valence electrons on, those carbon atoms close to or on the top edge are slightly different from the corresponding bulk values. For example, the optimized bond length is 1.45 Å for the C7–C21 bond, as compared to the value 1.42 Å in the bulk. The number of valence electrons for the carbon atoms are 4.07 electrons on C7, while in the bulk the number is 4.00. The corresponding parameters for the carbon atoms close to the bottom edge of the cluster are closer to the bulk values, e.g. 1.42 Å for the C35–C36 and C36–C37 bonds, 1.43 Å for the C36–C50 bond, 3.99 electrons on C35 and C37, and 4.01 electrons on C36 and C50. These results show that the hydrogen saturation on the bottom, left and right edges makes the behavior of carbon atoms more similar to those in the bulk, i.e. the carbon atoms close to the bottom edge can be used to approximate the internal bulk carbon atoms of the graphene layer.

The Computer Aided Chemistry (CAChe) work-system was used to calculate the electronic properties of designed clusters with and without substitutional boron atoms, by means of the semi-empirical Molecular Orbital Package (MOPAC, version 94). The AM1 potential parameters were employed to solve the Schrodinger equation for optimum geometry of the clusters, using the Mechanics (MM2) geometry as an initial input.

Table 1. Reactivities (R) of four surface active sites for various cases

Site #	R^a	R^b	R^c	R^d
4	0.820	1.680	0.534	0.920
6	1.100	0.074	1.153	1.000
8	1.100	0.074	0.261	1.000
10	0.820	1.680	1.659	0.920

[a] Pure graphite cluster.

[b] The graphite cluster with two boron substitutions on sites 6 and 8.

[c] The graphite cluster with two boron substitutions on the shallow internal lattice sites 19 and 21.

[d] The graphite cluster with two boron substitutions on the deep internal lattice sites 35 and 37.

3. RESULTS AND DISCUSSION

3.1 *Density of high energy electrons and reactivity*

Since oxidation of an atom is an electrophilic reaction in which the oxygen atom draws electrons from the atom, the ability of the atom to donate electrons involving in the reaction with oxygen can be considered to be oxidation reactivity of the atom. The more electrons the atom has in the reaction with oxygen, the easier the atom reacts with oxygen, and the higher oxidation reactivity the atom possesses. In bulk graphite, only the electrons occupying the states around the Fermi surface would contribute to the oxidation reaction [9]. In a larger carbon cluster with edges and corners, the electrons in the highest occupied molecular orbital (HOMO), and those orbitals close to the HOMO, are considered to make the main contribution to the oxidation reaction [16]. Therefore, the oxidation reactivity of the atoms depends on the populations of their electrons in the HOMO and the orbitals close to the HOMO. Such populations can be used as an index of the oxidation reactivity (R). In MOPAC, this reactivity (R) can be characterized through the coefficient C_j^i [16,17]

$$R=\sum_j 2\sum_i (C_j^i)^2 \qquad (1)$$

where C_j^i is the coefficient of LCAO (linear combination of atomic orbitals) on molecular orbital j, and i labels the atomic orbitals s, p_x, p_y and p_z, respectively. The summation runs over the high occupied molecular orbitals including the HOMO. In our model, the four highest occupied orbitals were taken into account to determine R. It should be emphasized that the electron density distributions presented below are also calculated for only those electrons occupying the four highest occupied orbitals, unless otherwise specified.

3.2 *Pure graphene layer*

The electron density distribution calculated from the four highest occupied orbitals in a pure carbon cluster is shown in Fig. 2, where the carbon atoms are represented by large dark circles and the hydrogen atoms are denoted by small light circles; the volume of the shaded regions around an atom, for instance, atoms 4, 6, 8 and 10, refers to the density of high energy electrons on this atom, and the light and dark colors within these regions represent high and low values for the electron density; if there is no shaded region around an atom, say, atom 36, it implies that this atom has no valence electrons on the four highest molecular orbitals; and the convention of using the volume of shaded region to represent electron density will be used consistently in the other figures. According to Fig. 2, most of the electrons with high energy are predominantly localized on the four surface active sites (4, 6, 8 and 10). The oxidation reactivities (R) on these sites are calculated and listed in Table 1. These values are much higher than those on other sites which are almost zero. It implies that, in an oxidizing environment, oxygen atoms will most likely first attack the carbon atoms at these hydrogen-free active sites. The reactivities of the carbon atoms on the corner sites (i.e. 1, 2, 12 and 13) are almost zero, and thus they are considered to be relatively inactive to an oxidation reaction even though they do not contain hydrogen. By comparing the reactivities on the four active sites, i.e. 4, 6, 8 and 10, listed in Table 1, we found that the reactivities on the 6 and 8 sites are greater than those on other two sites. This may imply that the carbon atoms on edge sites which are furthest away from the corner sites possess the greatest reactivity, i.e. the carbon atoms located at the middle of a edge of graphene layer are more susceptible to oxidation. The suggestion from the MOPAC simulation for the pure carbon cluster seems to be consistent with previous predictions [3].

3.3 *Boron dopants at surface sites*

In order to study the effect of boron doping, we replace the carbon atoms on two (6 and 8) of the four surface active sites with two boron atoms, and the resulting density distribution of high' energy electrons is shown in Fig. 3. One may notice a significant reduction in the density of high energy electrons on these sites as a result of boron substitution. The corresponding oxidation reactivities are calculated and listed in the second column of Table 1, which indicates a dramatic decrease on sites 6 and 8. However, the decrease in R on sites 6 and 8 is accompanied by an increase in R on the other two active sites, 4 and 10. Therefore, oxidation will most likely take place on the remaining active sites, and significantly slows down only if all the remaining actives sites are replaced by boron atoms. Figure 4

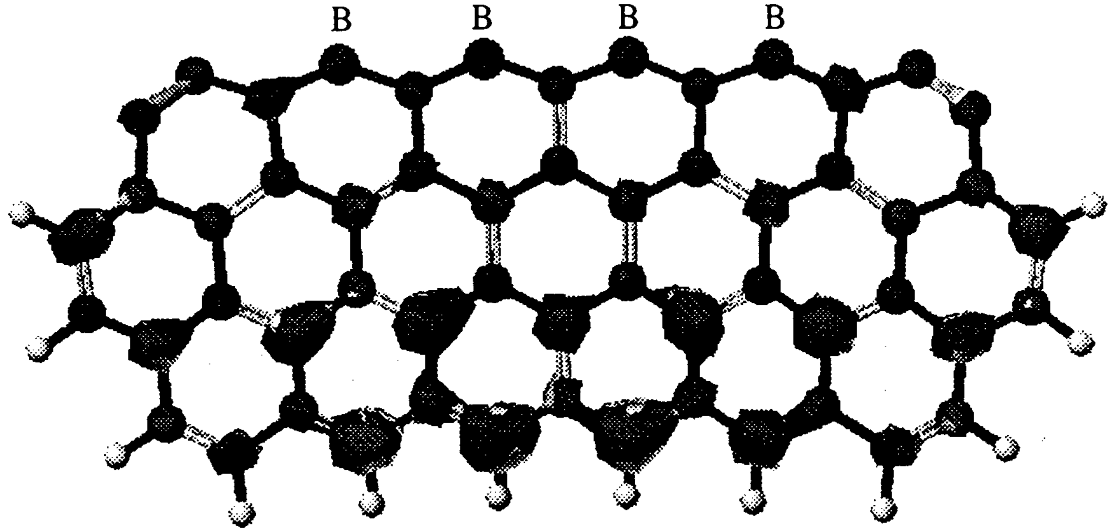

Fig. 4. The electron density distributions of the carbon cluster with four substitutional boron atoms on the surface specific active sites 4, 6, 8 and 10.

shows that when all of the surface active sites are occupied by substitutional boron atoms, the density of high energy electrons on all the originally active sites is dramatically reduced. At the same time, there is an increase in the density of high energy electrons at internal sites in the graphene layer which are, however, much less accessible to surface oxygen. Therefore, boron substitution for carbons on edge sites improves the oxidation resistance of the graphene layer by reducing the total number of surface active sites.

It was also found that substituting boron atoms for carbons on the nearest neighbor sites to the active sites can also reduce the density of high energy electrons on the active sites. For example, Fig. 5 shows that by replacing the carbon atoms on sites 5 and 7 with boron atoms, the density of high energy electrons on the active site 6 is significantly reduced (Fig. 5(a)), while replacement of carbons on sites 5 and 9 by boron atoms reduces the density of high energy electrons on the active sites 4 and 10 (Fig. 5(b)). Similar to the case in Fig. 3 (where two carbon atoms on the surface active sites are replaced by boron atoms), the remaining active sites show higher reactivity with oxygen than the pure graphene layer. Therefore, any reduction in the oxidation rates must be due to the decrease in the number of surface active sites by the boron substitution.

It is shown in Fig. 3 that the addition of surface boron atoms to the graphene layer results in a

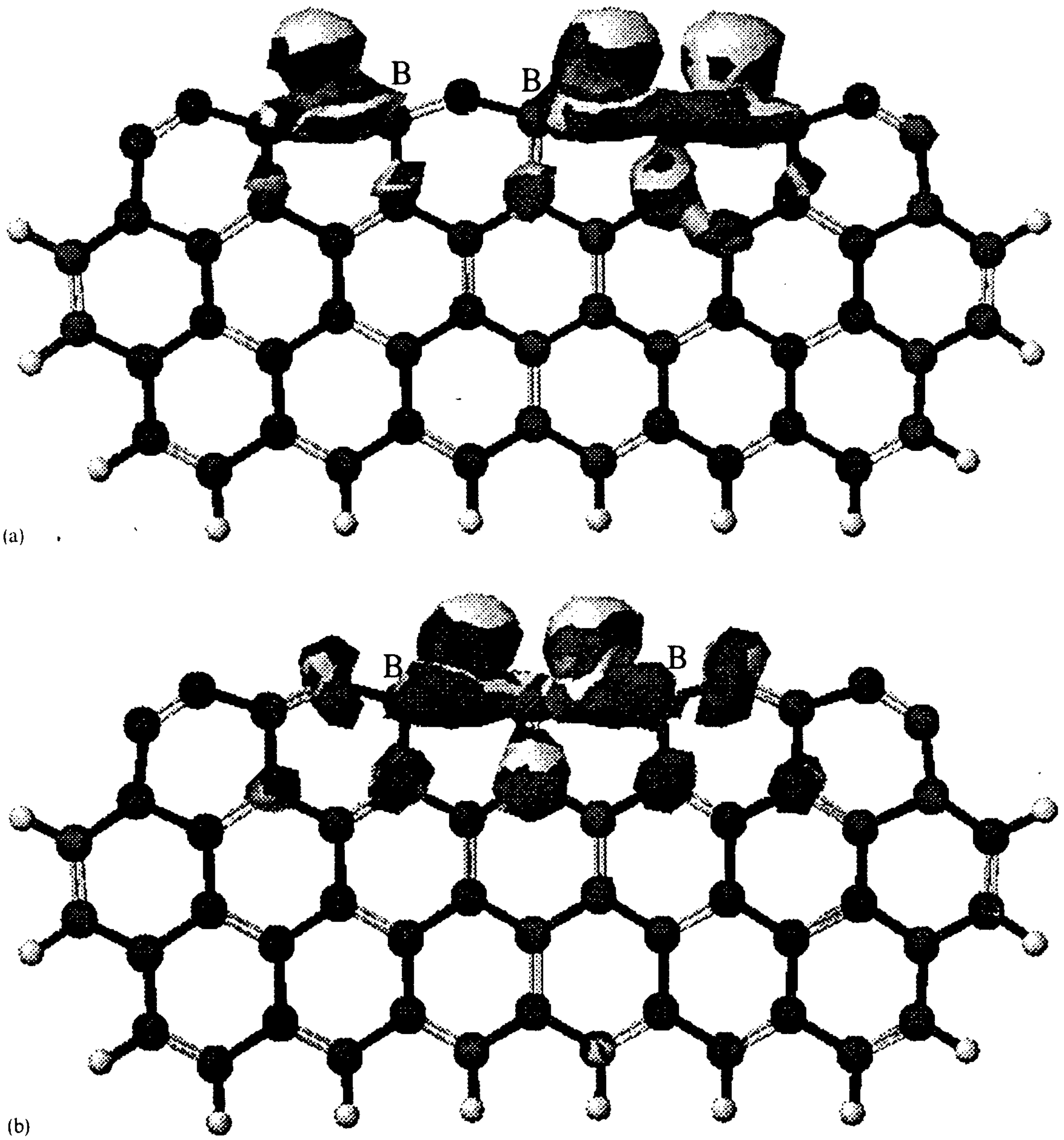

Fig. 5. The electron density distribution of the carbon cluster with two substitutional boron atoms on the shallow surface sites: (a) 5 and 7; (b) 5 and 9.

decrease in the density of high energy electrons around the boron atoms (sites 6 and 8) and an increase in the density of high energy electron around neighboring carbon atoms (sites 4 and 10). This situation can also be seen at the different sites in Fig. 5(a) and (b). Since the high energy electron density distribution is related to the oxidation reactivity of carbon atoms, and indirectly to the activation energy of the oxidation reaction, the simulation might imply different effects of boron substitution on the activation energy of the oxidation reaction depending upon the local structure. This is supported by experimental data. It was shown by Jones and Thrower [3] that doping mesophase pitch carbon-fibers at 2450°C with low boron concentration resulted in an increase in the activation energy for fiber oxidation, and once the boron concentration increased over 1000 ppm a noted decrease in the energy of activation was also observed. Allardice and Walker [18] showed similar measurements that doping graphitic carbon with boron at approximately 1000 ppm level lowered the activation energy for oxidation. It is possible that the cause of this variation in activation energy is due to the final distribution of boron in the graphite at different boron-doping concentration levels.

3.4 *Boron dopants at internal sites*

In order to compare the difference in the effectiveness of oxidation inhibition between boron atoms on the graphite edge sites and those in the internal

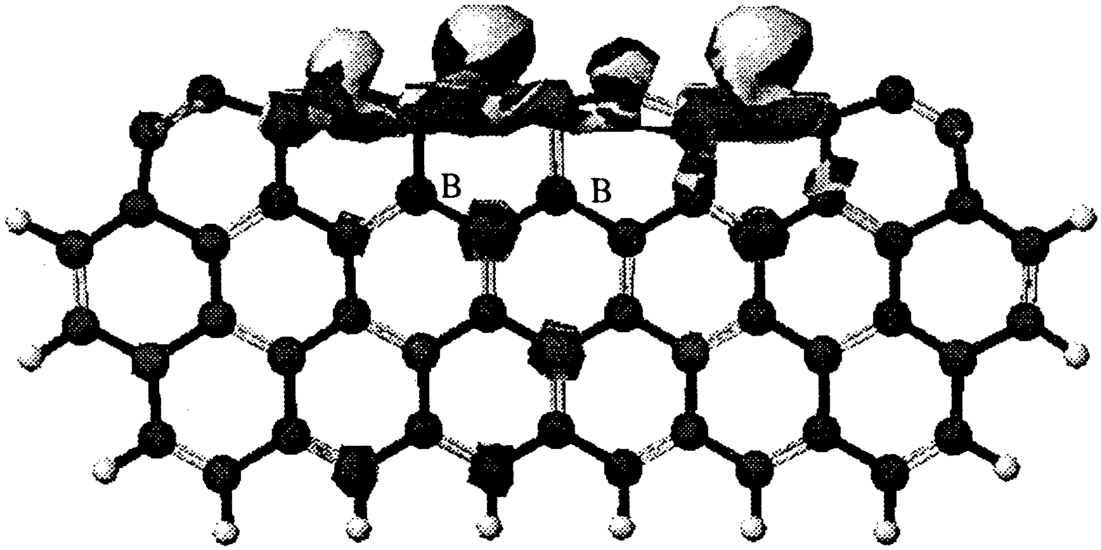

Fig. 6. The electron density distributions of the carbon cluster with two substitutional boron atoms on the shallow internal lattice sites 19 and 21.

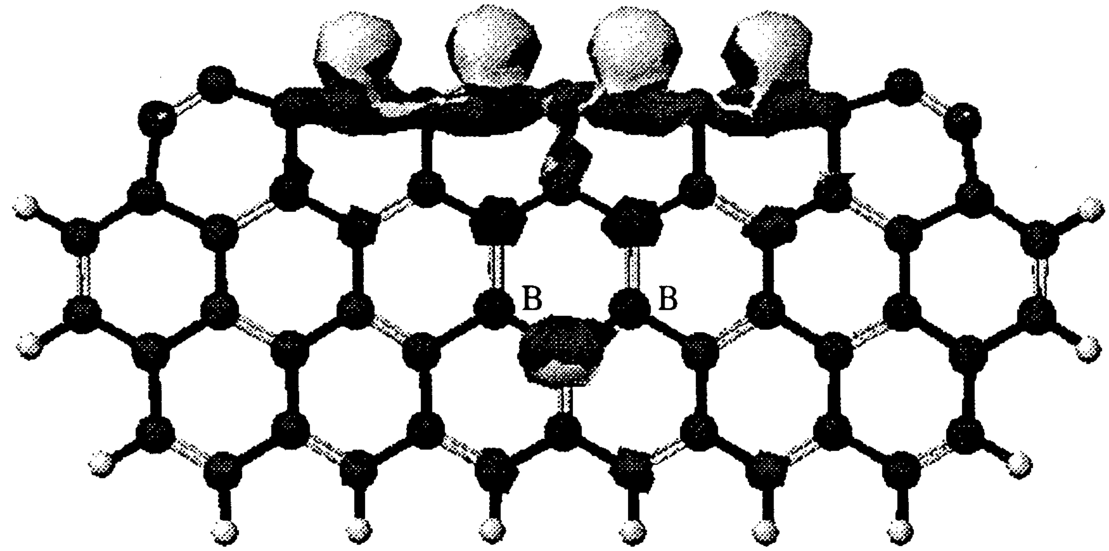

Fig. 7. The electron density distributions of the carbon cluster with two substitutional boron atoms on the deep internal lattice sites 35 and 37.

lattice sites, we also investigated the changes in the density of high energy electrons as a result of boron substitution in the internal lattice sites of the graphene layer. We distinguish two types of internal lattice sites: a) the shallow internal lattice sites near the surfaces or edges, such as sites 19, 21 and 23; and b) the deep internal lattice sites like the sites 35 and 37.

When the near-surface carbon atoms on sites 19 and 21 were replaced by boron atoms, there is a

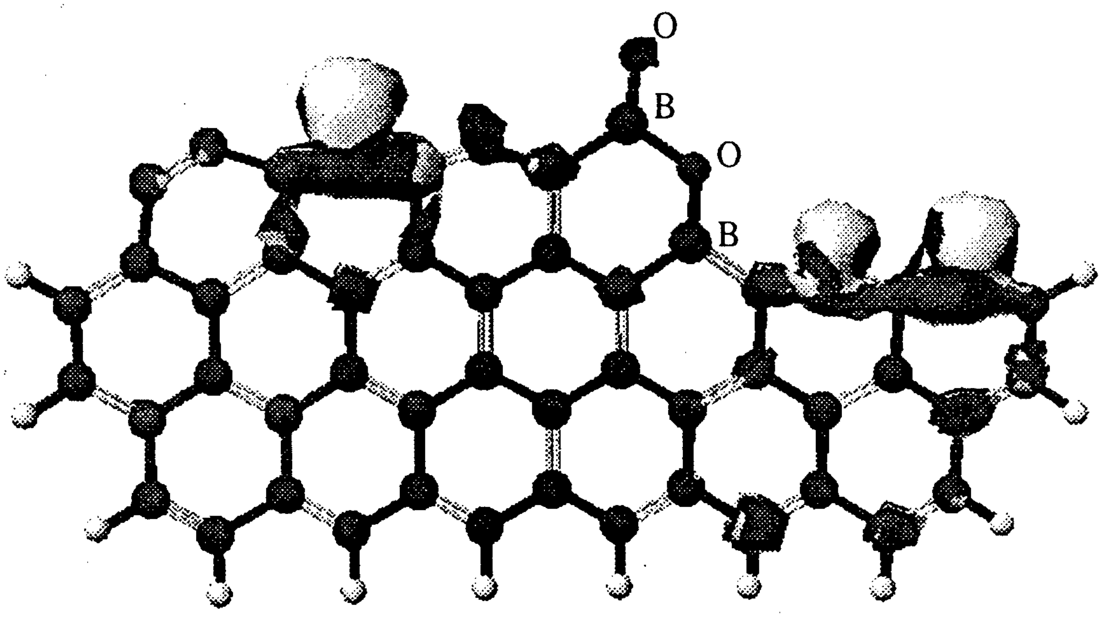

Fig. 8. The electron density distribution of the carbon cluster with the formation of boron oxide on the surface area.

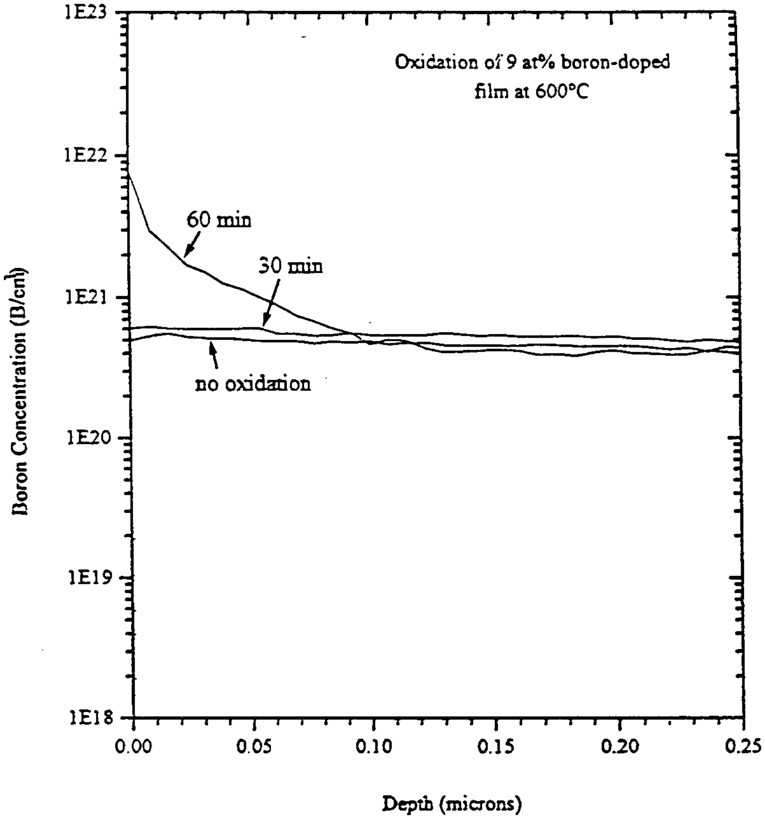

Fig. 9. SIMS profile of the $^{11}B^+$ in the 9 at% boron doped film showing the effect of oxidation on the surface boron concentration. The oxidation took place at 600°C under 5 mL min^{-1} flowing air.

noticeable change in the density distribution of high energy electrons on the active sites 4 and 8 (Fig. 6). The corresponding reactivities, R, on these two active sites are reduced from 0.820 and 1.100 to 0.534 and 0.261, respectively (column (c) of Table 1). This indicates that boron substitution on the near-surface sites may also enhance the oxidation resistance of graphite by reducing the reactivity of active sites on the surface, although the degree of reduction is not as high as in the case of direct substitution of boron atoms for carbons on the active sites.

The density distribution of high energy electrons is shown in Fig. 7 for the case of boron substitution on the deep internal sites 35 and 37. The resulting oxidation reactivities for the four surface active sites are listed in the last column (d) of Table 1. By comparing the values in column (a) of Table 1, it can be clearly seen that boron substitution in the deep internal lattice sites produces little changes in the reactivities of the active sites, indicating that the substitutional boron atoms on the deep internal lattice sites do not improve the oxidation resistance of the graphene layer.

In summary, boron substitution for carbon on the surface or near-surface sites will significantly reduce the density of high energy electrons on some of the surface active sites; whereas, boron substitution on the deep internal lattice sites does not have a significant effect on the electron distribution at the surface.

3.5 *Surface oxidation*

It must be pointed out that substitutional boron atoms on the surface could have possibility to be further oxidized and form boron oxide on the surface of the boron-doped graphene layer [19]. The boron in the boron oxide can still chemically bond together with the surface of the graphene layer. It has been suggested that the formation of the boron oxide may reduce the oxidation rate of the graphene layer by providing a physical diffusion barrier [3,19]. Our simulations indicate that the oxidized boron can also reduce the electron density with high energy at its neighboring active sites, as shown in Fig. 8, and hence play a role in the oxidation inhibition.

Therefore, the following is a proposed physical picture for describing the oxidation processes in boron-doped graphite. During the initial stage of oxidation, some of the surface sites will be occupied by carbon, and they will react with oxygen and be removed. As a result, new surface active sites will be created. If the new surface sites are again occupied by carbon atoms, the oxidation will most likely continue. The oxidation will be significantly slowed down when all the surface active sites, or their neighbors, are occupied by boron atoms or boron oxide. It is quite reasonable to expect, therefore, that boron atoms can accumulate on the graphite surface during the oxidation process. Figure 9 shows the SIMS profile of the ^{11}B ion in the 9 at% boron-doped chemical vapor deposition (CVD) film before and after oxidation at 600°C under 5 mL min^{-1} flowing air for 30 and 60 minutes. It can be seen that there is little change in the boron profile after 30 minutes of oxidation. However, a large buildup of boron is observed at the surface of the sample oxidized for 60 minutes. According to the SIMS analysis, the surface concentration of boron increases about one order of magnitude as a result of oxidation. Therefore, our proposed oxidation picture seems to agree with the experimental measurement. Of course, at higher temperature, the volatilization of boron oxide can compete with this accumulation of boron oxide at the surface.

4. CONCLUSION

The electronic structures of various carbon clusters have been simulated by MOPAC with AM1 parameters to investigate the oxidation behavior of graphene layers and the oxidation-inhibition in boron-doped graphite. The results show that 1) substitutional boron atoms on the surface play very significant roles in oxidation inhibition of the boron-doped graphene layer by changing the density distribution of high energy electrons along the edges of the layer; 2) substitutional boron atoms on the deep internal lattice sites do not produce any significant effect on the electron density distribution along the edges of the graphene layer; 3) a model is proposed for describing the oxidation process in boron-doped graphite. It is concluded that the mechanism of oxidation inhibition due to boron-doping of a graphene layer is chemical inhibition via the reduction of electron density at surface sites, and consequently, a reduction in the total number of active sites for gasification of carbon.

Acknowledgements—This work is supported by the AFOSR University Research Initiative Program at Penn State under Grant No F49620-93-1-0311. The calculations were partly performed on the CRAY at the Pittsburgh Supercomputing Center and the CPU time was provided by the Center under Grants No. 940015P and No. 960007P.

REFERENCES

1. Lowell, C. E., *J. Am. Ceram. Soc.*, 1967, **50**, 142.
2. Murty, H., Beiderman, D. and Heintz, E., *Fuel*, 1977, **56**, 305.
3. Jones, L. E. and Thrower, P. A., *Journal de Chimie Physique*, 1987, **84**, 1431; *Carbon*, 1991, **29**, 251.
4. Kaner, R. B., Kouvetakis, J., Warble, C. E., Sattler, M. L. and Bartlett, N., *Mater. Res. Bull.*, 1987, **22**, 399.
5. Way, B. M., Dahn, J. R., Teidje, T., Myrtle, K. and Kasrai, M., *Phys. Rev. B*, 1992, **46**, 1697.
6. Kouvetakis, J., Kaner, R. B., Sattler, M. L. and Bartlett, N., *J. Chem. Soc. Chem., Commum.* 1986, 1758.
7. Chesneau, M., Beguin, F., Conard, J., Erre, R. and Thebault, J., *Carbon*, 1992, **30**, 714.
8. Fecko, D. L., Jones, L. E. and Thrower, P. A., *Carbon*, 1993, **31**, 637.
9. Tomanek, D., Wentzcovitch, R. M., Louie, S. G. and Cohen, M. L., *Phys. Rev. B*, 1988, **37**, 3134.
10. Lee, Y. S. and Kertesz, M., J. Chem. Soc., Chem. *Commun.*, 1988, 75.

11. Wentzcovitch, R. W., Cohen, M. L. and Louie, S. G., *Phys. Lett. A*, 1988, **131**, 457.
12. Krishnan, K. M., *Appl. Phys. Lett.*, 1991, **58**, 1857.
13. Wang, Q., Chen, L.-Q. and Annett, J. F., *Phys. Rev. B*, 1996, **54**, R2271.
14. Wang, Q., Ma, X., Chen, L.-Q., Cermignani, W. and Pantano, C. G., *Carbon*, 1997, **35**, 307.
15. Magri, R., *Phys. Rev. B*, 1994, **49**, 2805.
16. Fukui, K., Yonezawa, T. and Shingu, H., *J. Chem. Phys.*, 1952, **20**, 722.
17. Fukui, K., Yonezawa, T., Nagata, C. and Shingu, H., *J. Chem. Phys.*, 1954, **22**, 1433.
18. Allardice, D. J., Walker, P. L., Jr, *Carbon*, 1970, **8**, 375.
19. Hoshii, S., Kojima, A. and Otani, S., *J. Mater. Res.*, 1996, **11**, 2536.

Final Technical Report on Theoretical Calculations

Long-Qing Chen

1. The relative stability and charge-transfer behavior of BC_3 ordered phases were investigated using the *ab initio* pseudopotential method. The total energies as well as the cohesive energies of four possible ordered structures of the BC_3 were calculated at 0K by relaxing both the unit cell parameters and the local atomic positions. Among them, the one with the hexagonal symmetry was found to have the lowest total energy, and is thus the most stable structure. The nearest-neighbor bond lengths in the most stable structure are 1.42 Å for C-C and 1.55Å for B-C, consistent with previous studies. Charge transfer occurs between nearest neighbor C-B bonds with charge transfer from B to C, and the amount of charge is about 0.45 from boron to three C atoms with 0.15 each.

2. The structural properties of three-dimensional (3-D) ordered phases of C_3B and C_5B compounds, in which C atoms in the graphite structure are regularly replaced by B atoms, were also studied using the ab initio pseudopotential method. Two different stacking sequences of graphite layers were considered: BC stacking in which B atoms are directly on top of C atoms, or vice versa; and BB stacking in which some of B atoms are on top each other. Results indicate that for C_3B, the structure with hexagonally symmetric distribution of B atoms and BC stacking is stable, whereas for C_5B, both BC and BB stackings are possible with BC stacking being more stable. In the case of C_3B, the interlayer spacing is 3.43-3.45 Å which is slightly larger than that in pure graphite, 3.30-3.35 Å, while for C_5B, the interlayer spacing is 3.00 Å, which is significantly smaller than pure graphite.

3. Based on the semi-empirical MOPAC method, the electronic properties of two clusters representing (a) pure carbon graphite and (b) graphite with boron on the edges, were respectively calculated to understand the oxidation-inhibiting mechanism of doped-boron. The results indicate that (1) the carbons on the edge of graphite are more susceptible to oxidation than the carbons on the corner and (2) the replacement of the edge carbons by boron atoms inhibits the oxidation process of C/C composite by means of significantly reducing the high-energy-orbital electronic

density on such positions. The comparison of estimated oxidation reaction heat of the two clusters shows that interaction of oxygen with the graphite having boron on the boundary is much weaker than that with the pure carbon graphite. It implies that the oxidation of the former is more difficult than that of the latter, which further supports the point that the boron doped on the edge of graphite inhibits the oxidation reaction between graphite and the surrounding oxygen atmosphere. This calculation also indicates that the C_2BC is a possible boundary structure of doped-boron graphite, which is consistent with the experimental observation.

4. The investigation of the electronic structures of pure and boron-doped graphite were further extended to large clusters of carbon atoms by using the semi-empirical Molecular Orbital Package (MOPAC). It is shown that boron-doping on the edge and internal lattice sites of graphite produces very different effects on the electronic structure, and hence on the oxidation resistance. A model was proposed for the oxidation-inhibition mechanism of boron-doping in graphite. The charge distributions of a boron atom in various local configurations on the graphite surface was compared. Based on the experimentally measured X-ray photoelectron spectroscopy (XPS) of the 1s-electron binding energies of boron in graphite and the semi-empirical relationship between the 1s-electron binding energy and the charge distribution of boron, several possible atomic configurations of boron on graphite surface were proposed. The results show that (1) the substitutional boron atoms on the surface play very significant roles in oxidation inhibition of the boron-doped graphite by changing the electron density distribution along the surface; (2) the substitutional boron atoms on the deep internal lattice sites do not affect the electron density distribution on the surface of graphite, and thus the boron atoms have no effect on the oxidation inhibition of the graphite from the chemical point of view; (3) five possible surface states of the substitutional boron atoms were determined by comparing the experimental spectrum of the 1s-electron binding energy of boron with the charge distribution on boron calculated through the simulations; (4) a model for describing the oxidation process in the boron-doped graphite was established and the prediction from this model about the increase of boron concentration on the surface during oxidation is consistent with the experimental observations; (5) the mechanism of

oxidation inhibition of the boron-doped graphite is the chemical inhibition via the reduction of electron density on the surface and the number of the accessible surface active sites.

List of publications and presentations at conference:

1. Q. Wang, L. Q. Chen, and J. F. Annett, "Stability and Charge Transfer of C_3B Ordered Structures", Phys. Rev.**B54**, R2271 (1996).
2. Q. Wang, L. Q. Chen, and J.F.Annett, "Ab initio Calculation of Structural Properties of C_3B and C_5B compounds", Phys. Rev. **B55**, 8 (1996).
3. Q. Wang, X. Ma, L. Q. Chen, W. Cermignani, and C. G. Pantano, "Effect of Boron on Graphite Oxidation - A Theoretical Study", Carbon **35**, 307 (1997).
4. X. Ma, Q. Wang, L. Q. Chen, W. Cermignani, H. H.Schobert, and C. G. Pantano, "Semi-Empirical Studies on Electronic Structures of a Boron-Doped Graphene Layer - Implication on the Oxidation Mechanism", **Carbon** 35, 1517-1525 (1997).
5. Q. Wang, X. Ma, L. Q. Chen, W. Cermignani, C. G. Pantano, and H. H. Schobert, "Effect of Boron-Doping on the Electronic State of Graphite Surface and Its Implications on the Oxidation Mechanism", Oral presentation at the 23rd Biennial Conference on Carbon, State College, PA, July 14-18, 1997.
6. X. Ma, Q. Wang, L. Q. Chen, W. Cermignani, C. G. Pantano, and H. H. Schobert, "Simulation on Oxidation Process of Pure and Boron-Doped Graphite by MOPAC", Poster presentation at the 23rd Biennial Conference on Carbon, State College, PA, July 14-18, 1997.

TASK 2.2

Fiber Formation of B/C Polymers and Transformation to Carbons

Dr. Ian R. Harrison

Post-spinning Modification of Polyacrylonitrile (PAN) Precursor Fiber

John Chen

AFOSR Project

April 24, 1998

1. Introduction

The act of drawing polyacrylonitrile (PAN) precursor fibers is essentially an attempt to improve mechanical properties (particularly elastic modulus and tensile strength) through molecular orientation. In this case, optimization of PAN precursor fibers would ideally result in enhanced performance of the resulting carbon fibers for use in aerospace applications specified by the Air Force (1). Since carbon fibers generally have the inherent combination of high strength, high stiffness, and light weight, they are uniquely qualified for use in primary and secondary structural components in the aerospace industry. Specifically, the primary structures of fighter aircraft today require the use of "extremely-high-performance carbon fibers," providing the driving force to produce carbon fibers with superior mechanical properties (2).

Not surprisingly, the final mechanical properties of carbon fibers are significantly influenced by the corresponding properties of their precursors. In fact, a study has revealed what appears to be a direct correlation between the primary Young's moduli of various PAN-based precursors and the resulting carbon fibers (data values are given in Table 1.1). The plot of carbon fiber modulus (E_c) versus precursor modulus (E_p) shown in Figure 1.1 depicts a straight line passing through the origin. The average ratio of the two (E_c / E_p) was found to be about 20 (3, 4, 5). With this result in mind, it is then feasible to further improve as-received precursors by drawing them prior to stabilization in an attempt to obtain a corresponding improvement in the resulting carbon fibers.

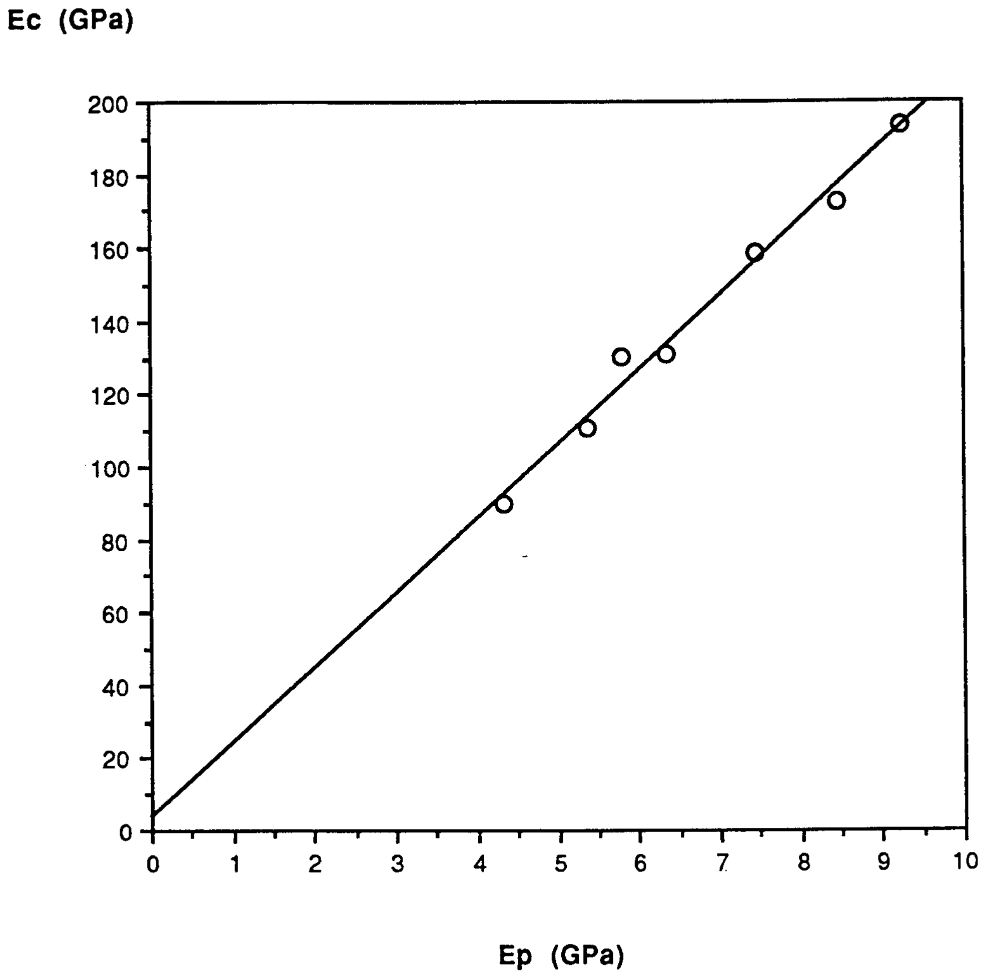

Figure 1.1: Relationship between carbon fiber and precursor modulus for various PAN-based fibers (4).

With the intention of removing surface defects and attenuating fiber diameter while simultaneously inducing molecular orientation, post-spinning modification of individual polyacrylonitrile fibers was performed using solution methods. Among the various organic and inorganic solutions tested, treatment using organic DMF offered far and away the best properties, giving a 17.5% improvement in elastic modulus and a 12.1% improvement in tensile strength over drawn, untreated PAN (73.1% and 53.1% respectively over as-received PAN).

As demonstrated in other studies (6), even unremarkable improvements in precursor properties sometimes translate into remarkable improvements in carbon fiber properties. Given the modest improvement in properties of DMF-treated PAN precursor, this possibility could not be ruled out. Carbonized SAF PAN fibers have been found to have an elastic modulus of 83.5 GPa (compared to 5.24 GPa for the as-received precursor). Keeping in mind the reported linear correlation of carbon fiber and precursor modulus, E_c / E_p for SAF PAN fibers would then be calculated to be about 16. Since DMF-treated PAN precursors gave modulus values as high as 9.07 GPa, it was thought that the corresponding carbonized fibers could provide modulus values as high as 145 GPa (a 74% improvement over regularly prepared carbon fibers) assuming that the correlation held. With this prospect in mind, the effect of carbonization on these modified fibers was investigated.

2. Experimental

Since previously drawn fibers were to be subsequently stabilized and carbonized, entire fiber tows were needed to accommodate the furnace and provide an adequate quantity of fibers for testing. Entire tows were drawn on the Instron testing apparatus (as opposed to one fiber at a time) to the desired draw ratio prior to heat treatment and subsequent tensile testing.

2.1 Drawing Fiber Tows

In preparing fiber tows for drawing, 15.5 inch (393.7 mm) lengths of tow were first cut and then secured approximately 1.5 inches (38.1 mm) from each end using epoxy putty. Tows that were to be solution treated were then saturated in the appropriate DMF solutions (30% DMF and 80% DMF) for specific times (1 min. and 10 s. respectively). Tows were then mounted into the Instron testing apparatus and environmental chamber at a gauge length of 9.5 in. (241.7 mm). Through preliminary drawing, maximum possible tow extension (just prior to failure) was predetermined for solution-treated tows. Drawing (to the appropriate extension) was then performed on tows using a 1 kN load cell and a crosshead speed of 5.00 mm/min. until sample failure.

2.2 Carbonizing Drawn Fiber Tow Samples

The difficulty in carbonizing tow samples is due not only to the 20 hour reaction required for each sample, but to the fragile nature of the carbonized sample making prompt removal of an intact specimen extremely difficult (especially for tows treated in 80% DMF). The preparatory method that has proven most effective is shown schematically in Figure 2.1. The method consists of first adding epoxy putty to the ends of the drawn tow followed by tying a Kevlar fiber and a stainless steel wire (0.006" diameter) directly into the curing epoxy at one end. The steel wire is left hanging freely outside the tube, while

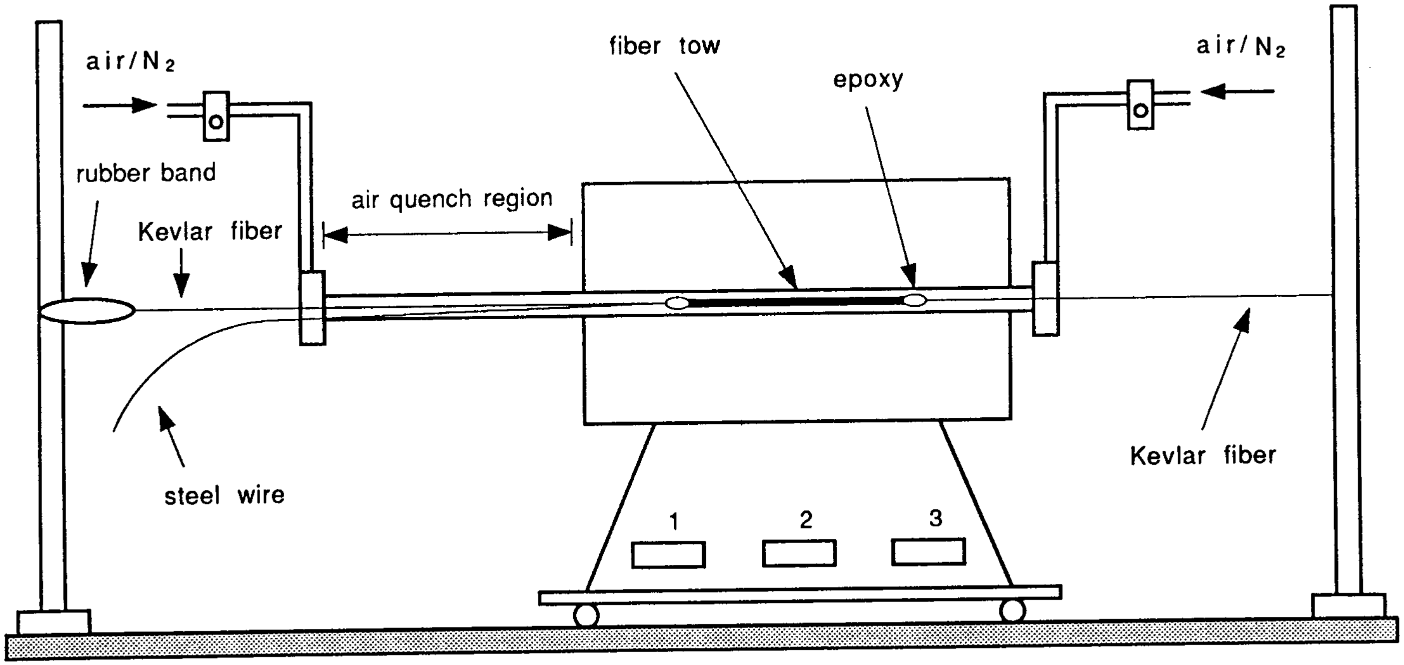
air/N_2
rubber band
Kevlar fiber
air quench region
fiber tow
epoxy
air/N_2
steel wire
1
2
3
Kevlar fiber

Figure 2.1: Furnace setup for stabilization and carbonization of fiber tows.

the Kevlar is tied to a rubber band attached to a post. At the other end, a Kevlar fiber is tied around the tow (in front of the epoxy) and also tied to the opposite post. The Kevlar fibers are intended to maintain tension as the tow shrinks during stabilization, while the rubber band allows an appropriate amount of slack when the tow is under extreme tension. The steel wire will not melt or burn off during carbonization and therefore allows easy sample removal after carbonization. The stabilization and carbonization conditions are identical to those described previously.

2.3. Tensile Testing Fiber Tow Samples

Due to their extremely fragile nature, the carbonized tows were again mounted onto modified paper tabs (cut this time from heavy-stock paper) to provide a level of stability while mounting samples into the Instron apparatus (see Figure 2.2). The tensile testing setup used was nearly identical to that shown previously for individual fibers mounted on paper tabs, except that this time a 1 kN load cell and a one inch grip distance (25.4 mm) was used. Upon loading the tensile tab in the grips of the Instron tester, the center portion of the tab was burned with a hot wire, and the sample was then subjected to a crosshead speed of 5.00 mm/min. until failure. For each sample type, three samples were selected at random and tested.

On the other hand, precursor tows were found to be inappropriate for use with paper tabs due to the observed tendency of the tows to slip during testing. As a result, precursor tow samples were prepared by cutting three-inch lengths of tow and wrapping the ends with masking tape, leaving a one-inch gauge length. Samples were then tested, again using a 1 kN load cell, a grip distance of one inch (25.4 mm), and a 5.00 mm/min. crosshead speed. For these tests, equivalent top and bottom grips were used as shown in Figure 2.3. For each sample type, three samples were selected at random and tested.

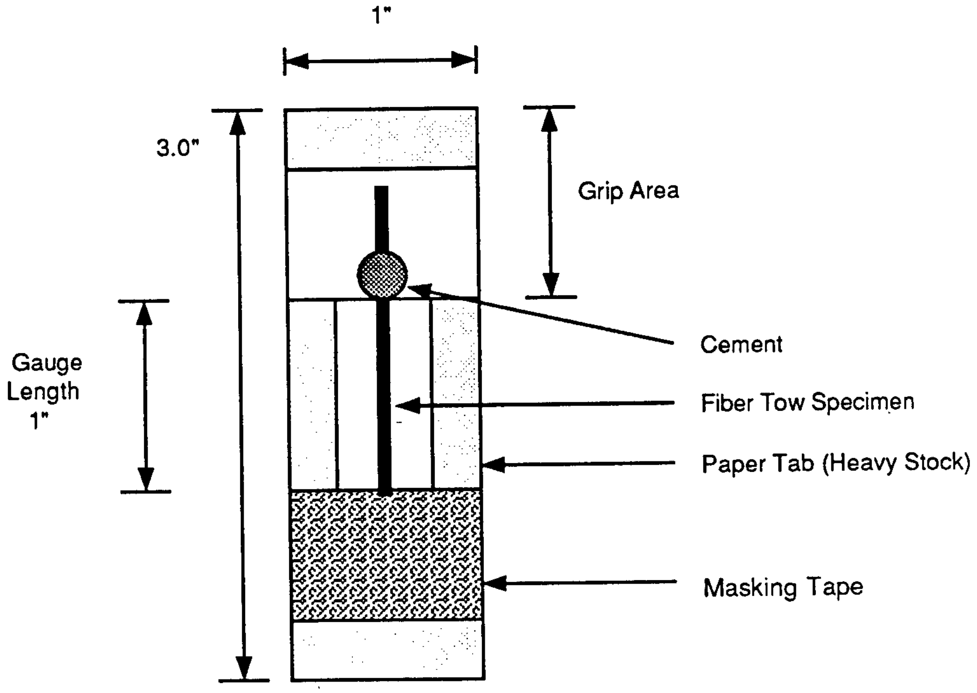
1"
3.0"
Grip Area
Gauge Length 1"
Cement
Fiber Tow Specimen
Paper Tab (Heavy Stock)
Masking Tape

Figure 2.2: Carbonized tow tensile tab.

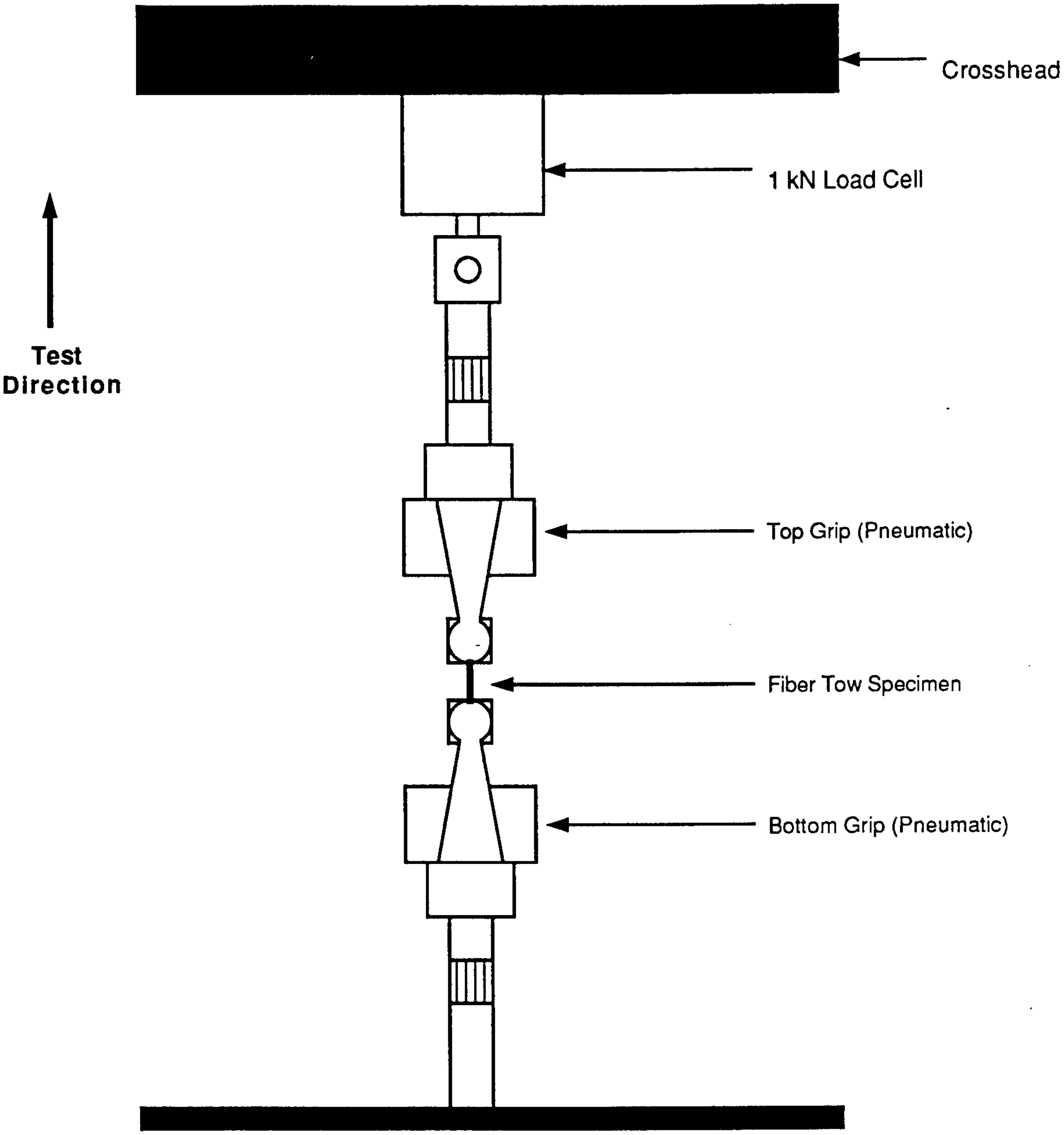
Crosshead
1 kN Load Cell
Test Direction
Top Grip (Pneumatic)
Fiber Tow Specimen
Bottom Grip (Pneumatic)

Figure 2.3: Tensile testing setup for precursor tows.

3. Results and Discussion

3.1. Individual Fibers Extracted from Drawn, Carbonized Tows

Clearly, the most ideal method of accurately determining the effects of drawing and carbonizing fibers is to do so using individual fibers (consistent with the previous precursor fiber testing using drawing tabs). However, since this method is not practical for carbonizing fibers (due to the size requirements of the furnace), the next best method is to first draw and carbonize entire tows followed by extraction of individual fibers for tensile testing (ten samples for each specimen type). In this context, a maximum solution concentration of only 30% DMF could be used because higher DMF concentrations caused the fibers in the tow to fuse together, making the removal of individual fibers impossible. Using 30% DMF, tows could be extended 14 mm, providing a maximum *tow* draw ratio of 1.06. Upon receiving this extension, tows were either immediately released from tension or maintained at this draw ratio for 30 minutes for comparison purposes. Individual fibers from these precursor or susequently carbonized tows were then mounted onto tensile tabs (one-inch slot) for testing. Results of these tests are given in Table 3.1 (in the Appendix) and in Figure 3.1. As shown in the plots, the benefit of maintaining extension for 30 minutes most clearly manifests itself in the modulus results. Although maintaining extension provides essentially no improvement in precursor modulus compared to immediate release, it does result in a 15% improvement in carbon fiber modulus (an example of unremarkable improvements in precursor fibers giving way to more notable improvements in their carbonized counterparts). In addition, the benefit of saturating fibers in 30% DMF compared to undrawn, untreated fibers is also readily apparent, providing an 81% improvement in precursor modulus and a 32% improvement in carbon fiber modulus over undrawn, untreated fibers (68% and 14% improvements in tensile strength respectively). It is also worth noting that the carbon fiber to precursor modulus ratio drops

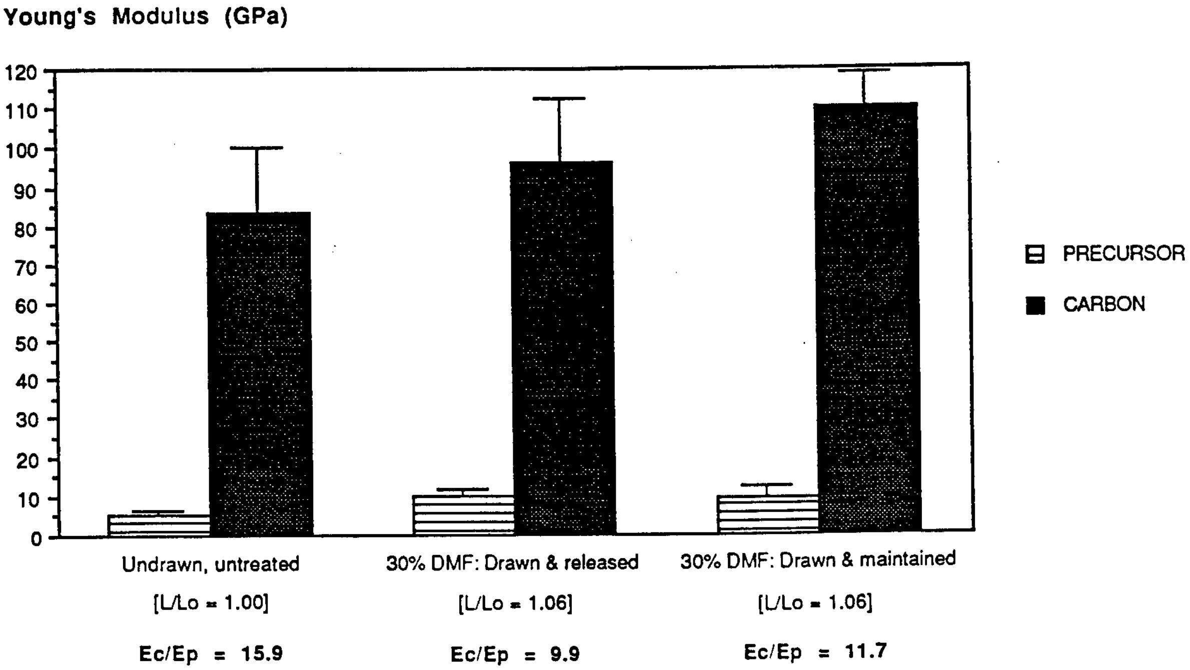
Young's Modulus (GPa)
120
110
100
90
80
70
60
50
40
30
20
10
0
PRECURSOR
CARBON
Undrawn, untreated
[L/Lo = 1.00]
Ec/Ep = 15.9
30% DMF: Drawn & released
[L/Lo = 1.06]
Ec/Ep = 9.9
30% DMF: Drawn & maintained
[L/Lo = 1.06]
Ec/Ep = 11.7

(a)

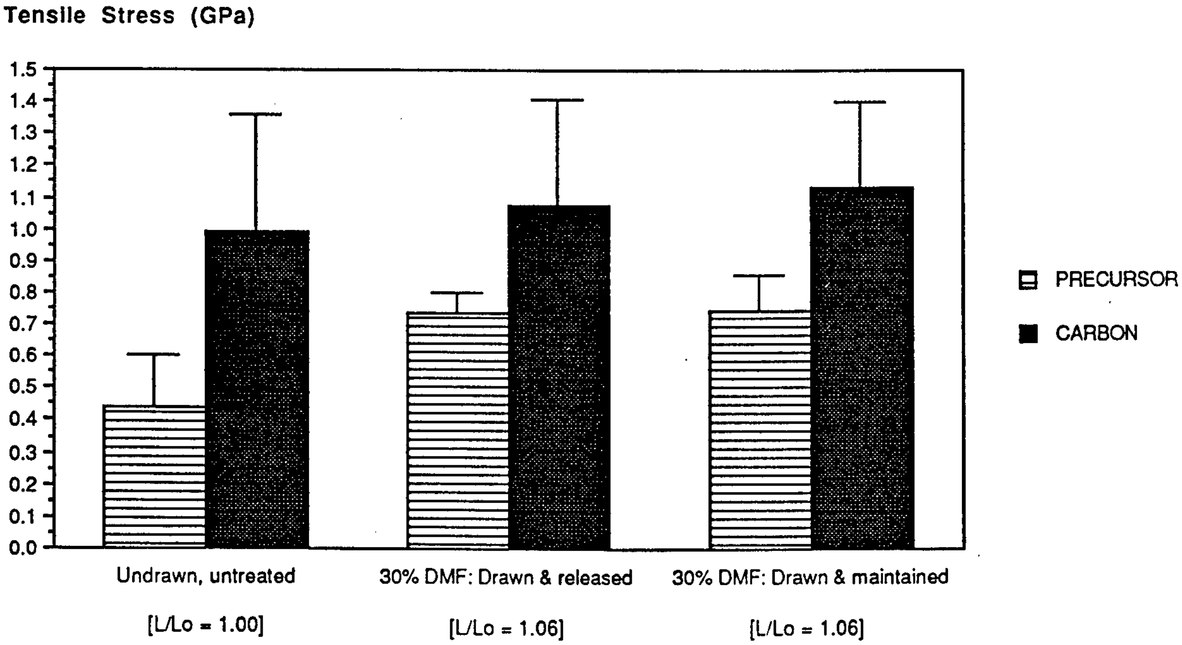
Tensile Stress (GPa)
1.5
1.4
1.3
1.2
1.1
1.0
0.9
0.8
0.7
0.6
0.5
0.4
0.3
0.2
0.1
0.0
PRECURSOR
CARBON
Undrawn, untreated
[L/Lo = 1.00]
30% DMF: Drawn & released
[L/Lo = 1.06]
30% DMF: Drawn & maintained
[L/Lo = 1.06]

(b)

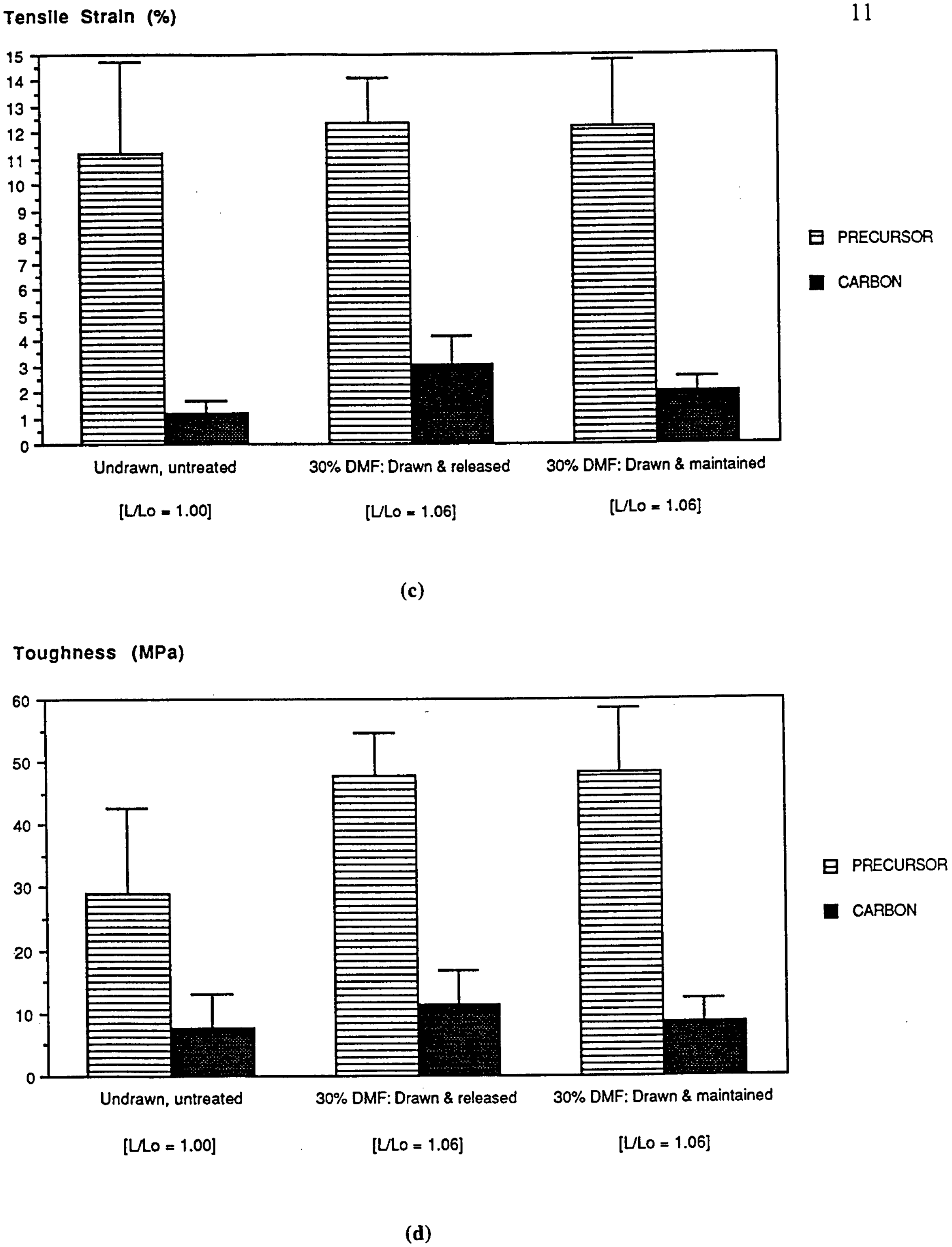

Figure 3.1: Tensile results for individual precursor and carbonized fibers extracted from drawn tows

(a) elastic modulus

(b) tensile stress

(c) tensile strain

(d) toughness.

slightly with treatment in 30% DMF, implying that any correlation between E_c and E_p is not likely to be linear for DMF-treated fibers as shown in Figure 3.2.

3.2. Tensile Test Results of Tows

The fact remains that when tested individually, precursor PAN fibers show the best properties when treated in 80% DMF for ten seconds at 100 °C. However, as mentioned earlier, obtaining test results from the corresponding individual carbon fibers is extremely difficult (if not impossible) due to both the scale of the carbonization process and the tendency of tow fibers to fuse together into a single strand upon solution treatment in high DMF concentration. It was believed that individual fiber properties should be able to translate to corresponding tow properties. As a result, an attempt was made to actually tensile test entire tows of fibers with the underlying objective of assessing the properties of carbonized fibers that were initially treated in 80% DMF.

In preparing drawn tows, a maximum draw ratio of 1.06 (maximum extension of 14 mm) could be given to tows treated in 30% DMF (for one minute at 80 °C), while a maximum draw ratio of 1.07 (maximum extension of 18 mm) could be given to tows treated in 80% DMF (for ten seconds at 100 °C). In comparison, the maximum draw ratios for individually drawn fibers tended to be considerably larger (e.g., as described previously, individual fibers treated in 80% DMF could be given a draw ratio of 1.20). Upon extension, tows were maintained at the appropriate draw ratio for 30 minutes before release.

Before tensile tests could be conducted, an accurate measure of tow diameter was needed to ensure reliable tensile results. To first estimate the number of fibers per tow, the maximum load was measured from an average of five untreated, undrawn precursor tows to be 257.7 (± 19.9) N. This value was then divided by the average maximum load for

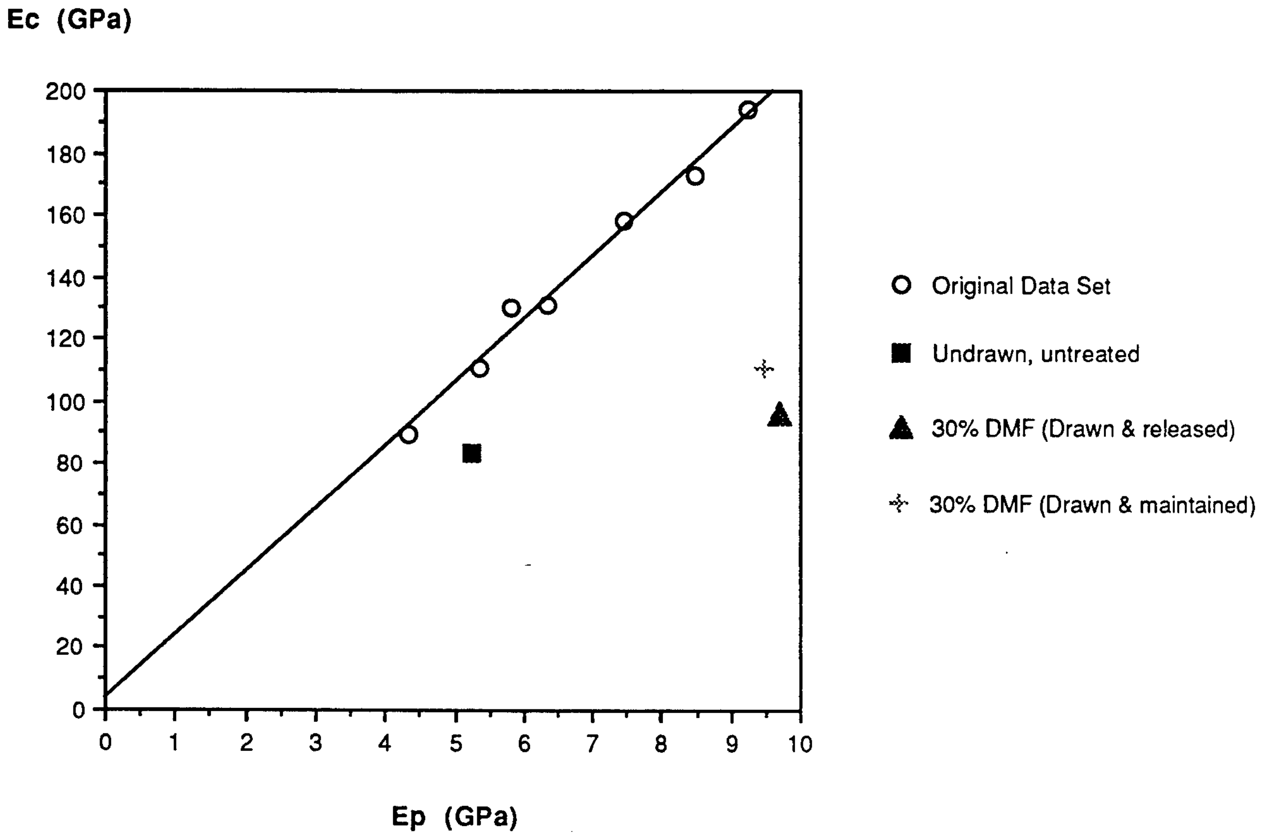

Figure 3.2: Properties of individual fibers extracted from drawn tows compared to original E_c v. E_p data.

individual fibers, determined previously to be 0.0467 (± 0.0164) N for precursor PAN (Series 1). The resulting estimated number of fibers per tow was then calculated to be ~ 5520, which is closely approximates the ~ 6000 fibers/tow value originally specified by Courtaulds.

Then, considering the overall tow cross-sectional area:

$$A_o = \pi R_o^2 = (\pi D_o^2) / 4$$

where A_o = initial cross-sectional area of the tow

R_o = initial radius of the tow

and D_o = initial diameter of the tow.

Therefore, $D_o = (4A_o / \pi)^{1/2}$.

Now consider A_o = (# of fibers / tow) x a_o = (# of fibers / tow) x $(\pi d_o^2) / 4$

where a_o = initial cross-sectional area of an individual fiber

and d_o = initial diameter of an individual fiber.

Therefore, through substitution:

$$\mathbf{D_o = [(\# \text{ of fibers } / \text{ tow}) \times d_o^2]^{1/2}.}$$

When considering untreated precursor, individual fiber diameter (d_o) was measured to be 11.8 µm (Series 1), resulting in a calculated initial tow diameter (D_o) of 0.877 mm (877 µm). Likewise, for carbonized fibers, individual fiber diameter (d_o) was measured to be 8.5 µm (Series 3), giving a calculated initial tow diamter of 0.632 mm (632 µm).

From these initial tow diameters, a final diameter, D (after treatment and drawing), could be calculated for precursor and carbon fibers (i.e., untreated, undrawn; 30% DMF, saturated 1 min., drawn @ 80 °C; and 80% DMF, saturated 10 s., drawn @ 100 °C) by considering respective draw ratios:

$$(L / L_o) = (D_o / D)$$

therefore $$D = (L_o / L) \times D_o.$$

Calculated final tow diameters are provided in Table 3.2.

Results of the tensile tests are given in Table 3.2 and the plots in Figure 3.3. General trends appear to be reversed from those observed previously for individually drawn fibers and individual fibers extracted from drawn tows. Here, higher draw ratios in higher solution concentrations result in overall decreases in elastic modulus, tensile strength, tensile strain, and toughness for both precursor and carbon fibers.

These observed trends may indicate a tendency of fiber tows (on a macroscopic scale) to form a skin-core morphology that is not readily apparent in individual fibers (on a microscopic scale). In other words, beyond a certain extension, there may be the continued formation and extension of an outer oriented sheath surrounding a less oriented core. The presence of this comparatively unoriented core may in fact explain why properties do not *increase* with increasing draw ratio and solution concentration, but it does not in itself explain the consistent decrease in properties.

The decrease is likely to be due to the introduction of flaws in the surface of the drawn tow fibers or the formation of internal voids, which may be much more difficult to control on this macroscopic scale. Surface flaws and internal voids would clearly act as stress concentrators, significantly limiting the corresponding tensile properties. The resulting stress concentrations would be magnified in carbonized tows due to their extremely brittle

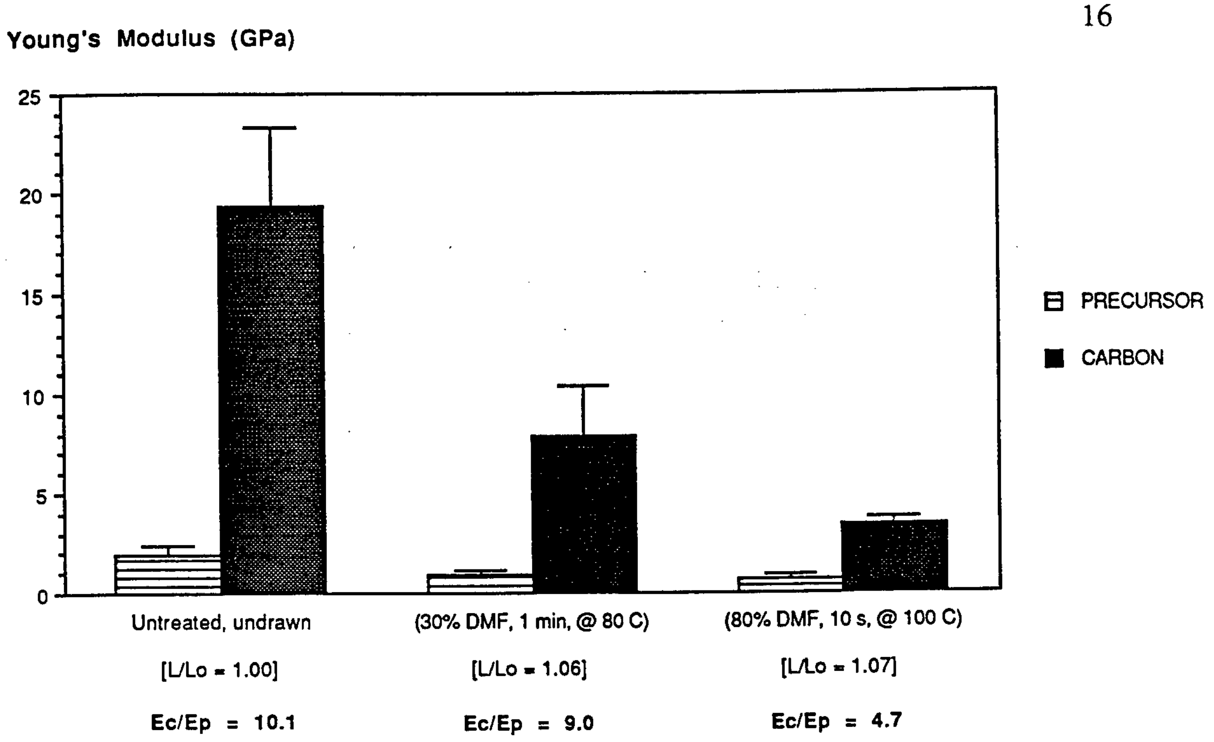
Young's Modulus (GPa)
25
20
15
10
5
0
▤ PRECURSOR
■ CARBON
Untreated, undrawn
[L/Lo = 1.00]
Ec/Ep = 10.1
(30% DMF, 1 min, @ 80 C)
[L/Lo = 1.06]
Ec/Ep = 9.0
(80% DMF, 10 s, @ 100 C)
[L/Lo = 1.07]
Ec/Ep = 4.7

(a)

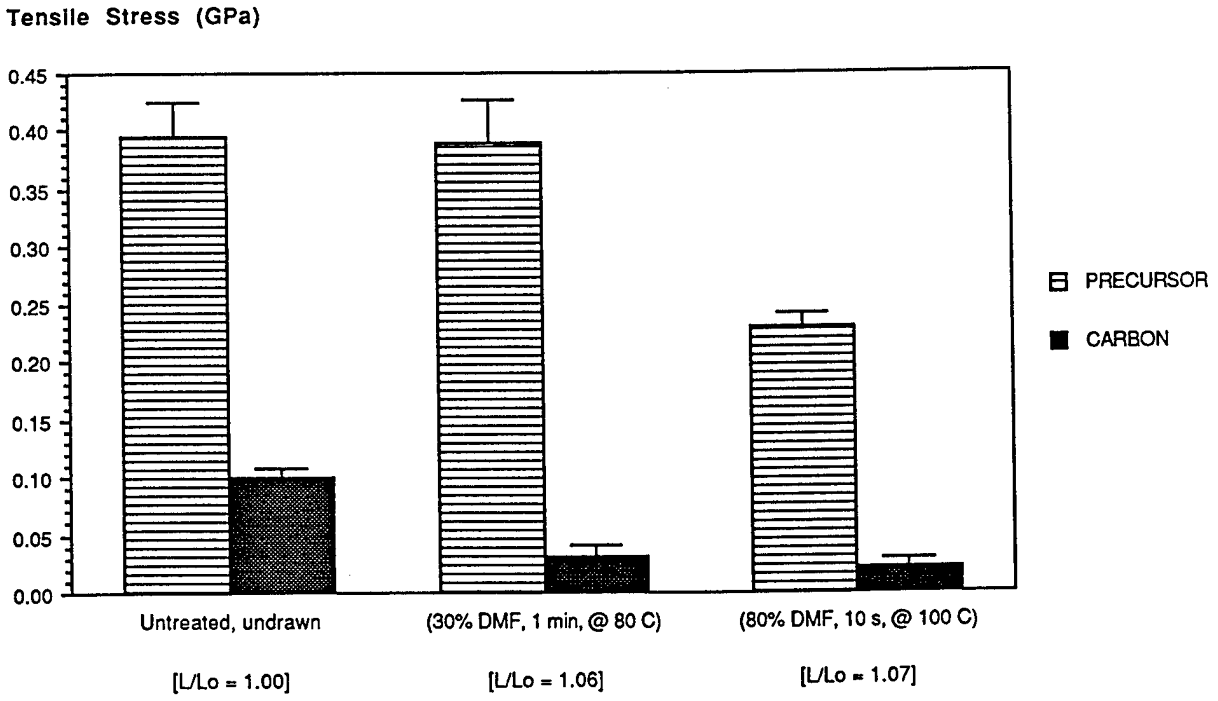
Tensile Stress (GPa)
0.45
0.40
0.35
0.30
0.25
0.20
0.15
0.10
0.05
0.00
▤ PRECURSOR
■ CARBON
Untreated, undrawn
[L/Lo = 1.00]
(30% DMF, 1 min, @ 80 C)
[L/Lo = 1.06]
(80% DMF, 10 s, @ 100 C)
[L/Lo = 1.07]

(b)

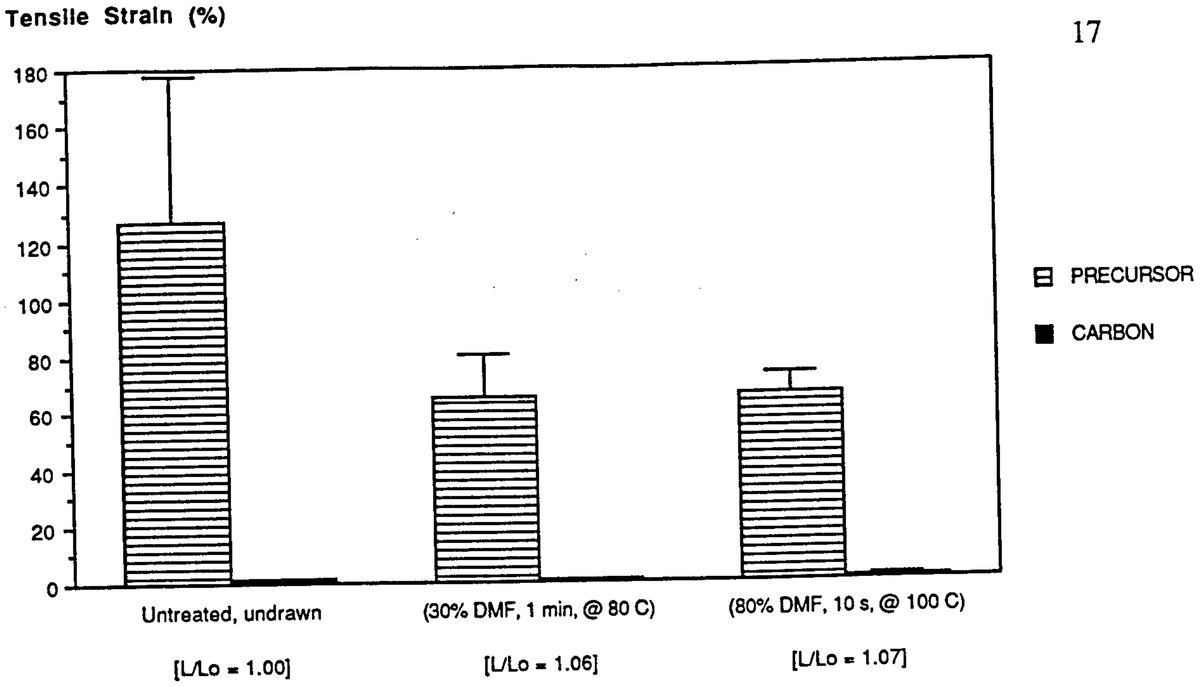

(c)

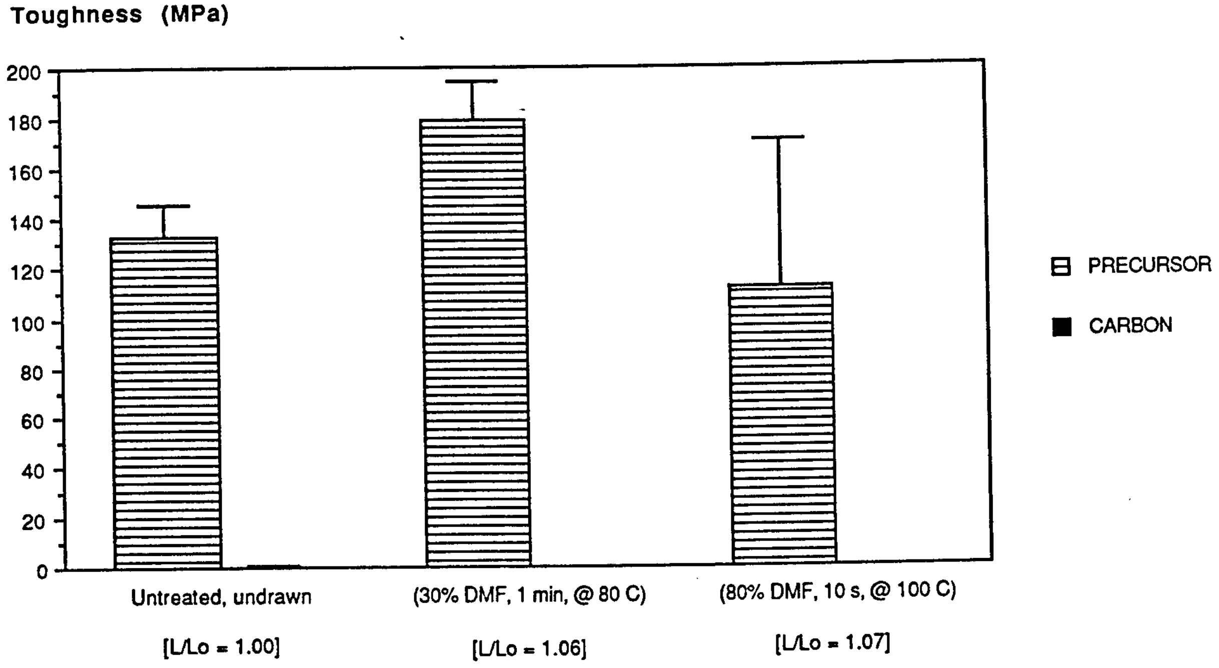

(d)

Figure 3.3: Tensile results for precursor and carbonized tows initially drawn in various DMF concentrations

(a) elastic modulus

(b) tensile stress

(c) tensile strain

(d) toughness.

and fragile nature. This possibility seems to be validated by the tensile strength results for the tows. Here, tensile strength values are dramatically lower for carbonized tows than for the corresponding precursor tows (contrary to previous results for fibers tested individually). These results are at least consistent with the hypothesis that tensile strength is severely limited by the presence of both internal and external defects. Likewise, while precursor values for strain and toughness are still higher than the carbon values (consistent with the results for individually tested fibers), here the carbon values are much lower in comparison (barely showing up on the given plots).

Another thing to consider is that for the standardized method for single filament testing, it is specified (ASTM D 3379-75) that the aspect ratio (L / D) for the fiber sample be greater than or equal to 2000. The previously reported results for individual fibers (mounted on paper tabs) meet this requirement handiliy (L / D = 25.4 mm / 0.0118 mm = 2150 for PAN precursor; L / D = 25.4 mm / 0.0085 mm = 2988 for carbon fibers). However, for the *tows* that were tested, the aspect ratio was two orders of magnitude lower than 2000 out of necessity (L / D = 25.4 mm / 0.877 mm = 29.0 for PAN precursor tow; L / D = 25.4 mm / 0.632 mm = 40.2 for carbonized tow). A tow aspect ratio even approaching 2000 is far beyond the scale and capabilities of the Instron testing apparatus. The establishment of this aspect ratio requirement was conceivably a direct effort to limit the relative size of individual flaws or defects per unit length.

3.2.1. E_c *v.* E_p

When considering E_c as a function of E_p for these tows, the existence of linearity cannot be argued (at least not to the extent that the values are in line with those reported for individual fibers). As shown in Figure 3.4, data points for the tows do not approach the original linear correlation values. When considering the results reported for untreated and solution treated tows and fibers alone (as shown in Figure 3.5), it might be argued that they

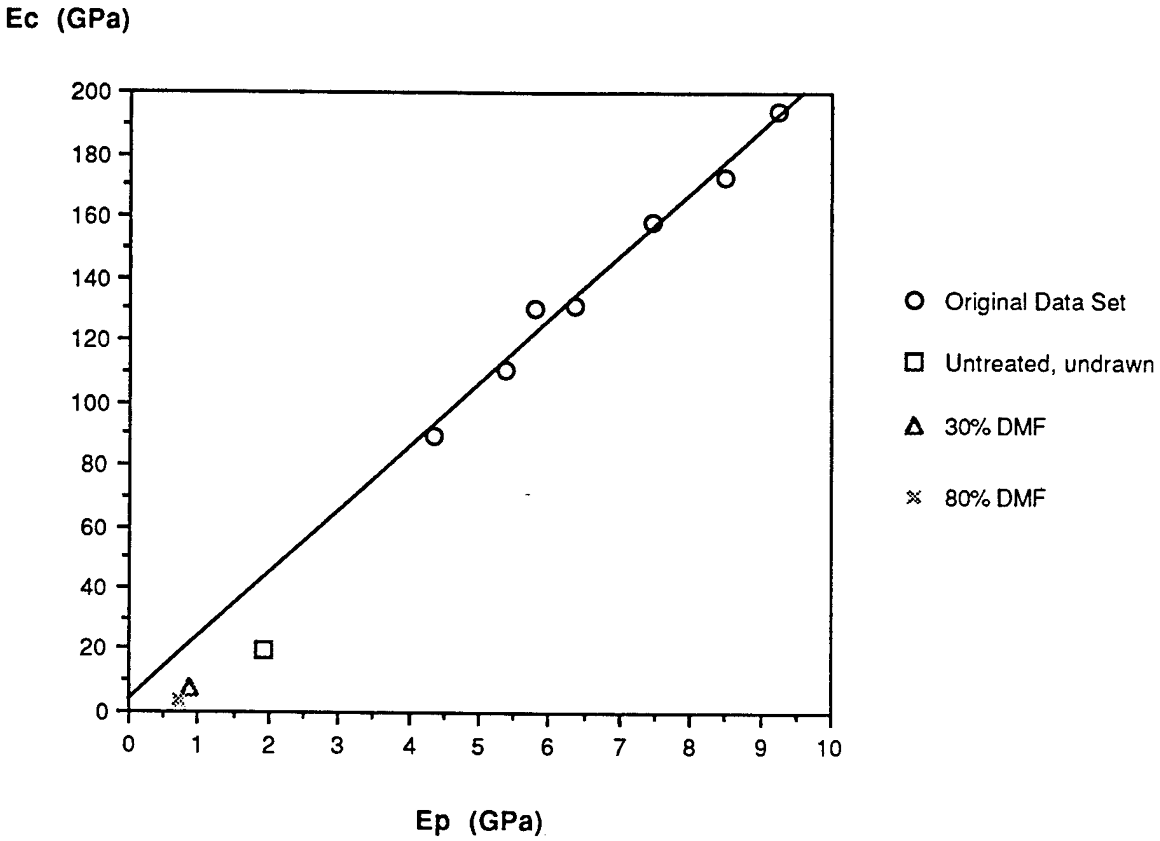

Figure 3.4: Properties of drawn tows compared to original E_c v. E_p data.

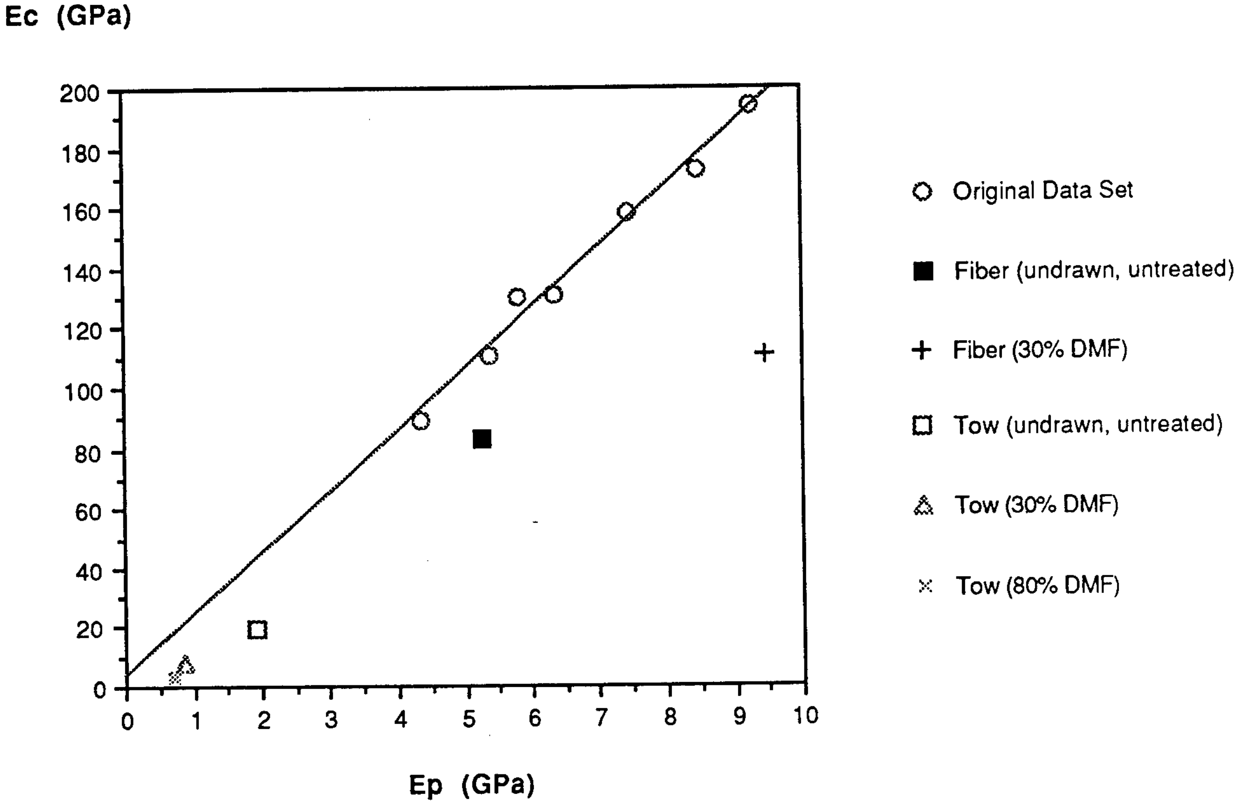

Figure 3.5: Consolidation of individual fiber and tow properties compared to original E_c v. E_p data.

follow their own consistent E_c v. E_p correlation, however, additional data would be needed to be more conclusive.

3.2.2. Morphological Observations

Scanning electron microscopy was conducted on various tow samples in an effort to illustrate how solution modification and carbonization can affect the observed properties of fiber tows. Taking an untreated, undrawn PAN tow, the micrograph in Figure 3.6 clearly shows that individual precursor fibers remain separated while carbonized fibers show a greater tendency to adhere to one another. More intriguing structural features manifest themselves with modification in 80% DMF solution.

As shown in Figure 3.7, solution modification in 80% DMF (saturated 10 s., drawn @ 100 °C) clearly causes the individual PAN fibers to partially dissolve and fuse together. At higher magnifications, some interesting "rippled" textures are evident, probably a remnant of precursor fibers that were twisted in the plane. These twisted fibers may in fact have contributed to the observed decreases in precursor strain and toughness with solution modification (see Figure 3.3), acting as entanglements and therefore limiting factors for extensibility (e.g., $L / L_o = 1.07$ for this tow compared to 1.20 for individual fiber).

Carbonization of these tows greatly facilitates the introduction of surface flaws (as shown in Figure 3.8 (a)) that would severly limit properties like tensile strength, strain, and toughness. Other carbonized tows (that were preferentially tensile tested) do not show such obvious surface defects as shown in Figure 3.8 (b) and (c), but the tensile properties were limited nonetheless (as previously observed in Figure 3.3). It is worth noting that in some cases, the twisted fibers observed for the precursor tows remained apparent in the carbonized tows (as shown in Figure 3.8 (d)).

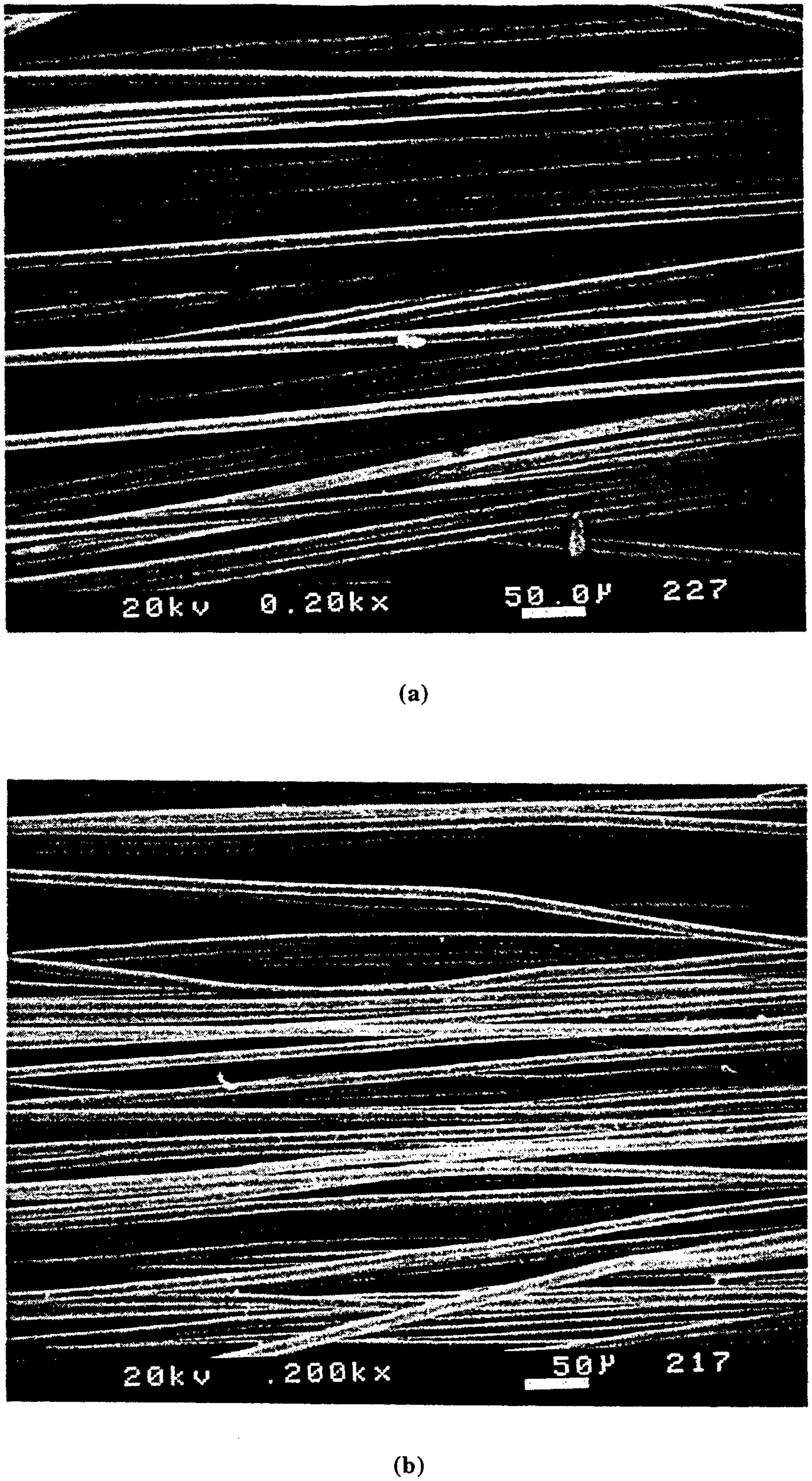
20kv 0.20kx 50.0µ 227
(a)
20kv .200kx 50µ 217
(b)

Figure 3.6: SEM micrographs of undrawn PAN fiber tows (200X magnification)
(a) precursor
(b) carbonized.

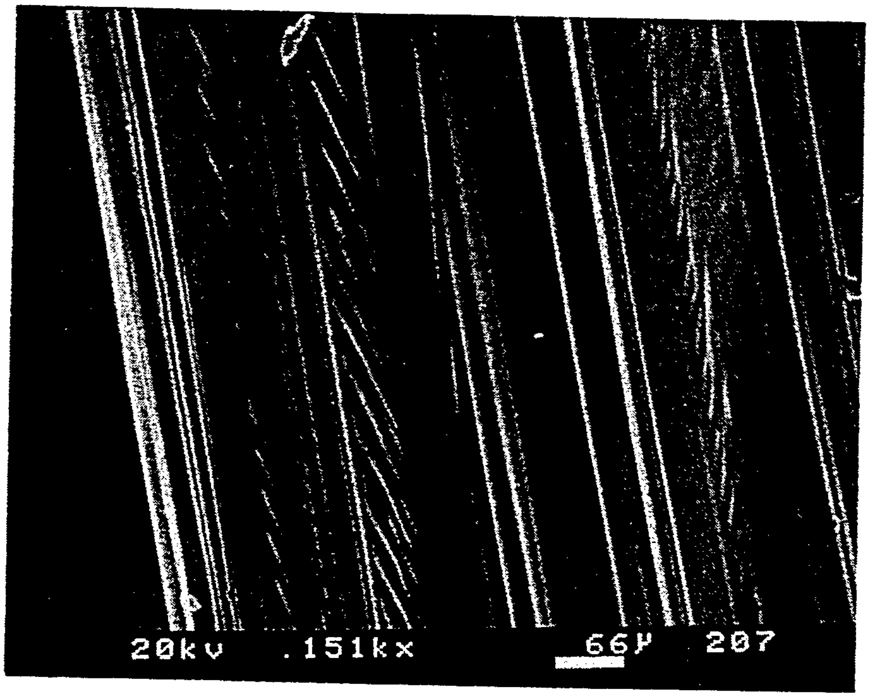
20kv .151kx
66μ 207

(a)

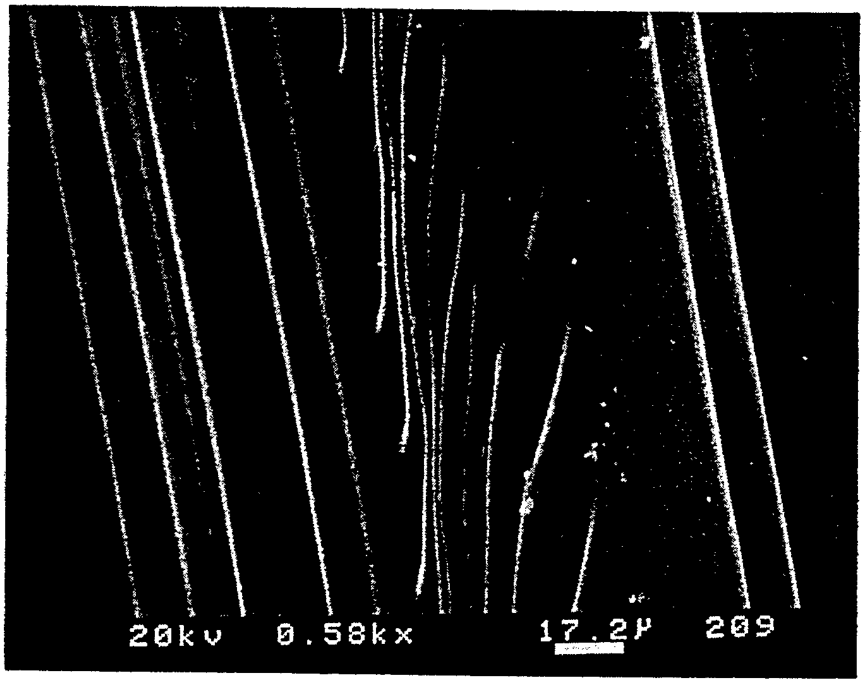
20kv 0.58kx
17.2μ 209

(b)

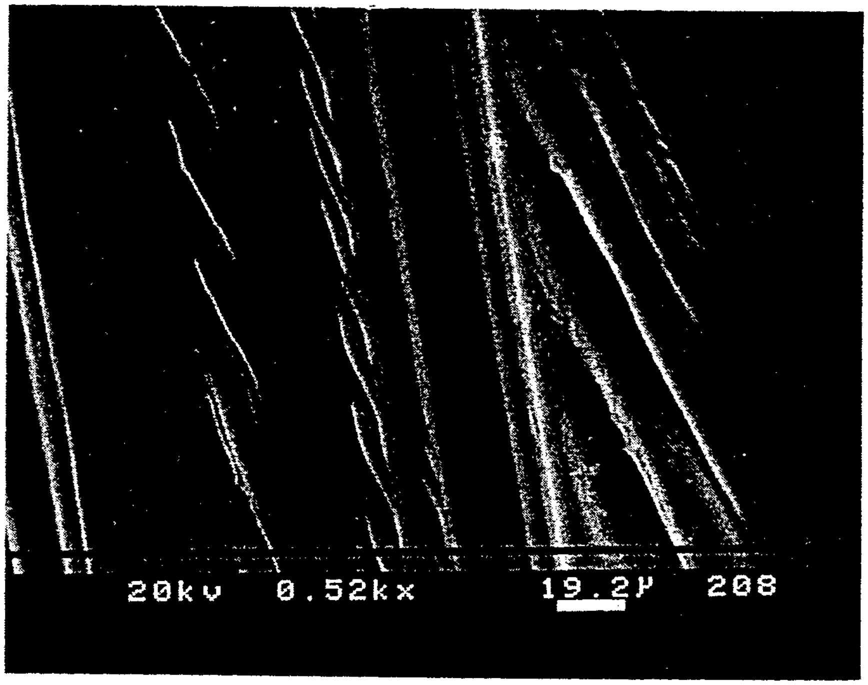
20kv 0.52kx
19.2µ 208

(c)

Figure 3.7: SEM micrographs of PAN precursor tow modified in 80% DMF (saturated 10 s., drawn @ 100 °C).

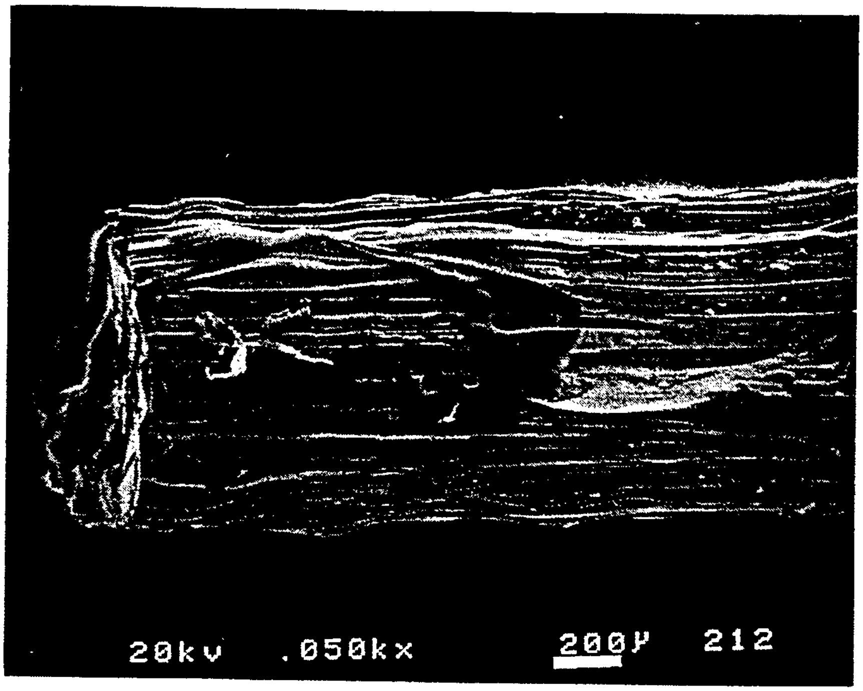
20kv .050kx 200μ 212

(a)

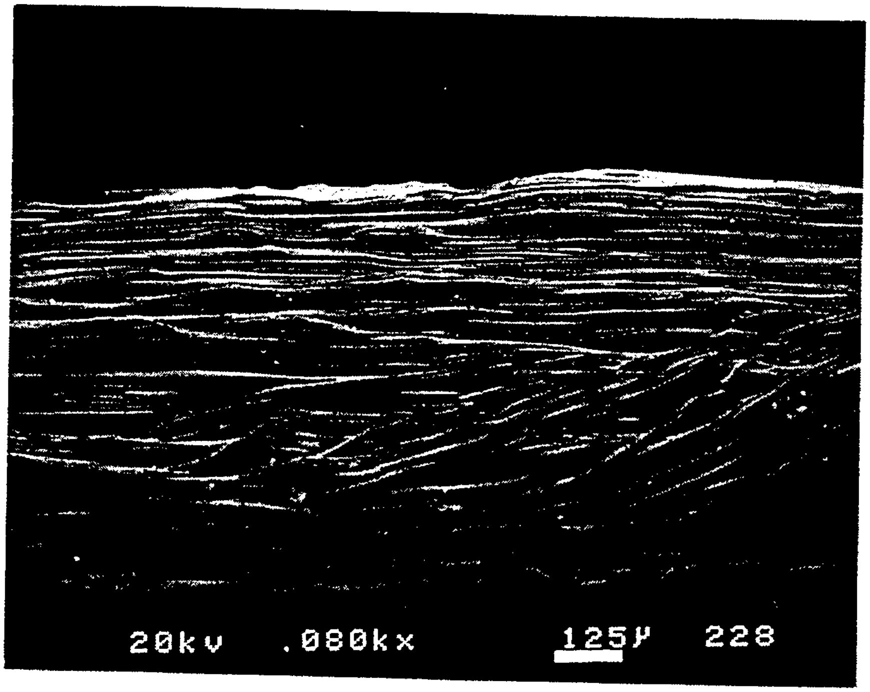
20kv .080kx 125μ 228

(b)

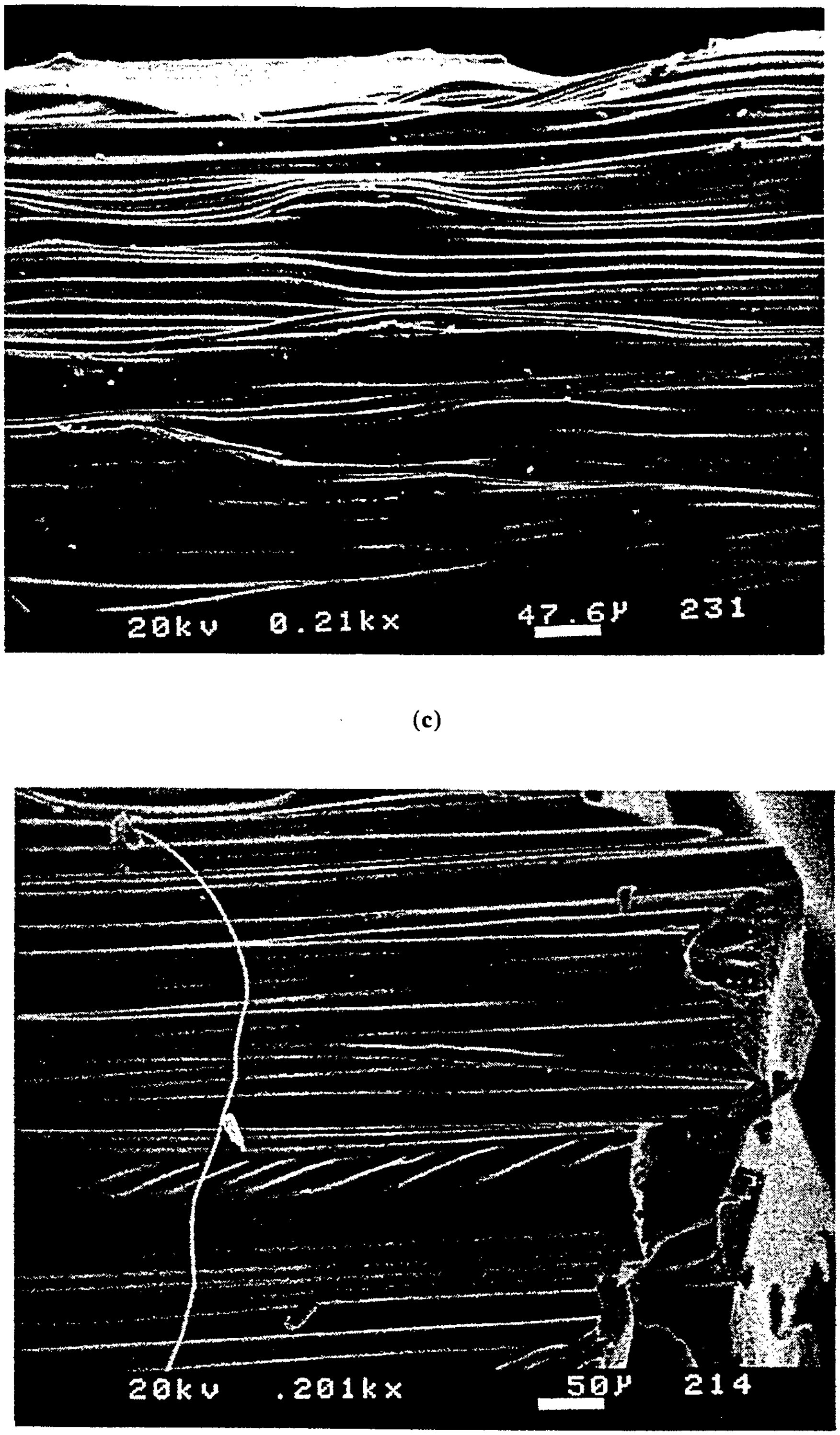
20kv 0.21kx 47.6µ 231
20kv .201kx 50µ 214

(c)

(d)

Figure 3.8: SEM micrographs of carbonized PAN tow initially modified in 80% DMF (saturated 10 s., drawn @ 100 °C).

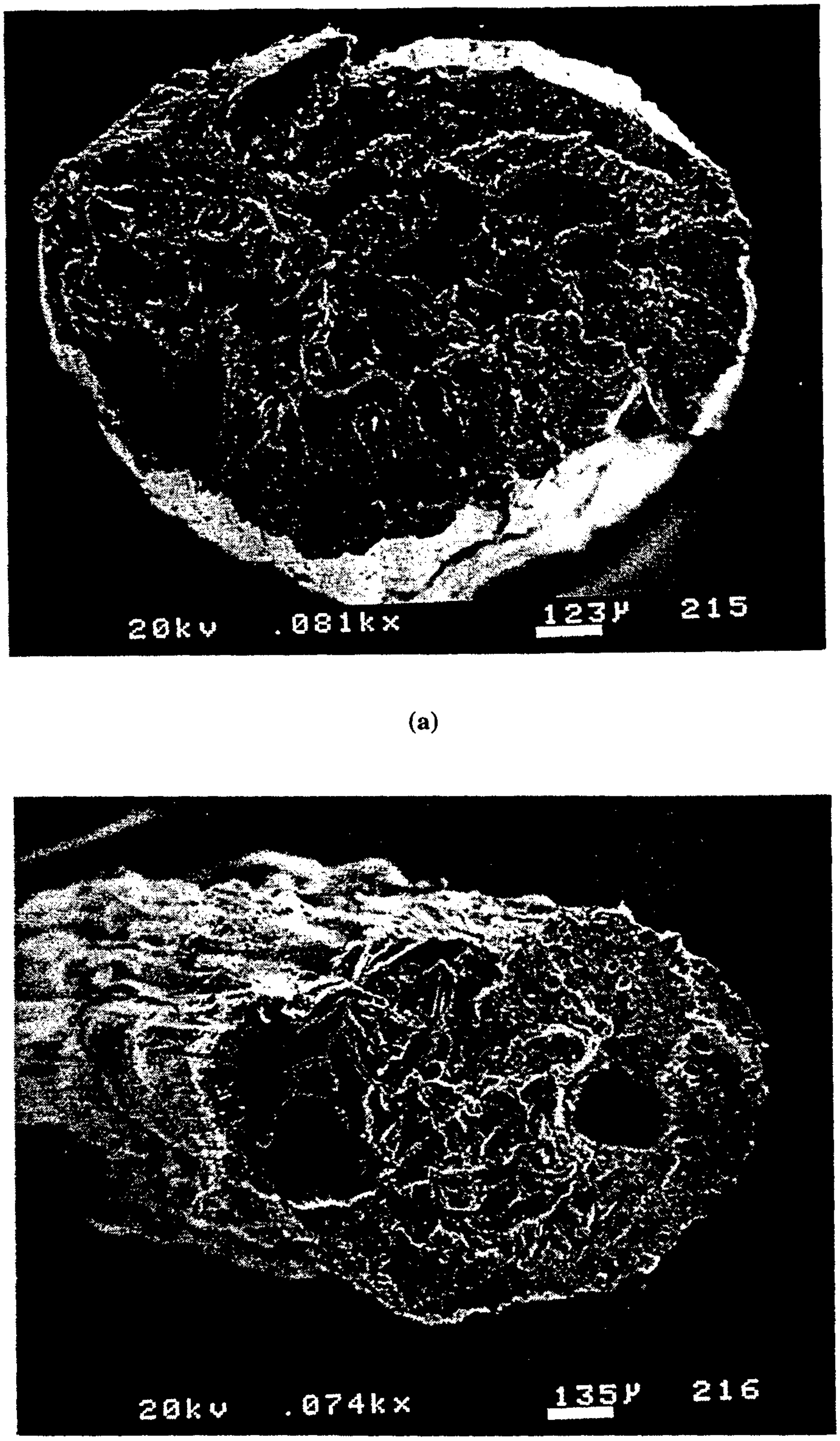
20kv .081kx 123μ 215
20kv .074kx 135μ 216

(a)

(b)

Figure 3.9: Cross-sectional view of PAN tows initially modified in 80% DMF (saturated 10 s., drawn @ 100 °C)

(a) precursor

(b) carbonized.

Focusing on the cross-sectional area of the solution-treated tows revealed a number of property-limiting features (as shown in Figure 3.9). The precursor tow sample shows the expected presence of internal voids, which limit properties such as tensile strength. Likewise, the carbonized tow sample shows two very prominent voids accompanied by numerous smaller voids which can again account for the decrease in tensile strength compared to untreated, undrawn fibers (Figure 3.3). Furthermore, close observation of the carbon tow cross-section verifies the presence of a skin-core morphology. Despite the successful formation of an oriented skin, the presence of the unoriented core in combination with bulk and surface flaws would be enough to deny any anticipated improvements in tow tensile properties. Such improvements would therefore seem limited to individually treated, individually drawn fibers.

4. Summary and Conclusions

In an effort to observe how individual precursor fiber properties translate into carbon fiber properties, entire fiber tows were drawn and tested to allow the possibility of carbonization in the tube furnace. In this context, sample preparation and testing was approached in two ways: first by solution-treating and drawing followed by extraction and tensile testing of individual fibers, and second by sequentially solution-treating, drawing, *and* tensile testing entire fiber tows. Results indicated that the former method is preferable over the latter, providing the anticipated increase in properties like elastic modulus and tensile strength (for precursor *and* carbon fibers) when 30% DMF solution is used. The latter method gave the counterintuitive result of decreasing modulus and tensile strength with increasing solution concentration. Scanning electron microscopy (SEM) analysis suggested that this outcome may have been the direct result of entanglements, surface flaws, internal voids, and a skin-core morphology, all of which were observed in the fiber tows. The effects of these features, while relatively benign in a large L / D scale (i.e., L / D

≥ 2000), appear to assert themselves when smaller L / D scales are used (in this case L / D << 2000).

References

1. E. Fitzer, *Carbon*, **27**, 621 (1989).
2. R.B. Mathur, O.P. Bahl, and J. Mittal, *Compos. Sci. Technol.*, **51**, 223 (1994).
3. A.K. Gupta, D.K. Paliwal, and P. Bajaj, *JMS - Rev. Macromol. Chem. Phys.*, **C31** (**1**), 1 (1991).
4. S.S. Chari, O.P. Bahl, and R.B. Mathur, *Fib. Sci. Technol.*, **15**, 153 (1981).
5. P.H. Wang, J. Liu, and R.Y. Li, *J. Appl. Polym. Sci.*, **52**, 1667 (1994).
6. O.P. Bahl, R.B. Mathur, and T.L. Dhami, *Mater. Sci. Eng.*, **73**, 105 (1985).

Appendix

Table 1.1: Elastic Moduli for a Variety of Precursor Fibers and Corresponding Carbon Fibers (4).

Fiber Type	**E_p (GPa)**	**E_c (GPa)**
sample 1	4.34	89.7
sample 2	5.38	111.0
sample 3	5.81	130.3
sample 4	6.34	131.0
sample 5	7.45	158.6
sample 6	8.48	172.4
sample 7	9.24	193.8

Table 3.1: Tensile Results for Individual Fibers (Extracted from Drawn, Carbonized Tows).

Fiber Type	**Fiber Diameter (mm)**	**Max. Load (N)**	**Tensile Stress (GPa)**	**Young's Modulus (GPa)**	**% Strain @ Max. Load (%)**	**Toughness (MPa)**
Series 1 *Precursor PAN* *Undrawn, untreated* *[L/Lo = 1.00]*	0.0118 (0.0007)	0.0467 (0.0164)	0.441 (0.163)	5.24 (1.43)	11.2 (3.6)	29.1 (13.6)
Series 3 *Carbonized PAN* *Undrawn, untreated* *[L/Lo = 1.00]*	0.0085 (0.0003)	0.0564 (0.0212)	0.993 (0.366)	83.5 (16.9)	1.15 (0.54)	7.79 (5.26)
Series 13 *Precursor PAN* *Drawn (14.0 mm)* *& released @ 80 °C* *(1 min., 30% DMF)* *[L/Lo = 1.06]*	0.0110 (0.0007)	0.0692 (0.0096)	0.733 (0.064)	9.70 (1.89)	12.4 (1.7)	47.9 (6.8)
Series 12 *Carbonized PAN* *Drawn (14.0 mm)* *& released @ 80 °C* *(1 min., 30% DMF)* *[L/Lo = 1.06]*	0.0083 (0.0004)	0.0577 (0.0171)	1.074 (0.331)	95.9 (16.6)	3.04 (1.13)	11.4 (5.3)
Series 14 *Precursor PAN* *Drawn (14.0 mm)* *& maintained @ 80 °C* *(1 min., 30% DMF)* *[L/Lo = 1.06]*	0.0114 (0.0011)	0.0751 (0.0091)	0.739 (0.115)	9.46 (2.53)	12.3 (2.6)	48.4 (10.1)
Series 15 *Carbonized PAN* *Drawn (14.0 mm)* *& maintained @ 80 °C* *(1 min., 30% DMF)* *[L/Lo = 1.06]*	0.0089 (0.0005)	0.0694 (0.0128)	1.135 (0.263)	110.3 (8.8)	2.02 (0.56)	8.57 (3.55)

Table 3.2: Tensile Results for Fiber Tows.

Fiber Type	**Fiber Diameter (mm)**	**Max. Load (N)**	**Tensile Stress (GPa)**	**Young's Modulus (GPa)**	**% Strain @ Max. Load (%)**	**Toughness (MPa)**
Precursor PAN Undrawn, untreated [L/Lo = 1.00]	0.877	239.0 (17.7)	0.3956 (0.0293)	1.92 (0.48)	126.6 (51.2)	132.9 (12.7)
Carbonized PAN Undrawn, untreated [L/Lo = 1.00]	0.632	31.2 (3.0)	0.0996 (0.0094)	19.3 (4.0)	1.69 (0.23)	0.409 (0.044)
Precursor PAN Drawn (14.0 mm) @ 80 °C (1 min., 30% DMF) [L/Lo = 1.06]	0.827	209.1 (20.0)	0.3893 (0.0372)	0.880 (0.228)	65.4 (14.7)	179.2 (15.8)
Carbonized PAN Drawn (14.0 mm) @ 80 °C (1 min., 30% DMF) [L/Lo = 1.06]	0.596	8.82 (2.48)	0.0316 (0.0089)	7.89 (2.41)	0.799 (0.170)	0.089 (0.076)
Precursor PAN Drawn (18.0 mm) @ 100 °C (10 s., 80% DMF) [L/Lo = 1.07]	0.820	121.8 (5.9)	0.2306 (0.0112)	0.711 (0.253)	65.9 (6.7)	112.6 (58.8)
Carbonized PAN Drawn (18.0 mm) @ 100 °C (10 s., 80% DMF) [L/Lo = 1.07]	0.591	5.90 (2.05)	0.0215 (0.0075)	3.37 (0.36)	1.04 (0.25)	0.071 (0.053)

ATTACHMENT III

Papers (f, g)

Pergamon

Carbon Vol. 34, No. 11, pp. 1427–1445, 1996
Copyright © 1996 Elsevier Science Ltd
Printed in Great Britain. All rights reserved
0008-6223/96 $15.00 + 0.00

PII: S0008-6223(96)00094-2

NEW ASPECTS IN THE OXIDATIVE STABILIZATION OF PAN-BASED CARBON FIBERS

A. GUPTA* and I. R. HARRISON†
Department of Materials Science and Engineering, The Pennsylvania State University, University Park, PA 16802, U.S.A.

(*Received* 14 *February* 1996; *accepted in revised form* 23 *May* 1996)

Abstract—Oxidative stabilization studies on PAN-based copolymer fibers indicate the presence of at least two distinct reactions occurring at temperatures below 380°C. Techniques such as thermal stress, percentage shrinkage, differential scanning calorimetry, wide-angle X-ray diffraction and small-angle X-ray scattering have been used to elucidate the mechanisms involved. Reactions initiate in the amorphous part of the copolymer at temperatures below 200°C and contribute to the major portion of the macroscopic shrinkage. This corresponds to the first "amorphous" peak observed in DSC. Crystalline morphology is largely maintained during this stage, although considerable randomization of crystal lamellae take place. Reactions propagate to crystalline components at higher temperatures and proceed to completion at ~380°C, giving rise to the second "crystalline" DSC peak. Additionally, a broad shoulder on the second peak is observed. Although its origin is not clear, it is speculated that it corresponds to certain intermolecular cross-linking reactions. The importance of using copolymer PAN as a carbon fiber precursor is outlined. Additionally, new models for morphological development during stabilization are proposed. Macroscopic shrinkage along the fiber axis is seen to be primarily an entropy-driven process, with "chemical" effects serving to only modify the entropic response. Intramolecular cyclization reactions serve as the basis for initial stabilization, with intermolecular cross-linking occurring in the presence of oxygen above ~300°C for oxidatively stabilized fibers. Copyright © 1996 Elsevier Science Ltd

Key Words—PAN, carbon fibers, oxidative stabilization.

1. INTRODUCTION

Carbon-fiber reinforced composites have today established their importance in the area of "lighter but stronger" materials. In addition they possess other properties which make them otherwise unique. They are elastic to failure at normal temperatures, making them creep- and fatigue-resistant, have excellent damping characteristics, are chemically inert even at high temperatures (except in strongly oxidizing environments and in contact with certain molten metals), and have excellent thermophysical properties. This blend of properties has made them the material of choice in many applications, both for high-technology needs and in the general engineering and transportation sectors. Uses include reinforcements in sporting goods, industrial applications including aerospace and automobiles, biocompatible materials in medical applications, fillers in conducting polymers, EMI and RF shielding, support structures for antenna and telescopes, etc. On the negative side, their usage is limited mainly by their low resistance to oxidation at high temperatures, their low strain to break and their low impact resistance. Other drawbacks include a high degree of anisotropy both in the direction of the fiber and perpendicular to it, and their high cost.

Carbon fibers can be grouped into three major categories depending on their origin, namely (1) polyacrylonitrile (PAN)-based, (2) pitch-based, and (3) vapor-grown fibers. All have their unique set of advantages and disadvantages. Currently, PAN-based carbon fibers dominate consumption, accounting for nearly 90% of all sales worldwide. On the other hand, commercial production of vapor-grown fibers is still in its infancy. Pitch-based (including mesophase) fibers are expected to increase their share of the market since they have a potential for lowering manufacturing costs as compared to PAN-based fibers.

Commercial PAN-based carbon fibers have been available for over 25 years, and as a result of this accumulated knowledge base, plus their inherent properties, they have established a list of impressive advantages. Amongst them are high tensile strengths and high strains to break. Constant research and development efforts have now realized PAN-based carbon fibers with tensile strengths of ~7.1 GPa and a Young's modulus of ~290 GPa (T-1000, experimental-grade fiber from Toray Industries, Inc.). The most important aspect of such fibers is their strain to failure of ~2.4% as compared to the ~1.5% normally achieved. Flaws, both internal and external, in the carbon fiber have been identified as the ma; or strength-limiting factor. For fibers subjected to low heat treatment temperatures (HTT), strength is limited mainly by surface flaws, whereas internal flaws limit the strength of high HTT fibers. The Young's modulus is primarily controlled by the degree of orientation of graphitic planes; carbonization of PAN leads essentially to a non-graphitic structure with poor orientation along the fiber axis. As a result, high-modulus PAN-based fibers are not to be expected.

---

*Corresponding author.

†Present address: Ciba-Geigy Corporation, 444 Saw Mill River Road, Ardsley, NY 10502, U.S.A.

2. STRUCTURE OF PAN

PAN is often considered to be a "laterally ordered" polymer, with no *c*-axis order [1]; this structure is based on the absence of meridional or off-axis WAXD reflections. It is generally believed that PAN forms relatively stiff, rod-like molecules due to the intramolecular dipole repulsions of its nitriles [2]. Figure 1(i) shows how PAN molecules form an irregular helix, and Fig. 1(ii) shows how these helices pack into laterally ordered domains or "crystals". Calorimetric experiments with water-plasticized PAN indicate an endothermic peak corresponding to "melting" of crystals and therefore establish this structural unit to be crystalline [3]. Disordered or "amorphous" regions between crystalline domains consist of entanglements, chain-ends, defects, co-monomer sequences, tie-chains, etc.

WAXD from an as-received PAN fiber is shown in Fig. 2. The two well-defined equatorial reflections correspond to *d*s of 5.3 and 3 Å. Additionally, six broad spots arranged in a circle spaced ~60° apart and corresponding to $d = 3.6$ Å are observed. A very weak meridional reflection at $d = 2.4$ Å is also seen. Similar patterns for PAN fibers have previously been published in the literature [4–7]. On account of these meridional and off-axis reflections, it is possible that there exists a certain degree of three-dimensional order to the semi-crystalline structure.

3. OXIDATIVE STABILIZATION

An essential and time-consuming step in the conversion of PAN fibers to high-performance carbon fibers is the oxidative stabilization step. Oxidative stabilization is normally done at temperatures between 200 and 300°C in the presence of oxygen and for extended periods of time, varying from 1 to 24 hours. Air is typically the medium of choice. This stabilization is necessary to cross-link PAN chains and prepare a structure that can withstand the rigors of high-temperature processing. The reaction is highly exothermic and if not controlled, can lead to runaway autocatalytic processes resulting in "melting" down and coalescing of fibers in a tow. Non-optimized processing cycles during oxidative stabilization can also lead to excessive weight-loss during subsequent carbonization and graphitization, and to carbon fibers with inferior properties.

The stabilization chemistry of PAN has been extensively studied in the past 35 years and there appears to be some general consensus on the mechanisms involved. However, it is by no means exhaustive, as there is still no direct evidence for cyclization reactions postulated to occur during the stabilization step. Various theories abound regarding initiation and propagation of various reactions, but no definitive mechanisms have been proposed. There also exist questions as to whether the stabilization step occurs by intra- or intermolecular polymerization [8]. Given the helical nature of the extended PAN molecule, and the strong intramolecular repulsion of neighboring pendant nitrile groups, it seems unlikely that intramolecular reactions would be a feasible possibility. However, intermolecular reactions would lead to non-cyclic $C{=}N$ structures, whereas electron microscopy has revealed the formation of graphitic structures at temperatures as low as 320°C [9]. Nevertheless, none of the mechanisms have been either conclusively proved or disproved.

The purpose of this study is to study morphological rearrangements occurring in the precursor fiber during oxidative stabilization. Some of the conclusions made are new, while others have been useful in justifying previously reported observations. It is hoped that the new understanding will help the carbon fiber manufacturer in optimizing the processing cycle.

4. EXPERIMENTAL

The progress of stabilization and the accompanying morphological changes were monitored through various measures, such as thermal stress development, percentage shrinkage, elemental analysis, differential scanning calorimetry, percentage weight-loss, color change, small-angle X-ray scattering and wide-angle X-ray diffraction.

4.1 *Precursors*

PAN fibers used in the study were designated "SAF", and were supplied by Courtaulds Fibers, U.K. This precursor fiber is most probably a co-polymer of acrylonitrile, methylacrylate and itaconic acid and is wet-spun from a sodium thiocyanate solution. As-received fibers were supplied in tows of 6000 fibers with an average denier of 1.09 and a mean diameter of 11.3 μm. For studies on homopolymer PAN, pure PAN powder supplied by Aldrich (Catalog #18131-5) was used.

4.2 *Stabilization*

Stabilization was carried out in a batch process using both the constant length and the constant tension modes. A three-zone tube furnace was used for all experiments. For constant length experiments, the precursor fiber was prestressed to a constant tension, and stabilization carried out in continuously flowing oxygen, air or argon (4 l min^{-1}) at a heating rate of 1°C min^{-1}. For constant tension experiments, the precursor fiber was free to shrink or stretch. The final HTT varied from 200 to 500°C. Sample collection involved heating the precursor fiber to the

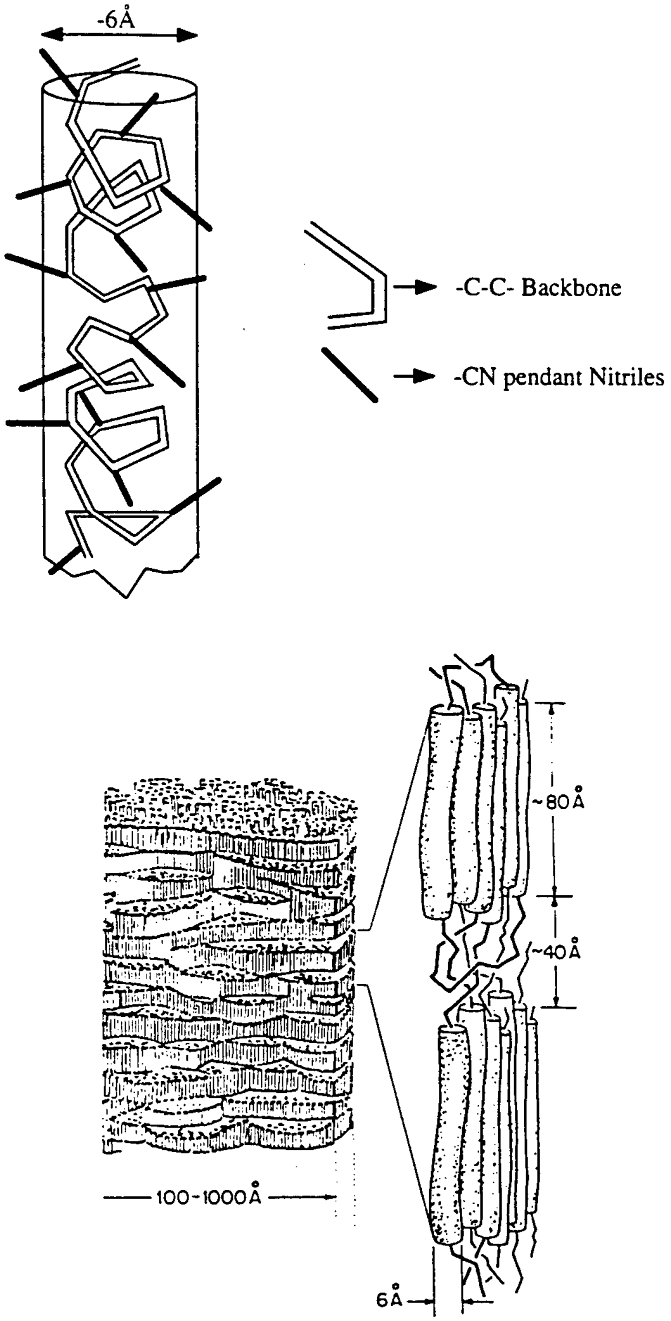

Fig. 1. (i) Irregular helical structure of PAN chains [2]. (ii) Morphological model of PAN fiber showing ordered and disordered regions [1].

desired HTT and rapidly quenching the stabilized fiber in the desired atmosphere.

4.3 *Thermal stress and percentage shrinkage*

Thermal stress in constant length experiments was monitored using a 5 lb load cell, wherein one end of the fiber was rigidly fixed, and the other end attached to the load cell. Output from the load cell was amplified and fed to a strip-chart recorder, which produced a trace of fiber thermal stress as a function of furnace temperature. Furnace temperature was measured by a thermocouple placed in the furnace tube adjacent to the fiber; temperatures displayed on the furnace controller deviated significantly from the measured furnace temperature, especially at high temperatures.

Experiments measuring percentage shrinkage were carried out in oxygen, in air and in argon. A fixed length of precursor fiber was tied to Kevlar® thread on both its ends. One end of the Kevlar® thread was rigidly fixed and the other end passed over a smooth pulley to a very small weight, corresponding

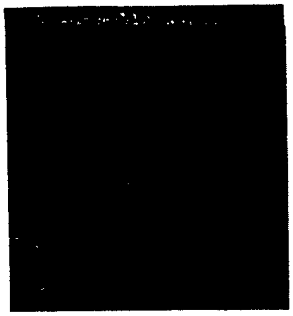

Fig. 2. Flat-plate WAXD pattern for as-received PAN fiber.

to a tension of 1 mgpd. Movement of the weight was monitored during the experiment, and converted to percentage shrinkage values. Results so obtained are referred to as free shrinkage, since the tension on the fibers was extremely small. Experiments were also carried out at higher tensions, corresponding to 8 and 34 mgpd. Change in Kevlar® length was negligible in the range of temperatures studied.

4.4 *Elemental analysis*

Percentage carbon, hydrogen and nitrogen for various samples were determined on a Leco elemental analyzer CHN-600. Percentage oxygen was then determined by difference. Elemental contents were converted to the number of hydrogen, nitrogen or oxygen atoms per repeat unit, which contains three carbon atoms, and are reported as atomic ratios per repeat unit. Since stabilized samples are extremely hygroscopic, care was taken to dry the samples thoroughly before subjecting them to elemental analysis.

4.5 *Thermal analysis*

Differential scanning calorimetry (DSC) experiments were carried out on a DuPont 2910 DSC instrument. Heating rates ranging from 1 to 30°C min^{-1} were used to study the influence of heating rate on the exothermic behavior of the precursor PAN fiber. Experiments were performed in oxygen, air and argon atmospheres. All experiments allowed the SAF fiber to shrink in the DSC capsule. The initial sample weight was used in calculating heat flow, and therefore y-axis values correspond to lower estimates of heat flow at high temperatures where significant weight loss occurs.

Crystalline melting points of PAN were observed using specially sealed high-pressure DSC capsules, wherein excess water was used to plasticize the polymer and suppress the stabilization exotherm. Percentage weight-loss experiments for SAF were carried out on a Perkin Elmer TGS-2 thermal gravimetric analyzer (TGA) at 1°C min^{-1}. Experiments were performed in oxygen, air and argon atmospheres. Plots obtained from the DSC and TGA plotter were digitized and converted to a form suitable for further analysis on a personal computer. Digitization led to some loss of smoothness in the curves.

4.6 *Small-angle X-ray scattering (SAXS)*

All SAXS experiments were performed with Cu Kα radiation ($\lambda = 1.5418$ Å) with the X-ray generator operating at 40 kV and 35 mA. Monochromatization was achieved using total reflection of X-rays from two nickel-coated mirrors placed at 90° to each other. Bending the nickel-coated mirrors also served to focus the X-ray beam. A three pin-hole collimation unit was used to produce an intense X-ray point source at the detector with minimal parasitic scatter. A two-dimensional solid-state X-ray detector interfaced to a personal computer was used for data acquisition and analysis [10]. The smallest possible scattering angle at which measurements could be made with a high level of accuracy corresponded to a Bragg spacing of ~ 150 Å. The sample-to-detector distance was maintained at 12 cm, and counting times were typically 12 hours per sample.

4.7 *Wide-angle X-ray diffraction (WAXD)*

WAXD experiments were performed on a set-up similar to the one used for SAXS, but with the detector replaced by a photographic film. The sample-to-detector distance was maintained at 3.5 cm, and exposure times were typically 6 hours.

4.8 *Other analysis*

Changes in color of the samples with progress of stabilization were monitored visually.

5. RESULTS AND DISCUSSION

5.1 *Experimental observations*

Development of thermal stress for constant length stabilization experiments (pre-tension of 0.05 gpd) in various atmospheres are shown in Fig. 3. It is immediately apparent that stabilization atmosphere has a great impact on the development of stress at high temperatures. Decay in pre-stress up to 90°C corresponds to molecular processes, e.g. creep, occurring below the T_g of PAN (T_g, PAN $\approx$ 80°C). At temperatures between 90 and 150°C, stress rises due to the entropic recovery of highly oriented molecular chains in the amorphous region.

The stress rise beyond 150°C is very much dependent on the atmosphere used, and has often been attributed to that arising from "chemical" forces [11]. Heating in the presence of oxygen leads to a much larger decay in stress between 150 and 200°C. It is also noticed that absolute values of thermal stress at temperatures above 200°C for a given atmosphere are independent of the amount of pre-tension (Figs 4 and 5).

The region between 200 and 340°C can be divided into two regimes; the initial portion corresponding to a stress rise, which is followed by a stress decay. On stabilization in air, it could be argued that between 175 and 267°C, adsorption of oxygen and rapid loss of hydrogen (see Fig. 6) leads to a "fluid-like" structure that is more capable of dissipating stress build-up through chain cleavage and/or chain slippage. This accounts for lower thermal stress observed on heating in presence of oxygen. Possible explanations for the initial rise and subsequent fall in stress will be discussed later. At temperatures above 320°C, adsorbed oxygen tends to stabilize the structure by intermolecular cross-linking and prevents stress from decaying to zero, as is observed in argon. In pure oxygen, it is proposed that most of the hydrogen loss occurs in the initial half of the cycle, little stress decay is observed later on.

The last stage of the reaction (> 320°C) corresponds to an increase in stress on heating in oxygen and in air. Oxidative degradation reactions set in and stress rises rapidly until tow breakage. On heating in argon, stress remains at near-zero levels.

Figure 7 shows the percentage free shrinkage of SAF on heating in oxygen, air and argon at 1°C min^{-1}. Shrinkage between 100 and 150°C corresponds to entropic shrinkage and is due to oriented amorphous polymeric chains reverting to their random coil configuration. Above 150°C, shrinkage sets in earliest on heating in oxygen, followed by heating in air, and lastly for heating in argon. Also, the absolute shrinkage on heating in oxygen is much higher than in air or argon. Percentage shrinkage rises rapidly at temperatures beyond 375°C on heating in oxygen and air due to oxidative degradation, ultimately leading to tow breakage. On heating in argon, the fiber starts stretching at temperatures beyond 340°C. At this stage the fiber is extremely fragile and breaks under very small loads.

Thus, although heating in the absence of oxygen leads to maximum thermal stress, contrary to intuition, it produces the minimum amount of shrinkage. Such behavior lends credibility to the observation made previously that heating in the presence of oxygen leads to a more "fluid-like" structure that is better able to absorb either self-generated or imposed stresses. Shrinkage experiments under high loads (~ 34 mgpd) seem to confirm the more "fluid-like" nature of the structure in oxygen. The results are displayed in Fig. 8. As expected, it is seen that shrink-

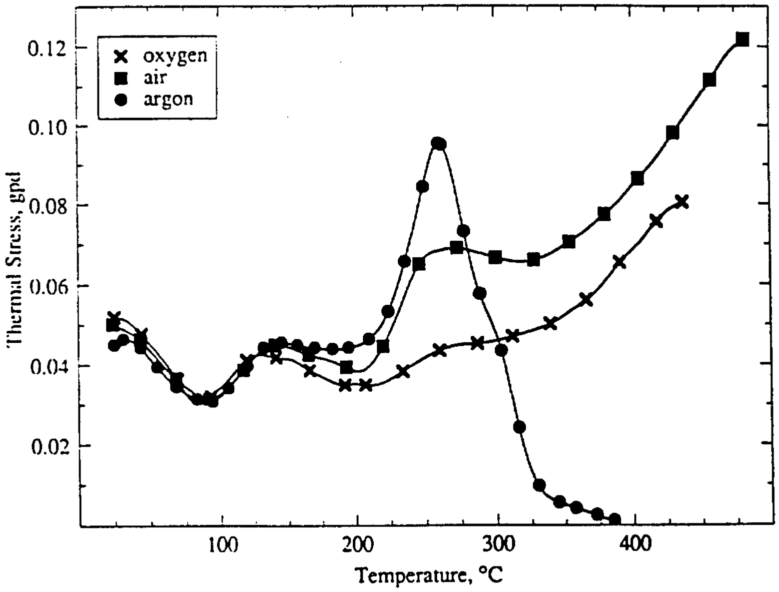

Fig. 3. Development of thermal stress on heating SAF in oxygen, in air and in argon at 1°C min^{-1}.

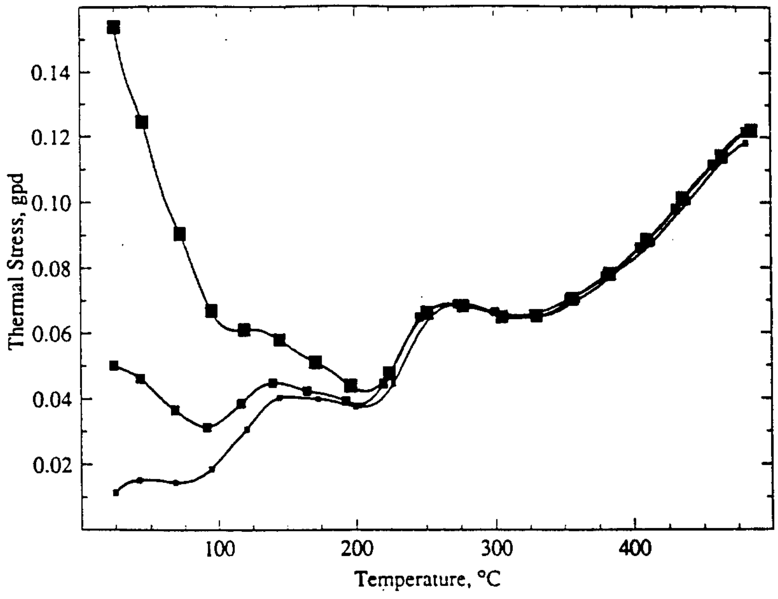

Fig. 4. Development of thermal stress in SAF with varying amounts of pre-tension (air, 1°C min^{-1}).

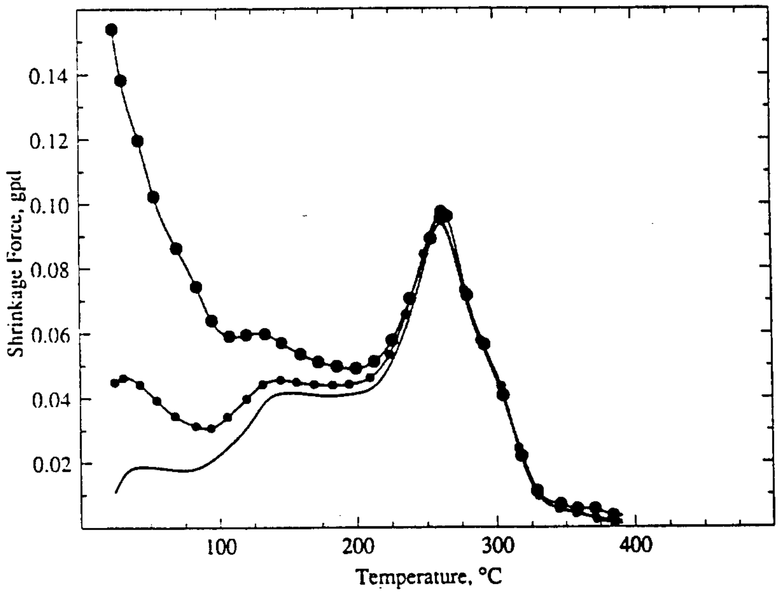

Fig. 5. Development of thermal stress in SAF with varying amounts of pre-tension (argon, 1°C min^{-1}).

age on heating in oxygen is absent at temperatures below 250°C, when compared to corresponding shrinkages on heating in air and argon. In fact, the fiber even stretches slightly. There also seems to be an "entropic" contribution to this so-called "chemical" shrinkage. At zero loads, shrinkage in oxygen is maximum (Fig. 7), however, at high loads, shrinkage is minimized. Based on these observations, if stretching of the fiber during stabilization is desired, an imposed load greater than that developed in a constant-length experiment (see Fig. 3) is necessary.

DSC curves for heating SAF in oxygen, air and argon at 1 and 4°C min^{-1} are shown in Fig. 9 and Fig. 10, respectively. At least two distinct exothermic peaks are seen below 400°C for stabilization in the presence of oxygen. Additionally, a broad shoulder is observed beyond the second peak. Exothermic behavior seen at temperatures close to 450°C is due to the oxidative degradation of the carbon residue and leads to a total weight loss at ~600°C. Peak-width is controlled by the rate of diffusion of oxygen through the skin and into the core of fiber. (This argument is supported by DSC experiments on pure homopolymer PAN, which exhibits a sharp exothermic peak in argon, and a much broader peak on heating in presence of oxygen, heating rates and other variables kept constant—see Fig. 11.) On heating in argon, a single exothermic peak is observed at ~275°C.

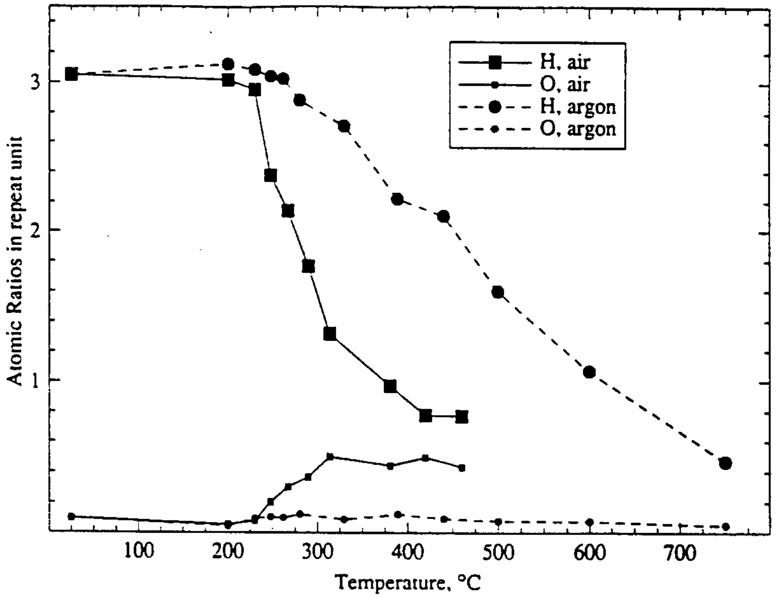

Fig. 6. Variation of H and O on heating in air and in argon to various HTT (1°C min^{-1}).

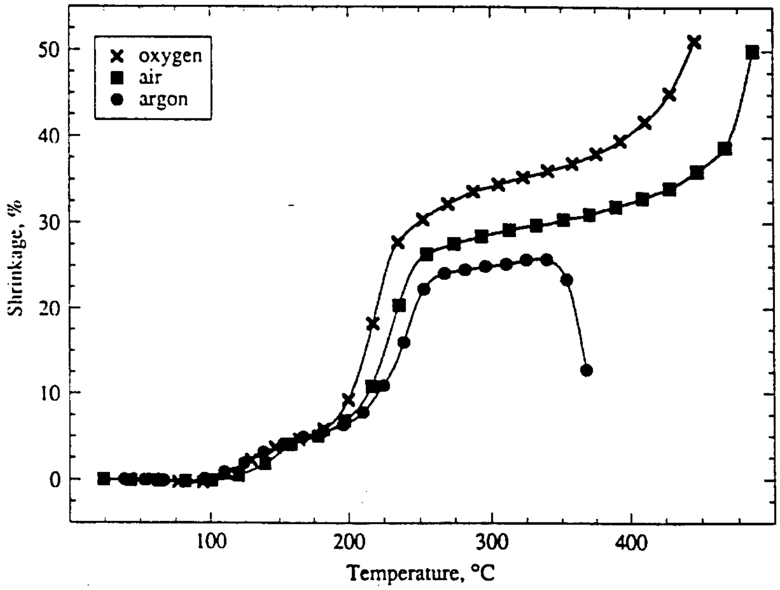

Fig. 7. Percentage free shrinkage on heating in oxygen, in air and in argon at 1°C min^{-1}.

Percentage shrinkage at various loads and DSC behavior for heating in air are shown in Fig. 12. The steep rise in shrinkage corresponding to the first DSC peak is influenced by varying load. The behavior beyond 255°C, coinciding with the second DSC peak, is identical in shape and slope, irrespective of loads imposed on the tow. Similar behavior is observed for heating in oxygen.

Figure 13 is a more detailed DSC plot on heating SAF in air at 1°C min^{-1}. It is generally believed that Peak I is due to cyclization/thermal stabilization reactions. Peak II has been reported before and has been atributed to "undesirable" oxidation reactions [11]. More recent studies based on results from WAXD and infrared spectroscopy assign it to additional intermolecular cross-linking reactions, as well as to aromatization of the structure [12,13]. However, it will be shown later in the course of this study that this is not the case; furthermore, definitive mechanisms accounting for the various peaks will be proposed.

The color changed from white for the precursor to dark brown at HTT of 200°C, turning to black at 230°C and remaining black thereafter. Color changes are noted in Table 1 for stabilization in both the presence and absence of oxygen.

In order to account for our earlier observations and to understand better various morphological

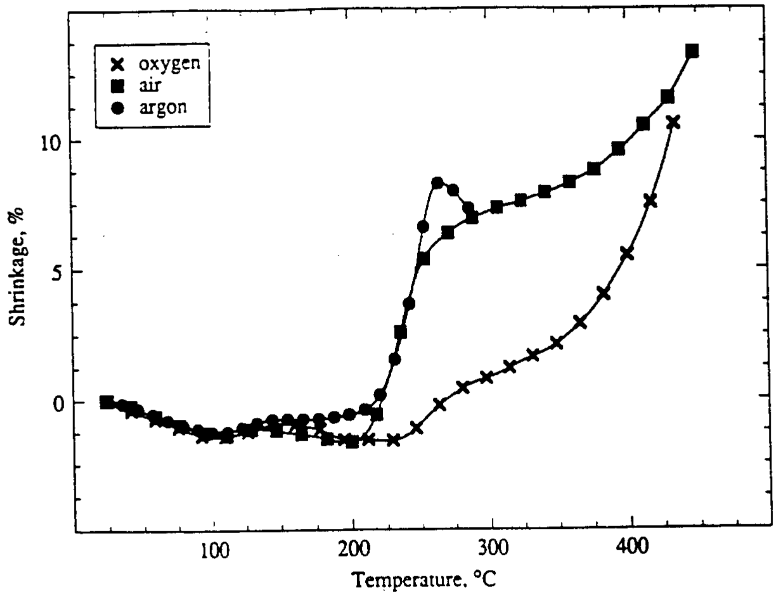

Fig. 8. Percentage shrinkage on heating in oxygen, in air and in argon at high loads (~34 mgpd).

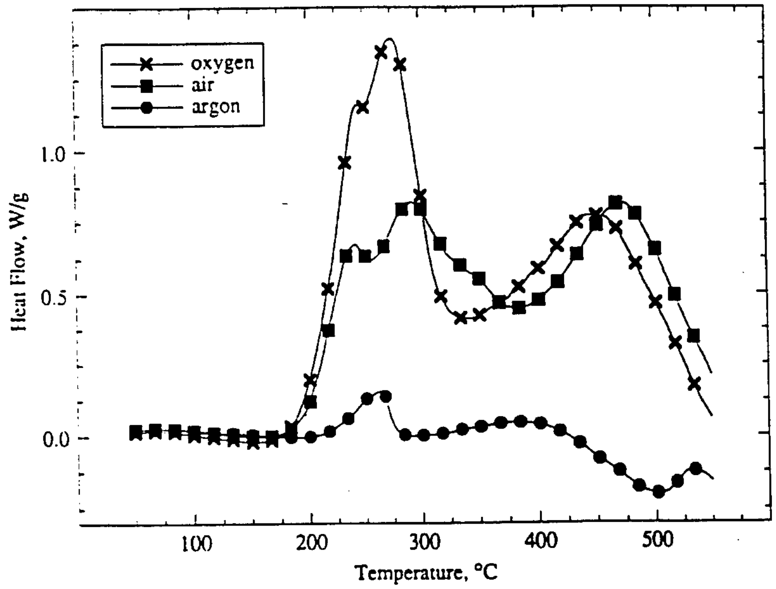

Fig. 9. DSC plots on heating SAF in oxygen, in air and in argon at 1°C min^{-1}.

rearrangements taking place during thermal stabilization, WAXD and SAXS studies were performed. Figure 14 shows WAXD flat-plate photographs taken after stabilizing the SAF fiber at 1°C min^{-1} in air at constant length (pre-tension: 0.15 gpd) to various HTT followed by immediate quenching in air in order to preserve the developed morphology. As-received SAF and various heat treatment temperatures from 95 to 420°C were used. It is seen that the precursor crystalline morphology is largely preserved up to 230°C, starting to break up, both in terms of crystallite size and crystal orientation, only between 230 and 267°C, and disappearing at temperatures close to 314°C.

SAXS results from several air-stabilized samples with HTTs between 200 and 267°C are shown in Fig. 15. The fiber axis is vertical in all cases. The as-received precursor does not show any scattering at small angles. This is due to a negligible electron density contrast between the crystalline and amorphous regions. However, at ~200°C, a weak meridional maximum starts to develop, corresponding to a long period of ~87 Å. The appearance of this maximum is attributed to stabilization reactions occurring preferentially in one of the phases, thereby leading to an increase in electron density contrast between the crystalline and amorphous regions. The maximum intensifies up to 230°C and diminishes thereafter,

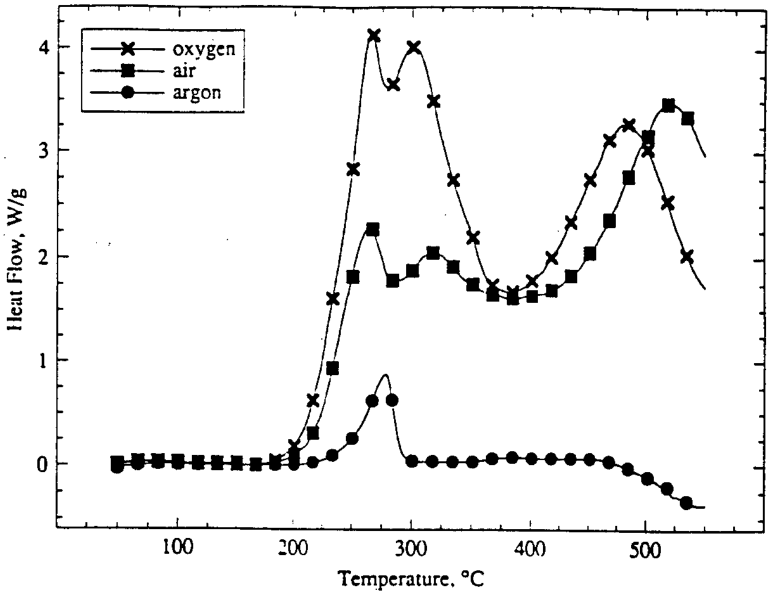

Fig. 10. DSC plots on heating SAF in oxygen, in air and in argon at 4°C min^{-1}.

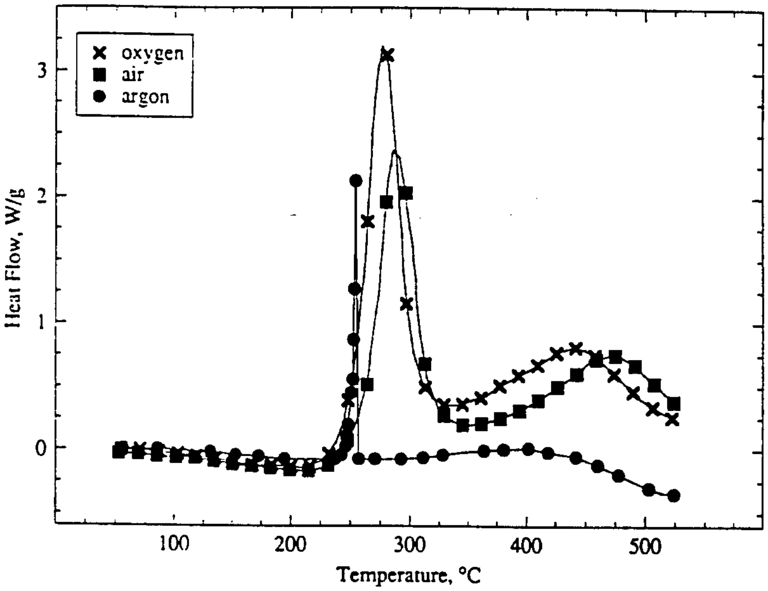

Fig. 11. DSC plots on heating homopolymer PAN in oxygen, in air and in argon at 1°C min^{-1}.

almost disappearing at ~267°C. The disappearance of the maximum at ~267°C is attributed to stabilization reactions having been completed in both the crystalline and amorphous phases, leading again to negligible electron density contrast and hence no small-angle scattering.

5.2 *Role of oxygen in the stabilization reactions*

5.2.1 *Stabilization in the presence of oxygen.*

Figure 16 is a composite summary of the various processes occurring in the SAF fiber as it is heated in air at 1°C min^{-1}. The following can be inferred:

The sharp rise in percentage shrinkage and the rise in thermal stress after the initial decrease in stress corresponds to reactions in the amorphous part of the polymer. This is an exothermic reaction (Peak I in Fig. 13) with very little weight loss (~2%). Based on observations from WAXD and SAXS, it is proposed that stabilization reactions initiate in one of the phases, most likely the disordered or amorphous phase, at temperatures below 200°C. At ~230°C, electron density differences are at their greatest, leading to a pronounced SAXS maxima.

Reactions in the crystalline region initiate near 215°C, and are completed at ~300°C. To test the proposed mechanism, melting endotherms of various water-plasticized stabilized samples were

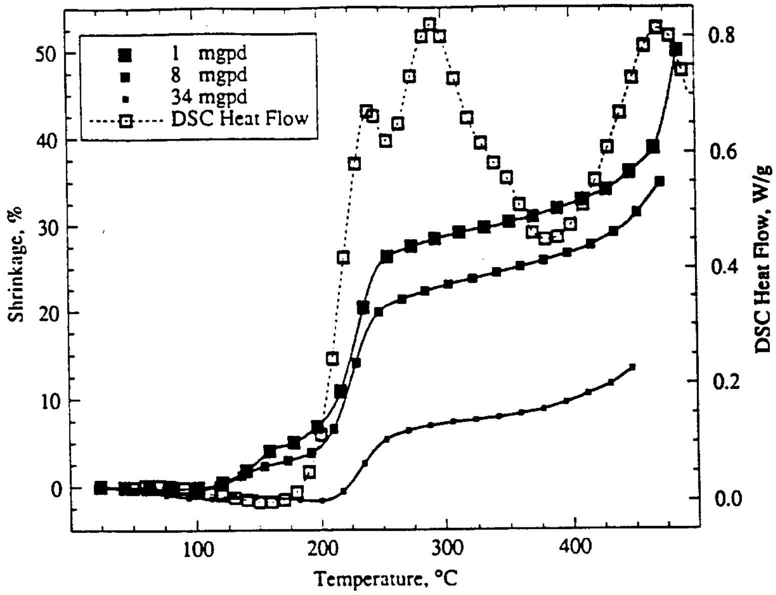

Fig. 12. Percentage shrinkage at various loads along with DSC behavior on heating in air (1°C min^{-1}).

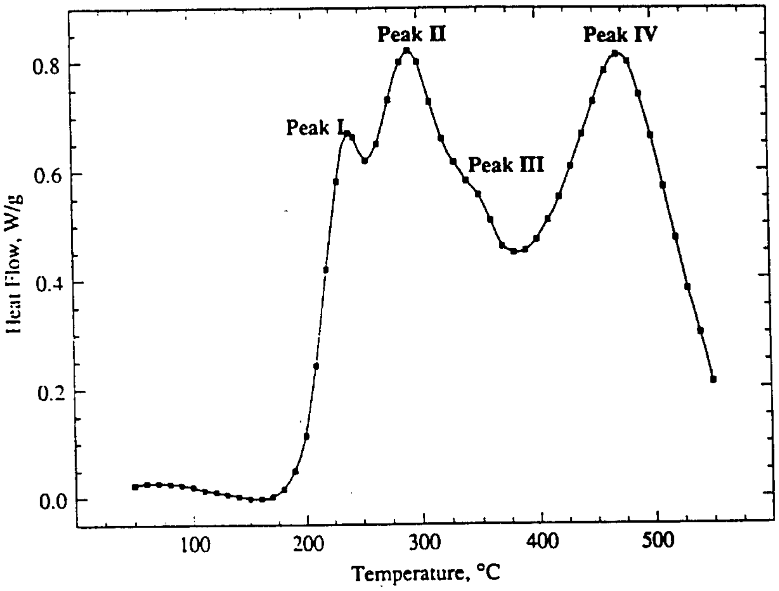

Fig. 13. DSC behavior on heating SAF in air at 1°C min^{-1}.

Table 1. Color changes upon heating SAF in air and in argon (constant length, 1°C min^{-1})

Temperature (°C)	Air	Argon
SAF, as-received	White	White
142	Light yellow	–
200	Dark yellow	Golden yellow
215	Dark brown	–
230	Black	Dark yellow
240	Black	–
248	Black	–
~264	Black	Brown
~285	Black	Dark brown
~330	Black	Black

obtained using high pressure DSC capsules. Results are shown in Fig. 17 for the as-received SAF and stabilized samples with HTT up to 200, 230 and 267°C. Even at 230°C, when most of the shrinkage has taken place and the fiber has turned black in color, a distinct melting endotherm can still be observed. Reactions in the crystalline part of the polymer lead to Peak II (Fig. 13) in the DSC curve and additional weight loss (~15%). Thermal stress decays, and percentage shrinkage is smaller in this region.

The origin of Peak III is not clear.

Oxidative degradation reactions set in at temperatures beyond 380°C, leading to a rapid increase

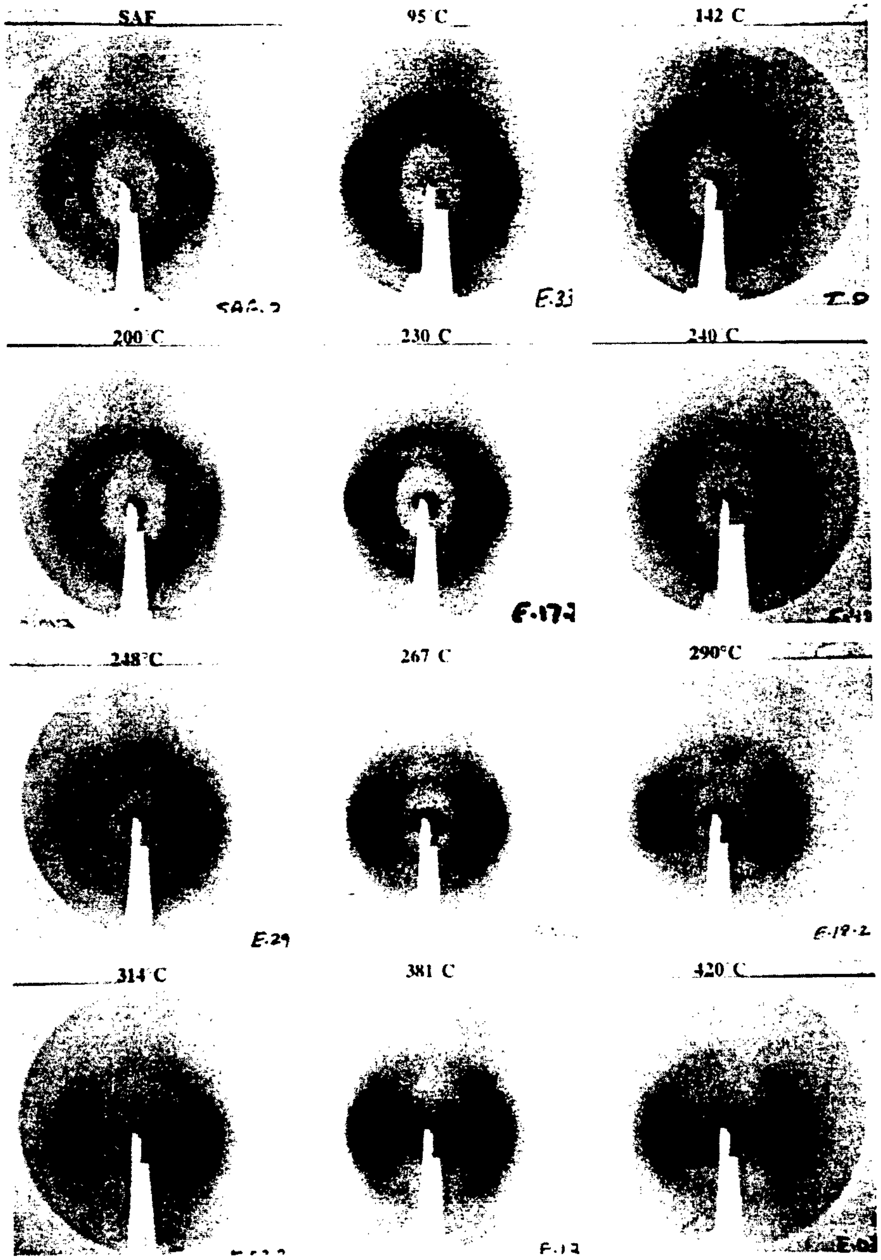

Fig. 14. WAXD flat-plate photographs for SAF stabilized at 1°C min^{-1} in air at constant length and to various HTTs.

in thermal stress, percentage shrinkage, weight loss and heat evolution (Peak IV in Fig. 13).

Possible reasons for the initiation of stabilization reactions in the amorphous part of the polymer are: (1) the presence of co-monomers in the amorphous phase, and (2) ease of diffusion of oxygen into the less dense amorphous phase as compared to the more dense crystalline phase. To study the relative importance of these two mechanisms, stabilization experiments were carried out in inert atmospheres. SAXS patterns from argon-stabilized samples with HTTs of 200, 230 and 248°C are shown in Fig. 18. It is seen that even in absence of atmospheric oxygen, a maximum does develop, although its intensity is much reduced when compared to stabilization in the presence of oxygen. The maximum disappeared completely at ~262°C. This leads us to believe that oxygen-containing co-monomers, present in the amorphous phase play a vital role in initiating stabilization reactions.

Figure 19 compares DSC plots for heating homopolymer PAN and co-polymer SAF in air at 1°C min^{-1}. Peak I in Fig. 13, corresponding to reactions in the amorphous phase of the co-polymer, is absent in the homopolymer. Also, Peak II of the co-polymer coincides with the sole exothermic peak observed for the homopolymer PAN. The crucial role of co-monomers in initiating stabilization reactions is again evident.

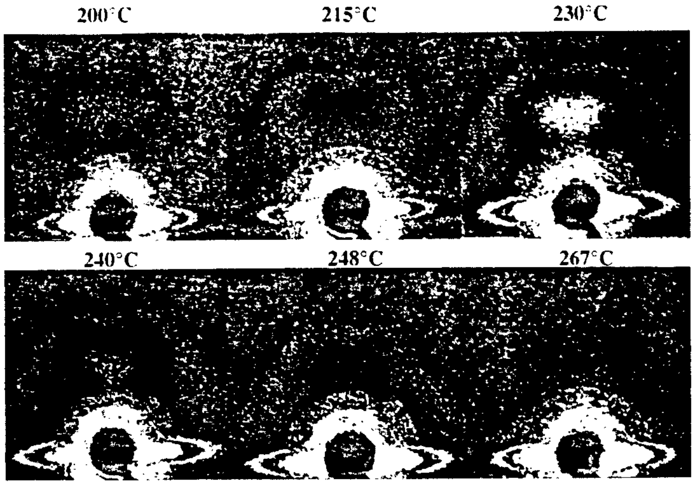

Fig. 15. SAXS patterns for SAF stabilized at 1°C min^{-1} in air at constant length and to various HTTs.

5.2.2 *Stabilization in the absence of oxygen.* Figure 20 is a composite summary of the stabilization behavior in the absence of oxygen. WAXD patterns for as-received SAF, and for samples stabilized in argon with HTTs between 200 and 280°C are shown in Fig. 21. As noted for oxidatively stabilized samples, crystalline morphology is largely preserved until ~250°C; at this temperature most of the thermal shrinkage, stress development and heat evolution have already taken place.

5.2.3 *Role of oxygen in stabilization.* Based on observations for stabilization in the presence and absence of oxygen, the following conclusions can be made:

For homopolymer PAN, the presence of a single DSC exotherm indicates only one stabilization reaction that proceeds at near equivalent rates in the crystalline and amorphous regions, both in the presence and absence of oxygen. The shape and width of the DSC peak (see Fig. 11) indicates that stabilization in oxygen is diffusion-controlled, whereas stabilization in argon is reaction-controlled.

For co-polymer PAN, (a) the presence of two distinct DSC exotherms for stabilization in presence of oxygen indicates the initiation of reactions in amorphous parts of the polymer and their eventual spread to the crystalline component. Reactions initiate in the amorphous regions and at much lower temperatures (~170°C in air at 1°C min^{-1}) than in the homopolymer (~220°C in air at 1°C min^{-1}) due to the presence of acid-group containing co-monomers. Stabilization in the absence of oxygen proceeds at near-equivalent rates in both the crystalline and amorphous regions, although WAXD observations and presence of a SAXS maxima at low temperatures do indicate that reactions initiate in one of the phases, most likely the amorphous phase with acid-group containing co-monomers.

Atmospheric oxygen plays a role in the formation of a well-crosslinked structure that is more physically conducive to high-temperature processing. Such structures are achieved by the rapid loss of hydrogen (see Fig. 6) and by the formation of intermolecular cross-links. Hydrogen levels for samples stabilized in argon ultimately reach levels present in oxidatively stabilized samples, though at slower rates and at much higher temperatures. This information could be used to regulate the levels of oxygen in stabilizing atmospheres in order to form structures more conducive to controlled high-temperature stretching. Higher degrees of stretching lead to enhanced modulus in the final carbon fiber. Moreover, a more gradual loss of hydrogen leads to the formation of more graphitizable carbons [14,15], which translates to higher-modulus carbon fibers.

5.3 *New concerns*

A number of mysteries have emerged from this study. Foremost is the cause for shrinkage at high temperatures. It has been proposed that "chemical" shrinkage is due to rotation of the initially parallel molecular chains by up to 120° in order to bring pendant nitrile groups into close proximity for further intermolecular reaction [16]. This rotation leads to tilting of chains and a net macroscopic shrinkage along the fiber axis. From our observations, we conclude that most of the shrinkage arises from reactions in the amorphous part of the polymer. If indeed the amorphous part shrinks, as has been proposed, the long period as measured from SAXS should show a steady decrease on going to higher HTT. In fact, we observe quite the opposite. SAXS from samples free to shrink and stabilized in air at 1°C min^{-1} are shown in Fig. 22. The long period increases from ~84 Å at 200°C to ~108 Å at 240°C, an increase of ~29%. This behavior is reminiscent of behavior in semi-crystalline polymers, which show an increase in long period upon annealing at temperatures close to the melting point.

The nature of SAXS is also puzzling. Close observa-

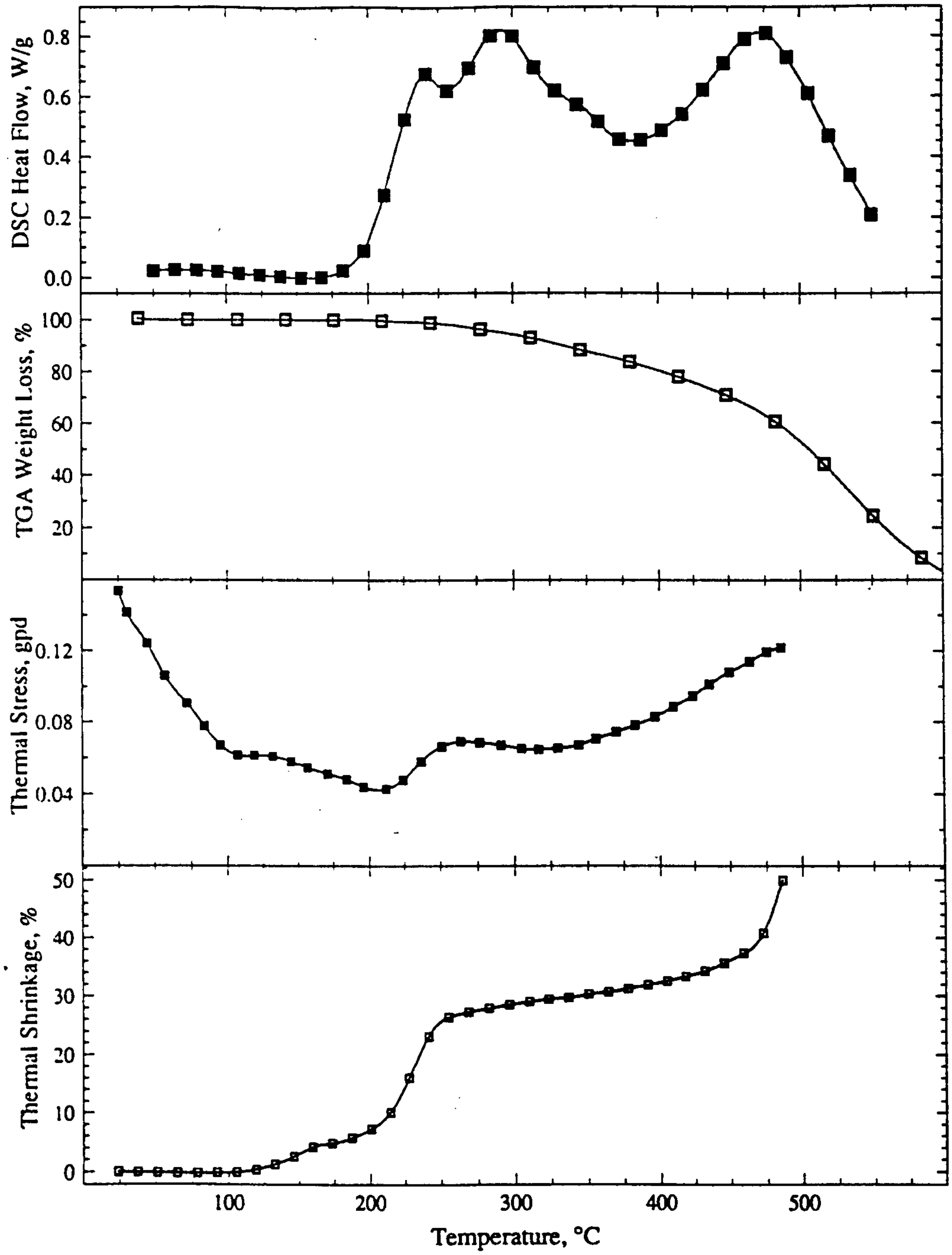

Fig. 16. Composite summary on heating SAF in air at 1°C min^{-1}.

tion of maxima indicates a split along the horizontal direction (Fig. 22). This behavior has been reported before, but no explanations were forwarded [17]. Normals to crystalline lamellae are tilted by ~14° to the fiber axis at 215°C. As temperature increases, the two maxima appear to move closer to each other, apparently merging at ~248°C. This would lead one to believe that the tilt angle decreases with increasing HTT, indicating better orientation of crystalline normals along the fiber axis. However, on deconvolution of peaks and taking into account the long period, the tilt angle actually increases from ~14° at 215°C to ~16° at 240°C (see Fig. 23). The increase in tilt angle is consistent with WAXD observations, indicating more randomization of structure with increasing HTT. Figure 24 compares WAXD from samples stabilized in air to HTTs between 200 and 314°C at constant length (pre-tension: 0.15 gpd) and at zero tension (free shrinkage). Similar crystalline morphologies are observed, with samples heated under zero

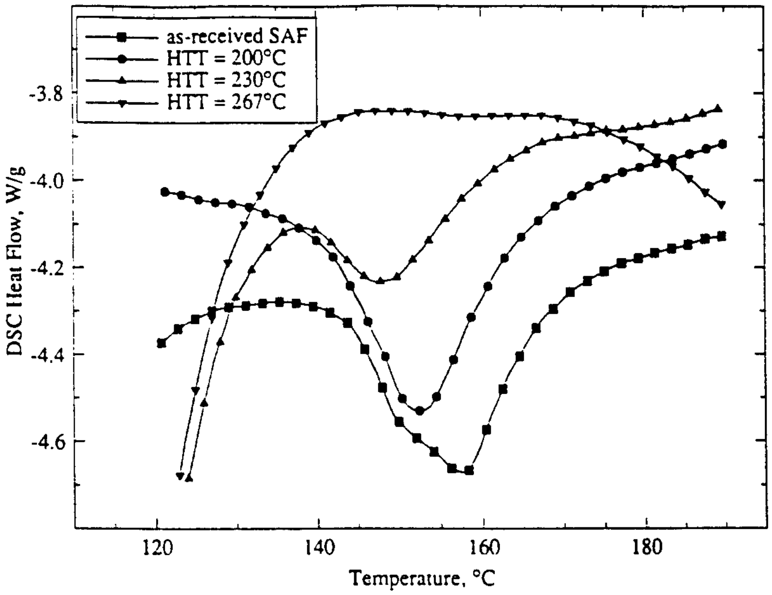

Fig. 17. DSC melting endotherms for as-received SAF and for oxidatively stabilized samples with HTTs of 200, 230 and 267°C.

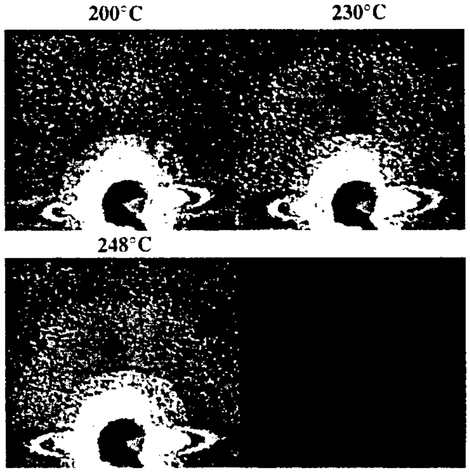

Fig. 18. SAXS patterns for SAF stabilized at 1°C min^{-1} in argon at constant length and to various HTTs.

tension displaying more randomized structures. Massive randomization of crystalline regions sets in at HTTs between 230 and 248°C, consistent with SAXS observations. It is also interesting to note that even for stabilization at constant length, a loss in orientation of crystalline regions on progressing from an HTT of 200 to 267°C is observed, indicating that stretching during stabilization may be necessary in order to preserve crystalline orientation. On stabilization in air at constant length, the long period increases from ~87 Å at 200°C to almost 110 Å at 240°C. Moreover, as thermal stress increases, the split SAXS maxima seem to be bending inwards (compare Figs 15 and 22), indicating that stresses generated in amorphous regions are being transferred to crystalline regions. This lends credence to the model proposed for PAN fibers, wherein amorphous regions are physically linked to crystalline regions (see Fig. 1).

5.4 *New models for morphological development during stabilization*

Based on observations previously noted, we propose a comprehensive model for morphological changes occurring during stabilization. Stabilization reactions initiate in the amorphous part of the copolymer and lead to a stress build-up for constant-length experiments. Crystalline morphology is largely preserved at this time; in fact, the crystals act as "cross-links", holding the structure together, and thereby contribute to the stress rise. As temperature is raised, reactions spread to the crystalline phase; this leads to a break-down of the "cross-linked" crystalline structure and a corresponding drop in thermal stress. This is readily apparent on stabilization in argon (see Fig. 20), where there is a dramatic drop in thermal stress above ~262°C. This drop in thermal stress is a result of the loss of inter-chain van der Waal's cohesive energy. This cohesive energy results from induced dipoles between chains owing to the highly polar pendant $-C{\equiv}N$ groups. Conversion of $-C{\equiv}N$ to $-C{=}N-$ upon stabilization implies a loss of inter-chain cohesive energy due to a loss in inter-chain dipole interactions. Stabilization in this temperature regime is proposed to be primarily intramolecular, due to the nature of thermal stress decay. If it were intermolecular, a cross-linked structure would result and stress decay would not be observed.

Stabilization in the presence of oxygen leads to a loss of inter-chain cohesive energy in the amorphous phase at much lower temperatures, resulting in a more "fluid-like" structure that is easily deformed.

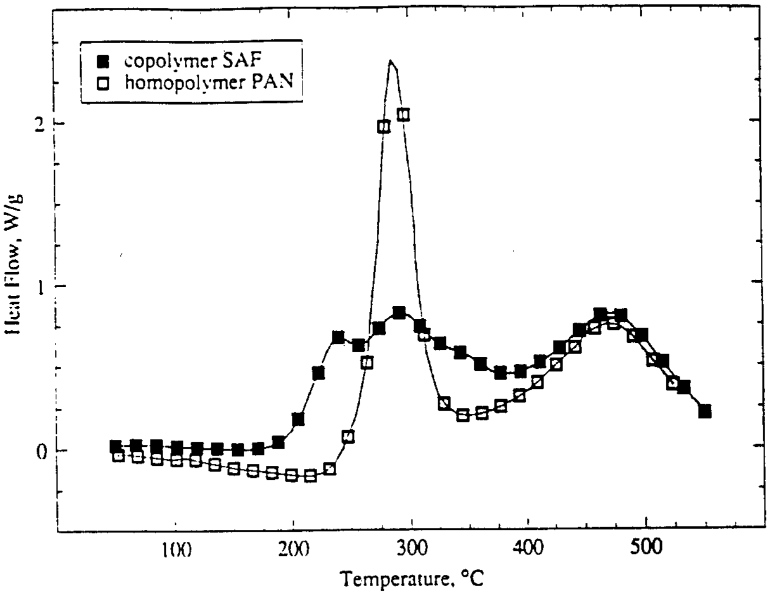

Fig. 19. DSC curves on heating co-polymer SAF and homopolymer PAN in air at 1°C min^{-1}.

This accounts for the much smaller rise in thermal stress on stabilization in the presence of oxygen as compared to stabilization in argon. Crystalline morphology is largely preserved, although considerable randomization of crystal lamellae take place. Reactions spread to crystalline regions at higher temperatures, resulting in stress decay due to breakdown of crystals acting as "crosslinks"; however, oxygen also prevents decay to zero stress at high temperatures, primarily by aiding in the formation of intermolecular cross-links above ~300°C in air. Although no proof exists, it is speculated that Peak III observed in the DSC of SAF in air (see Fig. 13) corresponds to certain intermolecular cross-linking reactions.

Macroscopic shrinkage along the fiber axis during stabilization is proposed to be primarily an entropy-driven process involving randomization of the highly oriented amorphous and crystalline morphology with increasing HTT. Most of the macroscopic shrinkage that has been shown to arise from the amorphous part of the polymer is a result of oriented chains in amorphous regions reverting to their "random coil" configuration. This reversion to the random-coil configuration is brought about by the loss of inter-chain van der Waal's cohesive energy forces due to intramolecular cyclization. Macroscopic shrinkage initiates earlier and also occurs to a much greater extent in the presence than the absence of oxygen (see Fig. 7). Thus there seems to be a "chemical" modification to this "entropic" process.

Randomization in the amorphous phase is transferred to crystalline regions due to the inherent connectivity of the amorphous and crystalline phases. This behavior is analogous to observations in highly oriented thermoplastic polymeric fibers, wherein exposure to temperatures near or above the melting point causes a randomization of structure and a net shrinkage along the fiber axis. Stabilization reactions in the crystalline phase do not contribute greatly to macroscopic shrinkage. This is because, by the time reactions reach the crystalline phase, the structure is already well relaxed and can easily accomodate localized variations in inter-chain cohesive forces.

6. CONCLUSIONS

A number of important findings have been made in this study. Conclusive evidence is provided which shows that oxidative stabilization reactions initiate in the amorphous part of a co-polymeric PAN fiber. These reactions contribute to the major portion of the macroscopic shrinkage. The importance of the co-polymer in initiating stabilization reactions is outlined. Crystalline morphology is largely maintained during this stage, although considerable randomization of crystal lamellae take place. Reactions propagate to crystalline components at higher temperatures and proceed to completion at ~380°C, giving rise to the second "crystalline" DSC peak. It is also possible that reactions can take place in the crystal at lower temperatures but with longer stabilization times. The effect of a constant ramp-up in temperature isothermal treatment at lower temperatures needs to be studied. Additionally, a broad shoulder on the second DSC peak is observed, but its origin is not clear. Based on thermal stress observations, it is speculated that it corresponds to certain intermolecular cross-linking processes.

Mechanisms are proposed that account for various morphological changes occurring in co-polymer PAN fiber on stabilization in the presence and

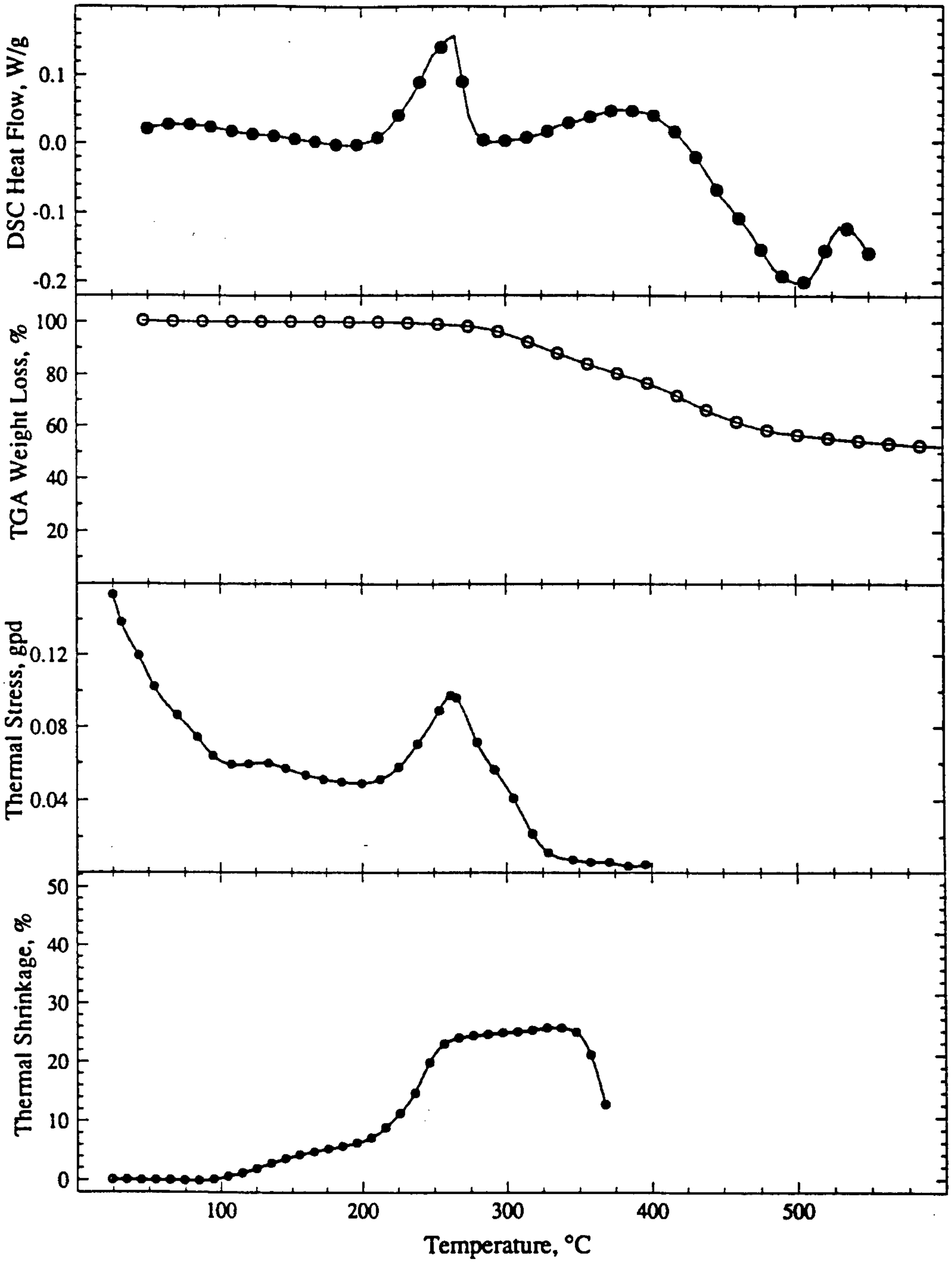

Fig. 20. Composite summary on heating SAF in argon at 1°C min^{-1}.

absence of oxygen. A model has been advanced for macroscopic shrinkage along the fiber axis observed upon heating PAN fibers; this model is similar to morphological changes observed upon heating highly oriented thermoplastic polymeric fibers. Thermal stress measurements lead us to believe that stabilization reactions are primarily intramolecular. This is in contrast to previous studies, wherein stabilization has been attributed to intermolecular reactions [16]. Intermolecular cross-linking occurs above ~300°C in the presence of oxygen. Macroscopic shrinkage observed during stabilization is proposed to be an "entropic" process, with "chemical" forces serving only to modify the observed response. A schematic illustration of the entire process is shown in Fig. 25. However, it should be noted that there are no clear-cut demarcations between various temperature regimes, and that considerable overlap exists.

A previous study has outlined a final HTT of

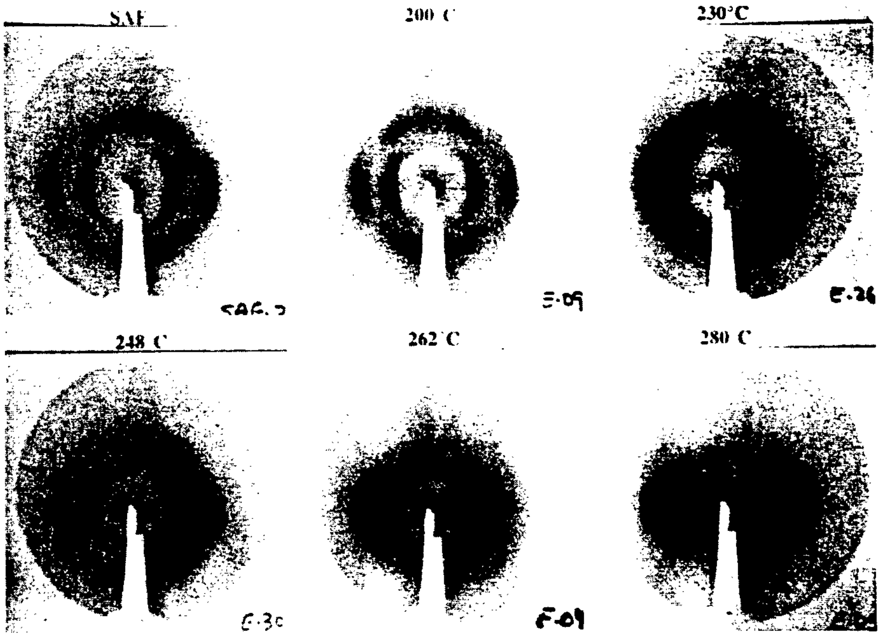
SAF
200°C
230°C
248°C
262°C
280°C

Fig. 21. WAXD flat-plate photographs for SAF stabilized at 1°C min^{-1} in argon at constant length and to various HTTs.

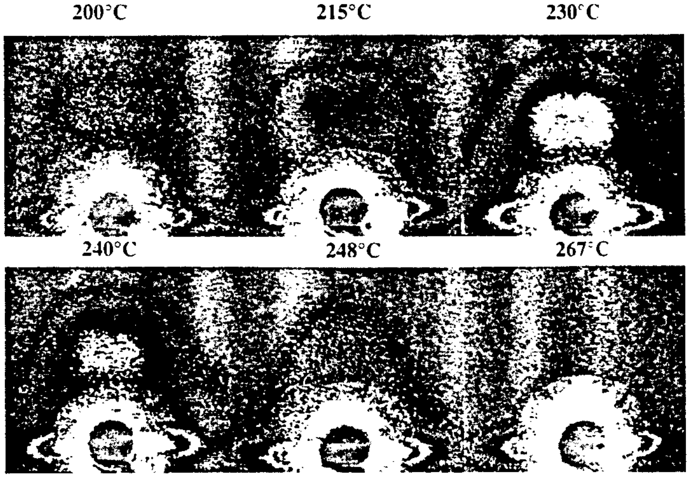
200°C
215°C
230°C
240°C
248°C
267°C

Fig. 22. SAXS patterns for SAF stabilized at 1°C min^{-1} in air at zero tension and to various HTTs.

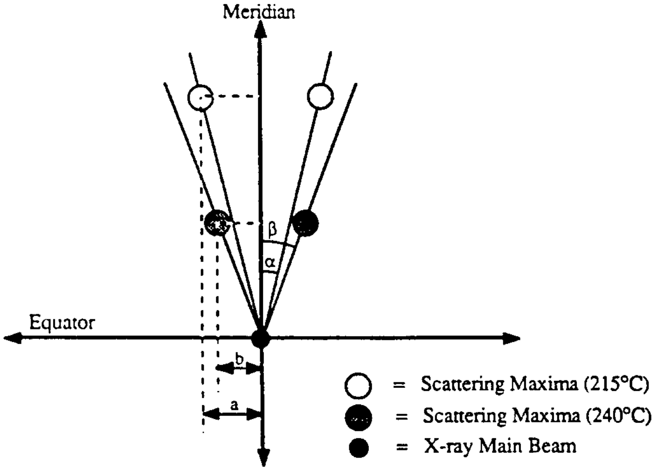
Meridian
Equator
β
α
b
a
○ = Scattering Maxima (215°C)
● = Scattering Maxima (240°C)
● = X-ray Main Beam

Fig. 23. Schematic of the changing split SAXS maxima with increasing HTT (215–240°C). Although the maxima seem to be getting closer to each other ($b<a$), normals to crystalline lamellae get further apart ($\beta>\alpha$).

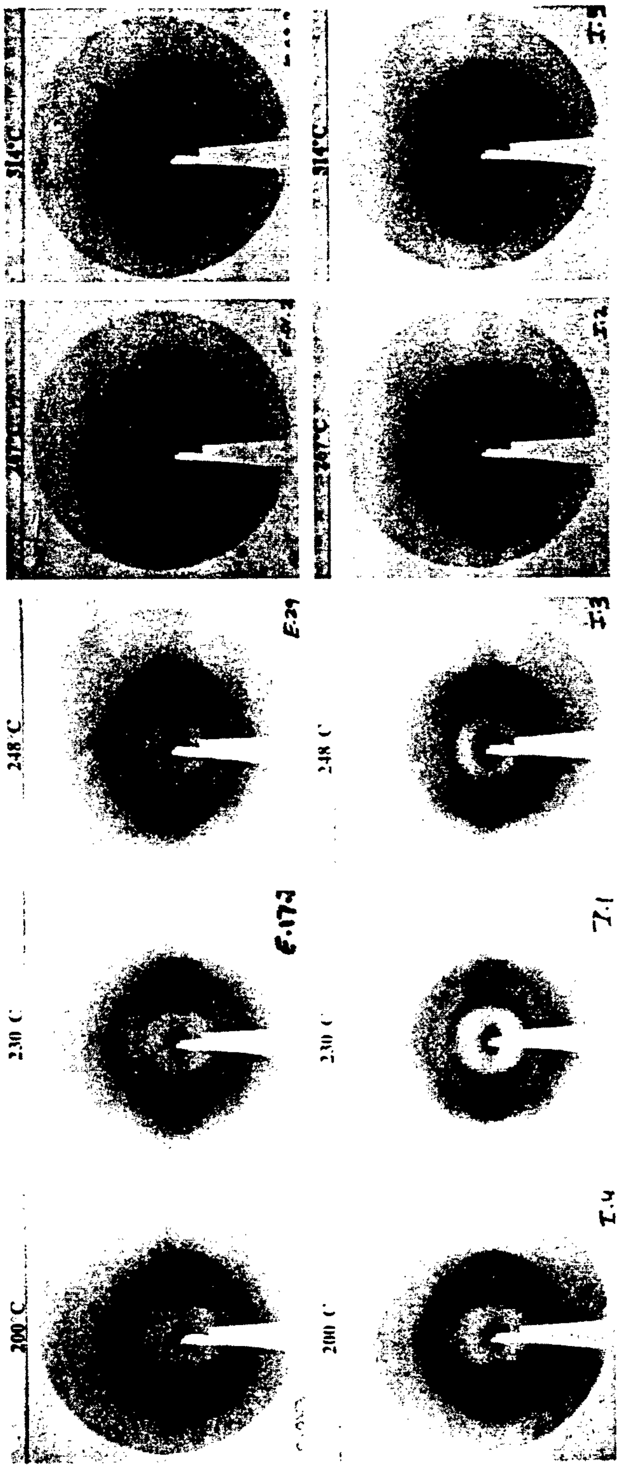
200°C
230°C
248°C
314°C
200°C
230°C
248°C
314°C

Fig. 24. WAXD flat-plate photographs for SAF stabilized at 1°C min^{-1} in air at constant length (top row) and at zero tension (bottom row) and to various HTTs.

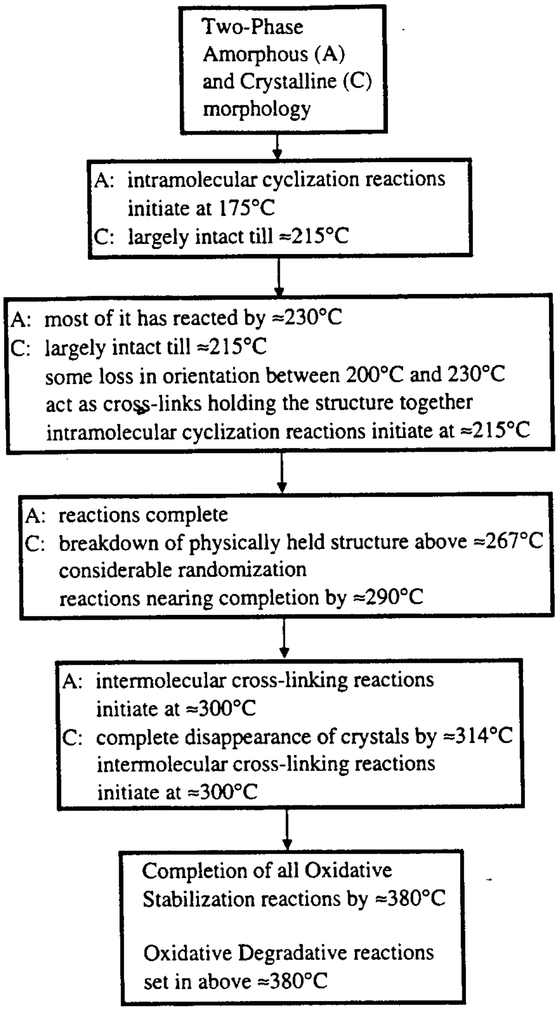
Two-Phase
Amorphous (A)
and Crystalline (C)
morphology
A: intramolecular cyclization reactions initiate at 175°C
C: largely intact till ≈215°C
A: most of it has reacted by ≈230°C
C: largely intact till ≈215°C
some loss in orientation between 200°C and 230°C
act as cross-links holding the structure together
intramolecular cyclization reactions initiate at ≈215°C
A: reactions complete
C: breakdown of physically held structure above ≈267°C
considerable randomization
reactions nearing completion by ≈290°C
A: intermolecular cross-linking reactions initiate at ≈300°C
C: complete disappearance of crystals by ≈314°C
intermolecular cross-linking reactions initiate at ≈300°C
Completion of all Oxidative Stabilization reactions by ≈380°C
Oxidative Degradative reactions set in above ≈380°C

Fig. 25. Schematic illustration of the oxidative stabilization process with increasing HTT in co-polymer PAN fibers held at constant length.

270°C achieved at a heating rate of 1°C min^{-1} for co-polymer PAN fibers (6% methylacrylate and 1% itaconic acid) as the most optimum and cost-effective stabilization process for producing carbon fibers with superior properties [11]. These results were based on the assumption that shrinkage measurements determined the criterion for the oxidative stabilization reaction. However, as shown in this study, most of the macroscopic shrinkage corresponds to stabilization in the amorphous part of PAN, and therefore cannot be used as a sufficient criterion for optimizing process conditions. A final HTT of ~380°C seems to be necessary for complete oxidative stabilization. It is possible that higher stabilization temperatures could cut processing times, at the same time producing carbon fibers with improved properties. Recent studies have indicated the beneficial aspects of high-temperature oxidative stabilization [12]. Oxidative degradative reactions set in beyond ~380°C.

For stabilization in argon, dehydrogenation is a slow process, leading us to believe that stretching of the precursor fiber could be carried out over a wide temperature range, ultimately producing high-modulus carbon fibers. Moreover, the presence of hydrogen promotes formation of more graphitic carbons, especially in directions perpendicular to the layers. Crystallites remain relatively mobile during the early stages of carbonization and little cross-linking occurs. Further studies on argon-stabilized samples are planned.

Various issues raised in this study will be addressed in subsequent work.

Acknowledgements—The authors were partially supported by work carried out at the Pennsylvania State University under contract from the Air Force Office of Scientific Research (AFOSR). Financial support of AFOSR is gratefully acknowledged.

REFERENCES

1. S. B. Warner, D. R. Uhlmann and L. H. Peebles, Jr, *J. Mater. Sci.* **14,** 1893 (1979).
2. G. H. Olive and S. Olive, *Adv. Polym. Sci.* **32,** 123 (1979).
3. B. G. Frushour, *Polym. Bull.* **4,** 305 (1981).
4. G. Hinrichsen and H. Orth, *Polym. Lett.* **9,** 529 (1971).
5. D. Grove, P. Desai and A. S. Abhiraman, *Carbon* **26,** 403 (1988).
6. G. S. Bhat, F. L. Cook, A. S. Abhiraman and L. H. Peebles, Jr, *Carbon* **28,** 377 (1990).
7. R. B. Mathur, O. P. Bahl, V. K. Matta and K. C. Nagpal, *Carbon* **26,** 295 (1988).
8. Z. Bashir, *Carbon* **29,** 1081 (1991).
9. W. Watt, D. J. Johnson and E. Parker, *Carbon Fiber Conference,* 3 (1974).
10. A. Gupta, M. S. Thesis, The Pennsylvania State University (1993).
11. E. Fitzer, W. Frohs and M. Heine, *Carbon* **24,** 387 (1986).
12. R. B. Mathur, O. P. Bahl and J. Mittal, *Carbon* **30,** 657 (1992).
13. J. Mittal, O. P. Bahl, R. B. Mathur and N. K. Sandle, *Carbon* **32,** 1133 (1994).
14. R. E. Franklin, *Proc. R. Soc. (London)* **A 209,** 196 (1951).
15. R. E. Franklin, *Acta. Cryst.* **3,** 107 (1950).
16. D. J. Muller, E. Fitzer and A. K. Fiedler, Proc. Int. Conf. Carbon Fibers, their Composites and Applications, London. p. 10. (1971).
17. C. Burger and W. Ruland, Proc. 20th Biennial Conf. Carbon, Santa Barbara. p. 276 (1991).

Pergamon

Carbon Vol. 35, No. 6, pp. 809–818, 1997
Copyright © 1997 Elsevier Science Ltd
Printed in Great Britain. All rights reserved
0008-6223/97 $17.00 + 0.00

PII: S0008-6223(97)00025-0

NEW ASPECTS IN THE OXIDATIVE STABILIZATION OF PAN-BASED CARBON FIBERS: II

A. GUPTA,* and I. R. HARRISON†
Department of Materials Science and Engineering, The Pennsylvania State University, University Park, PA 16802, U.S.A.

(*Received* 19 *June* 1996; *accepted in revised form* 3 *January* 1997)

Abstract—A model detailing the development of morphology in copolymer PAN (polyacrylonitrile) fibers during oxidative stabilization was recently proposed (Gupta and Harrison, *Carbon*, 1996, **34**, 1427). Some of the main features of this model are: (a) a two-step oxidative stabilization process wherein reactions initiate in the amorphous phase, and progress to the crystalline phase at high temperatures; (b) intramolecular cyclization reactions dominating the early part of the stabilization process, intermolecular cross-linking occurring at higher temperatures and in the presence of oxygen; (c) macroscopic shrinkage along the fiber axis primarily being an entropy-driven process, with "chemical" effects serving to modify the entropic response; and (d) a final heat treatment temperature (HTT) of ~380°C seemed to be necessary in order to effect complete oxidative stabilization. In the current work, results from tensile testing and X-ray experiments help in validating the proposed model. Studies on isothermal stabilization indicate no benefits when compared to a rapid and more effective constant temperature ramp process. Additionally, for stabilization in argon, dehydrogenation is a slow process, leading us to believe that stretching of precursor fiber could be carried out over a wide temperature range. © 1997 Elsevier Science Ltd

Key Words—A. Carbon fibers, B. oxidation, B. stabilization.

1. INTRODUCTION

An essential and time-consuming step in the conversion of PAN fibers to high-performance carbon fibers is the oxidative stabilization step. Oxidative stabilization is normally performed at temperatures between 200 and 300°C in the presence of oxygen and for extended periods of time, varying from 1 to 24 hours. Air is typically the medium of choice. This stabilization is necessary to cross-link PAN chains and prepare a structure that can withstand the rigors of high temperature processing. The reaction is highly exothermic and, if not controlled, can lead to run-away autocatalytic processes resulting in "melting down" and coalescing of fibers in a tow. Non-optimized processing cycles during oxidative stabilization can also lead to excessive weight-loss during subsequent carbonization and graphitization, and to carbon fibers with inferior properties.

The stabilization chemistry of PAN has been extensively studied in the past 35 years and there appears to be some general consensus on the mechanisms involved. However, it is by no means exhaustive, as there is still no direct evidence for cyclization reactions postulated as occurring during the stabilization step. Various theories abound regarding initiation and propagation of various reactions, but no definitive mechanisms have been proved. There also exist questions as to whether the stabilization step occurs by intramolecular or intermolecular polymerization [1]. Given the helical nature of the extended PAN-molecule, and the strong intramolecular repulsion of neighboring pendant nitrile groups, it seems unlikely that intramolecular reactions would be a feasible possibility. However, intermolecular reactions would lead to non-cyclic –C=N– structures, whereas, electron microscopy has revealed the formation of graphitic structures at temperatures as low as 320°C [2]. Nevertheless, none of the mechanisms have conclusively been either proved or disproved.

To further elucidate mechanisms involved, an extensive study detailing various aspects of the stabilization process was undertaken in our laboratories. Important aspects, including the role of environment on the progression of stabilization reactions, the nature of accompanying morphological rearrangements (especially orientational relaxations), and the role of stress fields in the progression of reactions were studied. A comprehensive model for morphological changes occurring during the oxidative stabilization of PAN-based carbon fibers was proposed (see Fig. 1) [3,4]. Stabilization reactions were found to initiate in the amorphous part of the copolymer and lead to a stress build-up for constant length experiments. Crystalline morphology is largely preserved at this time; in fact, the crystals act as "cross-links" holding the structure together and thereby contribute to the stress rise. As temperature is raised, reactions spread to the crystalline phase; this leads to a breakdown of the "cross-linked" crystalline structure and a corresponding drop in thermal stress. Drop in

---

*Present address: Ciba Specialty Chemicals, 540 White Plains Road, Tarrytown, NY 10591, U.S.A.

†Corresponding author.

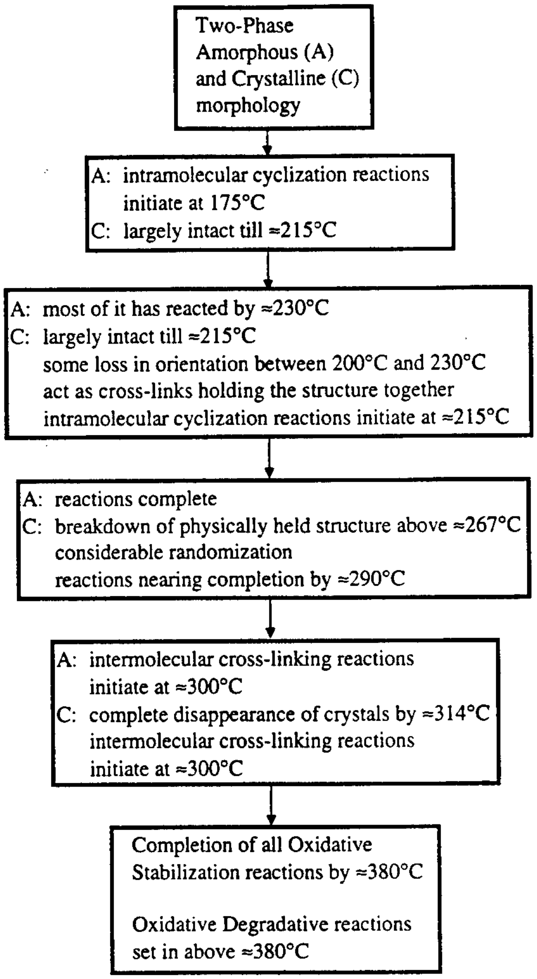
Two-Phase Amorphous (A) and Crystalline (C) morphology
A: intramolecular cyclization reactions initiate at 175°C
C: largely intact till ≈215°C
A: most of it has reacted by ≈230°C
C: largely intact till ≈215°C
some loss in orientation between 200°C and 230°C
act as cross-links holding the structure together
intramolecular cyclization reactions initiate at ≈215°C
A: reactions complete
C: breakdown of physically held structure above ≈267°C
considerable randomization
reactions nearing completion by ≈290°C
A: intermolecular cross-linking reactions initiate at ≈300°C
C: complete disappearance of crystals by ≈314°C
intermolecular cross-linking reactions initiate at ≈300°C
Completion of all Oxidative Stabilization reactions by ≈380°C
Oxidative Degradative reactions set in above ≈380°C

Fig. 1. Schematic of the oxidative stabilization process with increasing HTT in copolymer PAN fibers held at constant length [3].

thermal stress is a result of the loss of inter-chain Van der Waals cohesive energy. Stabilization in this temperature regime was proposed to be primarily intramolecular due to the nature of thermal stress decay. If it were intermolecular, a cross-linked structure would result and stress decay would not be observed.

Stabilization in the presence of oxygen leads to a loss of inter-chain cohesive energy in the amorphous phase at much lower temperatures, resulting in a more "fluid-like" structure that is easily deformed. This accounted for the much smaller rise in thermal stress on stabilization in the presence of oxygen as compared to stabilization in argon. Crystalline morphology is largely preserved, although considerable randomization of crystal lamellae takes place. Reactions spread to crystalline regions at higher temperatures, resulting in stress decay due to breakdown of crystals acting as "cross-links"; however, oxygen also prevents decay to zero stress at high temperatures, primarily by aiding in the formation of intermolecular cross-links, above ~300°C in air.

Macroscopic shrinkage along the fiber axis during stabilization was proposed to be primarily an entropy-driven process involving randomization of highly oriented amorphous and crystalline phases with increasing heat treatment temperature (HTT). Most of the macroscopic shrinkage was shown to arise from the amorphous part of the polymer as a result of oriented chains in amorphous regions reverting to their "random coil" configuration. Reversion to random-coil configuration is brought about by loss of inter-chain Van der Waal cohesive energy forces due to intramolecular cyclization. Macroscopic shrinkage initiated earlier and also occurred to a much greater extent in the presence of oxygen than in its absence. There thus seems to be a "chemical" modification to this "entropic" process. Randomization in the amorphous phase is transferred to crystalline regions due to the inherent connectivity of the amorphous and crystalline phases. This behavior is analogous to observations in highly oriented thermoplastic polymeric fibers, wherein exposure to temperatures near or above the melting point causes a randomization of structure and a net shrinkage along the fiber axis. Stabilization reactions in the crystalline phase do not contribute greatly to macroscopic shrinkage. Presumably, by the time reactions reach the crystalline phase, the structure is already well relaxed and can easily accommodate localized variations in inter-chain cohesive forces.

The current work was conducted as an extension of the previous study. Experiments were conducted in order to validate proposed mechanisms. Additionally, studies were carried out in order to investigate the beneficial aspects of isothermal oxidative stabilization as opposed to a constant temperature ramp-up stabilization. Stabilization in an inert atmosphere was also studied as an alternative to oxidative stabilization and in order to better understand morphological rearrangements taking place in PAN fiber subject to high temperatures.

2. EXPERIMENTAL

Progress of stabilization and the accompanying morphological changes were monitored through various measures, such as thermal stress development, differential scanning calorimetry, percentage weight-loss, tensile testing, small-angle X-ray scattering and wide-angle X-ray diffraction.

2.1 *Precursors*

PAN fibers used in the study were designated "SAF", and supplied by Courtaulds Fibers, U.K. This precursor fiber is most probably a copolymer of acrylonitrile, methylacrylate and itaconic acid and is wet-spun from a sodium thiocyanate solution. As-received fibers were supplied in tows of 6000 fibers with an average denier of 1.09 and a mean diameter of 11.3 μm.

2.2 *Stabilization*

Stabilization was carried out in a batch process using both the constant length and the constant tension modes. A three-zone tube furnace was used for all experiments. For constant length experiments, precursor fiber was pre-stressed to a constant tension, and stabilization carried out in continuously flowing oxygen, air or argon (4 l min^{-1}) at a heating rate of 1°C min^{-1}. For constant tension experiments, precursor fiber was free to shrink/stretch. Final HTT varied from 200 to 500°C. Sample collection involved heating the precursor fiber to the desired HTT and rapidly quenching the stabilized fiber in the desired atmosphere.

2.3 *Thermal stress*

Thermal stress in constant length experiments was monitored using a 5 lb load cell, wherein one end of the fiber was rigidly fixed, and the other end attached to the load cell. Output from the load cell was amplified and fed to a strip-chart recorder, which produced a trace of fiber thermal stress as a function of furnace temperature. Furnace temperature was measured by a thermocouple placed in the furnace tube adjacent to the fiber tow. These measurements may not account for temperatures inside the fiber tow which may be considerably different from those measured adjacent to the tow.

2.4 *Thermal analysis*

Differential scanning calorimetry (DSC) experiments were carried out on a DuPont 2910 DSC instrument. Heating rates ranging from 1 to 30°C min^{-1} were used to study the influence of heating rate on the exothermic behavior of precursor PAN fiber. Experiments were performed in oxygen, air and argon atmospheres. All experiments allowed the SAF fiber to shrink in the DSC capsule. Initial sample weight was used in calculating heat flow and therefore y-axis values correspond to lower estimates of heat flow at high temperatures where significant weight-loss occurs.

Percentage weight-loss experiments for SAF were carried out on a Perkin–Elmer TGS-2 thermal gravimetric analyzer (TGA) at 1°C min^{-1}. Experiments were performed in oxygen, air and argon atmospheres. Data from TGA was used in calculating percentage carbon yield for fibers heat treated to various HTTs. Plots obtained from the DSC and TGA plotter were digitized and converted to a form suitable for further analysis on a personal computer. Digitization led to some loss of smoothness in the curves.

2.5 *Fiber diameter measurements*

Fiber diameters were measured at magnifications of 500 × using an ISI-40 scanning electron microscope. Prior to measurements, samples were cut and attached to aluminium stubs using double-faced adhesive film. In order to prevent charging, samples were sputter coated with gold for 1 min. Care was taken to include at least 15 different fibers in a micrograph. The resulting micrograph was then scanned by a color/gray scanner and image transferred to a personal computer. After being digitized using an image analysis program "Image NIH", image magnification was increased electronically to 3000 × and fiber diameters recorded in microns. An average diameter along with standard deviation was calculated for each specimen.

2.6 *Tensile testing*

All tensile testing was done on single fiber samples. Paper tabs, with a 25.4 mm gauge length were cut as shown in Fig. 2. Using fine tweezers, a single fiber was removed from two inch sections of tow, making certain not to touch the fiber within its eventual gauge length. The fiber was placed on the paper tab, aligned according to tab guide lines and fixed to the tab with glue. The glue was placed at gauge length boundaries assuring that the fiber was fixed at the proper gauge length.

The test apparatus consisted of an Instron 4201 tensile tester equipped with an Instron 10 N load cell. The Instron unit was interfaced with a personal computer loaded with Instron Series IX mechanical testing software. With the interfacing of both components, testing, data acquisition and data analysis were all controlled by the personal computer.

From each of the various sample types, 15–20 fibers were tested. Samples were mounted in the tester grips as shown in Fig. 3. Prior to testing, sides of the gripped tensile tabs were severed by a pair of scissors or a hot wire, and average fiber diameters entered into the computer. Testing was performed at crosshead speeds of 5 mm min^{-1} for samples with elongation to break of $>5\%$ and 0.5 mm min^{-1} for samples with elongation to break of $<5\%$.

Average values of fiber tensile modulus, tensile strength and elongation to break were calculated for each specimen.

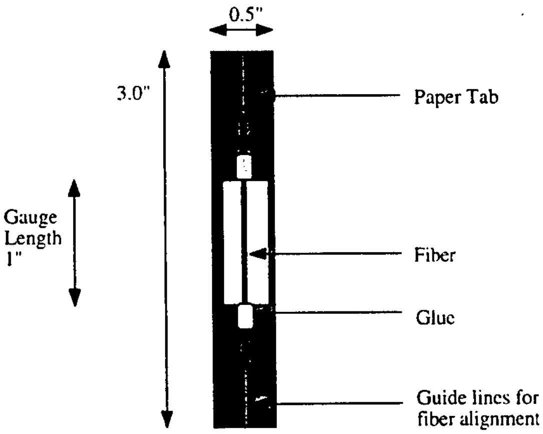

Fig. 2. Fiber tensile tab.

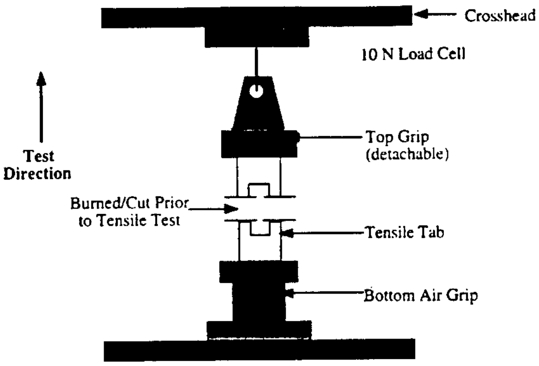

Fig. 3. Tensile testing apparatus.

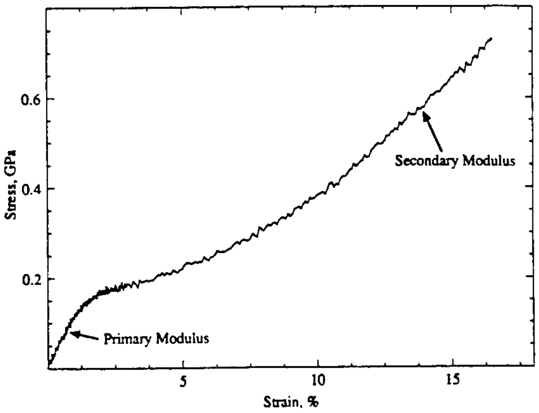

Fig. 4. Stress–strain behavior of as-received SAF precursor fiber.

2.7 *Small-angle X-ray scattering (SAXS)*

All SAXS experiments were performed with Cu Kα radiation ($\lambda = 1.5418$ Å) with the X-ray generator operating at 40 kV and 35 mA. Monochromatization was achieved using total reflection of X-rays from two nickel-coated mirrors placed at 90° to each other. Bending the nickel-coated mirrors also served to focus the X-ray beam. A three pin-hole collimation unit was used to produce an intense X-ray point source at the detector with minimal parasitic scatter. A two-dimensional solid-state X-ray detector interfaced to a personal computer was used for data acquisition and analysis [5]. The smallest possible scattering angle at which measurements could be made with a high level of accuracy corresponded to a Bragg spacing of ~150 Å. Sample to detector distance was maintained at 12 cm and counting times were typically 12 hours per sample.

2.8 *2.8 Wide-angle X-ray diffraction (WAXD)*

WAXD experiments were performed on a set-up similar to the one used for SAXS, but with the detector replaced by a photographic film. Sample to detector distance was maintained at 3.5 cm and exposure times were typically 6 hours.

3. RESULTS AND DISCUSSION

3.1 *Mechanical properties of stabilized fibers*

Figure 4 is a typical stress–strain curve for as-received SAF precursor fiber. The initial elastic portion (primary modulus) is due to a slight reversible straightening of the polymer chains. As the yield point is approached, chains start to move relative to each other because the Van der Waals cohesive energy between the chains is being overcome. Flow and a straightening of non-aligned chains causes a more equable distribution of load between chains so that the cohesive energy of more and more dipoles have to be overcome which accounts for the increasing resistance to flow and increasing secondary stress (secondary modulus). Finally the fiber breaks by a combination of chain fracture and pull out.

Variations in tensile strength, primary Young's modulus and elongation for the various oxidatively stabilized fibers are shown in Figs 5–7.

On stabilization in air, a drop in strength is seen on heating to ~314°C. This decrease in strength is due to the loss of inter-chain cohesive energy as a result of intramolecular cyclization reactions (*cf* Fig. 5). If there is any appreciable intermolecular

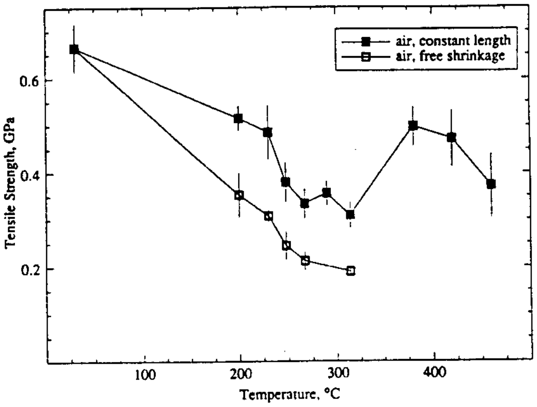

Fig. 5. Change in tensile strength of SAF fibers as a function of stabilization temperature (air, 1°C min^{-1}).

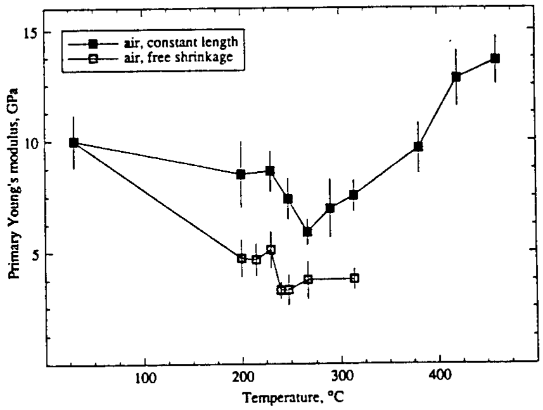

Fig. 6. Change in primary Young's modulus of SAF fibers as a function of stabilization temperature (air, 1°C min^{-1}).

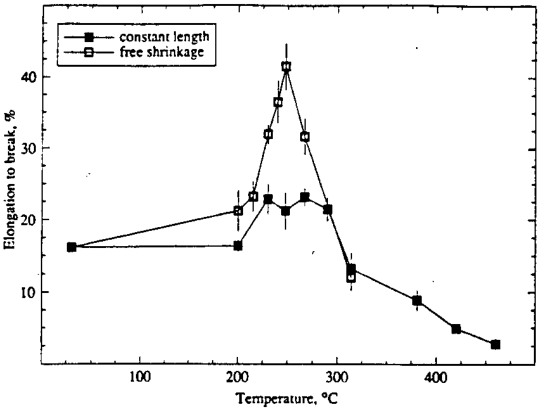

Fig. 7. Change in percentage elongation to break of SAF fibers as a function of stabilization temperature (air, 1°C min^{-1}).

crosslinking, as has been postulated by many [6,7], it should lead to an increased resistance to plastic flow and therefore higher strength for stabilized fibers. However, this is not observed. Also, for fibers free to shrink during stabilization, strength loss is much higher. Upon comparison of resulting stress–strain curves for fibers stabilized at constant length and under free shrinkage conditions to HTTs of 230°C (Fig. 8) and 248°C (Fig. 9), it is apparent that when the fiber is free to shrink, development of secondary modulus at high strains is much reduced (see Fig. 10). It is proposed that rotation of the lateral –CN groups during shrinkage permits a greater probability of these groups being approximately oriented for a conjugation reaction. This reaction results in a higher degree of intramolecular cyclization, leading to a lower concentration of intact polar nitrile groups, and therefore a lower inter-chain cohesive energy at high strains. For stabilization at constant length, predominantly isotactic sequences cyclize leaving many unreacted –CN groups which lead to a build-up in secondary modulus at high strains. Beyond ~314°C, strength rises due to inter-molecular cross-linking reactions. Oxidative degradative reactions set in at ~380°C and lead to a rapid drop in strength at high temperatures.

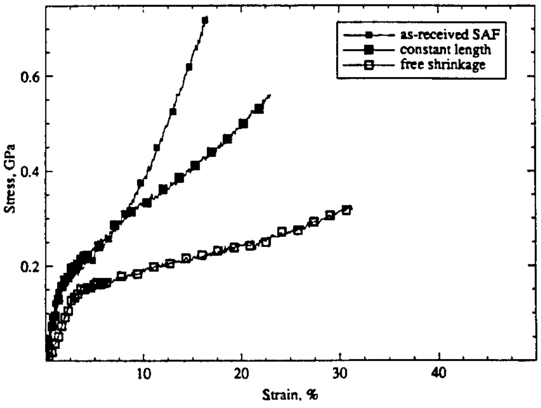

Fig. 8. Stress–strain curves of SAF and fibers stabilized to a HTT of 230°C under constant length and free shrinkage conditions (air, 1°C).

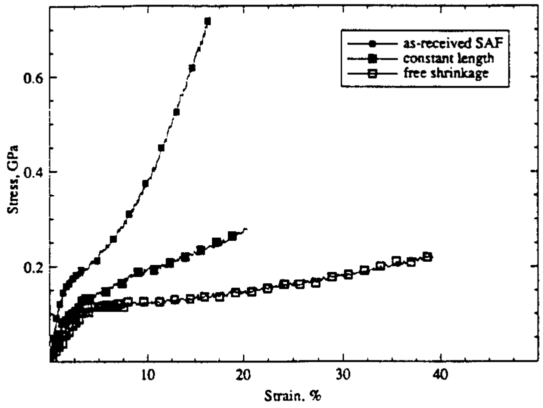

Fig. 9. Stress–strain curves of SAF and fibers oxidatively stabilized to a HTT of 248°C under constant length and free shrinkage conditions.

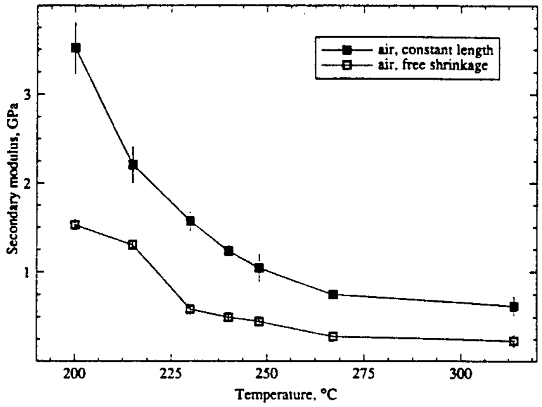

Fig. 10. Behavior of secondary modulus of fibers stabilized under constant length and free shrinkage conditions (air, 1°C min^{-1}). Secondary modulus of SAF: 5.29 ± 0.41 GPa.

Similar behavior in strength is observed for stabilization in argon; however, the strength falls to near zero values at ~270°C due to the absence of any stabilizing intermolecular cross-links. At this stage the fiber is extremely fragile and breaks under very small loads.

Trends observed in the behavior of strength are also mirrored in values of the primary Young's modulus (*cf* Fig. 6). For stabilization in air at constant length, modulus falls rapidly between 215 and 267°C and is attributed to randomization of crystalline morphology. When fibers are free to shrink during stabilization, modulus is much lower than corresponding values for stabilization at constant length due to greater randomization of both the amorphous and crystalline morphology. However, trends observed for stabilization under constant length and free shrinkage conditions are the same. Increase in modulus at higher temperatures is due to inter-molecular cross-linking reactions.

It was also observed that on stabilization in argon, decrease in secondary modulus is very slow when compared to fibers heated in presence of oxygen, indicating that cyclization reactions propagate at a much slower rate (see Fig. 11).

Elongation to break values for fibers free to shrink during oxidative stabilization show a dramatic increase between 215 and 248°C when compared to corresponding values for fibers stabilized at constant length (*cf* Fig. 7). This increase is attributed to the uncoiling at high strains of the cyclized segments in the amorphous region of the polymer. If macroscopic shrinkage was indeed "chemical" in nature, as has been postulated [6], uncoiling at high strains should not be observed. At higher temperatures, percentage elongation to break drops due to intermolecular cross-linking reactions and the formation of a network structure.

Behavior in tensile strength, Young's modulus and percentage elongation to break lend credence to our hypothesis that macroscopic shrinkage observed during stabilization is an entropy-driven process. Additionally, stabilization at low temperatures is primarily intramolecular, with intermolecular reactions occurring at higher temperatures, >300°C, in the presence of oxygen.

3.2 *Optimum conditions for oxidative stabilization*

3.2.1 *Maximum HTT for optimum oxidative stabilization.* An extensive previous study has outlined a final HTT of 270°C achieved at a heating rate of 1°C min^{-1} for copolymer PAN fibers (6% methylacrylate and 1% itaconic acid) as the most optimum and cost-effective stabilization process for producing carbon fibers with superior properties [8]. These results were based on shrinkage measurements as determining the criterion for the oxidative stabilization reaction. However, as shown in this study, most of the macroscopic shrinkage corresponds to stabilization in the amorphous part of PAN and therefore cannot be used as a sufficient criterion for optimizing process conditions. Based on DSC and WAXD results, a final HTT of ~380°C seems to be necessary for complete oxidative stabilization. It is possible that higher stabilization temperatures could cut processing times, at the same time producing carbon fibers with improved properties. Recent studies have indicated the beneficial aspects of high temperature oxidative stabilization. Significant improvement in mechanical properties of Type III carbon fibers prepared at 1000°C from samples that had been exposed to temperatures as high as 400°C when compared to a HTT of only 267°C were reported [9]. Tensile strength rose by up to ~28% and Young's modulus improved by ~9%. Moreover, upon oxidative stabilization to high temperatures, samples have low hydrogen contents [2] and, as such, there should be little formation of tar due to evolution of condensable hydrocarbons during carbonization. For carbon fiber manufacturing facilities, this translates to more production time since frequent cleaning of the reactors can be avoided.

However, in terms of cost-effective production, oxidative stabilization to high temperatures seems to be disadvantageous. Percentage yield for fibers carbonized in a TGA to 750°C dropped from a maximum of ~69% for a HTT of 290°C to ~63% for a HTT of 380°C (see Fig. 12). Moreover, the effect of high temperature oxidation on properties of carbon fibers carbonized and graphitized to temperatures approaching 2000–3000°C (Type II and Type I carbon fibers) has not been studied. It is likely that high temperature graphitization of such fibers will cause voids and other defects in the structure due to volatilizing carbon–oxygen, leading to inferior mechanical properties.

3.2.2 *Isothermal oxidative stabilization.* Oxidative stabilization studies, so far, have dealt with constant ramp-up temperature profiles. It is also possible that stabilization reactions take place in the crystal at lower temperatures but with longer

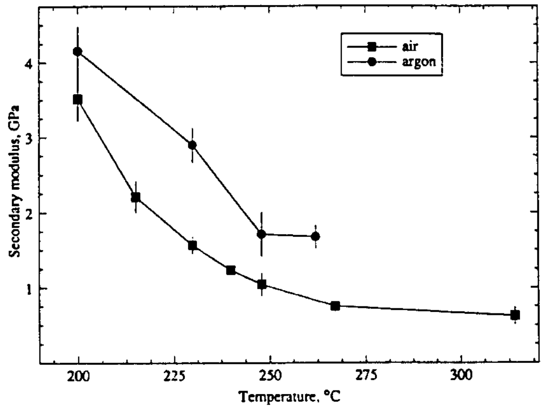

Fig. 11. Behavior of secondary modulus of fibers stabilized at constant length in air and argon (1°C min^{-1}). Secondary modulus of SAF: 5.29±0.41 GPa.

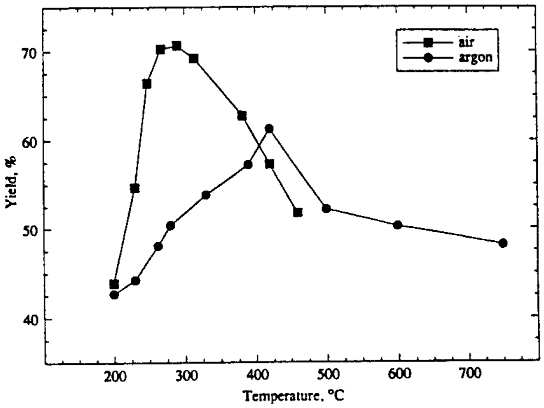

Fig. 12. Percentage yield for fibers stabilized in air and in argon to various HTTs and carbonized to 750°C in an inert atmosphere.

stabilization times. The effect of a constant ramp-up in temperature vs isothermal treatment at a lower temperature was therefore studied.

Figures 13 and 14 show the behavior in thermal stress for SAF held isothermally at various HTT for long periods of time, up to 20 hours, as a function of temperature and time, respectively. For isothermal stabilization at 314°C for 20 hours, a drop in thermal stress, corresponding to break down of the crystalline component, is seen at temperatures between 314 and 390°C (*cf* Fig. 13). This leads us to believe that oxidative stabilization is not complete even for isothermal stabilization at temperatures as high as 314°C. However, as seen by the behavior in thermal stress (*cf* Fig. 14), oxidative degradation reactions set in and lead to a gradual rise in stress at long times. For isothermal stabilization at 381°C, degradative reactions set in quickly, and the fiber tow breaks in <6 hours.

Similar behavior is mirrored in the behavior of heat flow as measured by DSC (see Fig. 15). Samples were heated in air at 1°C min^{-1} to various HTT, held isothermally for ~20 hours, and ramped up again at 1°C min^{-1} to ~500°C. Distinct shoulders can be seen in the DSC curves after isothermal treatment, even for isothermal treatments at temperatures as high as 314°C. This is seen more clearly in Fig. 16 which plots the thermal stress and DSC behavior for the sample isothermally treated at 269°C for 20 hours. The decay in thermal stress coincides with the shoulder on the DSC curve, indicating that oxidative stabilization reactions are still taking place.

Behavior in thermal stress and heat flow lead us to believe that oxidative stabilization reactions are not at all complete at low temperatures, as has been previously believed. Further reactions in the crystalline component are activated at high temperatures. Isothermal treatment could serve to initiate/propagate reactions in the crystalline phase, but temperatures as high as ~380°C are necessary to see them to completion. However, isothermal treatment at high temperatures lead to oxidative degradation and may cause poor mechanical properties in carbonized fibers. It may be more beneficial to stabilize the fibers using a constant heating rate profile to high temperatures, ~380°C, thereby exposing the fibers to high temperatures for a short

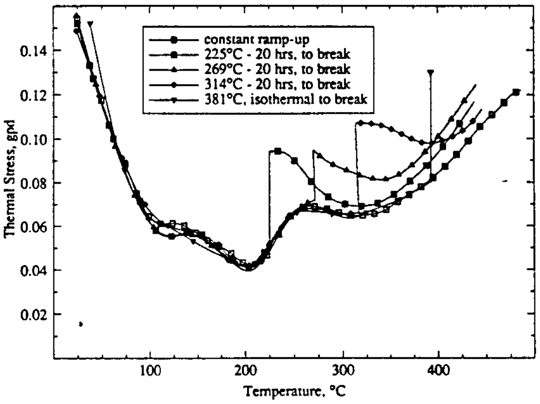

Fig. 13. Development of thermal stress in SAF held isothermally at various HTT as a function of temperature (air, 1°C min^{-1}).

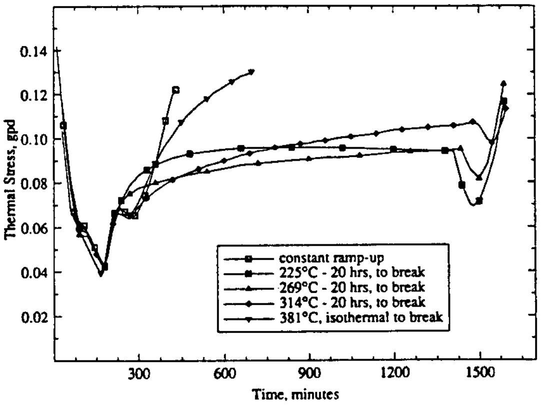

Fig. 14. Developmentof thermal stress in SAF held isothermally at various HTT as a function of time (air, 1°C min^{-1}).

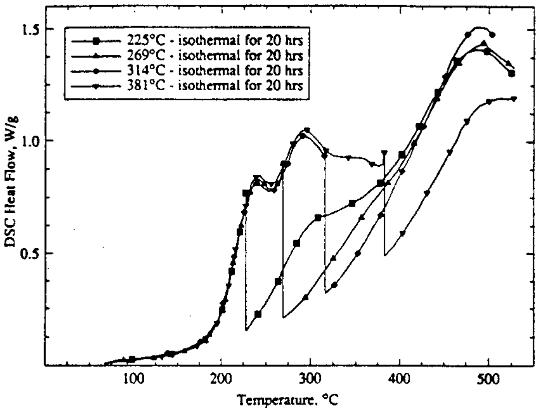

Fig. 15. DSC curves of SAF held isothermally at various HTT as a function of temperature (air, 1°C min^{-1}).

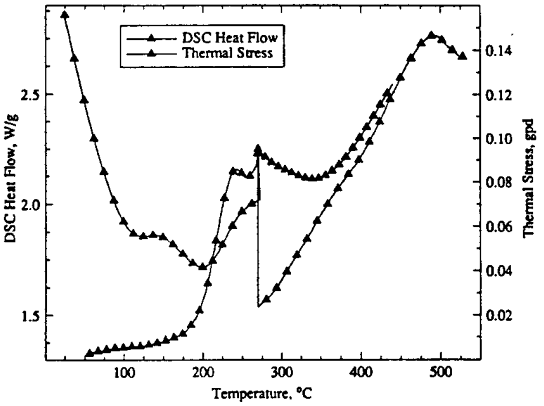

Fig. 16. Comparison of thermal stress and DSC behavior of SAF held isothermally at 267°C for 20 hours (air, 1°C min^{-1}).

period of time and preventing oxidative degradation, thus resulting in well-stabilized fibers.

3.3 *Behavior at high temperatures of fibers stabilized in inert atmospheres*

Stabilization of SAF copolymer in an inert atmosphere at HTT up to ∼330°C leads primarily to intramolecular cyclization with little or no intermolecular cross-linking [2]. Appearance of a very weak SAXS maxima at temperatures between ∼200 and ∼248°C indicates a preferential reaction in the amorphous phase. The maxima disappears above ∼248°C and is due to reactions propagating into the crystalline component of the copolymer, thereby leading once again to negligible electron density contrast between crystalline and amorphous phases. Appearance of SAXS maxima was attributed to the presence of acid-group containing comonomers in the amorphous phase. Intramolecular cyclization reactions were considered complete at temperatures close to ∼330°C. At this stage, the stabilized fiber is extremely weak and breaks under very small loads.

Further heat treatment of these fibers leads to the formation of another meridional SAXS maxima with a long period of about 79 Å (see Fig. 17). Similar behavior has been reported before [10]. The second maxima is stable between ∼389 and ∼600°C and disappears at higher temperatures, >∼600°C (see

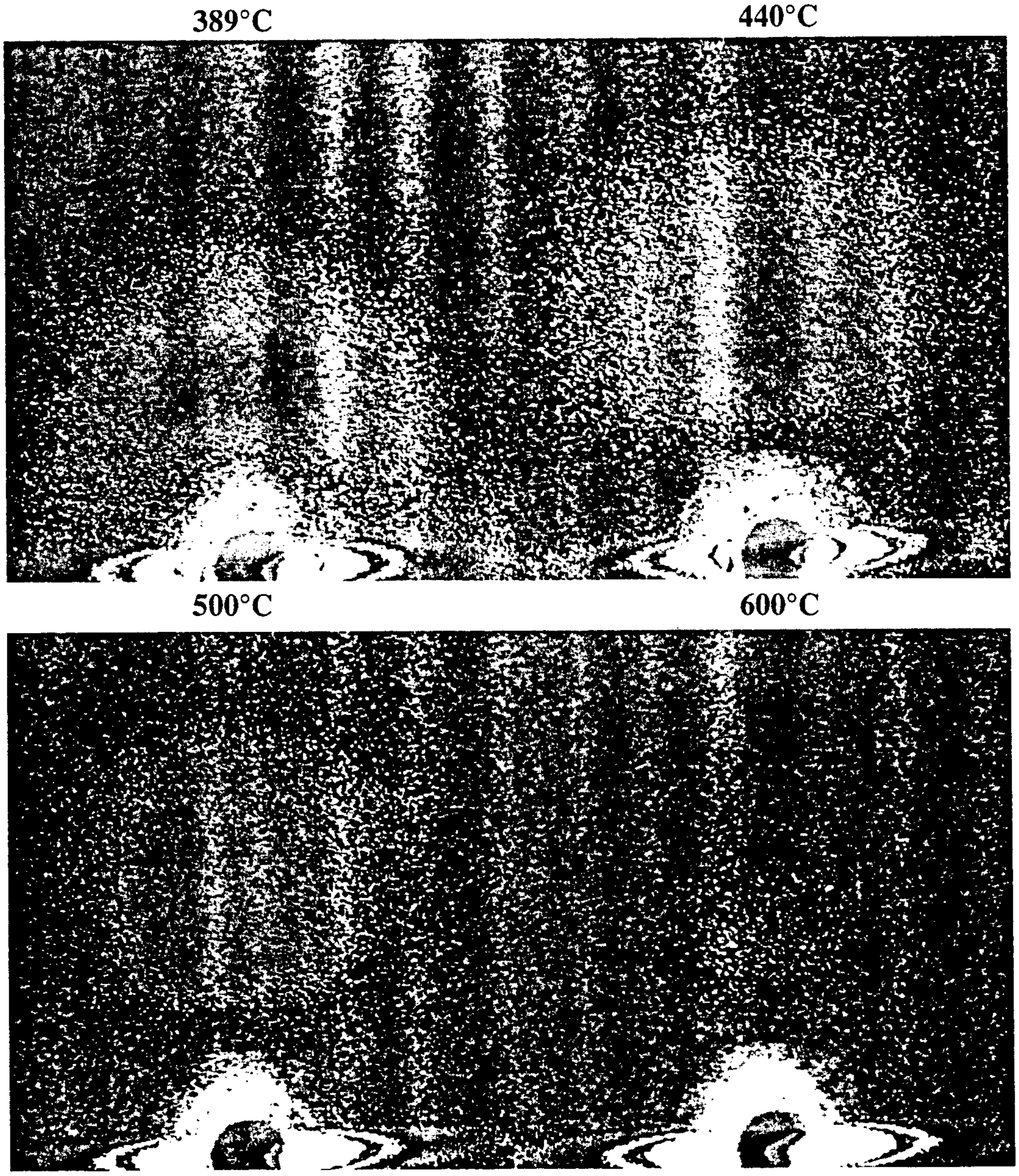

Fig. 17. SAXS patterns of SAF stabilized in inert atmospheres at constant length and to high temperatures (argon, 1°C min^{-1}).

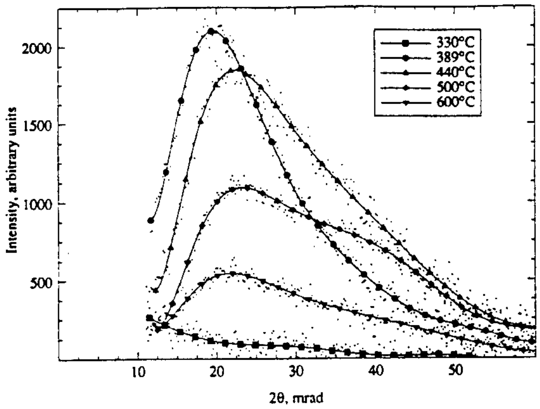

Fig. 18. SAXS curves of SAF stabilized in inert atmospheres at constant length and to high temperatures (argon, 1°C min^{-1}).

Fig. 18). Appearance of this SAXS maxima is accompanied by the formation of two relatively sharp WAXD reflections at *d*s of 5.82 and 3.44 Å, and with similar preferred orientations (see Fig. 19). Appearance/disappearance and the preferred orientation of WAXD reflections also corresponds to those of the SAXS maxima, indicating that the origins of both the WAXD and SAXS reflections are the same and that two distinct species with similar molecular packing exist in the fiber at HTT between ~389 and ~600°C. It is speculated that these two distinct species correspond to:

(1) cyclized chain segments (of a lower density); and
(2) aromatized chain segments (of a higher density).

With increasing HTT, more and more cyclized segments convert to aromatic sheets and once again lead to a negligible electron density contrast between the two phases and the disappearance of the SAXS maxima. This interpretation can justify the behavior

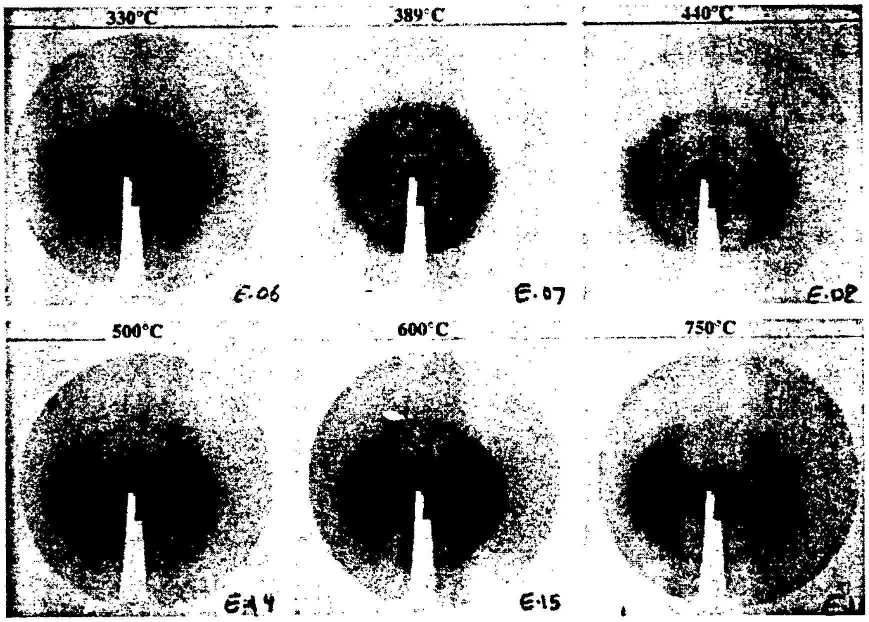

Fig. 19. WAXD flat-plate photographs of SAF stabilized in inert atmospheres at constant length and to high temperatures (argon, 1°C min^{-1}).

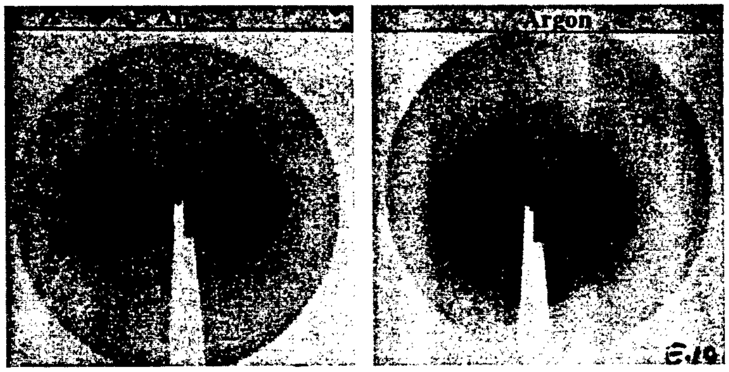

Fig. 20. WAXD flat-plate photographs of carbon fibers prepared at 1000°C from SAF stabilized in air and in inert atmospheres.

in SAXS and WAXD reflections with increasing HTT. However, the appearance of the SAXS maxima at ~389°C still cannot be accounted for.

Thermal stress in the fiber falls to near zero values for stabilization in argon, corresponding with the completion of intramolecular cyclization reactions in the amorphous and crystalline phases [2]. As temperature is increased beyond 400°C, thermal stress in the fiber recovers from zero and rises, although to very small values. At a HTT of ~1000°C, the fiber is sufficiently strong to withstand tensile testing, and has a tensile strength of 1.04 GPa and a Young's modulus of 74 GPa.

Figure 20 compares WAXD of carbon fiber carbonized without tension to a HTT of 1000°C at 3°C min^{-1} in argon and prepared from:

(1) fiber stabilized in air (HTT of 314°C, 1°C min^{-1}) at constant length; and
(2) fiber stabilized in argon (HTT of 600°C, 1°C min^{-1}) at constant length.

As seen from the spread of the 002 graphitic reflection, fibers prepared from argon stabilized precursor have a much broader spread in the orientation of graphitic planes than fibers stabilized in air. This accounts for the low modulus of carbon fibers stabilized in argon as compared to oxidatively stabilized carbon fibers (~74 GPa vs ~110 GPa). However, it is speculated that stretching of fibers stabilized in argon, during the carbonization stage, could ultimately produce a much higher orientation of graphitic planes along the fiber axis and subsequently a carbon fiber with a higher modulus. Minimum cross-linking and the relatively high mobility of crystallites during the early stages of carbonization due to the presence of hydrogen [2] would promote formation of more graphitic carbons which can be easily oriented by mechanical stretching.

Percentage yield however drops from ~63% for oxidatively stabilized fibers to ~48% for fibers stabilized in inert atmospheres to a carbonization temperature of 750°C (*cf* Fig. 12).

4. CONCLUSIONS

The present work has served to validate proposals made in the previous study. The drop in strength of fibers oxidatively stabilized at constant length to 314°C indicates that reactions in this temperature regime are primarily intramolecular. The large elongation to break of similar fibers but free to shrink during stabilization also confirms some sort of an "uncoiling" mechanism; this would not have appeared had stabilization been primarily intermolecular. Conclusive evidence is provided which shows that oxidative stabilization reactions initiate in the amorphous part of a copolymeric PAN fiber. Reactions spread to the crystalline components at higher temperatures. It is also possible that reactions take place in the crystal at lower temperatures but with longer stabilization times. However, this isothermal process results in incomplete stabilization of the crystalline component and therefore offers no advantages when compared to a constant temperature ramp process. A maximum HTT of ~380°C seems to be necessary in order to affect "optimum" stabilization of the precursor fiber.

For stabilization in argon, dehydrogenation is a slow process, leading us to believe that stretching of precursor fiber could be carried out over a wide temperature range, ultimately producing high modulus carbon fibers. However, such a process would result in a poor yield of carbon and would therefore be cost-ineffective. X-ray results indicate the presence of two distinct species at high temperatures; although their appearance has not been accounted for, it is postulated that they correspond to cyclized chain segments of a lower density and aromatized chain segments of a higher density.

Acknowledgements—The authors were partially supported by work carried out at The Pennsylvania State University under contract (Contract No. F49620-93-1-0311) from the Air Force Office of Scientific Research (AFOSR). Financial support of AFOSR is gratefully acknowledged.

REFERENCES

1. Bashir, Z., *Carbon*, 1991, **29**, 1081.
2. Watt, W., Johnson, D. J. and Parker, E., *Carbon Fiber Conf.*, 1974, 3.
3. Gupta, A. and Harrison, I. R., *Carbon*, 1996, **34**, 1427.
4. Gupta, A., Ph.D. thesis, The Pennsylvania State University, 1996.
5. Gupta, A., M.S. thesis, The Pennsylvania State University, 1993.
6. Muller, D. J., Fitzer, E. and Fiedler, A. K., *Proceedings of the International Conference on Carbon Fibers, their Composites and Applications*, Paper 2, 1971.
7. Fitzer, E. and Muller, D. J., *Makromol. Chem.*, 1971, **144**, 117.
8. Fitzer, E., Frohs, W. and Heine, M., *Carbon*, 1986, **24**, 387.
9. Mathur, R. B., Bahl, O. P. and Mittal, J., *Carbon*, 1992, **30**, 657.
10. Mayer, M. and Ruland, W., *Proc. 20th Biennial Conf. Carbon*, Santa Barbara, 1991, p. 250.

TASK 3.

Oxidation Resistance of Inhibited C/C Composites

Dr. L. Radovic
Dr. Peter A. Thrower

ATTACHMENT IV

Paper (h)

EFFECTS OF THE SUBSTRATE ON DEPOSIT STRUCTURE AND REACTIVITY IN THE CHEMICAL VAPOR DEPOSITION OF CARBON

F. A. Quli, P. A. Thrower, and L. R. Radovic
Department of Materials Science and Engineering,
The Pennsylvania State University, University Park, PA 16802

Submitted to *Carbon*, January 1998

ABSTRACT

The objective of this work was to determine the effects of the carbon substrate on matrix structure and composite reactivity upon infiltration of carbon cloths with pyrolytic carbon. Pyrolysis of propylene at 750°C was used to produce carbon fiber/carbon matrix composites. Carbon (and ceramic) substrates of differing crystalline order and surface area were infiltrated with pyrolytic carbon at various partial and total propylene pressures. The infiltrated substrates (composites) were heat-treated to 2900°C in order to determine the effect of porosity on the graphitization behavior of the pyrolytic carbon matrices. Under the conditions examined, the kinetics of pyrolytic carbon formation were controlled by the surface area of the substrate. It was found that the mesoporous surface was entirely covered by pyrolytic carbon, but only the larger micropores were accessible to the products of propylene pyrolysis. The oxidation resistances of heat-treated composites prepared by infiltration of low-temperature (ungraphitized) substrates were greater than those of composites produced from infiltration of high-temperature substrates. This was attributed to stress-enhanced graphitization of the matrix due to pore shrinkage.

Keywords: A. carbon composites, A. pyrolytic carbon, B. chemical vapor infiltration,

B. heat treatment, D. reactivity

1. Introduction

Carbon fiber/carbon matrix composites continue to be an important high strength, high temperature-resistant material, especially for aerospace applications. Such composites are often prepared by densifying a fibrous preform with a pyrolytic carbon matrix through a chemical vapor deposition/infiltration (CVD/CVI) process.

The CVD of carbon from the pyrolysis of a hydrocarbon gas is a complex phenomenon and despite decades of research it is not fully understood [1, 2]. Depending on the CVD conditions, the reactions leading to the formation of solid carbon may be predominantly homogeneous (in the gas phase) [3] or heterogeneous (at the substrate surface) [4]. This particular study concentrates on the effects of the substrate on pyrolytic carbon deposition and the resultant reactivity of the composite.

The influence of the substrate on the formation and properties of pyrolytic carbon is an unresolved issue. The catalytic effects of non-carbon substrates such as metals have been well documented [5], but the effects of carbon substrates are debatable. Fitzer [6] has presented evidence of nucleation and growth of carbon crystallites on surface defects. Hoffman [7] has shown the effects of the substrate active surface area on the cracking of hydrocarbons. Other researchers consider the gas phase conditions to be much more important to the formation of pyrolytic carbon. Griswald has shown evidence that the precursors to pyrolytic carbon are large complex hydrocarbons which form in the gas phase [3]. In their study of the CVI of carbon fiber felts, McAllister et al. found that the surface plays a role only initially, and after a layer of carbon is deposited the surface loses any catalytic effect [8]. The role of the substrate, if any, seems to be highly dependent on the CVD conditions.

In this study, carbon CVD was carried out on substrates of varying pore structure and crystallinity and under various total and partial pressures of propylene. The resultant composites were analyzed to determine whether or not the substrate surface was an important deposition factor. The efficiency of propylene pyrolysis was examined in the presence and absence of substrate material in order to identify the mechanisms responsible for pyrolytic carbon formation. The reactivities of the resultant composites were examined prior to and after heat treatment to determine the substrates's influence on the oxidation resistance of the matrix.

2. Experimental

Pyrolytic carbon was deposited from either pure propylene at reduced pressure, or propylene in a nitrogen carrier stream at atmospheric pressure. Fibrous substrates were infiltrated at 750°C in a 50-mm id horizontal tube furnace. Table 1 summarizes the CVD conditions used in this work. The process exhaust stream was sampled with a 1-mL syringe and analyzed using a Perkin Elmer (model 8500) gas chromatograph equipped with a flame ionization detector and a 5-ft x 1/8-in stainless steel column packed with Supelco 45/60 Carboxen 1000 adsorbent.

The substrates used in this study were mainly commercial cloths made of carbon fibers of differing crystal structure and porosity, although some non-porous carbons and ceramic substrates were also used. Key properties of the main substrate cloths are given in Table 2. Some samples of both carbon cloths were heat treated to 2900°C (samples designated "HT") in order to increase their crystallite size. Some samples of the carbon cloths were also reacted to varying levels of burn-off (samples denoted "B.O.") in carbon dioxide in order to increase the porosity and surface area: VCL at 850°C and WCA, HT WCA and HT VCL at 950°C. An activated pitch-based carbon fiber in an unpressed wool form (Ashland AM-D-15-D) was used to loosely pack the reactor tube isothermal zone to determine the effect of substrate on propylene pyrolysis efficiency. Non-porous graphite, 3Å and 5Å alumino silicate-based molecular sieves (Davison Chemical) and non-porous Nextel alumina fibers were also used as substrates.

Because of the nature of the porous carbons used as substrates, the determination of mass increase after a CVD run was not a straightforward procedure. Desorption of water and oxygen upon heating could result in as much as 15-20% weight loss. Therefore, samples were first degassed overnight at 200°C at 3 x 10^{-3} torr prior to weighing before deposition, or the weight loss from desorption was estimated from thermogravimetric analysis (TGA) of similar samples.

The pore structure and surface areas of the substrates and composites were studied by measuring the nitrogen and carbon dioxide equilibrium adsorption (77 K and 273 K respectively) in a Carlo Erba Sorptomatic 1800. The BET equation was used to measure the nitrogen BET surface area (16.2 $Å^2$ used as adsorbed nitrogen molecular area) and the D-R equation [9] was used to calculate the nitrogen and carbon dioxide pore volumes (1.044 and .808 g/cc used as the density of adsorbed carbon dioxide and nitrogen, respectively.)

Scanning electron microscopy (SEM) was used to study the microstructure of the substrates and composites prior to and after heat treatment to 2900°C. Oxidation resistance studies were performed by non-isothermal TGA at a heating rate of 5°C/min in 100 sccm of oxygen in a Cahn 113x microbalance.

3. Results and Discussion

This study was in based in part on our research group's previous investigations into the oxidation behavior of C/C composites obtained by chemical vapor infiltration of different carbon cloths [10]. The choices of many of the experimental parameters were based on the findings of that work. In particular, it was found that for the conditions examined there existed no relationship between the surface area of the substrate and the pyrolytic carbon yield; the substrate had little effect on the kinetics of the carbon CVD. In order to examine the effects of the substrate, it was first necessary to find conditions under which the nucleation and growth of pyrolytic carbon occurred on the internal surfaces of the porous carbon substrates. Lower total pressures and partial pressures were therefore used, and a low temperature for propylene pyrolysis was selected.

3.1 CVD Matrix Yields

The variation in pyrolytic carbon yield for substrates of differing surface area was used as an indication of conditions favoring surface nucleation. The rayon-based carbon fabrics described above were reacted to varying levels of burn-off in order to provide substrates covering a range of surface areas as summarized in Table 3. Unless otherwise noted, all substrates used in this study were prepared from these "activated" carbon fabrics. Figure 1 presents the matrix yields for the various deposition conditions used in this study. In all cases it can be seen that the surface area of the substrate had an effect on the matrix yield. For deposition runs conducted at both low pressures and atmospheric pressures, the matrix yields were always greatest for the substrates of the highest surface area, even for propylene concentrations as high as 25%. This surface area effect may have been present even at high concentrations due to the time necessary for reaching the higher partial pressures of propylene. The concentration of propylene starts out low, and only later (after approximately 7 minutes) reaches the higher partial pressures which would favor gas-phase reactions. The surface may play an important role before the higher concentrations are achieved.

Although the matrix yields are consistently higher for substrates of higher porosity, the relationship between matrix yield and surface area and pore volume does not appear to be simple. If the entire surface was covered by CVD carbon, a mass increase of 30% would be reached for a 850 m^2/g substrate after only a few monolayers of pyrolytic carbon. However, as will be shown in Section 3.4, the deposited film had a thickness on the order of 10 nm. The entire pore-surface is not accessible to the infiltrating gas and the first few layers of pyrolytic carbon must drastically reduce the surface area.

The percentage of matrix yield for the VCL samples is very similar in all cases, as opposed to the other two substrates. This may be because of the variation in surface area of the heat-treated samples, especially the WCA. It also may be due to the sample surface having a significant impact on CVD kinetics only for a short period of time, after which the internal surface is blocked off and deposition proceeds at a much slower steady-state rate.

The Nextel fibers, molecular sieves, and non-porous graphite showed negligible weight increase after deposition. In the case of the Nextel fibers and graphite, this can be attributed to the low specific surface areas of the substrates (less than 1 m^2/g), but the same argument does not hold for the molecular sieves which have extremely high surface area. It is likely that their small pore sizes do not allow the precursors of pyrolytic carbon to infiltrate the pore structure before cracking. Any deposition occurs on the external surface (possibly enhanced by the acidic nature of the molecular sieves [11]) and quickly blocks off the pores.

The kinetics of pore filling were further examined for conditions of low propylene total and partial pressures, as shown in Figure 2. Deposition was examined for VCL at 40% burn-off (P_{tot}=1 torr, 200cm/min flow rate; and P_{tot} = 1 atm, 0.13% propylene at 20 cm/min and 200 cm/min flow rates) to examine the effects of concentration, flow rate, and total pressure. For all conditions, it is clear that deposition does proceed rapidly initially and then tapers off to a steady state. According to this figure, flow rate did not have a major effect on either the rate of deposition or the matrix level at which steady state was achieved. This suggests that diffusion through a boundary layer was not a limiting factor in the reaction [12].

Deposition carried out at 1 torr continues to occur at a higher rate for the same level of infiltration as compared to the deposition carried out at atmospheric pressure, and a higher level of infiltration is achieved before the reaction approaches a steady-state rate. This implies that at low pressure the precursors to pyrolytic carbon "see" a greater fraction of the total surface area than at higher pressures. Apparently, these precursors are able to diffuse further into the pore network before forming pyrolytic carbon. As this available surface area and pore volume decreases, there ceases to be any diffusional advantage to low-pressure deposition, and a steady-state rate similar to that of the atmospheric pressure cases is reached. In all cases, the level of infiltration at which point the surface ceases to be a factor is far below that which would be required if the entire pore was filled with pyrolytic carbon, even using conservative pore volumes.

This is in disagreement with our former work in which it was concluded that surface area had minimal effects on the kinetics of carbon CVD under similar conditions [10]. This may have been because in the previous study the loss of mass due to desorption (up to 20%) may not have been completely accounted for when determining matrix yield. Pore size effects may also have contributed to the discrepancy, as will be discussed below.

3.2 Adsorption Studies

Studies of the substrates and composites' surface areas and pore volumes were conducted at various levels of infiltration in order to determine where the pyrolytic carbon was actually being deposited, and how much of the pore volume was accessible to CVD carbon. Nitrogen and carbon dioxide equilibrium adsorption was used to determine the respective pore volumes of composites infiltrated at 0.13% propylene at atmospheric pressure and at 1 torr. These results are shown in Figures 3 and 4.

Figure 3 shows that the N_2 pore volume decreases more gradually at first for the deposition done at low pressure. The results for the CO_2 pore volume were different, as shown in Figure 4. For both atmospheric pressure and low pressure cases the CO_2 pore volume remains relatively constant at first, or even rises slightly. At higher levels of densification it drops steeply for the low-pressure case, but for the atmospheric-pressure CVD it continues to rise slightly.

This lack of a gradual reduction in CO_2 pore volume is most likely due to the fact that the pyrolytic carbon precursors do not diffuse into the narrower micropores that the CO_2 pore volume includes. Due to kinetic restrictions at 77 K, N_2 is unable to adsorb in the smaller micropores [13]. The N_2 pore volume therefore represents the larger micropores and smaller mesopores. At 273 K, the CO_2 pore volume is an indication of the microporous volume. According to the data, pyrolytic carbon is being deposited primarily in the mesoporous regions, especially at atmospheric pressure, thus constricting the pores into micropores. This has the two-fold effect of reducing N_2 pore volume and increasing CO_2 pore volume. At lower pressures, the precursors to pyrolytic carbon are able to diffuse further into the micropores, and at some point the micropores begin to be blocked off, and the amount of adsorbable CO_2 is reduced.

Further information is obtained from studying the CO_2 D-R plots for the original substrate and after high levels of densification for both the atmospheric and low-pressure infiltration as shown in Figures 5 and 6. After atmospheric-pressure infiltration, the slope of the D-R curve does not change considerably, indicating that the pore width is essentially unchanged [14] from 0.7 nm. For the low-pressure infiltration case it shows that the slope has increased to an average pore width of 1.1 nm, even though the overall pore volume has decreased. This is most likely because the smaller pores have been closed by pyrolytic carbon at this point, and all that is left is shallower, larger pores. It is therefore not surprising that a significant amount of carbon was not deposited in the molecular sieve samples, as their pore sizes are smaller than those of the carbon fibers. Although propylene has been found to diffuse and deposit in pores of nominal size 4 -5 Å at a temperatures of 600°C [15], in this study such pores were apparently not able to contribute significant surface area for carbon deposition.

3.3 Analysis of Propylene Pyrolysis Efficiency

It is clear from the matrix yields and kinetic data shown in Section 3.1 that pyrolytic carbon is nucleated on the substrate surface. But these data do not indicate whether the propylene is chemisorbed and cracked on the surface in a heterogeneous manner as described by Tesner [4] and Hoffman [7], or if the propylene forms pyrolytic carbon precursors in the gas phase, as described by Grisdale [3], which then adsorb on the carbon surface. The efficiency of propylene cracking was analyzed using gas chromatography in order to determine the effect of the carbon substrate on propylene pyrolysis.

Figure 7 shows the results of the analysis of propylene concentration before cracking, after a steady state is achieved by flowing propylene through the CVD reactor at 400 cc/min at 750°C with no substrate, and at several stages in which propylene is cracked at the same conditions, but with the reactor tube loosely packed with approximately 5 grams of Ashland Carboflex activated carbon fiber (BET surface area of approximately 1000 m^2/g).

The substrate clearly influences the cracking of propylene. At first, when the available carbon surface area is high, the propylene concentration in the exhaust stream is extremely small. Even at later times when the substrate's BET surface area is reduced to less than 20 m^2/g, the propylene concentration in the exhaust stream is less than half of that found in the absence of the substrate.

In their study of pyrolytic carbon deposition from propylene, McAllister et al. [8] analyzed the gas-phase products of propylene pyrolysis and concluded that the substrate had little catalytic effect on pyrolysis, except perhaps at initial stages before steady state was achieved. This may be due to the higher partial pressures of propylene used in their study or their reactor design. Their experiments were conducted in a TGA where the reactor-to-substrate surface area ratio was likely to be very high, so that the introduction of a small amount of substrate was not likely to have significantly increased the amount of surface area available for the catalysis of propylene cracking, and thus was not likely to significantly change the propylene cracking efficiency.

The improved efficiency of propylene pyrolysis in the presence of a substrate indicates that propylene pyrolysis is taking place on the substrate surface. Combined with the kinetic data, this suggests that for the experimental conditions examined in this study, the dominant mechanism responsible for pyrolytic carbon nucleation and growth is a direct surface decomposition of the hydrocarbon gas.

3.4 Microstructural Analysis

Figures 8-10 are the micrographs of the three main substrates examined prior to CVD. The CVD coatings were difficult to examine using the SEM, due to the lack of contrast between the fiber and matrix and the strength of the fiber-matrix bond. Only in some cases were the coatings exposed after slight debonding occurred after sectioning with a steel razor as shown in Figures 11 and 12. Figure 11 is an example of the coating deposited at 1 torr on a WCA fiber (no burn-off prior to CVD). In this case the coating could be imaged as it does not cover the length of the fiber. Figure 12 is the clearest example of the pyrolytic carbon, in this case deposited on a Nextel fiber at 1 torr.

Figures 13 and 14 show the micrographs of the heat-treated composites produced by infiltrating heat-treated and non-heat-treated VCL fibers with pyrolytic carbon at 10 torr for 10 hours. There seems to be a large amount of matrix debonding (upon sectioning for SEM mounting) for the fiber that had seen high temperature prior to deposition (Figure 13). This is probably due to the thermal stresses encountered during heat treatment. For the non-heat-treated VCL, the pyrolytic carbon matrix seems to be bound much more strongly to the fiber (Figure 14). This debonding upon heat treatment suggests that the microstructure of the pyrolytic carbon is much more amorphous than that of the high-temperature fibers (see also X-ray diffraction crystallite parameters in Table 4). Ehrburger et al. have shown that coatings with an isotropic texture (as opposed to smooth laminar) undergo reorientation upon heat treatment [16]. Both the pyrolytic carbon matrix and the non-heat treated VCL fiber simultaneously undergo reorientation upon heat treatment and the interface is not significantly weakened. The HT VCL does not undergo any additional reorientation upon heat treatment, and the result is a weakened fiber-matrix interface. This interaction between the fiber and matrix during heat treatment becomes important to the composites' oxidation resistance as discussed below.

3.5 Oxidation Resistance Studies

Non-isothermal TGA was used in order to compare the relative reactivities of the substrates and composites examined in this study. The composites used in the TGA studies were cut to size prior to infiltration in order to minimize substrate exposure through cutting at a later stage.

Figure 15 compares the oxidation resistance of the substrates used in this study, before and after burn-off. As expected, the cloth that had seen the lowest heat treatment temperature and has the smallest crystallite size (see Table 4), VCL, is the most reactive and oxidizes extremely rapidly with a reproducible ignition. The WCA and HT WCA show little difference in reactivity, due to the fact that the WCA had already seen a high temperature during its manufacturing process. The fact that after heat treatment the VCL is not as oxidation-resistant as the WCA agrees with the slight difference in crystallite size: this suggests that the WCA fibers received some kind of stressing during their heat treatment. Activation in CO_2 decreases the already low oxidation resistance of the VCL only slightly. The activated HT VCL and WCA reacted much more quickly than their non-porous precursors, especially the WCA fibers. As the WCA fibers are slightly more graphitic, this increase in reactivity must be due to its higher surface area as shown in Table 3.

The oxidation resistance profiles of the activated substrates and their composites produced by CVD at 10 torr are shown in Figure 16. Even though the matrix is likely to be less crystalline than the substrate, and hence more reactive, the VCL-based composite's oxidation resistance is greater than that of the substrate due to a reduction in surface area. The oxidation resistance of the composite produced by infiltration of the HT VCL fibers is less than that of the substrate prior to deposition. This is not surprising: little porosity was created through the activation of the HT VCL, and since the matrix is much less ordered than the fiber, the composite reactivity should be higher.

The WCA-based composite, in which significant porosity was developed, shows the same trend as the HT VCL-based composite, but to a greater extent, probably due to the greater matrix yield. It is clear from its two-step reactivity profile that for the WCA case the matrix is less oxidation-resistant than the substrate, the reactivity starts out high, and once the point is reached where the matrix should be burned away (approximately 15% mass loss), the reactivity decreases slightly.

Figure 17 shows the oxidation resistance profile of the composites produced at 10 torr after heat treatment. The oxidation resistance of all the composites increases significantly, indicating that although the pyrolytic carbon matrices may not have been very graphitic, they were very graphitizable, and this increase in crystallite ordering results in a reduction of reactivity [17]. This is especially true for the VCL-based composite, which proves to be the most oxidation-resistant material. It is possible that this enhancement in the oxidation resistance of the VCL-based composite exists simply because the pyrolytic carbon is more graphitizable than any of the fibers and, since this fiber results in the highest matrix yield, the result is a more oxidation-resistant composite. This issue will be addressed later in this section. It is also possible that the weakening of the fiber-matrix interface occurring upon heat treatment of composites produced from high-temperature fibers is limiting the oxidation resistance of those composites [1].

Further studies were conducted for composites infiltrated at 1 torr and 100 torr of propylene, and those infiltrated at atmospheric pressure at a propylene concentration of 1.3%. The trends were very similar to the case of the composites infiltrated at 10 torr, although those produced at lower total and partial pressures of propylene tended to be less reactive, probably due to the higher level of pore filling under these conditions. The most striking result was the consistently high oxidation resistance of heat-treated composites produced from the activated VCL fibers. The initial oxidation resistance of these composites surpassed that of the most graphitic substrate, the WCA fiber, as shown in Figure 18. In order to determine if this was simply due to a combination of high graphitizability of the matrix and high matrix yield of the VCL-based composites, an additional study was conducted by varying the infiltration time.

The VCL cloth at 40% burn-off was infiltrated for 5 and 10 hours in order to produce composites with differing matrix yields (approximately 22% and 30%, respectively). As shown in Figure 19, before heat treatment, the composite with more matrix was slightly more oxidation-resistant, most likely due to the reduction of porosity and surface area. But after heat treatment, the composite with lower matrix yield was more oxidation-resistant. This implies that the oxidation resistance enhancement is purely an interfacial phenomenon: there exists a thin layer of carbon most resistant to oxidation, and any additional carbon deposited over this layer is less oxidation-resistant (than the interfacial layer), and therefore *increases* the overall reactivity of the composite.

This phenomenon of more oxidation-resistant composites being produced from more reactive materials was initially found for composites produced by liquid phase impregnation [19]. This "synergistic" effect was attributed to an enhancement of graphitization due to stresses at the fiber-matrix interface. Low temperature substrates (those that haven't seen graphitizing temperatures) are likely to undergo crystallite ordering and reduction of porosity upon heat treatment. Carbon deposited in the porous regions was hypothesized to undergo enhanced stresses leading to a more graphitic structure than the surrounding carbon. Kamiya and Suzuki have shown a preferred alignment of carbon layers around pores in their study of the hardening and carbonization of phenol formaldehyde resin [20]. In their studies of the microstructures of resin-based C/C composites, Rellick et al. [21] and Rellick and Adams [22] have found regions of lamellar graphite in fiber/matrix interfacial regions where the restraint of matrix shrinkage produces local stresses.

It is postulated here that a similar effect is found in these CVI matrix composites. Upon heat treatment, the pore structure of the VCL-based composite undergoes a reduction in volume, stressing the pyrolytic carbon deposited in the pores. This can account for the fact that the oxidation resistance of VCL-based composites surpassed that of all the other composites and fibers. The increased oxidation resistance of the HT VCL-based composites over the original substrate can be accounted for by assuming that the graphitizability of their matrices surpasses that of the fibers. One point that remains unclear is why the matrix of the WCA-based composites proves to be so reactive, even upon heat treatment. More investigations into the structure of these coatings will be needed to clarify this issue.

4. Conclusions

The CVD of carbon from propylene pyrolysis was investigated for a variety of deposition conditions and substrates in an attempt to understand how the porosity and crystal structure of the substrate affected the deposited carbon and subsequent oxidation resistance of the composite.

For all the conditions examined, the substrate surface area affected the initial rate of carbon deposition and the matrix yield at which steady state deposition occurred. At high propylene concentrations this may have been due to the time necessary to reach the desired partial pressure of propylene.

The flow rate of propylene was not found to have much of an effect on the level of infiltration at which steady state deposition occurred. Lower pressures did have such an effect, however. At lower pressures the initial rate was higher than that of the same concentration of propylene at atmospheric pressure, as was the level of densification at which the reaction achieved steady state, indicating that at lower pressures the pyrolytic carbon precursors are able to diffuse further into the pore network and "see" a higher surface area for deposition. For atmospheric-pressure and low-pressure infiltration at the same propylene concentration, the steady-state reaction rates were very similar.

Gas adsorption studies verified that at lower pressures the pyrolytic carbon is able to form in narrower pores, but not those that are only accessible to carbon dioxide adsorption. Upon deposition, the nitrogen pore volume decreases gradually, while the carbon dioxide pore volume decreases suddenly. The D-R plots for carbon dioxide adsorption show that instead of decreasing, the average pore width increases after this sudden drop in pore volume, indicating that the narrower pores have been blocked, resulting in wider but shallower pores.

Data from the analysis of the propylene pyrolysis efficiency in the presence of a substrate and without a substrate indicates that the cracking of propylene occurs by heterogeneous reaction on the substrate surface under the CVD conditions examined. This suggests that the surface decomposition mechanism is responsible for pyrolytic carbon nucleation and growth. It could not be ascertained whether the propylene cracking and pyrolytic carbon nucleation occurred preferentially over carbon active sites, or whether the entire carbon surface is catalytic towards propylene cracking.

TGA studies show that in order to produce the most oxidation-resistant composite it is not necessary to infiltrate fibers of low reactivity. The most oxidation-resistant composites were produced with fibers of low crystallite ordering and high porosity. This enhancement of oxidation resistance is attributed to enhanced graphitization of the pyrolytic carbon matrix in the fiber pores due to stresses encountered upon heat treatment. This stress graphitization must occur in the larger micropores and mesopores, as the gas adsorption data suggest that the smaller micropores are not infiltrated with pyrolytic carbon.

References

1. Lieberman, M. L., *Proc. 3rd Int. Conf. on CVD,* American Nuclear Society, 1972, 95-119.

2. Kotlensky, W. V., in *Chemistry and Physics of Carbon* Vol. **9** (Edited by P. L. Walker, Jr. and P. A. Thrower), Marcel Dekker, New York, 1973, 173-262.

3. Grisdale, R. O., *J. Appl. Phys.* **24,** 1082 (1953).

4. Tesner, P. A., in *Seventh Symposium on Combustion,* Academic Press, New York, 1959, 546-553.

5. Baker, R. T. K., Harris, P. S., Henderson, J., and Thomas, R. B., *Carbon* **13,** 17 (1975).

6. Fitzer, E., *J. Phys. IV* **1,** 509 (1991).

7. Hoffman, W. P., Ph. D. Thesis, The Pennsylvania State University, 1979.

8. McAllister, P., Hendricks, J. F., and Wolf, E. E., *Carbon* **28,** 579 (1990).

9. Dubinin, M. M., *Carbon* **27,** 457 (1989).

10. Cordero, T., Thrower, P. A., and Radovic, L. R., *Carbon* **30,** 365 (1992).

11. *Zeolite Technology and Applications* (Edited by J. Scott), Noyes Data Corporation, Park Ridge, N. J., 1980.

12. Oh, I. and Takoudis, C. G., *Proc. 11th Int. Conf. on CVD,* Electrochemical Society, 1990, 75-81.

13. Garrido, J., Linares-Solano, A., Martín-Martínez, J. M., Molina-Sabio, M., Rodríguez-Reinoso, F., and Torregrosa, R., *Langmuir* **3,** 76 (1987).

14. Dubinin, M. M., and Stoeckli, H. F., *J. Colloid Interf. Sci.* **75,** 34 (1980).

15. Cabrera, A., L., Zehner, J. E., Coe, C. G., Gaffney, T. R., Farris, T. S., and Armor, J. N., *Carbon* **31,** 969 (1993).

16. Ehrburger, P., Lahaye, J. and Bourgeois, C., *Carbon* **19,** 1 (1981).

17. Dacic, B. and Marinkovic. S., *Carbon* **25,** 409 (1987).

18. Lahaye, J., Louys, F., and Ehrburger, P., *Carbon* **28,** 137 (1990).

19. Rodríguez-Mirasol, J., Thrower, P. A., and Radovic, L. R., *Carbon* **33,** 545 (1995).

20. Kamiya, K. and Suzuki, K., *Carbon* **13,** 317 (1975).

21. Rellick, G. S., Chang, D. J., and Zaldivar, R. J., *J. Mater. Res.* **10,** 2798 (1992).

22. Rellick, G. S. and Adams, P. M., *Carbon* **32,** 127-144 (1994).

Table 1. CVD conditions used in this study.

Temperature	750°C
Flow Rate	20 cm/min*
Concentrations	0.1, 1, 10, & 100 torr (pure C_3H_6) 0.13, 1.3, 2.6, 13.2, and 25% (balance N_2)

*Some experiments were carried out at 200 cm/min in order to determine the effect of flow rate.

Table 2. Key properties of cloths used for C/C composite preparation.

Property	VCL	WCA	Nextel
Density, (g/cm^3)	1.44 (He) 1.75 (Hg)	1.42 (He) 1.42 (Hg)	3.93 (He)
Surface area, (m^2/g)	1 (Kr) 454 (CO_2)	1 (Kr)	<1 (Kr)
Composition (wt.)	97% Carbon 0.75% Ash	99.9% Carbon 0.01% Ash	>99% Al_2O_3 0.4-0.7% Fe_2O_3 0.2-0.3% SiO_2

Table 3. Surface properties of the activated carbon substrates used in this study.

Substrate	N_2 BET Surface Area (m^2/g)	CO_2 Pore Volume (cc/g)
VCL 40% B.O.	850	0.56
HT VCL 40% B.O.	<10	0.09
WCA 60% B.O.	44-125	0.16
HT WCA 60% B.O.	120	0.15

Table 4. Crystallite dimensions of substrate carbon cloths as determined by x-ray diffraction.

Sample	d_{002} (nm)	L_c (nm)	L_a (nm)
VCL	0.389	1.3	5.9
HT VCL	0.360	3.0	6.8
WCA	0.360	3.1	7.0

Figure Captions

1. Pyrolytic carbon yields under various conditions for the three porous carbon substrates.

2. Mass increase vs. deposition time for CVD on VCL (40% B.O.): ◇, P_{tot} = 1 torr at 20 cm/min; ○, P_{tot} = 1 atm (0.13% C_3H_6) at 20 cm/min; □, P_{tot} = 1 atm (0.13% C_3H_6) at 200 cm/min.

3. Nitrogen pore volume vs. % mass increase for VCL (40% B.O.) after CVD: ◇, P_{tot} = 1 torr at 20 cm/min; ○, P_{tot} = 1 atm (0.13% C_3H_6) at 20 cm/min; □, P_{tot} = 1 atm (0.13% C_3H_6) at 200 cm/min.

4. Carbon dioxide pore volume vs. % mass increase for VCL (40% B.O.) after CVD: ◇, P_{tot} = 1 torr at 20 cm/min; ○, P_{tot} = 1 atm (0.13% C_3H_6) at 20 cm/min; □, P_{tot} = 1 atm (0.13% C_3H_6) at 200 cm/min.

5. Carbon dioxide D-R plots for VCL (40% B.O.) prior to and after CVD at 1 atm (0.13% C_3H_6): ○, no deposition; □, after CVD to 17% mass increase.

6. Carbon dioxide D-R plots for VCL (40% B.O.) prior to and after CVD at P_{tot} = 1 torr (100% C_3H_6): ○, no deposition; □, after CVD to 15% mass increase.

7. Propylene concentration prior to and after cracking at 750°C with and without the presence of a substrate.

8. Scanning electron micrograph of VCL fibers.

9. Scanning electron micrograph of HT VCL fibers.

10. Scanning electron micrograph of WCA fibers.

11. Scanning electron micrograph of WCA fibers after CVD at P_{tot} = 1 torr (100% C_3H_6) for 100 hours.

12. Scanning electron micrograph of Nextel fibers after CVD at P_{tot} = 1 torr (100% C_3H_6) for 100 hours.

13. Scanning electron micrograph of HT VCL fibers after CVD at P_{tot} = 10 torr (100% C_3H_6) for 10 hours and subsequent heat treatment to 2900°C.

14. Scanning electron micrograph of VCL fibers after CVD at P_{tot} = 10 torr (100% C_3H_6) for 10 hours and subsequent heat treatment to 2900°C.

15. Oxidation resistance profiles of substrate carbon cloths prior to and after activation: ●, VCL; ○, VCL 40% B.O.: ■, HT VCL; □, HT VCL 40% B.O.; ◆, WCA; ◇, WCA 60% B.O.

16. Oxidation resistance profiles of activated substrates and composites produced by CVD at 10 torr (100% C_3H_6) for 10 hours: ○, VCL; ●, VCL/CVD; □, HT VCL; ■, HT VCL/CVD; ◇, WCA; ◆, WCA/CVD.

17. Oxidation resistance profiles of activated substrates and composites produced by CVD at 10 torr (100% C_3H_6) for 10 hours and heat treated (HT) to 2900°C: ○, VCL; ●, VCL/CVD-HT; □, HT VCL; ■, HT VCL/CVD-HT; ◇, WCA; ◆, WCA/CVD-HT.

18. Oxidation resistance profiles of substrates and composites most resistant to oxidation: □, HT VCL (no burn-off); ◇, WCA (no burn-off); ○, HT VCL (40% B.O.) after CVD and heat treatment; ●, VCL (40% B.O.) after CVD and heat treatment.

19. Effect of matrix yield on the oxidation resistance profiles of VCL (40% B.O.) composites produced by CVD at 1 atm (1.3% C_3H_6): ○, 5 hours CVD; □,10 hours CVD; ●, 5 hours CVD, heat treated; ■, 10 hours CVD, heat treated.

Figure 1

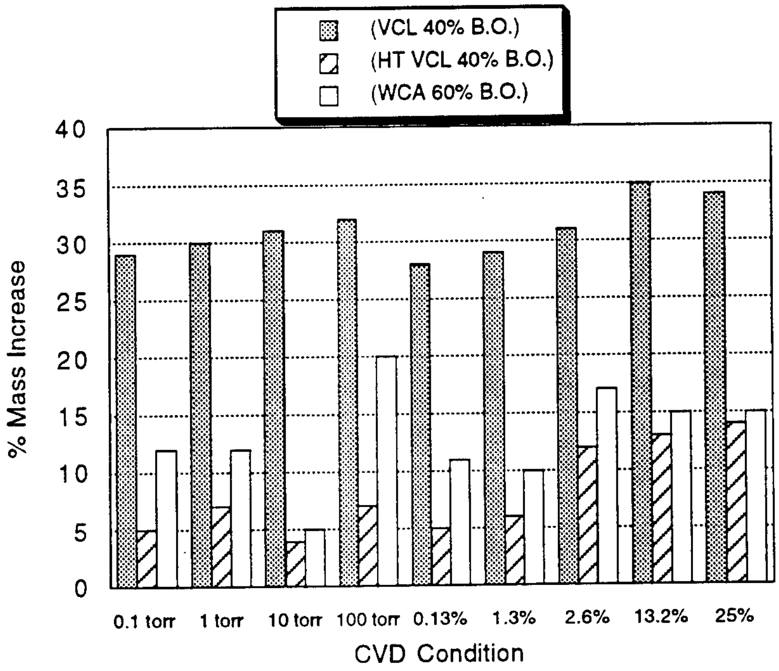

(VCL 40% B.O.)
(HT VCL 40% B.O.)
(WCA 60% B.O.)
40
35
30
25
20
15
10
5
0
% Mass Increase
0.1 torr
1 torr
10 torr
100 torr
0.13%
1.3%
2.6%
13.2%
25%
CVD Condition

Figure 2

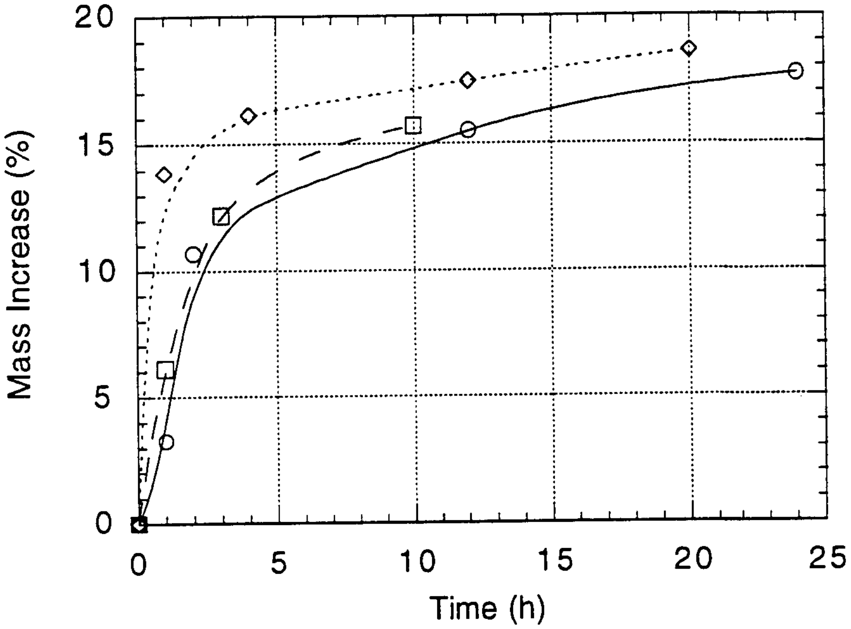

Figure 3

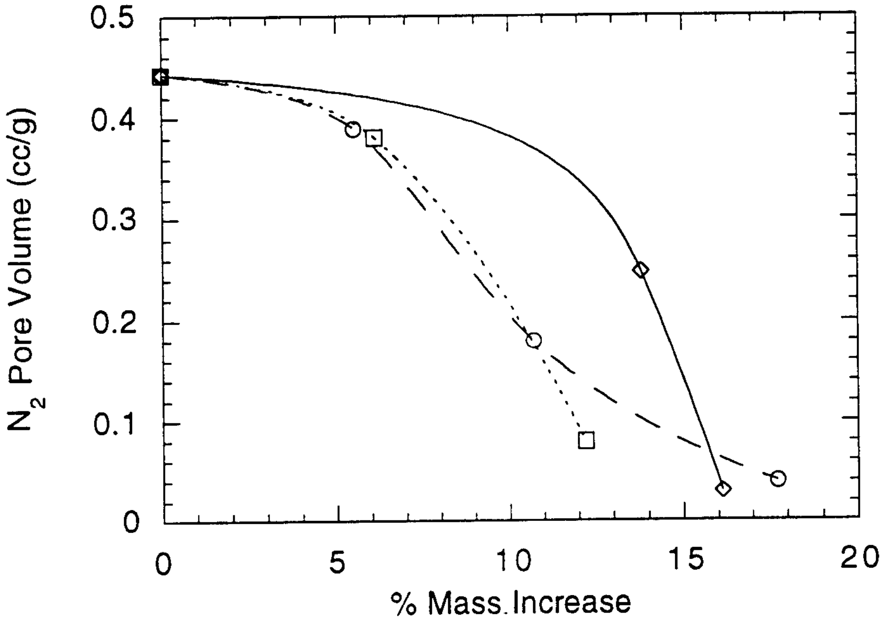

Figure 4

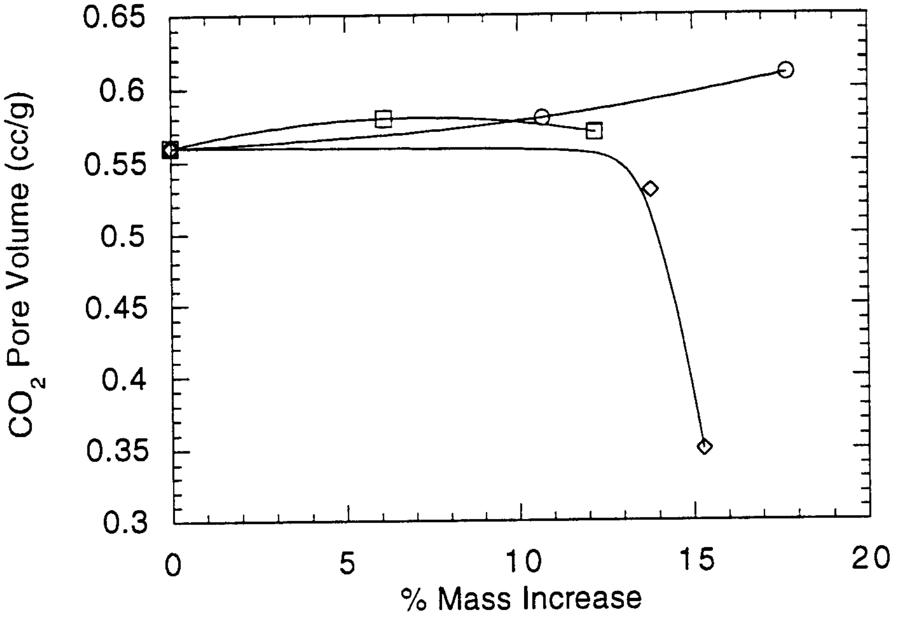
0.65
0.6
0.55
0.5
0.45
0.4
0.35
0.3
CO_2 Pore Volume (cc/g)
0
5
10
15
20
% Mass Increase

Figure 5

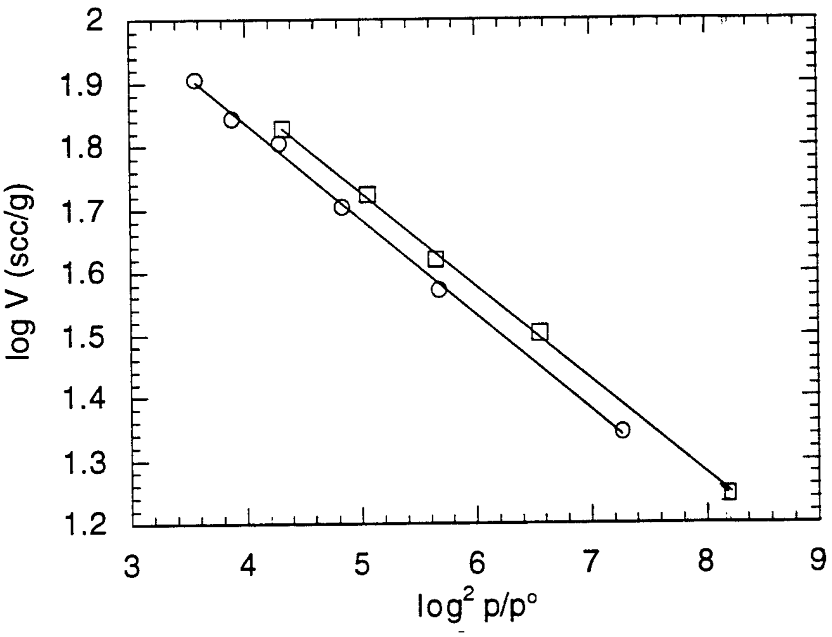

Figure 6

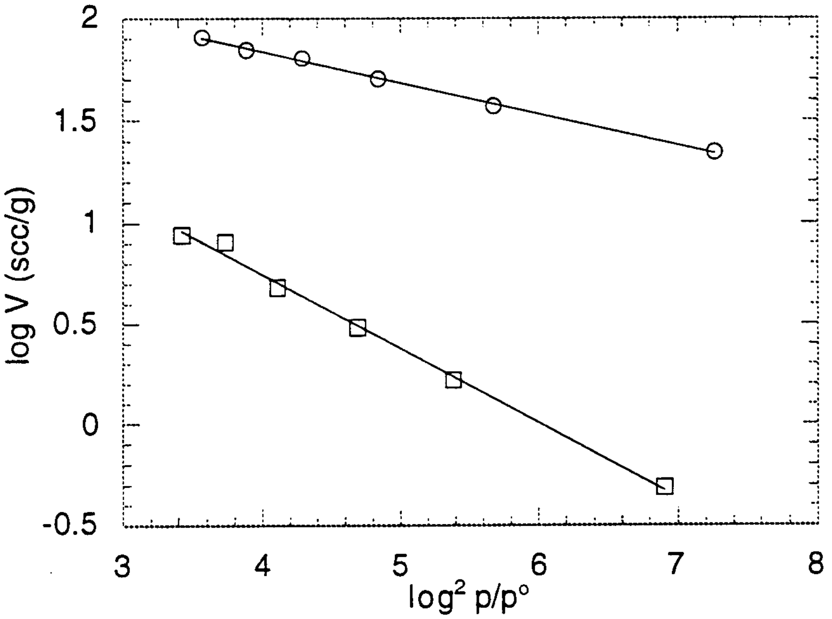

Figure 7

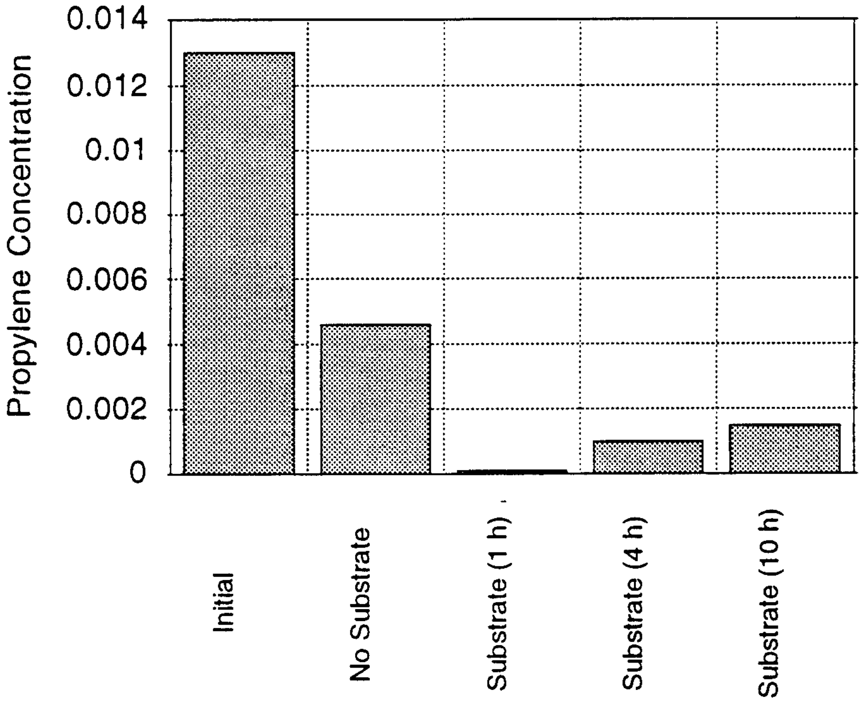
0.014
0.012
0.01
0.008
0.006
0.004
0.002
0
Propylene Concentration
Initial
No Substrate
Substrate (1 h)
Substrate (4 h)
Substrate (10 h)

Figure 8

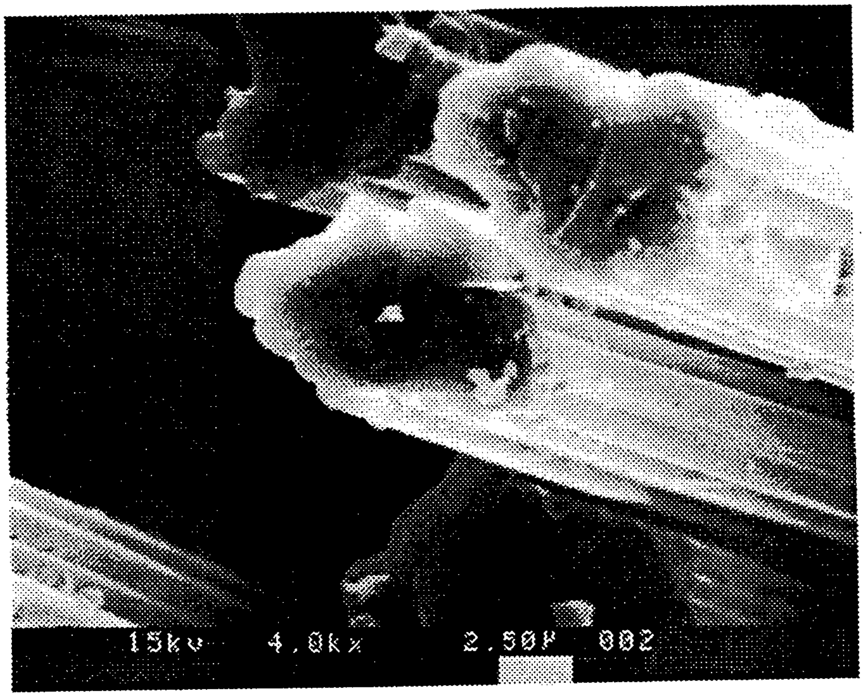
15kv 4.0kx 2.50µ 002

Figure 9

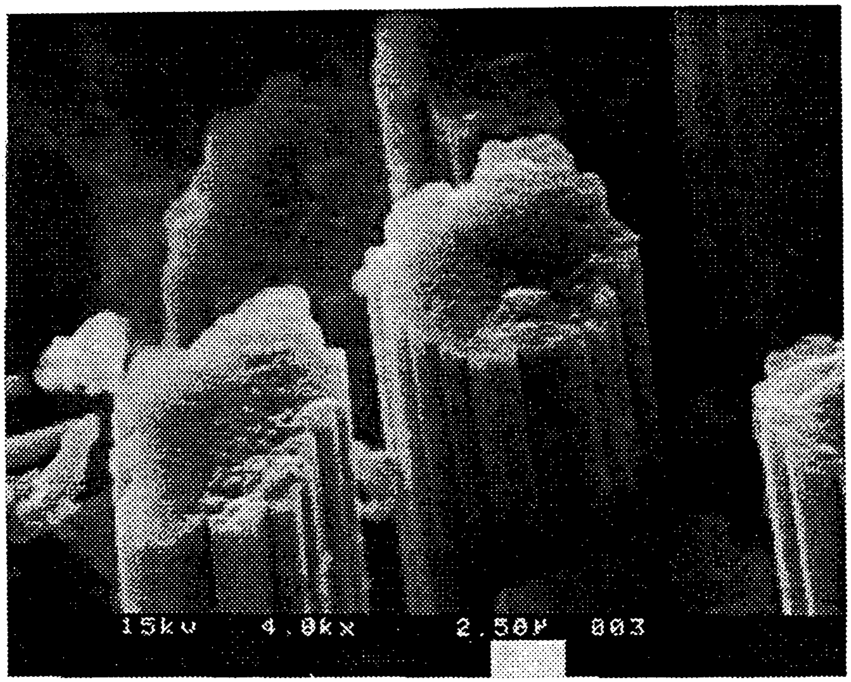
15kv 4.0kx 2.50μ 003

Figure 10

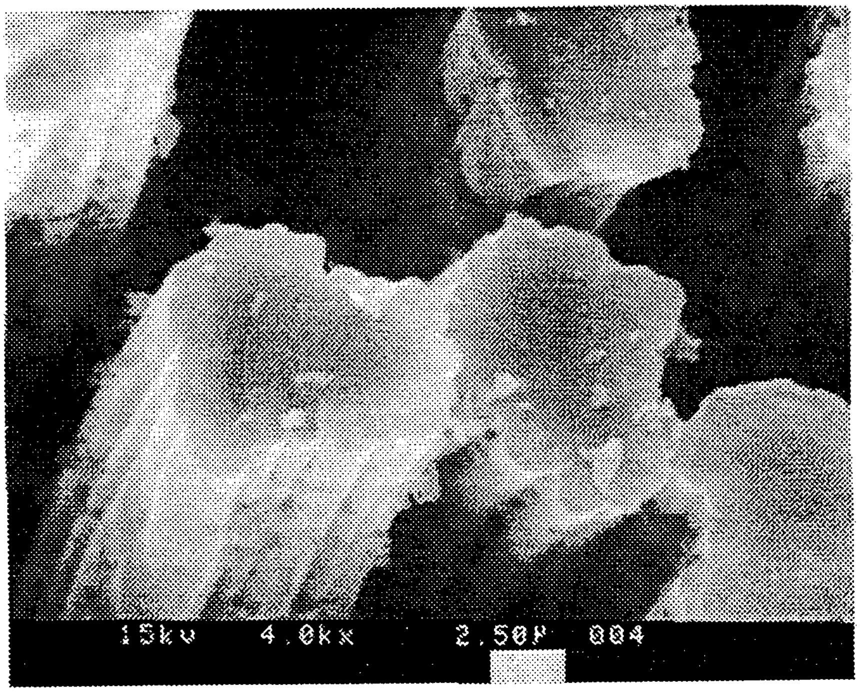
15kv 4.0kx 2.50µ 004

Figure 11

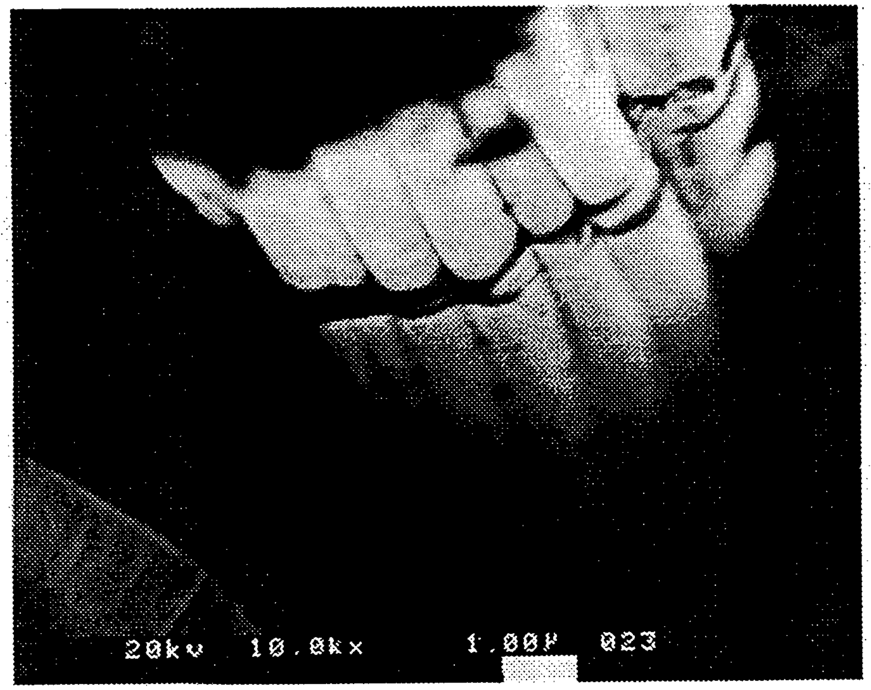
20kv 10.0kx 1.00µ 023

Figure 12

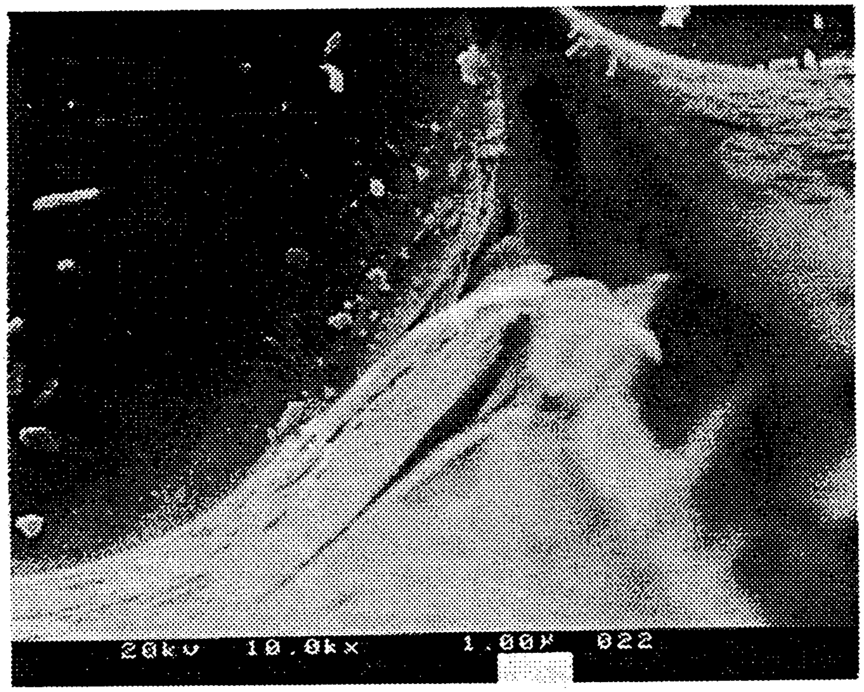
20kv 10.0kx
1.00µ 022

Figure 13

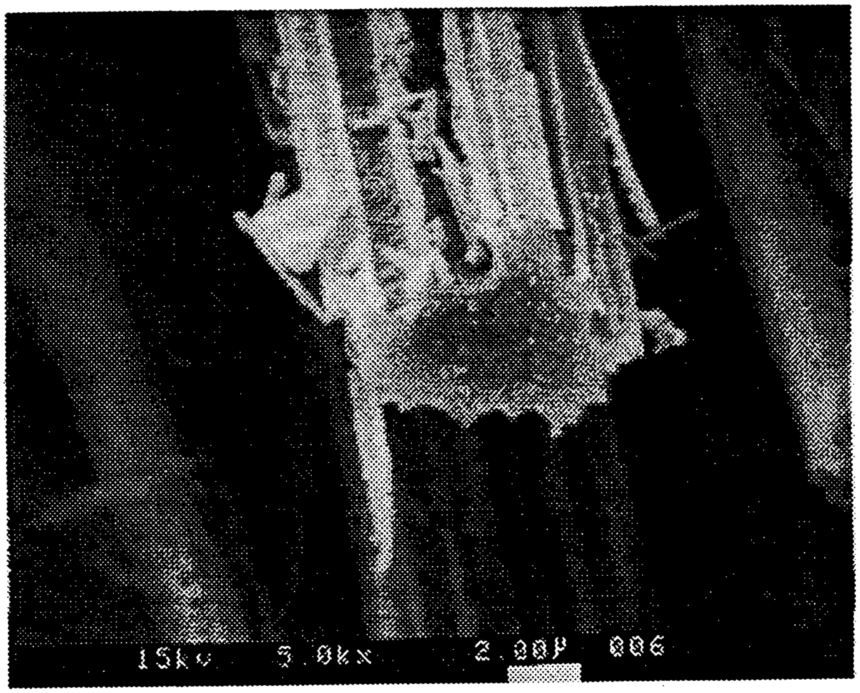
15kv 3.0kx 2.00µ 006

Figure 14

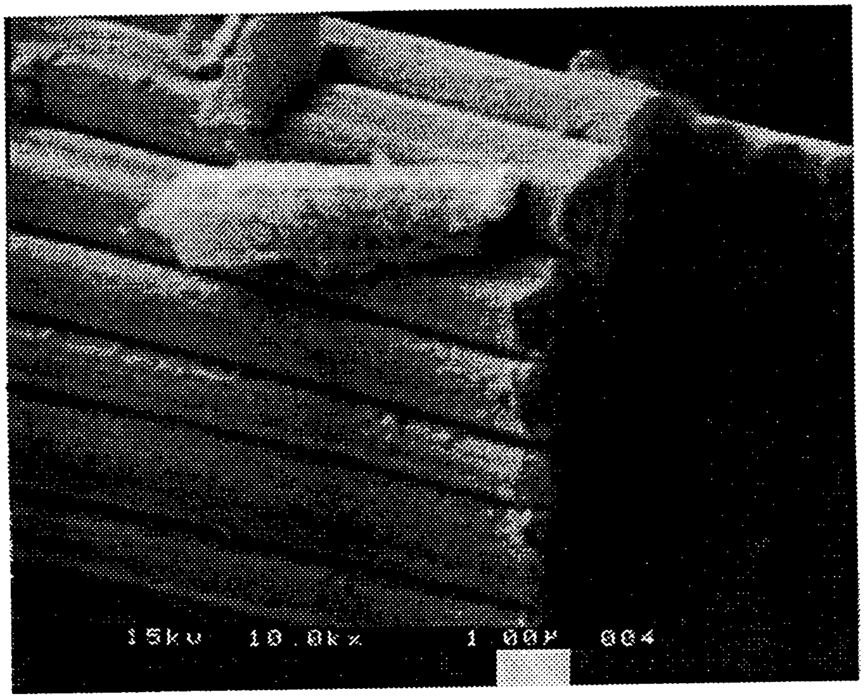
15kV 10.0kx 1.00µ 004

Figure 15

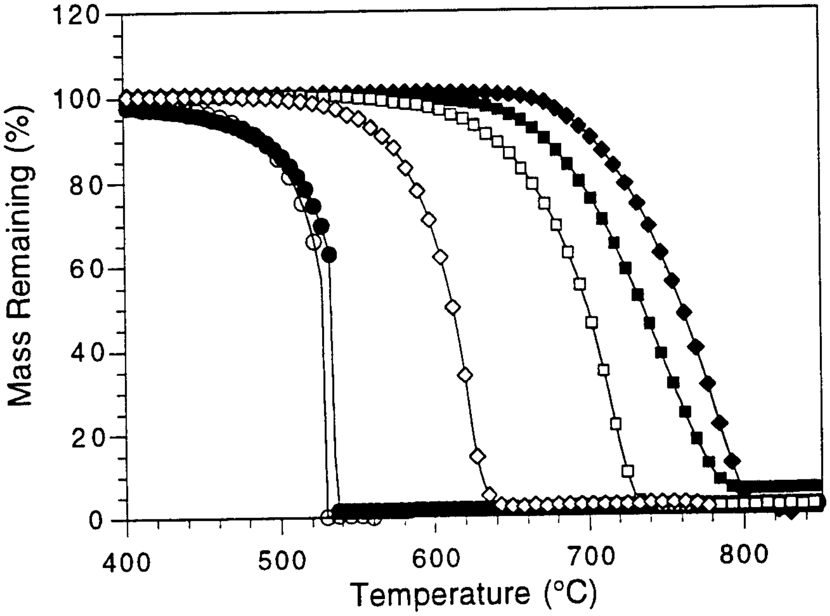

120
100
80
60
40
20
0
Mass Remaining (%)
400
500
600
700
800
Temperature (°C)

Figure 16

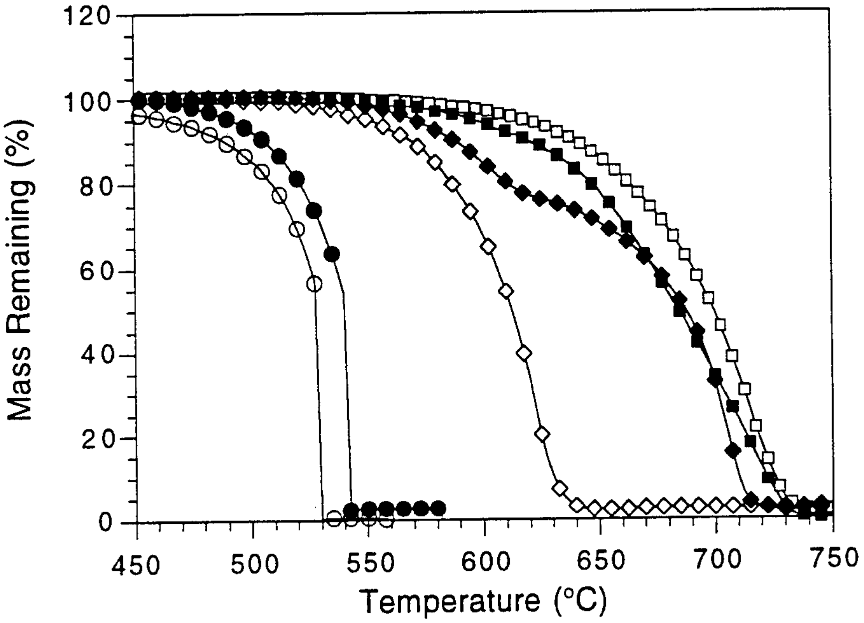

120
100
80
60
40
20
0
Mass Remaining (%)
450
500
550
600
650
700
750
Temperature (°C)

Figure 17

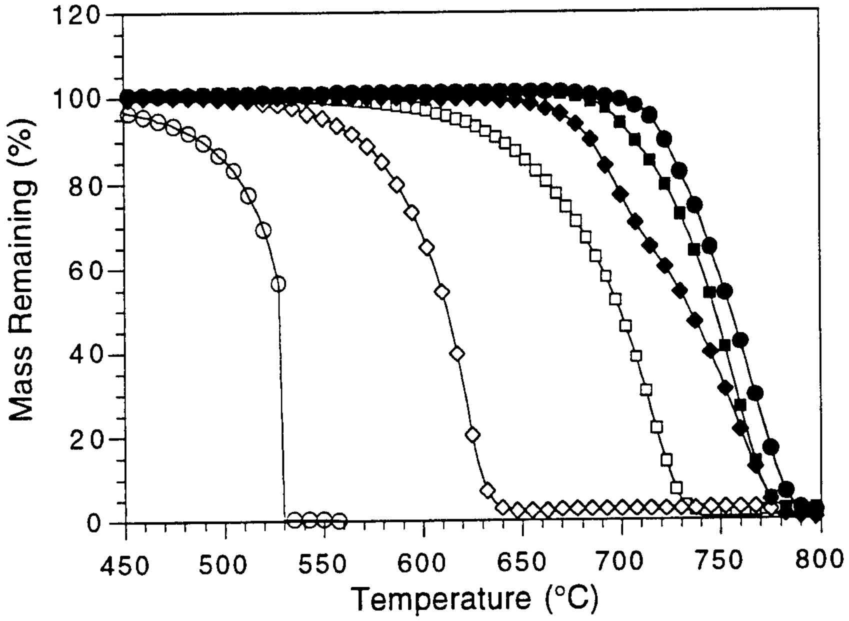

120
100
80
60
40
20
0
Mass Remaining (%)
450
500
550
600
650
700
750
800
Temperature (°C)

Figure 18

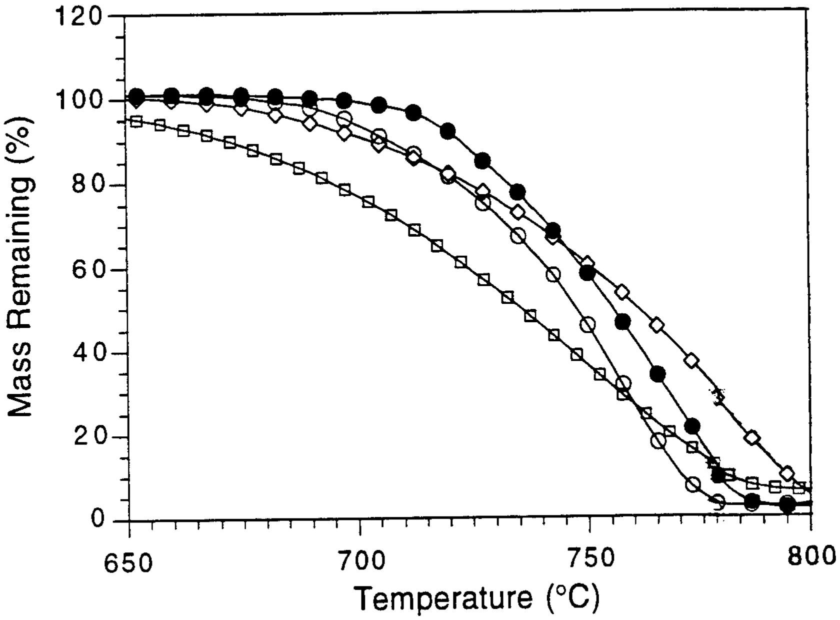

120
100
80
60
40
20
0
Mass Remaining (%)
650
700
750
800
Temperature (°C)

Figure 19

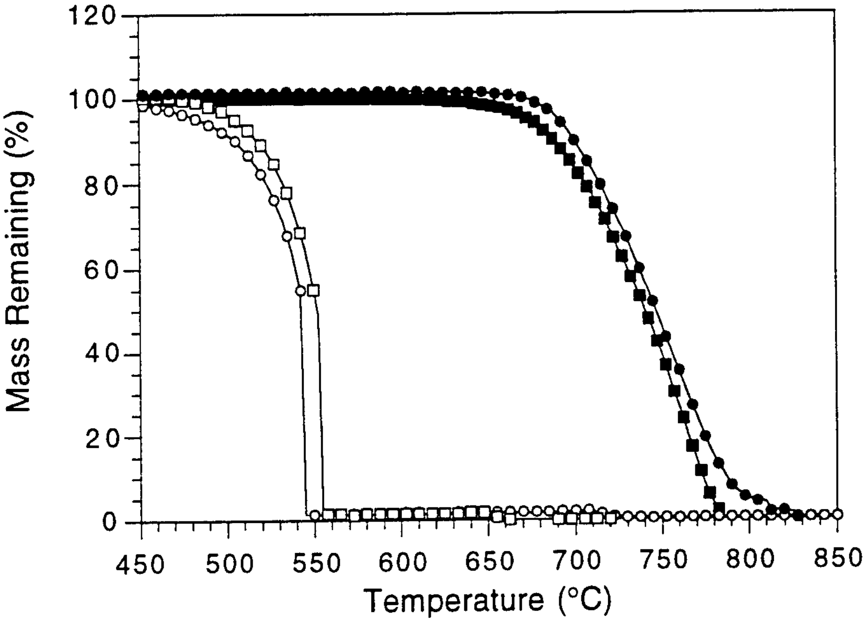

Mass Remaining (%)
0
20
40
60
80
100
120
Temperature (°C)
450
500
550
600
650
700
750
800
850

ATTACHMENT V

Photographs

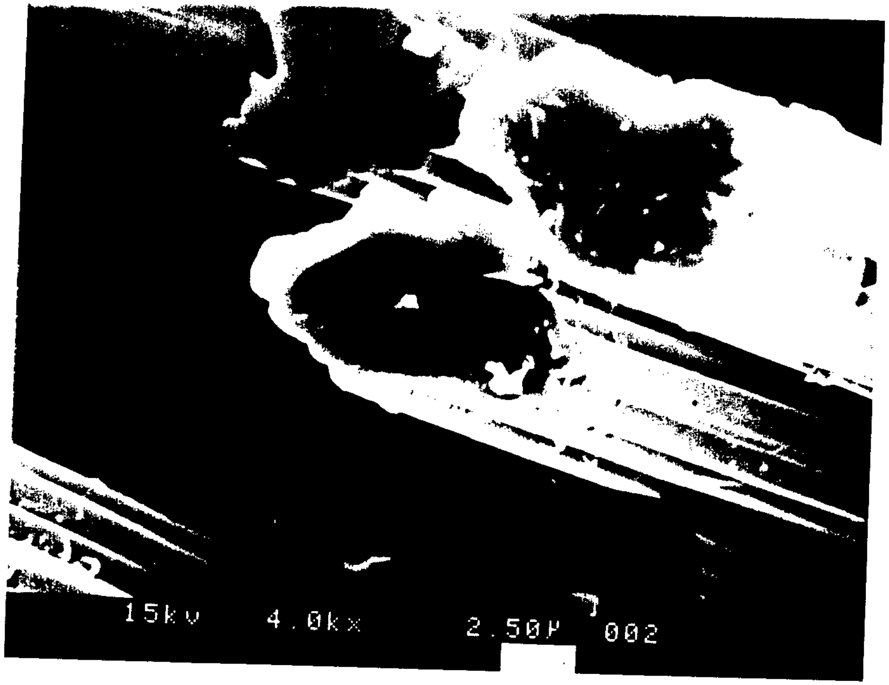
15kv 4.0kx 2.50µ 002

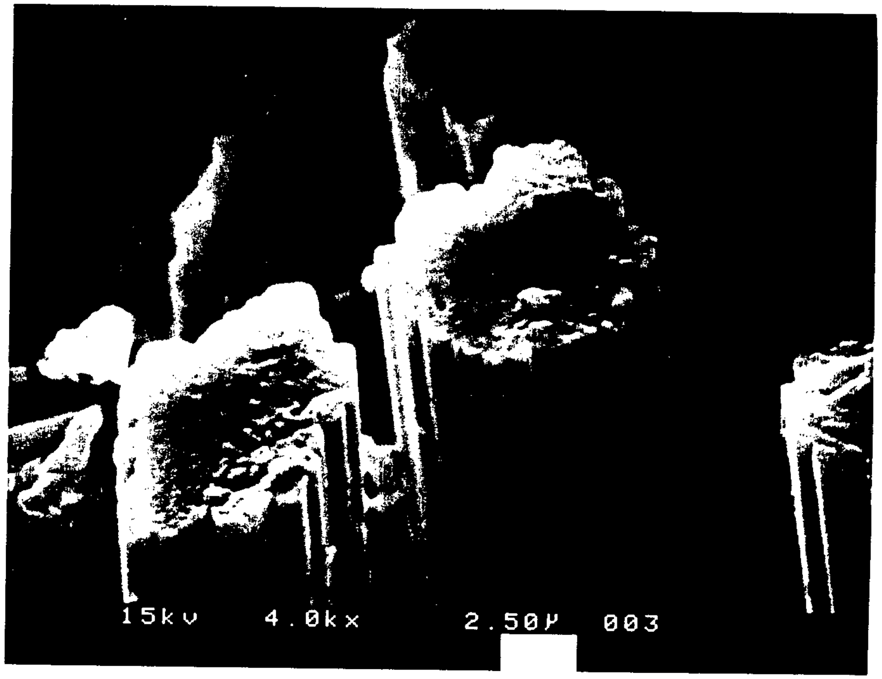
15kv 4.0kx 2.50µ 003

11

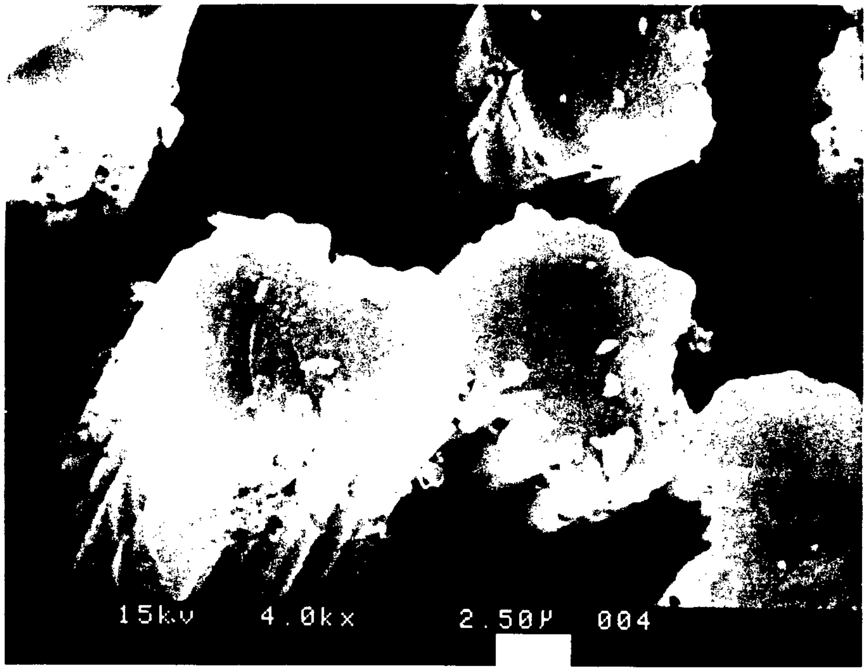
15kv 4.0kx 2.50µ 004

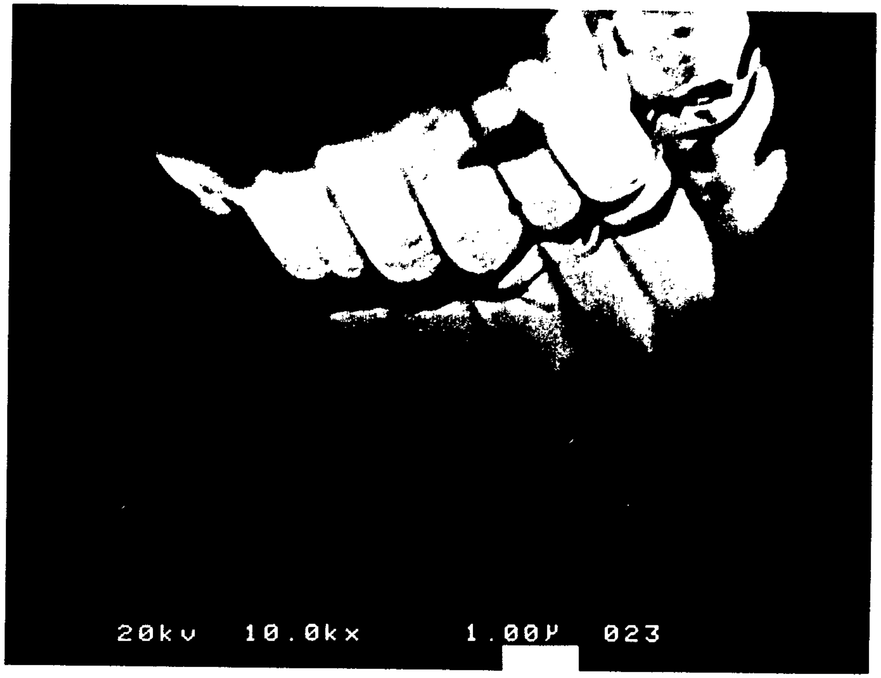
20kv 10.0kx 1.00µ 023

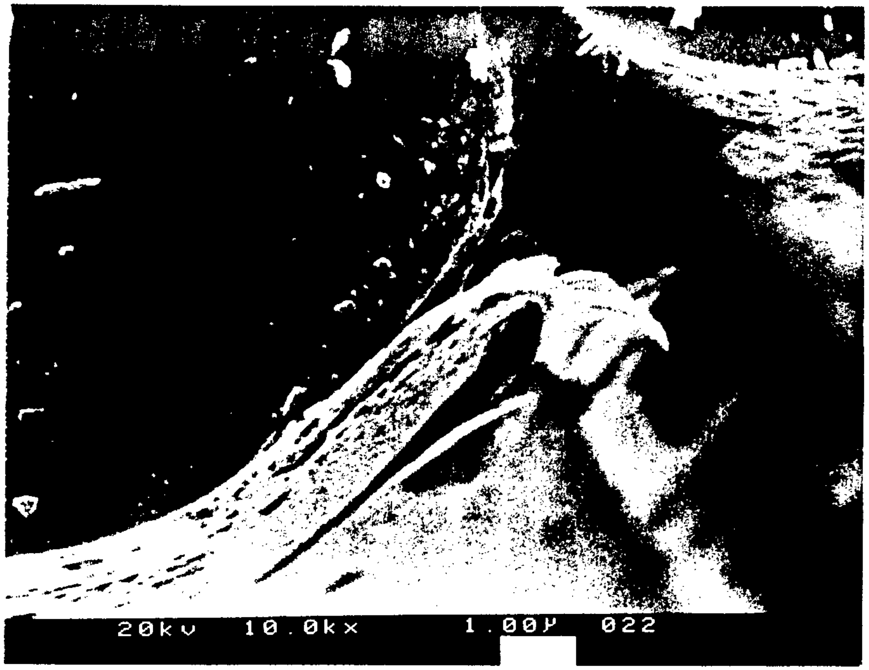
20kv 10.0kx 1.00µ 022

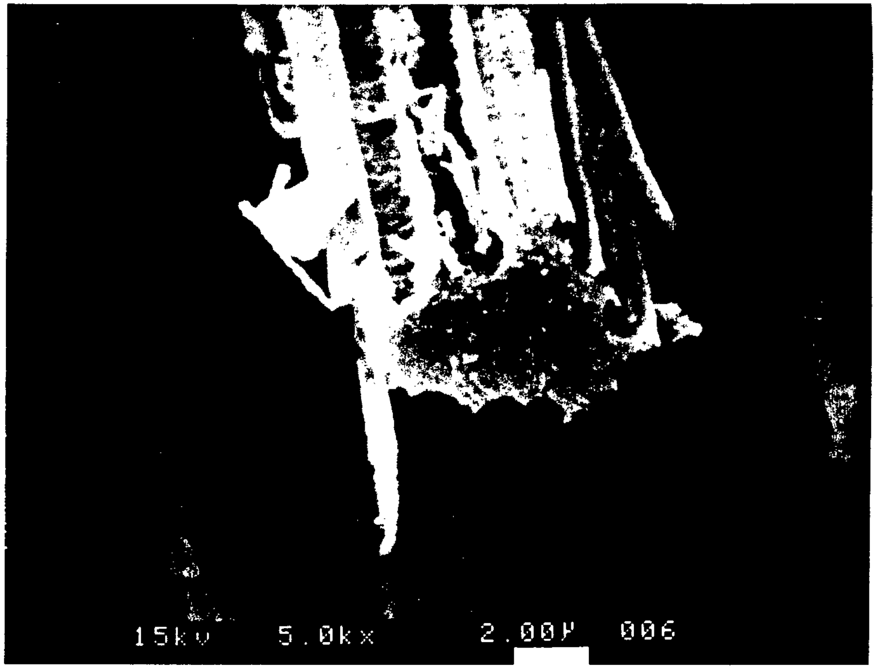
15kv 5.0kx 2.00µ 006

13

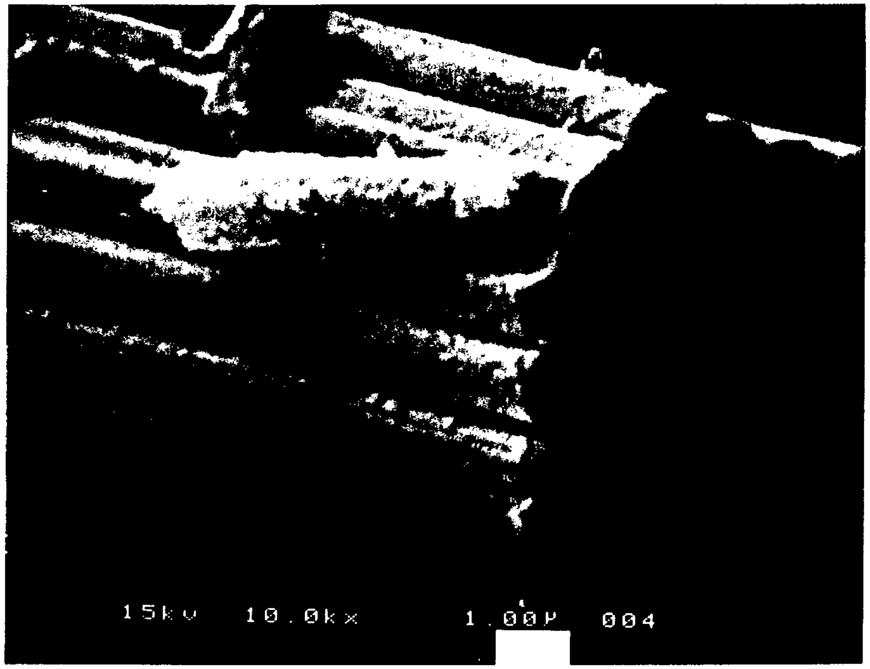
15kv 10.0kx 1.00µ 004

14

ATTACHMENT VI

Paper (i)

Submitted to CARBON
March 1998

ON THE ROLE OF SUBSTITUTIONAL BORON IN CARBON OXIDATION

Ljubisa R. Radovic, Murthy Karra, Kristina Skokova and Peter A. Thrower

Fuel Science Program
Department of Materials Science and Engineering
The Pennsylvania State University
University Park, PA 16802

Keywords: A. doped carbons, B. oxidation, C. molecular simulation, C. thermal analysis, D. electronic structure

ABSTRACT

An experimental and theoretical study of carbon oxidation in the presence of substitutionally doped boron has been carried out. The effects of boron loading, reaction temperature and degree of burnoff were analyzed for a range of carbon materials. Both inhibiting and catalytic effects were observed. Several semiempirical molecular orbital modeling approaches were used in an attempt to rationalize these intriguing experimental findings in terms of electronic effects in the graphene layer. In particular, a critical analysis of the key adjustable parameters was performed. The oxidation results were discussed in terms of a balance between three potentially competing effects of substitutional boron: (a) reduced total electron density, (b) decreased contribution of delocalized π electrons to the electron density of the remaining carbon atoms, and (c) σ electron localization on carbon atoms due to the higher electronegativity of carbon with respect to boron.

1. INTRODUCTION

The carbon oxidation reaction has been investigated very thoroughly. Its general mechanistic and kinetic features are reasonably well understood [1, 2, 3, 4]. Yet there are many practical and fundamental 'details' that still need to be sorted out. Among the most important ones are the following:

(a) What is the exact nature of the relationship between 'reactive' C(O) intermediates and 'stable' C-O complexes on the carbon surface?

(b) What is the reason for the commonly observed "compensation effect" in both uncatalyzed and catalyzed carbon gasification?

(3) What structural features of the carbon surface govern the magnitude of the CO/CO_2 ratio in the products of oxidation and, in particular, how exactly is CO_2 formed?

(4) Is it possible that, when carbon is doped with boron, both a catalytic and an inhibiting effect can be observed?

Much has been written about the first issue and very little is known about the second. Elsewhere [5, 6] we address both of them and argue that the elusive concept of the compensation effect and the intriguing balance between reactive and stable carbon-oxygen surface complexes may both have an analogous explanation to the one offered here for the role of boron in carbon oxidation. We have recently completed a detailed analysis of the third issue [6] and it will be reported elsewhere. Here we analyze in detail the fourth question.

The general issue of the electronic effects of heteroatom substituents on the structure and reactivity of carbon materials is one whose time has come. In particular, the practically important question of the role of substitutional boron has resurfaced. In the 1950's and 1960's it was driven by the use of graphite as a moderator in nuclear reactors [7, 8, 9, 10, 11, 12]; today it is motivated by the need for oxidation protection of carbon-carbon (C-C) composites [13, 14, 15, 16, 17, 18, 19]. Boron is considered to be one of the very few promising candidates for chemical protection of C/C composite materials against oxidation [20]. Oxidation protection is of paramount importance for the use of these strategic materials in demanding (e.g., structural) aerospace applications. Most ceramic coatings have a thermal expansion mismatch with carbon and thus develop cracks which inevitably result in carbon exposure to high-temperature O_2. Even in the increasingly important higher-volume and less demanding applications of C/C composites (e.g., friction materials in high-performance and heavy-duty vehicles), oxidation protection is an important issue.

The conventional wisdom is that boron inhibits carbon oxidation. Its inhibiting effect can be manifested in three different ways: (a) Substitutional boron enhances the graphitization of carbon [14, 21, 22]. (b) As the surface carbon atoms are consumed, substitutional boron forms an oxide surface film, which acts as an O_2 diffusion barrier and an active site blocker [10, 11, 13, 14, 17, 20]. (c) Substitutional boron causes a redistribution of the π electrons in the basal plane (graphene layer), lowers the Fermi level of carbon, and hence presumably inhibits the desorption of CO and CO_2 [14, 17, 20]. This last mode of inhibition is of great fundamental interest because it offers the opportunity not only to reduce the number of carbon reactive sites, i.e., to achieve a proportional reduction of carbon reactivity, but also to suppress the intrinsic reactivity (or turnover frequency) of these sites and thus achieve an exponential reduction of carbon reactivity. It had not been verified in the past. As a consequence of our recent results [19, 23], and upon examining both some early and some very recent studies, its closer scrutiny is warranted.

We provide such a scrutiny in the present communication. The experimental results are complemented by a theoretical analysis based on molecular orbital (MO) calculations. In contrast to some recent such analyses, the assumptions made are clearly stated and their validity is discussed in detail.

2. EXPERIMENTAL SECTION

Three widely differing carbon materials were used: a heat-treated ('graphitized') carbon black (Graphon, Cabot Corp.), Saran char (produced by pyrolysis of a PVC/PVDC copolymer manufactured by Dow Chemical Co.) and a glassy carbon (a phenolic-resin-derived material, Alfa-Aesar). Boron was introduced, presumably substitutionally into the quasi-graphitic lattice, by heating these carbons, physically mixed with boron powder (99.999%, Alfa-Aesar) at different levels (1, 2 and 5 wt. % B), to ~2450 °C in Ar. Some loss of boron occurred during this treatment and the boron loadings quoted above are therefore upper values.

Isothermal carbon oxidation experiments (~10 mg samples; 1 atm; 21% dry O_2, 99.994%; 250 cc/min) were performed with these samples in a Mettler TGA. The reaction temperature was achieved after heating the sample in N_2 at 25 °C/min; negligible gasification occurred during this nonisothermal period. In a few selected cases, the reactive surface area (RSA) [24] of the carbon was determined as a function of burnoff (percent conversion) using a commercial transient kinetics apparatus (SSITKA 2000, Altamira Instruments). The integrated area under the transient decay curves for CO and CO_2, after switching from O_2 to inert gas at different conversion levels, was used as a first approximation to true RSA values [25].

3. THEORETICAL SECTION

Both the simple Hückel molecular orbital (SHMO) theory [26] and a generalized Hückel theory, the so called self-consistent field Pariser-Parr-Pople (SCF-PPP) approach [27] , were used extensively to rationalize the experimental results. In addition, a preliminary study using the highest-level semiempirical approach, AM1, was used. (The PM3 method has not been parameterized for boron.) The choice of the semiempirical Hückel methods was based on the following considerations: (a) their simplicity, unobscured physical insight and demonstrated usefulness in the analysis of π electron systems; (b) the ability to use a 'representative' (i.e., relatively large) model cluster for a graphene layer; and (c) essentially aromatic character of the graphene layers, both in the absence and presence of substitutional boron.

The third consideration needs careful elaboration, because the validity of any semiempirical method obviously depends on a judicious selection of its adjustable parameters. The issue is the following: To what extent does substitutional (and thus sp^2-hybridized) boron disrupt the delocalized π system of the graphene layer and/or modify the distribution of π electrons? That B is an electron acceptor in a heteroaromatic system has been well established for decades [7, 28, 29]. However, the degree of charge transfer from the more electronegative carbon atoms has been a matter of debate and some confusion (see Sections 3.1 and 5).

This fundamental question is related to the more practical one of the appropriate choice of parameters h_B and k_{C-B} in the Coulomb (α) and resonance (β) integrals of the SHMO method,

$$\alpha_B = \alpha_0 + h_B\beta_0$$

$$\beta_{C\text{-}B} = k_{C\text{-}B}\beta_0$$

where α_0 and β_0 are reference values for homonuclear systems. These parameters are readily available [26, 30, 31], though the values used by different authors are often not the same. Their critical evaluation has not been performed recently and here we attempt to provide one. As stated by McWeeny [32], "a totally unrealistic charge distribution could easily result unless parameter values [are] chosen with extreme care."

3.1 Background. The pioneering work appears to be that of Roothaan and Mulliken [33] in which they used a semiempirical MO method to conclude that the resonance integral for benzene is some 0.3 eV larger (-2.6 vs. -2.3 eV) than that of borazine, $B_3N_3H_6$, the inorganic analogue of benzene. Many years later, Kaufman and Hamann [34] and Chalvet et al. [35] used these results to confirm that h_B and h_N should be -1.0 and 1.0, respectively, and many other investigators confirmed the aromatic character of borazine, albeit somewhat attenuated by the large electronegativity difference between B and N. Dewar et al. [36] used this idea about borazine aromaticity [29] to synthesize a number of new heteroaromatic compounds. The same research group [37, 38] used the charge transfer spectra of π-complexes (formed by trinitrobenzene or tetracyanoethylene with a number of homo- and heteroaromatic hydrocarbons) to derive values of MO parameters for boron. They argued for symmetric effects of B (which contributes 0 π electrons to the ring) and N (which contributes either 1 or 2 electrons) on electron delocalization and thus proposed the following Hückel parameters: $h_B = -1.59$; $h_N = 1.59$; $k_{C\text{-}B} = k_{C\text{-}N} = 0.90$. Matteson [39] used SHMO theory to study the properties of ethyleneboronic acid and concluded that the upper values of h_B and $k_{C\text{-}B}$

should be -1.0 and 0.7, respectively, while Good and Ritter [40] proposed these same values after analyzing the UV and NMR spectra of methylvinylboranes and noted the modest degree of resonance stabilization (with respect to the isoelectronic vinyl carbonium ions). In a follow-up study Matteson [41] noted that, since B does not contribute an electron to the π-bond system (along with its empty p-orbital), the value of its Coulomb integral cannot be extrapolated precisely and thus proceeded to use h_B as a variable parameter in the range -1.0 to -0.5. He concluded, however, that there is no doubt about substantial delocalization of electrons into the vacant p-orbital of boron and its consequent large chemical effects. By analyzing the reactivity of dibutyl ethyleneborate, he finally adopted a value of -0.7 for h_B and commented that the much higher value proposed by Dewar and Rogers [38] "does not appear to correlate with the present and previous experimental results." The results of Shriver et al. [42] on phenyl-substituted borazines were consistent with the argument [33, 38] that $h_B = -h_N$, but not with the high value of -1.59 proposed by Dewar and Rogers [38]. In the same period, Davies [43] performed self-consistent MO calculations on borazine and confirmed its similarity to benzene by quantifying more precisely the degree of electron delocalization (e.g., leading to values of 1.42 vs. 1.39 Å for bond lengths of borazine and benzene). In an even more detailed study of borazine, Chalvet et al. [44] compared the results of SCF MO calculations using various semiempirical approaches and the following three electron-distribution models as bases for the selection of input parameters: (I) with no preconceived notion about B–N bonding, Mulliken's electronegativity-based Hückel parameters [33] were used, implying electron transfer from B to N; (II) boron has three (sp^2) electrons in its σ-frame and a fourth extra electron which it donates to the π system; and (III) the three boron atoms contribute no electrons to the π

system, while the three nitrogens contribute all six of them. They concluded that, in agreement with Model I, σ-electron charge is transferred from B to N while π electron charge is transferred from N to B. Perkins and coworkers were also able to confirm the existence of π charge on B in a series of vinylboranes [45, 46, 47] , borazines [48] and cyclic boron-oxygen compounds [49, 50]. Brown and McCormick [51] used the value of 1.0 for the resonance integral parameter of substituted borazines; the corresponding values of the Coulomb parameter were -0.8 and -0.9.

After this extensive research effort, and following in the footsteps of the classic treatise by Streitwieser [26], Purcell and Singer [30] summarized the reported values of SHMO parameters for ten different heteroatoms including boron. Most of the h_B values clustered around -1.0, with a range of 0.5, while k_{C-B} values mostly coincided at a value of -0.7. Interestingly, the above mentioned study by Dewar and Rogers [38] was not cited.

Chakrabarty et al. [52] argued that the study by Dewar and Rogers [38] demonstrated the success of the SHMO in "explaining the properties of some boron-nitrogen compounds." They used a similar approach to study B-N bonds in aminoboranes but adopted the parameters recommended by Streitwieser [26]. Labarre et al. [53] compared the aromaticities of borazines and boroxines and concluded that the latter are less aromatic (e.g., with values of k_{B-N} and k_{B-O} of 0.74 and 0.63), not only in agreement with the lower degree of π electron delocalization in the presence of the more electronegative oxygen, but also because of the much larger gradient of bonding electron population (both π and σ) between B and O than between B and N. Ramsey and Ito [54] performed MO calculations on various boranes with the commonly used value h_B=-0.9, but concluded that the charge density and bond order values reported by Armstrong and Perkins [46, 47] were too high.

In a related study on phenylboronic acid, Ramsey [55] argued in favor of an h_B value lower than -1.0 (e.g., -0.9), instead of the "most widely used value" of -1.0 or higher.

Another summary of heteroatom HMO parameters was prepared by McGlynn et al. [56]. In addition to citing Streitwieser's recommendations [26], their compilation contained values from two additional sources, but neither of these included boron.

Next to the most often cited summary by Streitwieser [26] is the study by Van-Catledge [31], who used the SCF-PPP method to obtain a complete set of Hückel parameters, including those for the first-row elements B, C, N, O and F, based on a study of ethylene properties. A subsequent study by Matteson and Moody [57] employed these parameters, instead of the ones proposed previously by Matteson [39]. In the most recent such study, Abraham and Smith [58] parameterized the Coulomb and resonance integrals based on CNDO-calculated π densities and experimental dipole moments of a large number of compounds including substituted olefins and aromatics (albeit without B). They concluded that the latter "[give] in general more consistent results and [are] to be preferred."

Table 1 compares the h_X parameters proposed by Streitwieser[26] along with those adopted by Dewar and Rogers [38], Van-Catledge [31] and Abraham and Smith [58]. The values of Pauling electronegativity for the first-row elements from B to F are shown for comparison. The increasing core potential, due to increasingly incomplete screening of nuclear charge [26], is reflected in increasing h_X values. Furthermore, because the π electron is attracted more by a more electronegative element, h_B will have a negative value, while h_N, h_O and h_F will have positive values. A simplistic approach to the quantification of this effect is its proportionality with the electronegativity difference between carbon and the heteroatom [26]. The results of Abraham and Smith [58] do not follow this trend, however. An additional important factor is that different heteroatoms contribute zero, one or two electrons to the delocalized π system; the difference in h_X for pyridine- vs. pyrrole-type N, or between formaldehyde- vs. phenol-type O, was estimated as 1-1.5 units [26], and this is confirmed by the results of Van-Catledge [31] and Abraham and Smith [58].

Regarding $k_{C\text{-}X}$ values, the variations reported in the literature are much smaller and appear to be less critical. Typically, the values are close to 1.0 (as for $k_{C\text{-}C}$) and they decrease with increasing number of electrons donated by the heteroatom to the π system [26, 59].

Additional insight into the aromatic character of B-C cyclic compounds comes from studies of the seven-membered ring in borepin (C_6H_7B) [60]. In the early work of Schulman et al. [61], a comparison was made between the geometries of borepin, tropylium cation and cycloheptatriene. The authors concluded that borepin is a weakly conjugated system and that the origin of its small extent of electron delocalization is the "small electronegativity of boron, which makes it unable to obtain a π-electron density comparable to the carbons." In a subsequent report, Schulman and Disch [62] corroborated these conclusions by finding that the C–C and B–C bond lengths are consistent with some π delocalization; however, the resonance energy of borepin was much lower than that of either benzene or pyridine. Ashe and coworkers [63, 64, 65] also published studies of borepin and its derivatives in which they concluded that borepin is certainly planar but only weakly aromatic.

The most relevant studies to the present communication are, of course, those devoted to borabenzene or borinine (C_5H_5B). The first detailed quantum chemical analysis of this hypothetical molecule appears to be that of

Raabe and coworkers [66, 67]. They explored the reasons for its extremely high reactivity and concluded that, despite its definitely aromatic character, borabenzene is destabilized by "pronounced acceptor properties, which are due to a low-lying σ^* orbital" (at 0.099 eV) mainly localized on the boron atom [68]. Table 2 compares the energy levels of borabenzene (in eV) with those of benzene and pyridine, as determined by the semiempirical MNDO technique. More recently, Simkin et al. [69] made a similar comparison and concluded that borabenzene is inferior in its aromatic character to pyridine, which in turn is slightly inferior to benzene. The relevant aromaticity parameters, the MNDO-based aromatic stability indices and the homodesmotic stabilization energies (measured or calculated for reactions where the number of bonds of every formal type is equal in reactants and products), were 0.939, 0.971 and 1.0 and 19.2, 25.4 and 24.7 kcal/mol, respectively, for borabenzene, pyridine and benzene. Interestingly, the latter HSE values are identical to the empirical resonance energy values determined by Schulman and Disch [70]. Simkin et al. [69] concluded, in agreement with previous investigators, that the "elusive nature of borabenzene cannot be attributed to insufficient aromaticity which, according to HSE values amounts to 78% of benzene's aromaticity. Rather, it will be explained by high reactivity due to the σ-acceptor properties of a low-lying σ^*-MO. The stabilization of borabenzene is indeed achieved through formation of complexes with σ-donors." Schulman and Disch [70] compared the thermochemical properties of borabenzene and borepin. The B–C bond length in the former is shorter than that in the latter (1.435 vs. 1.537 Å). In agreement with this larger resonance stabilization of borabenzene, its empirical resonance energy is lower than that of pyridine or benzene, as mentioned above, but it is much higher than that of borepin. (The ERE value for borepin was 12.7 kcal/mol.)

The existence of a free borabenzene molecule had not been proven[68], however, until quite recently [71]. Both Fu and coworkers [72, 73, 74] and Herberich and coworkers [75, 76] reported on the synthesis, structure and reactivity of several borabenzene complexes, again confirming the high reactivity of borabenzene, which is both a Lewis acid and an aromatic compound.

Perhaps the best summary of the current state of knowledge about B-containing aromatic compounds has been provided by Sugihara et al. [77]. Their unique properties arise from a certain measure of π type overlap between the p (or sp^2) orbitals of boron and carbon, by virtue of which B participates in cyclic conjugation and at the same time behaves as π electron acceptor. In addition, B is more electropositive than carbon and its π negative charge is decreased by polarization of the σ bonds. The uncertainties about the balance between these two opposing effects make it difficult to assign a unique Coulomb integral to boron and unique carbon-boron resonance integrals.

Finally, it is worth pointing out that the state-of-the-art semiempirical MO method, AM1, may suffer from the same parameterization uncertainties [78]. For the reasons which have been made obvious above, most of the B-C compounds whose properties are used in the parameterization process are not aromatic. The very few that are (e.g., $C_6H_5B(OH)_2$ and its halogen analogues) display relatively large errors (>15%) in the calculated heat of formation, which appears to be their only measured property.

3.2 Approach. The HMO calculations were performed using the HMO 2.0.3 program of A. Wissner [79]. In the SHMO calculations, the resonance parameter for boron, $k_{C\text{-}B}$, was 0.73; the corresponding Coulomb parameter, h_B, was varied between -0.5 and -1.5. In a few selected cases, the iterative ω-technique of Wheland and Mann [80] was used to take into account the fact that the tendency of an atom to withdraw or release electrons depends on the charge that it already has; thus the Coulomb parameters were adjusted in a self-consistent (iterative) manner depending on the resulting values of π electron densities.

The SCF-PPP calculations were carried out using the one-center electron repulsion integrals derived from valence state ionization potentials of Hinze and Jaffé [81]. The VSIP value for B (8.42 eV) corresponds to its promoted but non-hybridized state ($2s^1 2p_x^1 2p_y^1$) and that of C (11.16 eV) corresponds to its hybridized state. The correction of Sane and Sane [82] was applied. The nearest-neighbor core resonance integrals were calculated using the formula proposed by Ohno [83]. The two-center electron repulsion integrals were calculated using the formula of Nishimoto and Mataga [84, 85]. Self-consistency was achieved when the updated bond lengths, determined from π-bond orders, were consistent with the calculated integrals.

A few theoretical experiments were carried out with the AM1 method using the MOPAC 5.0 computer program [86].

4. RESULTS

4.1 Experimental Findings. Figure 1 shows that boron acts as a catalyst of oxidation of glassy carbon. Figure 2 summarizes the kinetic data (at the same conversion level) for the boron-doped Saran char. In agreement with the behavior observed for boron-doped Graphon [23], boron is seen to act as a catalyst at low B loadings and as an inhibitor at higher B loadings. The global activation energy does not seem to depend in a consistent way on B content. It is governed rather by the nature of the carbon: as almost invariably reported in the literature, it increases as the degree of crystalline order in the carbon increases (33±3 kcal/mol for undoped and boron-doped Saran char vs. 44±5 kcal/mol for undoped and B-doped Graphon).

Figure 3 shows the x-ray diffraction profiles for undoped and B-doped Saran chars. At the highest B loadings, the signature of enhanced graphitization – splitting of the (10) turbostratic peak (at ~43 °2θ) into (100) and (101) graphitic peaks (at ~42 °2θ and ~44 °2θ) – is observed.

Figures 4 and 5 summarize the intriguing catalytic and/or inhibiting effects of boron in carbon oxidation as a function of the reaction temperature and burnoff. In agreement with the data shown in Figure 2 and in our earlier work [23], the net effect depends on the concentration of B in the carbon. It is surprising that boron, present presumably as predominantly substituent atoms in the carbon lattice, acts as a catalyst at low loadings and as an inhibitor at higher loadings. This is in contrast to all other reports in the literature [10, 11, 17, 20], where an inhibiting effect was found at all B concentration levels when dry O_2 was used as the reactant. Interestingly, Thomas and Roscoe [8] did observe a catalytic effect in moist O_2. More recently Rodriguez and Baker [87] confirmed the inhibiting effect of the B_2O_3 layer, but reported a catalytic effect of boron carbide.

4.2 Theoretical Observations. Before analyzing the qualitative and quantitative impact that boron substitution is predicted to have on the electron distribution in a graphene layer, it is important to evaluate the ability of selected models to predict some well established features of both boron-free and boron-containing aromatic compounds.

Table 3 shows the bonding and anti-bonding (*) MO energy levels for benzene, pyridine and borabenzene obtained with the SCF-PPP method, while Table 4 and Figures 6 and 7 summarize the corresponding π-electron densities and free valences derived using SHMO and SCF-PPP methods. Both methods make the same qualitative predictions which are well established: in contrast to N, which contributes an electron to the π system and raises the electron density both at the more electronegative N atom and at the alternant positions (see Figure 8), the effect of substitutional boron is to both reduce the π electron density and accept substantial electron density (especially as predicted by SCF-PPP) into its vacant $2p_z$ orbital.

Clearly, the SCF-PPP method does provide acceptable qualitative predictions of borabenzene's properties but it appears to overestimate the degree of π electron delocalization. This may not be too surprising, having in mind the fact that borabenzene has a singly occupied MO, while the method implemented in the HMO 2.0.3 software has been optimized for closed-shell systems. Indeed, as shown in Figure 8 for a closed-shell molecule, the consistency of prediction of π electron distribution in pyridine is much better. The performance of the model in predicting the properties of borepin was therefore of interest as well.

Table 5 summarizes the results of bond length calculations using the various models, Table 6 shows the MO energy levels and Figure 9 summarizes the π electron density trends in borepin. Even though it is a closed-shell molecule, the SCF-PPP method again appears to overestimate the π electron density at the B position and thus overestimate the loss of electron density on adjacent C atoms. Therefore, this artifact must be attributed to some other feature of the SCF-PPP model. One obvious possibility is the VSIP value selected for boron. Indeed, if it is reduced to 4.5 eV, Figure 9 shows good agreement with SHMO results. Whether or not this value is more reasonable than 8.42 eV (see Section 3.2) is beyond the scope of this investigation. Suffice it to point out that (a) orbital (as opposed to ground-state) electronegativities [81, 88], including those of vacant orbitals such as $2p_z$ of boron, are dependent on partial charges on the atoms, and (b) this issue is still an active area of research [58, 89, 90, 91, 92].

With this important background analysis we can now present, with some degree of confidence, the results that are thought to be directly relevant to the reactivity of carbon materials. Tables 7 and 8 summarize the effects of substitutional boron, in various positions, on the π electron distribution in polyaromatic hydrocarbons (model graphene layers) of increasing size. (In this way the range of boron doping from 16.7% in benzene to 4.2% in coronene has been covered.) In both instances, as intuitively expected, there is a general decrease in π electron density on the peripheral (edge) carbon atoms. A greater decrease is predicted by the SCF-PPP method; this is consistent with a similar effect in borepin and borabenzene, where a much greater (and unrealistic!?) electron withdrawal from the π system into the vacant 2p orbital of B was found. Indeed, there is a consistent trend of increasing electron density on the peripheral B atom with increasing size of the model aromatic cluster.

The preliminary results obtained using the AM1 method for coronene are summarized in Table 9, together with the analogous free valence (FV) data obtained from SHMO theory. Interestingly, the FV on the carbon atoms is predicted to increase or decrease in the presence of boron, depending on their exact position with respect to the boron atom. Both methods show an increase in the total FV on the edge atoms (with the exception of B at position #20, for which AM1 predicts a decrease). Furthermore, as expected, the FV values are clearly higher at the edge carbon atoms.

5. DISCUSSION

In light of the results presented in Section 4, the premises on which some of the earlier work was based [14, 17, 20] need to be reexamined.

There is no doubt that boron catalyzes the graphitization of a wide range of carbons. Figure 3 confirms this well known effect. This in turn leads in general to a decrease in reactive surface area [24, 93] and thus to oxidation inhibition.

On the basis of results shown in Figures 4 and 5, there is no compelling reason to doubt either that B_2O_3 is formed upon oxidation of boron-doped carbons [8]. It is worth noting, however, the recent important study by Cermignani et al. [94] in which X-ray photoelectron spectroscopy was used to identify the boron-containing species after heat treatment and oxidation of boron-doped CVD carbon films. After oxidation at 600 °C for 4 h, they saw no clear evidence that B_2O_3 was the predominant species formed; instead, they identified boron oxycarbides as the dominant surface species.

What needs reevaluation is the proposed [14] electronic effect of boron (mechanism (c) in Section 1). The origin of this proposal lies in its presumed analogy with the electronic effect of a carbon gasification catalyst which, upon oxygen adsorption, induces type (b) distribution of the π electrons in the graphene layer [95], as shown in Figure 10. By accepting electrons from the graphene layer (e.g., into unfilled d bands of a transition metal), a catalyst is thought to facilitate both O_2 adsorption (by increasing the C-O bond strength) and product desorption (by weakening the adjoining C-C bonds).

In contrast to the oxygen-transfer theory [96], this electron-transfer theory of catalysis [97] has not found much support in the carbon gasification literature and had not been confirmed experimentally. Nevertheless, a recent theoretical study of potassium-catalyzed graphite oxidation [98] does indicate that the electron-donating K catalyst lowers the work function of graphite and thus enhances the dissociation probability of O_2 on the surface. This is opposite to the well known electronic effect of substitutional boron, which does not contribute electrons to the delocalized π system of the graphene layer and lowers the Fermi level of graphite [10, 11]. Boron would thus be expected to decrease, to some extent at least, the dissociation (chemisorption) probability of O_2. Indeed, Allardice and Walker [10] concluded that boron inhibits the chemisorption of CO_2 in the C/CO_2 reaction.

Our theoretical results are consistent, for the most part, with these conclusions. Molecular orbital theories offer at least three reactivity indices: π electron density, free valence and the energy levels of frontier orbitals [99]. The free valence index is typically used as a measure of ease of attack by free radicals, but it also provides a measure of residual bond-forming affinity of the reactive sites.

The results summarized in Tables 7 and 8 are consistent with the notion that carbon oxidation, assumed to be an electrophilic reaction, is inhibited by a lower electron density on the reactive sites. This is in agreement with the fact that positions of high electron density (e.g., edges of carbon crystallites) are most prone to attack by electrophilic reagents [32]. (It should be noted, however, that the absolute values of electron densities on the various atoms may not be reliable because they do not reflect well the large differences between edge and basal-plane sites.)

Ma and coworkers [100, 101] adopted a similar approach and used the AM1 MOPAC software to calculate a reactivity index from the electron population in four highest occupied MOs. They reported large variations in this index, depending on the precise location of the substituent B atoms in a 54-atom aromatic cluster. In spite of several apparent inconsistencies in their results (e.g., an increase in electron density at edge carbon atoms in the vicinity of edge B atoms, and comparable electron densities at armchair edge carbon atoms and basal-plane carbon atoms), they attributed the inhibiting effect of substitutional boron to a dramatic reduction of the "density of high energy electrons on all the originally active sites." In a previous *ab initio* modeling study of the BC_3 analogue of graphite[102], the same research group had concluded exactly the opposite. Charge transfer was postulated to occur from B to C (i.e., the electronegativity effect apparently prevails over that of π electron delocalization), which in turn means that "[t]his charge transfer [...] is partly responsible for reducing the oxidation of C in C/C composite," presumably because "an electronegative O will prefer to react with B than C in a graphite doped with B, and the resulting B_2O_3 [...] would protect the oxidation of C." Clearly, there is a pressing need to (attempt to) reconcile these and other [14, 15, 19, 23, 100, 101] contradictory statements about the role of substitutional boron in carbon oxidation.

The first and foremost issue is the direction of electron transfer in the graphene layers. Based on the experimentally verified behavior in borabenzene and borepin structures (see Sections 3.1 and 4.2), as well as the experimental and modeling results presented above, we conclude that the dominant reactivity-determining effect is π electron transfer from C to B.

Consequently, the reduced electron density on edge carbon atoms is thought to cause inhibition of O_2 chemisorption.

The second issue is the significance of free valence changes in the presence of substitutional boron. The predicted increase (Table 9), assuming the same maximum bond order around a boron atom as around an sp^2-hybridized carbon atom in trimethylenemethane, is consistent with boron's catalytic effect in carbon graphitization, as the higher edge reactivity in free radical condensation reactions promotes crystallite growth and preferential increase in crystallite width [103]. Whether or not it is consistent with a suggested catalytic effect on carbon oxidation [104] remains to be clarified, both theoretically and experimentally. In particular, the effects of both reduced electron density and enhanced free valence on the carbon surface coverage by stable and reactive surface intermediates, which governs not only the reactivity but also the CO/CO_2 ratio in the reaction products, deserves greater attention.

Experimental evidence has been presented here (Figures 1,2,4,5) that substitutional boron is not only an inhibitor but also a catalyst of carbon oxidation. The catalytic effect is clearly observed for the first time (assuming that it is not due to the presence of B_4C[87] in these samples); this is attributed to the fact that samples possessing relatively high surface areas were used, and the catalytic effect was not masked by the ubiquitous inhibiting effect of B_2O_3.

The reinterpretation of the relevance of Figure 10 is thus as follows: The redistribution of π electrons in the presence of substitutional boron results not in the weakening of C-O bonds and strengthening of C-C bonds [14], but in exactly the opposite effect: being essentially a π electron 'acceptor', as discussed in detail in Section 4.2, upon O_2 adsorption boron is predicted to induce type (b) distribution of π electrons and thus weaken C-C bonds and strengthen C-O bonds. In fact, Allardice and Walker [11] used this precise argument, together with the observed decrease in the activation energy for oxidation of graphite, to anticipate the *catalytic* effect of substitutional boron (even though in their study this effect was masked and overwhelmed by the inhibiting effect of B_2O_3).

The fact that boron appears to be a catalyst under conditions favoring desorption control (lower temperatures and higher oxygen partial pressures) and inhibitor under conditions favoring adsorption control (higher temperatures and lower oxygen partial pressures) [105] is quite intriguing. It suggests that this phenomenon is yet another example of the well known (and still essentially mysterious) compensation effect, which we tentatively interpret as a "macroscopic complementarity principle" [106]: in the presence of substitutional boron the turnover frequency for carbon atom removal increases (due to the catalytic effect of C-C bond weakening), but the number of reactive sites decreases (due to the inhibiting effect on O_2 adsorption). Preliminary evidence for the latter statement is provided in Figure 11: there is a consistent decrease in reactive surface area with both increasing B content and increasing carbon burnoff.

6. CONCLUSIONS

Electron distribution in the graphene layer in the presence of substitutional boron is a balance between three potentially competing effects: (a) reduced total electron density, (b) decreased contribution of delocalized π electrons to the electron density on the remaining carbon atoms, and (c) σ electron localization on C atoms due to higher electronegativity of C with respect to B.

While these effects are the origin of considerable uncertainty regarding the most appropriate semiempirical MO parameters for the B/C system, the results of our study all point in the same direction regarding carbon reactivity: in the presence of substitutional boron, the dominant electronic effect appears to be reduced electron density on reactive carbon atoms. This is thought to suppress O_2 chemisorption, thus having an inhibiting effect on carbon oxidation and reinforcing the inhibition due to B_2O_3 formation. Nevertheless, the very redistribution of π electrons that inhibits (but does not prevent) O_2 chemisorption is thought to be responsible for a catalytic effect on CO and CO_2 desorption. The net effect appears to be a complex balance between the influences of boron content and distribution, carbon nature (e.g., surface area) and reaction conditions. While some of the fundamental issues discussed here need to be further clarified by carefully designed experiments and computer simulations, it is clear that a molecular engineering approach to the design of boron-doped carbons [103] is necessary for achieving maximum oxidation inhibition in materials of practical interest.

ACKNOWLEDGMENTS

Partial grant for the SSITKA apparatus was kindly provided by George Marcelin of Altamira Instruments. This research was carried out under Grant URI F49620-93-1-0311 from the Air Force Office of Scientific Research (T. Erstfeld and G. Pechenik, Project Managers). Fruitful collaboration with G. S. Rellick (The Aerospace Corporation) and discussions with X. Ma, C. G. Pantano, Y. Uchiyama and Y.-J. Lee are also acknowledged.

REFERENCES

1. Laurendeau, N.M., *Prog. Energy Combust. Sci.*, 1978, 4, 221.
2. Essenhigh, R.H., in *Chemistry of Coal Utilization, 2nd Suppl. Vol.* (Elliott, M.A., Ed.), Wiley, New York, 1981, p. 1153.
3. Lahaye, J. and Ehrburger, P., Eds., *Fundamental Issues in Control of Carbon Gasification Reactivity,* Kluwer Academic Publishers, Dordrecht (The Netherlands), 1991.
4. Walker Jr., P.L., *Carbon*, 1991, 29, 411.
5. Skokova, K. and Radovic, L.R., in *American Chemical Society, Div. Fuel Chem. Preprints,* Vol. 41 (1), New Orleans , 1996, p. 143.
6. Skokova, K.A. and Radovic, L.R., in preparation.
7. Soule, D.E., in *Fifth Biennial Conference on Carbon,* University Park, PA (Pergamon Press), 1961, p. 13.
8. Thomas, J.M. and Roscoe, C., in *Second Conference on Industrial Carbon and Graphite,* London (Society of Chemical Industry), 1965, p. 249.
9. Woodley, R.E., *Carbon*, 1968, 6, 617.
10. Allardice, D.J. and Walker, Jr., P. L., *Carbon*, 1970, 8, 773.
11. Allardice, D.J. and Walker, Jr., P. L., *Carbon*, 1970, 8, 375.
12. Djurkic, T., Peric, A., Lausevic, M., Dekanski, A., Neskovic, O., Veljkovic, M. and Lausevic, Z., *Carbon*, 1997, submitted.
13. Ehrburger, P., Baranne, P. and Lahaye, J., *Carbon*, 1986, 24, 495.
14. Jones, L.E. and Thrower, P.A., *J. Chim. Phys.*, 1987, 84, 1431.
15. Jones, L.E. and Thrower, P.A., *Carbon*, 1991, 29, 251.
16. Zaldivar, R.J., Kobayashi, R.W., Rellick, G.S. and Yang, J.-M., *Carbon*, 1992, 30, 711.

17. Kowbel, W., Huang, Y. and Tsou, H., *Carbon*, 1993, 31, 355.

18. Kouvetakis, J., McElfresh, M.W. and Beach, D.B., *Carbon*, 1994, 32, 1129.

19. Karra, M., Thrower, P. A. and Radovic, L.R., in *American Chemical Society Div. Fuel Chem. Preprints*, Vol. 41(1), New Orleans ,1996, p. 211.

20. McKee, D.W., in *Chemistry and Physics of Carbon, Vol. 23* (Thrower, P.A., Ed.), Marcel Dekker, New York, 1991, p. 173.

21. Marinkovic, S., Suznjevic, C. and Dezarov, I., *Carbon*, 1969, 7, 185.

22. Zaldivar, R.J., Kobayashi, R.W., Rellick, G.S. and Yang, J.-M., *Carbon*, 1991, 29, 1145.

23. Karra, M., Zaldivar, R.J., Rellick, G.S., Thrower, P.A. and Radovic, L.R., in *22nd Biennial Conference on Carbon*, San Diego, CA, 1995, p. 646.

24. Radovic, L.R., Lizzio, A.A. and Jiang, H., in *Fundamental Issues in Control of Carbon Gasification Reactivity* (Lahaye, J. and Ehrburger, P., Eds.), Kluwer Academic Publishers, Dordrecht (The Netherlands), 1991, p. 235.

25. Lizzio, A.A., Jiang, H. and Radovic, L.R., *Carbon*, 1990, 28, 7.

26. Streitwieser Jr., A., *Molecular Orbital Theory for Organic Chemists*, John Wiley & Sons, Inc., New York, 1961.

27. Murrell, J.N. and Harget, A.J., *Semi-empirical self-consistent-field molecular orbital theory of molecules*, Wiley-Interscience, London, 1972.

28. Maitlis, P.M., *Chem Rev.*, 1962, 223.

29. Dewar, M.J.S., in *Boron Chemistry, Vol. 1* (Steinberg, H. and McCloskey, A.L., Eds.), The MacMillan Company, New York, 1964, p. 235.

30. Purcell, W.P. and Singer, J.A., *J. Chem. Eng. Data*, 1967, 12, 235.

31. Van-Catledge, F.A., *J. Org. Chem.*, 1980, 45, 4801.

31. Van-Catledge, F.A., *J. Org. Chem.*, 1980, 45, 4801.

32. McWeeny, R., *Coulson's Valence*, Oxford University Press, Oxford, UK, 1979.

33. Roothaan, C.C.J. and Mulliken, R.S., *J. Chem. Phys.*, 1948, 16, 118.

34. Kaufman, J.J. and Hamann, J.R., *Adv. Chem. Ser.*, 1964, 42, 95.

35. Chalvet, O., Daudel, R. and Kaufman, J.J., *Adv. Chem. Ser.*, 1964, 42, 251.

36. Dewar, M.J.S., Kubba, V.P. and Pettit, R., *J. Chem. Soc.*, 1958, 3073.

37. Dewar, M.J.S. and Lepley, A.R., *J. Amer. Chem. Soc.*, 1961, 83, 4560.

38. Dewar, M.J.S. and Rogers, H., *J. Amer. Chem. Soc.*, 1962, 84, 395.

39. Matteson, D.S., *J. Amer. Chem. Soc.*, 1960, 82, 4228.

40. Good, C.D. and Ritter, D.M., *J. Amer. Chem. Soc.*, 1962, 84, 1162.

41. Matteson, D.S., *J. Chem. Phys.*, 1962, 27, 4293.

42. Shriver, D.F., Smith, D.E. and Smith, P., *J. Amer. Chem. Soc.*, 1964, 86, 5153.

43. Davies, D.W., *Trans. Faraday Soc.*, 1960, 1713.

44. Chalvet, O., Daudel, R. and Kaufman, J.J., *J. Amer. Chem. Soc.*, 1965, 87, 399.

45. Armstrong, D.R. and Perkins, P.G., *Theor. Chim. Acta*, 1966, 4, 352.

46. Armstrong, D.R. and Perkins, P.G., *Theor. Chim. Acta*, 1966, 5, 11.

47. Armstrong, D.R. and Perkins, P.G., *Theoret. Chim. Acta*, 1966, 4, 69.

48. Perkins, P.G. and Wall, D.H., *J. Chem. Soc. A*, 1966, 235.

49. Armstrong, D.R. and Perkins, P.G., *J. Chem. Soc. A*, 1967, 123.

50. Armstrong, D.R. and Perkins, P.G., *J. Chem. Soc. A*, 1967, 790.

51. Brown, D.A. and McCormick, C.G., *Theor. Chim. Acta*, 1966, 6, 350.

52. Chakrabarty, M.R., Thompson, C.C. and Brey Jr., W.S., *Inorg. Chem.*, 1967, 6, 518.

53. Labarre, J.-F., Graffeuil, M., Faucher, J.-P., Pasdeloup, M. and Laurent, J.-P., *Theor. Chim. Acta*, 1968, 11, 423.
54. Ramsey, B.G. and Ito, H., *Theor. Chim. Acta*, 1970, 17, 188.
55. Ramsey, B.G., *J. Phys. Chem.*, 1970, 74, 2464.
56. McGlynn, S.P., Vanquickenborne, L.G., Kinoshita, M. and Carroll, D.G., *Introduction to Applied Quantum Chemistry*, Holt, Rinehart and Winston, Inc., New York, 1972.
57. Matteson, D.S. and Moody, R.J., *Organometallics*, 1982, 1, 20.
58. Abraham, R.J. and Smith, P.E., *J. Comput. Chem.*, 1987, 9, 288.
59. Kakitani, T. and Kakitani, H., *Theor. Chim. Acta*, 1977, 46, 259.
60. Disch, R.L., Sabio, M.L. and Schulman, J.M., *Tetrahedron Lett.*, 1983, 24, 1863.
61. Schulman, J.M., Disch, R.L. and Sabio, M.L., *J. Amer. Chem. Soc.*, 1982, 104, 3785.
62. Schulman, J.M. and Disch, R.L., *Mol. Phys.*, 1996, 88, 213.
63. Ashe III, A.J. and Drone, F.J., *J. Amer. Chem. Soc.*, 1987, 109, 1879.
64. Ashe III, A.J., Klein, W. and Rousseau, R., *Organometallics*, 1993, 12, 3225.
65. Ashe III, A.J., Kampf, J.W. and Waas, J.R., *Organometallics*, 1995, 14, 3141.
66. Raabe, G., Heyne, E., Schleker, W. and Fleischhauer, J., *Z. Naturforsch. A*, 1984, 39, 678.
67. Raabe, G., Schleker, W., Heyne, E. and Fleischhauer, J., *Z. Naturforsch. A*, 1987, 42, 352.
68. Maier, G., Reisenauer, H.P., Henkelmann, J. and Kliche, C., *Angew. Chem.*, 1988, 27, 295.

69. Simkin, B.Y., Minkin, V.I. and Glukhovtsev, M.N., in *Advances in Heterocyclic Chemistry, Vol. 56* (Katritzky, A.R., Ed.), Academic Press, San Diego, 1993, p. 303.
70. Schulman, J.M. and Disch, R.L., *Organometallics*, 1989, 8, 733.
71. Cioslowski, J. and Hay, P.J., *J. Amer. Chem. Soc.*, 1990, 112, 1707.
72. Hoic, D.A., Davis, W.M. and Fu, G.C., *J. Amer. Chem. Soc.*, 1995, 117, 8480.
73. Hoic, D.A., Robbins Wolf, J., Davis, W.M. and Fu, G.C., *Organometallics*, 1996, 15, 1315.
74. Qiao, S., Hoic, D.A. and Fu, G.C., *J. Amer. Chem. Soc.*, 1996, 118, 6329.
75. Herberich, G.E., Schmidt, B. and Englert, U., *Organometallics*, 1995, 14, 471.
76. Herberich, G.E., Rosenplänter, J., Schmidt, B. and Englert, U., *Organometallics*, 1997, 16, 926.
77. Sugihara, Y., Miyatake, R., Yagi, T., Murata, I., Jinguji, M., Nakazawa, T. and Imamura, A., *Tetrahedron*, 1994, 50, 6495.
78. Dewar, M.J.S., Jie, C. and Zoebisch, E.G., *Organometallics*, 1988, 7, 513.
79. Wissner, A., *Tetrahedron Comp. Methodol.*, 1990, 3, 63.
80. Wheland, G.W. and Mann, D.E., *J. Chem. Phys.*, 1949, 17, 264.
81. Hinze, J. and Jaffé, H.H., *J. Amer. Chem. Soc.*, 1962, 84, 540.
82. Sane, K. and Sane, K.V., *Ind. J. Chem. A*, 1977, 15, 740.
83. Ohno, K., *Theor. Chim. Acta*, 1964, 2, 219.
84. Nishimoto, K. and Mataga, N., *Z. Physik. Chem.*, 1957, 12, 335.
85. Mataga, N. and Nishimoto, K., *Z. Physik. Chem.*, 1957, 13, 140.
86. Stewart, J.J.P., *J. Computer-Aided Molec. Des.*, 1990, 4, 1.
87. Rodriguez, N.M. and Baker, R.T.K., *J. Mater. Res.*, 1993, 8, 1886.

88. Hinze, J., Whitehead, M.A. and Jaffé, H.H., *J. Amer. Chem. Soc.*, 1963, 85, 148.

89. Labanowski, J.K., Dammkoehler, R.A. and Motoc, I., *J. Comput. Chem.*, 1989, 10, 1016.

90. Houser, J.J. and Klopman, G., *J. Comput. Chem.*, 1992, 13, 990.

91. Park, J.M., No, K.T., Jhon, M.S. and Scheraga, H.A., *J. Comput. Chem.*, 1993, 14, 1482.

92. Sternberg, U., Koch, F.-T. and Möllhoff, M., *J. Comput. Chem.*, 1994, 15, 524.

93. Radovic, L.R., Walker, P.L., Jr. and Jenkins, R.G., *Fuel*, 1983, 62, 849.

94. Cermignani, W., Paulsen, T.E., Onneby, C. and Pantano, C.G., *Carbon*, 1995, 33, 367.

95. Walker Jr., P.L., Shelef, M. and Anderson, R.A., in *Chemistry and Physics of Carbon, Vol. 4* (Walker Jr., P.L., Ed.), Marcel Dekker, New York, 1968, p. 287.

96. McKee, D.W., in *Chemistry and Physics of Carbon, Vol. 16* (Walker Jr., P.L. and Thrower, P.A., Eds.), Marcel Dekker, New York, 1981, p. 1.

97. Long, F.J. and Sykes, K.W., *Proc. Roy. Soc.*, 1952, A215, 100.

98. Janiak, C., Hoffmann, R., Sjövall, P. and Kasemo, B., *Langmuir*, 1993, 9, 3427.

99. Yates, K., *Hückel Molecular Orbital Theory*, Academic Press, New York, 1978.

100. Ma, X., Wang, Q., Chen, L.-Q., Cermignani, W., Pantano, C.G. and Schobert, H.H., in *23rd Biennial Conference on Carbon*, State College, PA, Vol. I, 1997, p. 444.

101. Ma, X., Wang, Q., Chen, L.-Q., Cermignani, W., Schobert, H.H. and Pantano, C.G., *Carbon*, 1997, 35, 1517.

102. Wang, Q., Chen, L.-Q. and Annett, J.F., *Phys. Rev. B*, 1996, 54, 2271.

103. Hu, R. and Chung, T.C., *Carbon*, 1996, 34, 1181.

104. Skokova, K., Thrower, P.A. and Radovic, L.R., in *23rd Biennial Conference on Carbon*, State College, PA, Vol. I, 1997, p. 452.

105. Karra, M., The role of boron in carbon oxidation: inhibitor and catalyst. M. S. Thesis, The Pennsylvania State University, in progress.

106. Radovic, L.R., Karra, M. and Skokova, K., in *22nd Biennial Conference on Carbon*, San Diego, CA ,1995, p. 636.

107. van der Kerk, S.M., *J. Organometal. Chem.*, 1981, 215, 315.

FIGURE CAPTIONS

Figure 1. Typical TGA plots for boron-free and boron-doped glassy carbon.

Figure 2. Arrhenius plots for Saran char doped with different amounts of boron and gasified at 1 atm (21% O_2): x, 0% B, 33 kcal/mol; ■, 1.1% B, 33 kcal/mol; Δ, 1.9% B, 30 kcal/mol; ○, 3.8% B, 36 kcal/mol.

Figure 3. X-ray diffraction patterns for Saran char doped with different concentrations of boron.

Figure 4. Effect of reaction temperature on the inhibition effect of boron-doped Saran char for various levels of initial boron concentration: ■, 1.1% B; ●, 1.9% B; ▲, 3.8% B. (R_i and R_o are the reaction rates for doped and undoped samples.)

Figure 5. Effect of conversion level on the inhibition effect of boron-doped Saran char for various levels of initial boron concentration.
(R_i and R_o are the reaction rates for doped and undoped samples.)

Figure 6. Distribution of π electron density in borabenzene according to different MO models. (Values of the Coulomb parameter h_B are shown in parentheses.)

Figure 7. Distribution of free valence in borabenzene according to different MO models. (Values of the Coulomb parameter h_B are shown in parentheses.)

Figure 8. Distribution of π electron density in pyridine according to different MO models.

Figure 9. Distribution of π electron density in borepin according to different MO models. (Values of the Coulomb parameter h_B or valence state ionization potential for B are shown in parentheses.)

Figure 10. Postulated electron distribution in carbon in the presence of a catalyst that exerts an electronic effect. Adapted from Ref. [97].

Figure 11. Reactive surface area vs. conversion for Saran char doped with boron: ○, 0% B; ●, 1.1% B; □, 1.9% B. (RSA estimated at 700 °C and 1 atm, 5% O_2.)

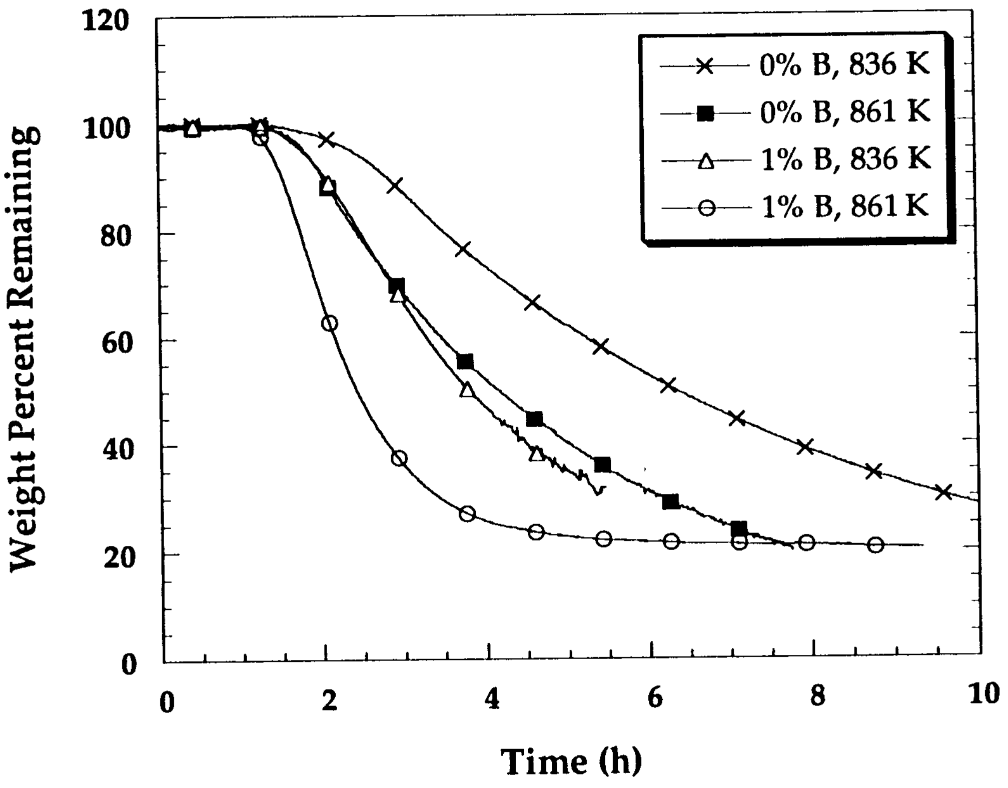
120
100
80
60
40
20
0
Weight Percent Remaining
0
2
4
6
8
10
Time (h)
0% B, 836 K
0% B, 861 K
1% B, 836 K
1% B, 861 K

Figure 1

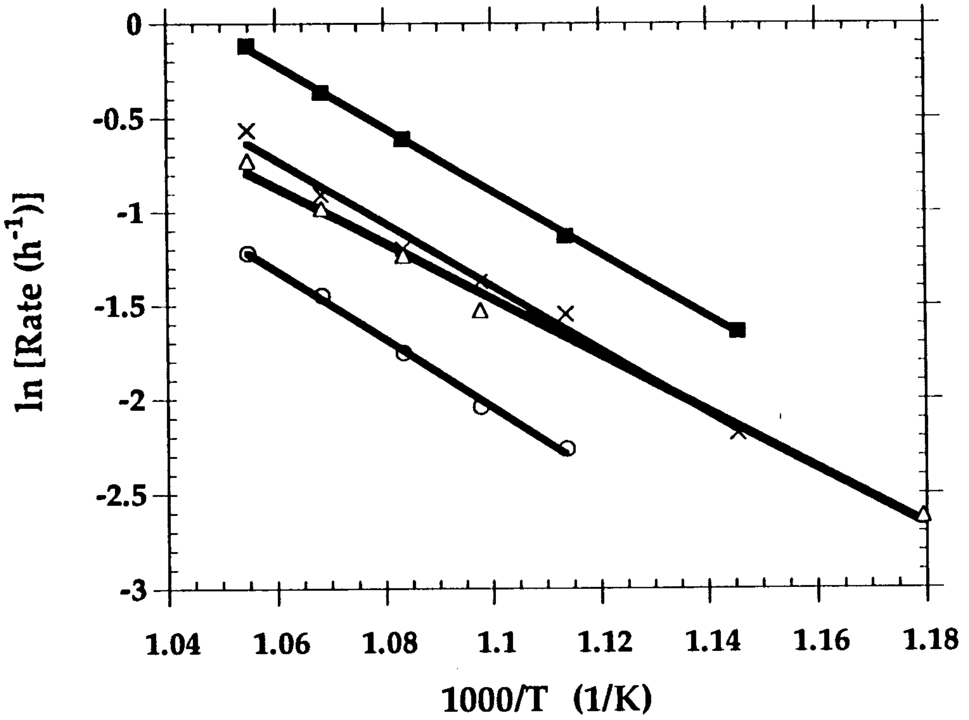

Figure 2

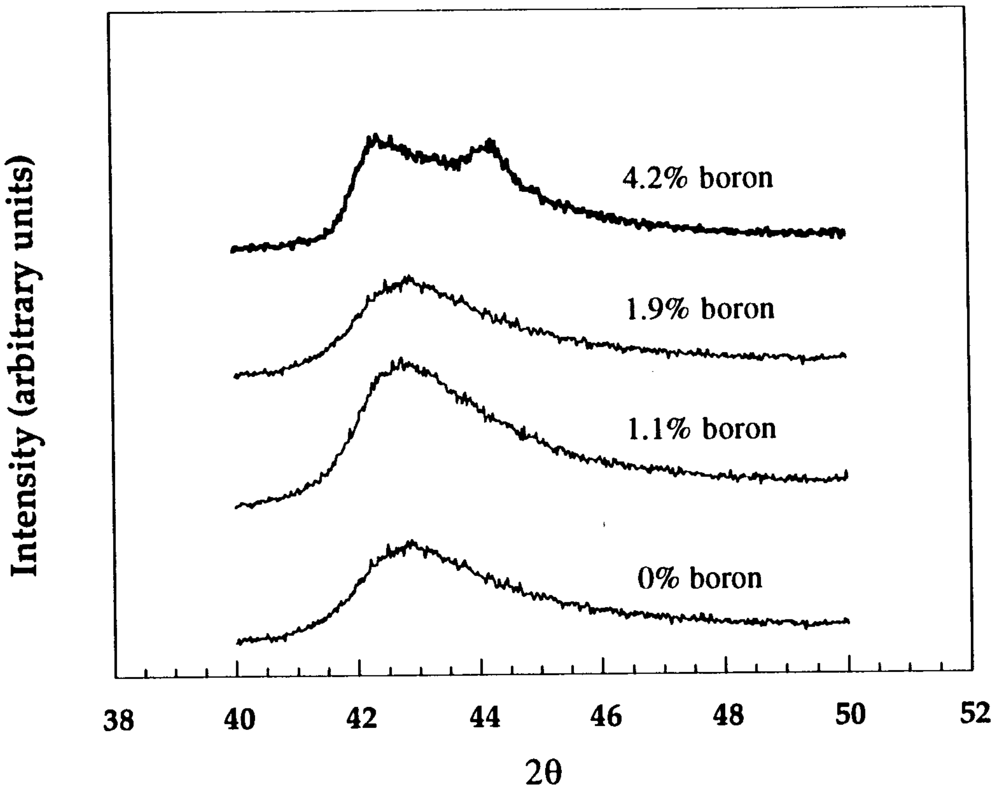
Intensity (arbitrary units)
4.2% boron
1.9% boron
1.1% boron
0% boron
38
40
42
44
46
48
50
52
2θ

Figure 3

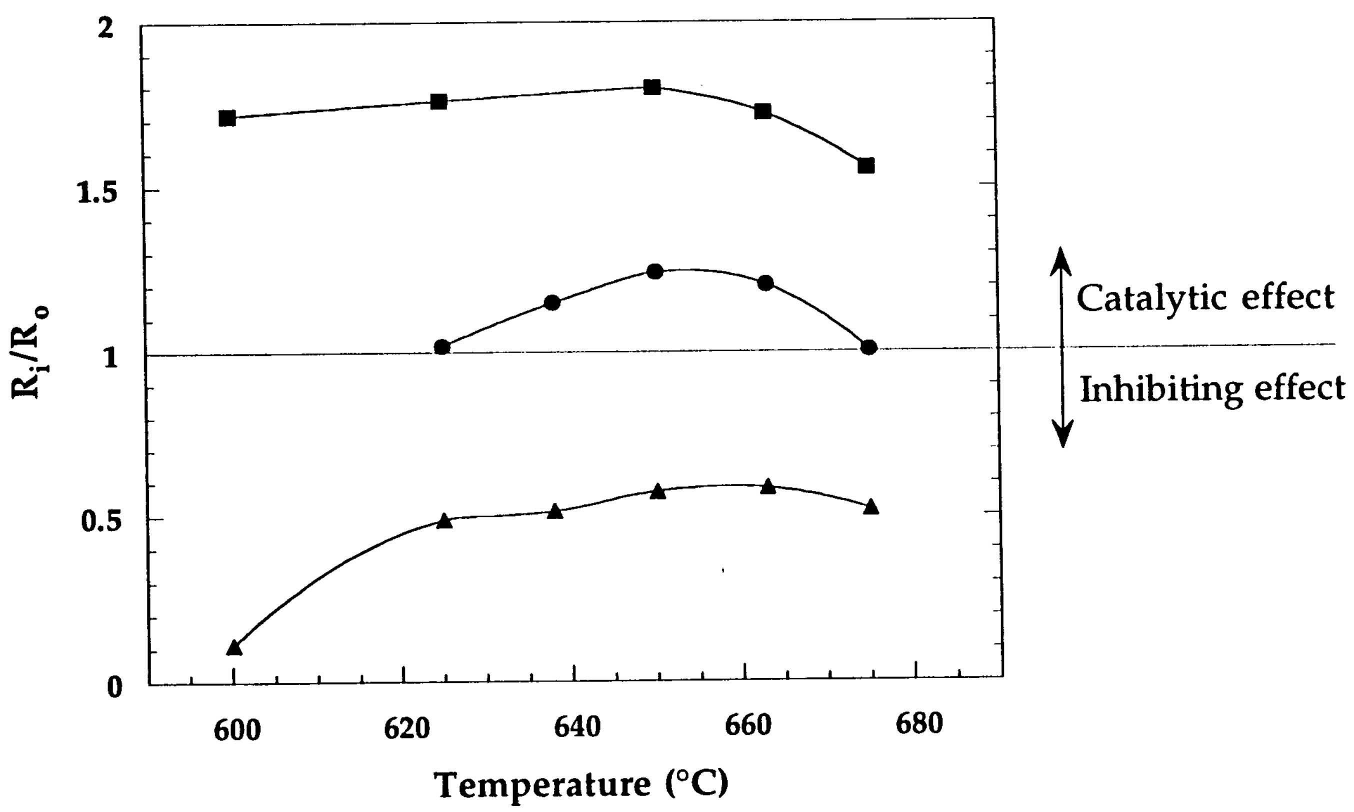
2
1.5
1
0.5
0
R_i/R_o
600
620
640
660
680
Temperature (°C)
Catalytic effect
Inhibiting effect

Figure 4

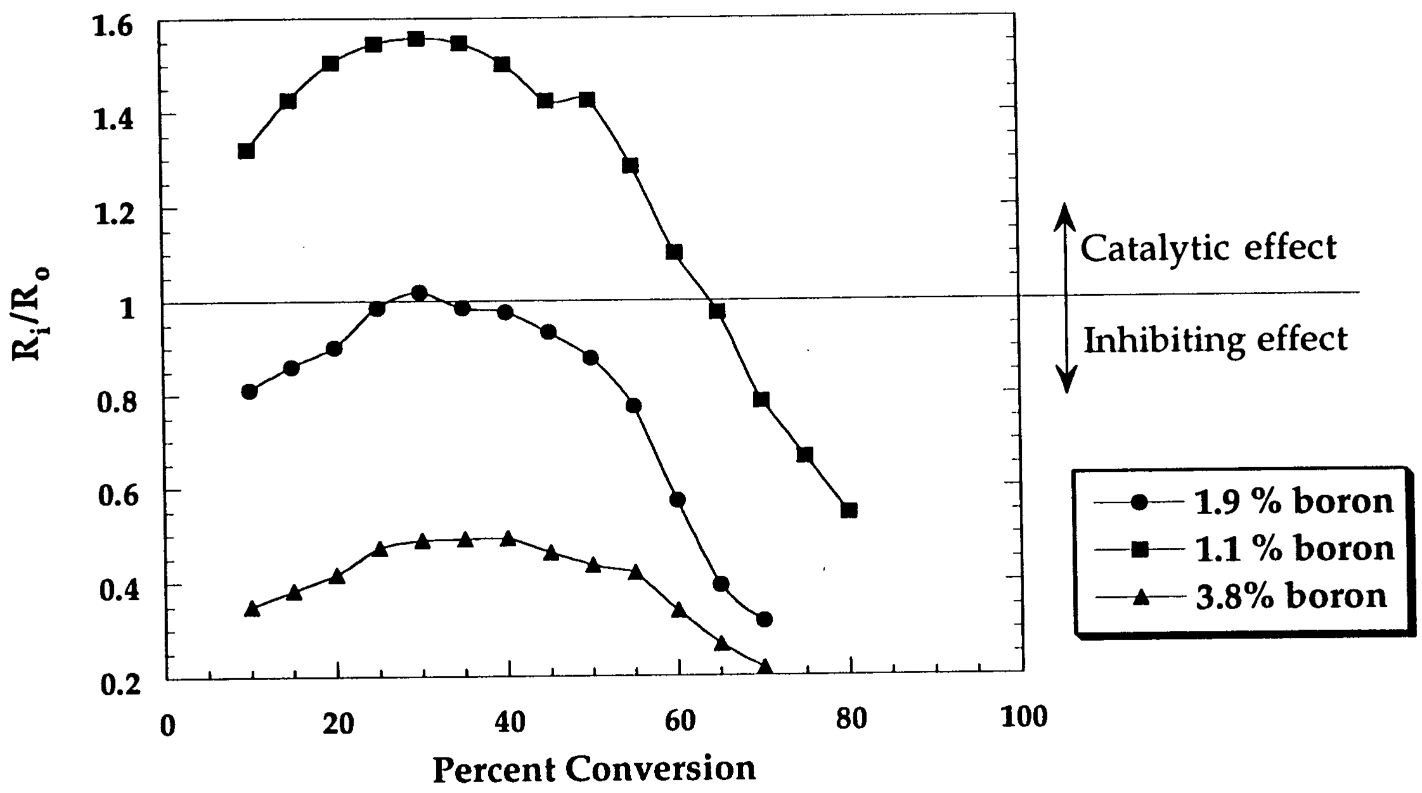
1.6
1.4
1.2
1
0.8
0.6
0.4
0.2
R_i/R_o
0
20
40
60
80
100
Percent Conversion
Catalytic effect
Inhibiting effect
● 1.9 % boron
■ 1.1 % boron
▲ 3.8% boron

Figure 5

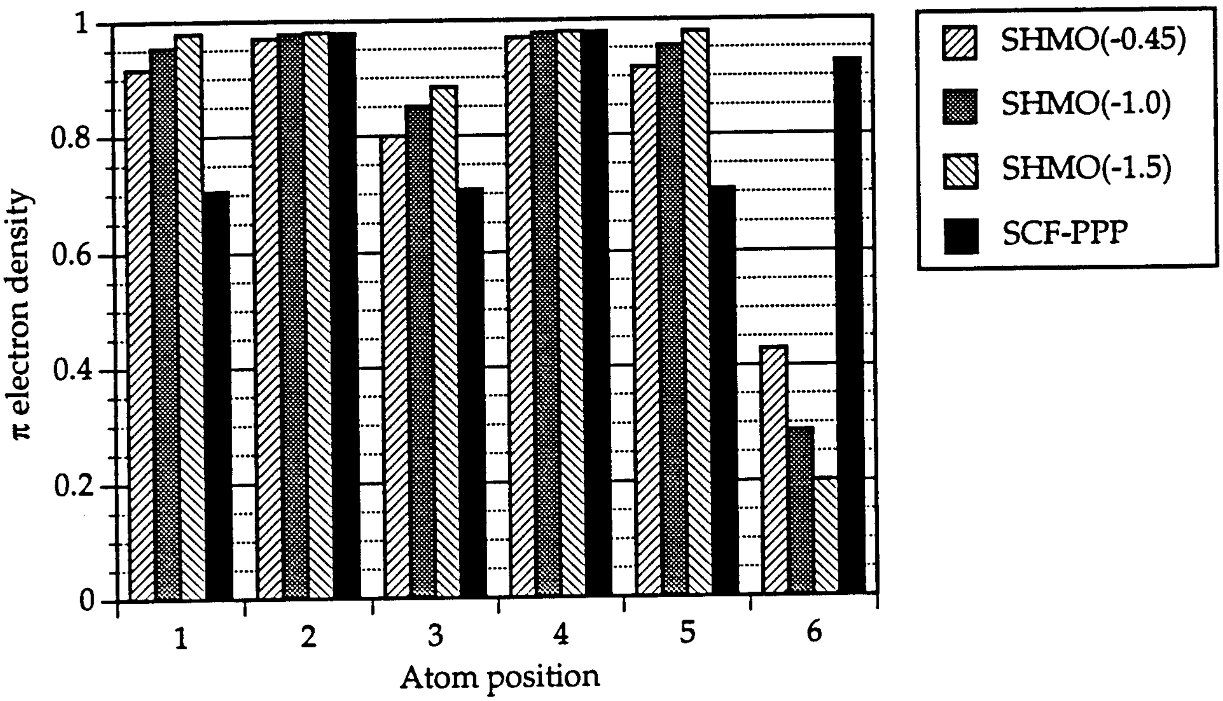
π electron density
1
0.8
0.6
0.4
0.2
0
1
2
3
4
5
6
Atom position
SHMO(-0.45)
SHMO(-1.0)
SHMO(-1.5)
SCF-PPP

Figure 6

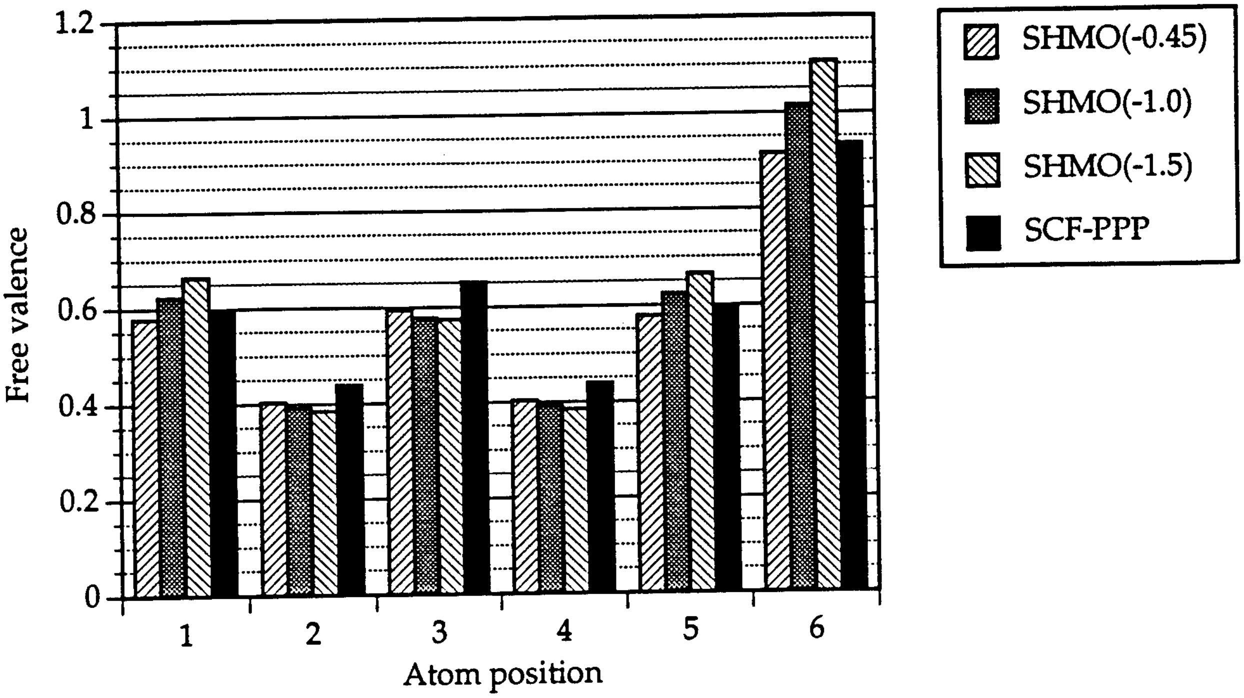
1.2
1
0.8
0.6
0.4
0.2
0
Free valence
1
2
3
4
5
6
Atom position
SHMO(-0.45)
SHMO(-1.0)
SHMO(-1.5)
SCF-PPP

Figure 7

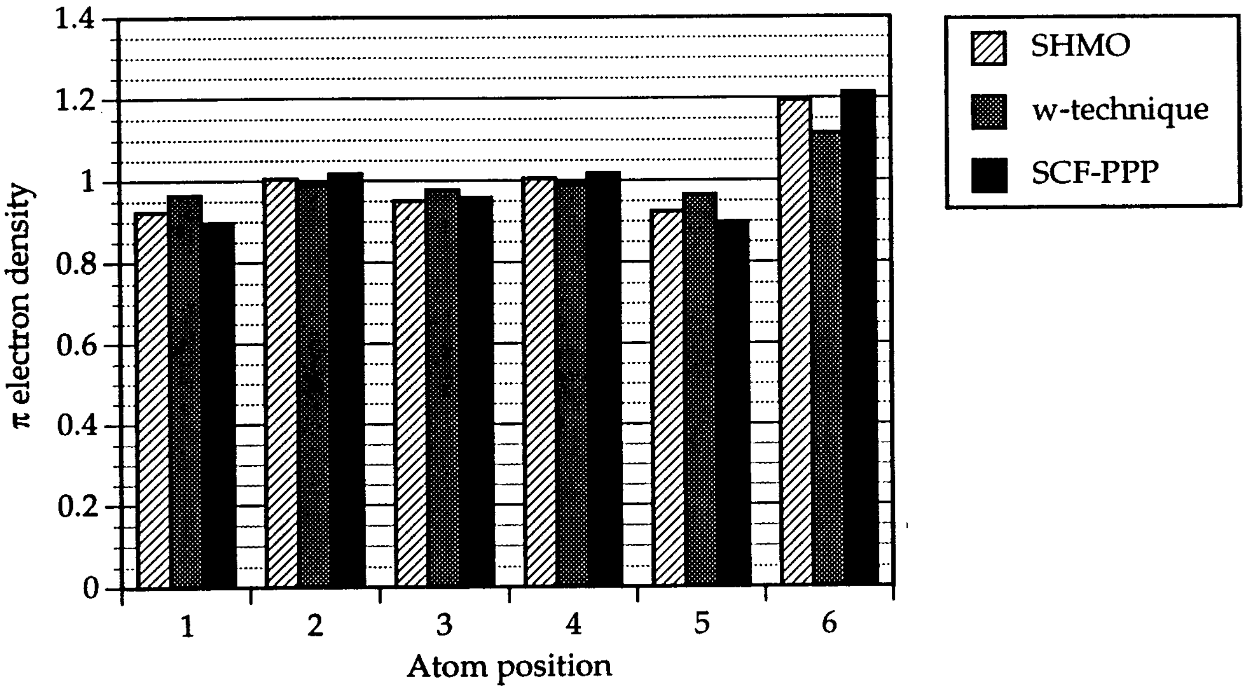
1.4
1.2
1
0.8
0.6
0.4
0.2
0
π electron density
1
2
3
4
5
6
Atom position
▨ SHMO
▩ w-technique
■ SCF-PPP

Figure 8

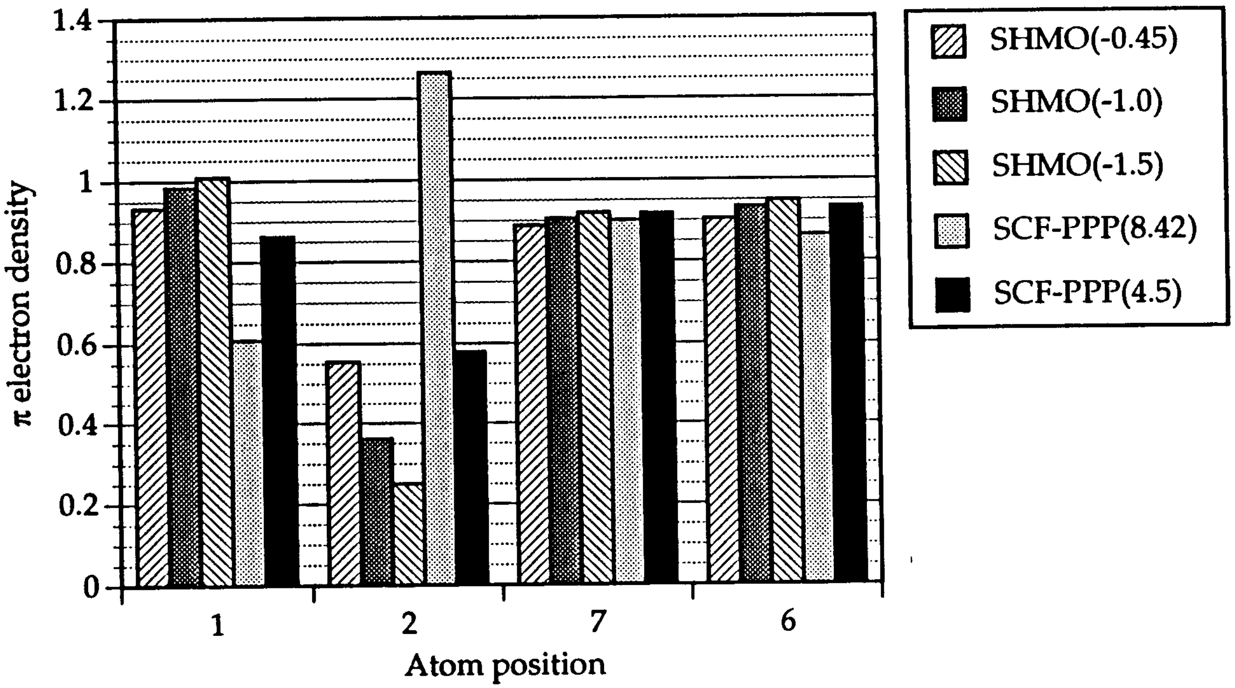
1.4
1.2
1
0.8
0.6
0.4
0.2
0
π electron density
1
2
7
6
Atom position
SHMO(-0.45)
SHMO(-1.0)
SHMO(-1.5)
SCF-PPP(8.42)
SCF-PPP(4.5)

Figure 9

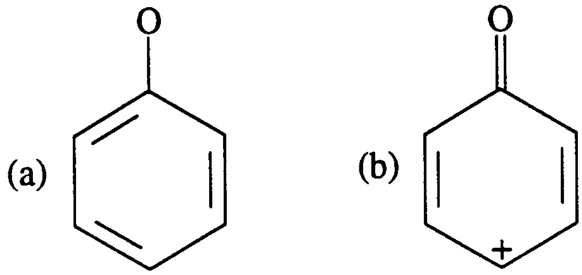

Figure 10

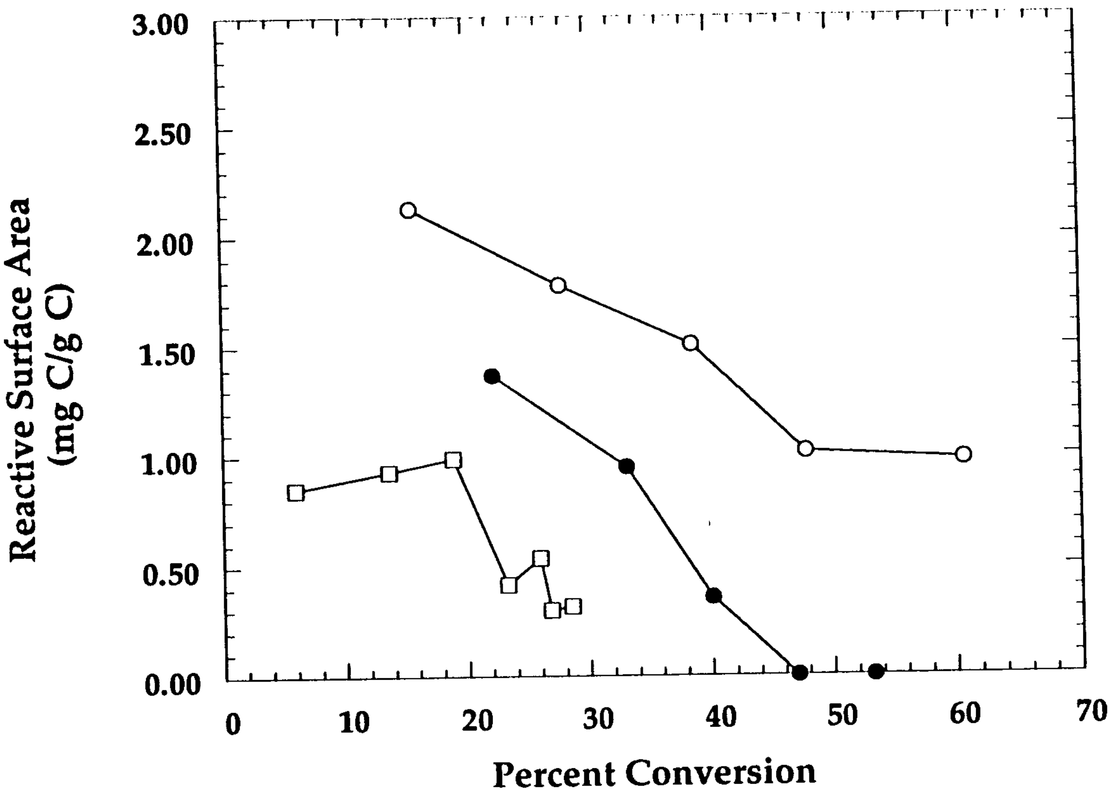
3.00
2.50
2.00
1.50
1.00
0.50
0.00
Reactive Surface Area
(mg C/g C)
0
10
20
30
40
50
60
70
Percent Conversion

Figure 11

Table 1

A compilation of values of electronegativities and Coulomb parameters (h_X) for the 1st row elements of the periodic table

	B	C	N	O	F
Electronegativity (Pauling)	2.0	2.5	3.0	3.5	4.0
Streitwieser [26]					
0 π electrons	-1.00				
1 π electron		0.00	0.50	1.00	
2 π electrons			1.50	2.00	3.00
Dewar and Rogers [38]					
0 π electrons	-1.59				
1 π electron		0.00			
2 π electrons			1.59		
Van-Catledge [31]					
0 π electrons	-0.45				
1 π electron		0.00	0.51	0.97	
2 π electrons			1.37	2.09	2.71
Abraham and Smith [58]					
0 π electrons	-				
1 π electron		0.00	0.33	0.31	
2 π electrons			1.48	1.69	1.67

Table 2

Bonding and antibonding (*) molecular energy levels in pyridine, benzene and borabenzene (in eV)[a]

Energy Level	C_5H_5N	C_6H_6	C_5H_5B
E1	-12.783	-12.613	-12.573
E2	-10.514	-9.393	-9.366
E3	-9.688	-9.393	-8.857
E4*	0.006	0.369	0.197
E5*	0.119	0.369	1.221
E6*	2.565	2.678	3.338

[a] from [66]

Table 3

Molecular energy levels in pyridine, benzene and borabenzene (in eV) calculated using the SCF-PPP theory

Energy Level	C_5H_5N	C_6H_6	C_5H_5B
E1	-12.885	-12.193	-12.781
E2	-10.048	-9.264	-10.186
E3	-9.270	-9.264	-8.774
E4*	-0.200	0.115	-2.765
E5*	0.095	0.115	-0.530
E6*	2.956	3.044	1.243

*antibonding orbitals

Table 4

Electronic properties of benzene, pyridine and borabenzene determined by SHMO and SCF-PPP methods

	C_5H_5N		C_6H_6		C_5H_5B	
			SHMO			
Atom #	Electron density	Free valence	Electron density	Free valence	Electron density	Free valence
1	0.923	0.410	1.0	0.399	0.916	0.578
2	1.004	0.398	1.0	0.399	0.970	0.403
3	0.950	0.401	1.0	0.399	0.800	0.594
4	1.004	0.398	1.0	0.399	0.970	0.403
5	0.923	0.410	1.0	0.399	0.916	0.578
6	1.194	0.084	1.0	0.399	0.428	0.916
			SCF-PPP			
1	0.897	0.416	1.0	0.399	0.706	0.595
2	1.017	0.402	1.0	0.399	0.978	0.439
3	0.958	0.394	1.0	0.399	0.707	0.651
4	1.017	0.402	1.0	0.399	0.978	0.439
5	0.897	0.416	1.0	0.399	0.706	0.595
6	1.213	0.083	1.0	0.399	0.926	0.936

Table 5

Bond lengths in borepin (in Å) according to different MO models

Bond	SHMO [a]		ω-technique [a]	SCF-PPP	*Ab initio*	
	hB=-0.45	hB=-1.5			(b)	(c)
1–2	1.578	1.578	1.578	1.578	1.523	1.537
1–7	1.381	1.376	1.363	1.412	1.345	1.351
6–7	1.414	1.417	1.436	1.390	1.451	1.438
5–6	1.388	1.385	1.370	1.416	1.344	1.349

[a] using the following correlation: bond length = 1.524 - (0.194)(bond order);

[b] from [61];

[c] from [64].

Table 6

Bonding and antibonding (*) MO energy levels in borepin (in β units)

	SHMO (this study)		ω-technique	SHMO ([107])	
Energy level[a]	h_B=-0.45	h_B=-1.5	(h_B=-0.45)	(a)	(b)
E1	1.866	1.843	1.941	1.85	1.86
E2	1.247	1.247	1.333	1.25	1.22
E3	0.892	0.716	0.848	0.76	0.88
E4*	-0.445	-0.445	-0.375	-0.45	-0.49
E5*	-0.548	-0.900	-0.674	-0.77	-0.61
E6*	-1.660	-1.802	-1.710	-1.80	-1.81
E7*	-1.802	-2.159	-1.814	-1.84	-1.82

[a] h_B = -1.0, $k_{C\text{-}B}$ = 0.7;

[b] h_B = -0.6, $k_{C\text{-}B}$ = 0.8 (with additional Coulomb correction for C bound to B).

Table 7

Effect of substitutional boron on the π electron densities of edge carbon atoms in pyrene

Boron position	15	16	13	12	11	2	1	7	8	9	Average
	SHMO (h_B = -0.45)										
-	1.00	1.00	1.00	1.00	1.00	1.00	1.00	1.00	1.00	1.00	1.000
15	0.55	0.95	0.89	1.00	0.89	0.96	0.96	0.92	1.00	0.91	0.942*
10	0.99	0.91	0.88	1.00	0.90	0.93	0.92	0.86	1.00	0.89	0.928
5	0.91	0.94	0.86	1.00	0.86	0.94	0.91	0.86	1.03	0.86	0.917
	SCF-PPP										
-	1.01	1.01	1.02	1.00	1.02	1.01	1.01	1.02	1.00	1.02	1.010
15	1.36	0.60	0.89	1.00	0.93	0.97	0.96	0.91	1.00	0.83	0.900*
10	0.71	0.96	0.95	1.00	0.93	0.98	0.98	0.85	1.00	0.65	0.901
5	0.94	0.89	0.94	1.02	0.94	0.89	0.95	0.89	0.95	0.89	0.930

*without considering atom #15

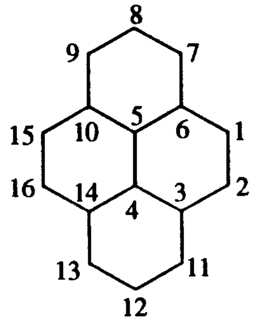
8
9
7
15
10
5
6
1
16
14
4
3
2
13
11
12

(legend for Table 7)

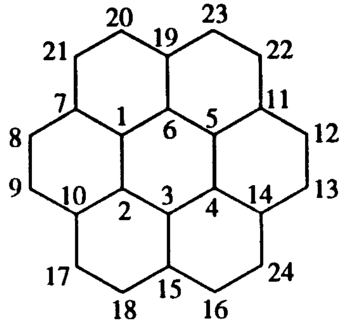
20
23
21
19
22
7
11
1
6
5
8
12
9
10
3
14
13
2
4
17
15
24
18
16

(legend for Tables 8 and 9)

Table 8

Effect of substitutional boron on the π electron densities of edge carbon atoms in coronene

Boron position	8	21	20	23	22	12	13	24	16	18	17	9	Average
	SHMO (h_B = -0.45)												
-	1.00	1.00	1.00	1.00	1.00	1.00	1.00	1.00	1.00	1.00	1.00	1.00	1.000
8	0.52	0.93	0.97	0.98	0.99	0.99	0.95	0.93	0.99	0.99	0.97	0.98	0.970*
7	1.03	1.03	0.94	0.94	0.92	0.94	1.00	1.00	0.94	0.92	0.94	0.94	0.962
1	1.00	1.00	0.91	0.94	0.94	0.96	1.00	1.00	0.96	0.94	0.94	0.91	0.956
6	0.94	0.91	1.00	1.00	0.91	0.94	0.94	0.96	1.00	1.00	0.96	0.94	0.956
	SHMO (h_B = -1.0)												
-	1.00	1.00	1.00	1.00	1.00	1.00	1.00	1.00	1.00	1.00	1.00	1.00	1.000
8	0.32	0.94	0.98	0.99	0.99	0.99	0.97	0.95	0.99	0.99	0.98	1.01	0.981*
7	1.06	1.06	0.95	0.96	0.94	0.95	1.00	1.00	0.95	0.94	0.96	0.95	0.975
1	0.99	0.99	0.91	0.96	0.96	0.98	1.00	1.00	0.98	0.96	0.96	0.91	0.968
6	0.96	0.91	0.99	0.99	0.91	0.96	0.96	0.98	1.00	1.00	0.98	0.96	0.968
	SHMO (h_B = -1.5)												
-	1.00	1.00	1.00	1.00	1.00	1.00	1.00	1.00	1.00	1.00	1.00	1.00	1.000
8	0.21	0.95	0.98	0.99	1.00	1.00	0.98	0.96	1.00	1.00	0.98	1.03	0.987*
7	1.06	1.06	0.95	0.97	0.95	0.96	1.00	1.00	0.96	0.95	0.97	0.95	0.982
1	0.99	0.99	0.92	0.98	0.98	0.99	1.00	1.00	0.99	0.98	0.98	0.92	0.976
6	0.98	0.92	0.99	0.99	0.92	0.98	0.98	1.00	1.00	1.00	0.99	0.98	0.976
	SCF-PPP												
-	1.02	1.02	1.02	1.02	1.02	1.02	1.02	1.02	1.02	1.02	1.02	1.02	1.020
8	1.46	0.93	0.98	0.98	0.96	0.97	1.02	1.00	0.98	0.98	0.93	0.59	0.938*
7	0.80	0.80	0.96	0.98	0.96	0.96	1.03	1.03	0.97	0.96	0.98	0.96	0.949
1	1.00	1.00	0.91	0.98	0.98	0.96	1.03	1.03	0.95	0.98	0.98	0.91	0.975
6	0.98	0.91	0.99	1.00	0.90	0.98	0.98	0.96	1.03	1.03	0.96	0.98	0.975

*without considering atom #8

Table 9

Free valence data for coronene (model graphene layer) in the presence and absence of substitutional boron

Atom #	SHMO				AM1			
	No B	B at 11	B at 5	B at 12	No B	B at 11	B at 5	B at 12
8*	0.449	0.478	0.469	0.453	0.288	0.333	0.290	0.288
9*	0.449	0.449	0.450	0.472	0.288	0.292	0.297	0.290
21*	0.449	0.494	0.477	0.453	0.288	0.239	0.269	0.245
7	0.118	0.122	0.128	0.134	0.238	0.348	0.240	0.284
10	0.118	0.146	0.141	0.118	0.238	0.257	0.231	0.242
17*	0.449	0.449	0.450	0.484	0.288	0.292	0.298	0.302
20*	0.449	0.470	0.480	0.460	0.288	0.268	0.281	0.295
1	0.150	0.155	0.148	0.153	0.222	0.229	0.209	0.227
2	0.150	0.158	0.160	0.152	0.222	0.216	0.291	0.230
18*	0.449	0.478	0.469	0.453	0.288	0.333	0.291	0.292
19	0.118	0.147	0.119	0.126	0.238	0.342	0.231	0.225
6	0.150	0.147	0.158	0.156	0.222	0.222	0.324	0.221
3	0.150	0.155	0.148	0.153	0.222	0.229	0.209	0.230
15	0.118	0.122	0.128	0.146	0.238	0.348	0.240	0.265
23*	0.449	0.461	0.528	0.473	0.288	0.163	0.472	0.314
5	0.150	0.202	-	0.143	0.222	0.416	-	0.247
4	0.150	0.147	0.158	0.190	0.222	0.222	0.324	0.306
16*	0.449	0.494	0.477	0.451	0.288	0.239	0.269	0.296
22*	0.449	0.472	0.442	0.455	0.288	0.249	0.334	0.258
11	0.118	-	0.200	0.149	0.238	-	0.402	0.361
14	0.118	0.147	0.119	0.117	0.238	0.342	0.231	0.254
24*	0.449	0.470	0.480	0.473	0.288	0.268	0.281	0.316
12*	0.449	0.472	0.442	-	0.288	0.249	0.334	-
13*	0.449	0.461	0.528	0.563	0.288	0.163	0.472	0.572
Σ^a	5.388	5.648	5.692	-	3.456	3.088	3.888	-
Σ^b	4.939	5.176	5.250	5.190	3.168	2.839	3.554	3.468

* edge atoms;

[a] total free valence at the periphery of the graphene layer;

[b] calculated without atom #12.

ABSTRACT

The goal of this study was to gain a fundamental understanding of the role of boron in carbon oxidation. Boron-doped carbons were synthesized via CVD, ion implantation and high temperature doping and subsequently characterized. It was found that high temperature doped HOPG carbons were ideal for oxidation studies because their surface could be reproduced, their surface structures were determined and they were able to be characterized by XPS, AFM and SEM. The direct analysis of the chemical structures and atomic arrangements in boron-doped carbon or carbon surfaces by these techniques was critical in determining the effect of boron on carbon oxidation.

XPS was utilized in this work to determine the local bonding environment of boron in carbon before and after oxidation. It was necessary to obtain an accurate calibration of the B1s binding energy scale which was accomplished by obtaining photoemission spectra of boron-doped carbons with known structures (local boron bonding environments), such as boron oxide, boron carbide, triphenylboroxine, tourmaline, boric acid, danburite and high temperature boron-doped graphite. All of the aforementioned standards contain boron in a unique bonding environment and thus their spectra formulated a complete conversion of B1s binding energies to boron chemical environments which had not been reported in the past. It was clearly established that a chemical shift for substitutional boron in graphite exists at 186.5 eV with a FWHM of 1.2. The chemical structures of the boron in the standards were related to the binding energy using a Pauling charge

distribution model and a modification of the Sanderson electronegativity method. This approach was used to determine whether the B1s binding energy would change depending upon the specific location of boron in the graphite or graphite surface. This model was used, along with XPS, TEM and Raman results, to show that edge sites are preferred lattice sites in graphite for boron substitution.

The oxidation behaviors of the synthesized high temperature doped samples were studied with TGA, SEM, XPS and AFM. It was found that boron caused the gasification rates of the carbons to decrease. The SEM and AFM results showed that the pits that were formed in the undoped and doped carbons were different in size, depth and orientation. A semi-empirical Molecular Orbital Package method and experimental results were used to show that the reactivity of the zig-zag edge sites of a pit wall could be reduced by the replacement of carbon atoms with boron atoms at these sites; hence, the oxidation would be inhibited in the a-direction of a graphene layer. Conversely, boron doping on an armchair edge surface of a pit wall results in increased reactivity at these sites and the subsequent formation of boron oxide during oxidation, which does not prevent oxidation in the a-direction of a graphene layer. Rather, the build-up of boron oxide clusters prevented oxidation in the c-direction. A model was proposed for the oxidation inhibition mechanism in boron-doped graphite based upon the stability of pits with boron substitution on the zig-zag sites.